Thermo-hygro-chemo-mechanical model of concrete at early ages and its extension to tumor growth numerical analysis

Giuseppe Sciumè

UNIVERSITÀ DEGLI STUDI DI PADOVA

ENS CACHAN

THESE DE DOCTORAT
DE L'ECOLE NORMALE SUPERIEURE DE CACHAN
ET DE L'UNIVERSITÉ DE PADOUE

Présentée par

Monsieur Giuseppe SCIUME'

pour obtenir le grade de

DOCTEUR DE L'ECOLE NORMALE SUPERIEURE DE CACHAN ET PHILOSOPHIAE DOCTOR (PHD) DE L'UNIVERSITÉ DE PADOUE

Domaine :

MECANIQUE - GENIE MECANIQUE - GENIE CIVIL

Sujet de la thèse :

MODELE THERMO-HYDRO-CHEMO-MECANIQUE DU BETON AU JEUNE AGE ET SON ADAPTATION POUR L'ANALYSE NUMERIQUE DE LA CROISSANCE DES TUMEURS CANCEREUSES

Thèse présentée et soutenue à Padoue le 18 Mars 2013 devant le jury composé de :

Ferdinando AURICCHIO	Professeur	Examinateur
Farid BENBOUDJEMA	Maître de conférences	Co-encadrant de thèse
Yves BERTHAUD	Professeur	Co-directeur de thèse
Stefano DAL PONT	Professeur	Examinateur
Caroline DE SA	Professeure agrégée	Co-encadrant de thèse
Umberto PEREGO	Professeur	Rapporteur
Bernhard SCHREFLER	Professeur	Co-directeur de thèse
Jean-Michel TORRENTI	Directeur de recherche	Rapporteur et Président du jury

Langue du document: Anglais

LMT - Ecole Normale Supérieure de Cachan - 61, avenue du Président Wilson, 94235 Cachan
Dipartimento ICEA - Università degli Studi di Padova - Via Marzolo 9, 35131 Padova

PhD Thesis in ***co-tutelage*** between:

UNIVERSITÀ DEGLI STUDI DI PADOVA
Dipartimento d'Ingegneria Civile, Edile ed Ambientale
Scuola di Dottorato di Ricerca in Scienze dell'Ingegneria Civile ed Ambientale - Ciclo XXV
&
ÉCOLE NORMALE SUPÉRIEURE DE CACHAN
Laboratoire de Mécanique et Technologie (LMT-Cachan)
École Doctorale Sciences Pratiques

THERMO-HYGRO-CHEMO-MECHANICAL MODEL OF CONCRETE AT EARLY AGES AND ITS EXTENSION TO TUMOR GROWTH NUMERICAL ANALYSIS

Director of the Italian PhD School: Prof. Stefano LANZONI
Italian PhD Co-Director: Prof. Bernhard SCHREFLER
French PhD Co-Director: Prof. Yves BERTHAUD

PhD Student: Giuseppe SCIUME'

PhD mobility partially funded by

UNIVERSITÀ ITALO FRANCESE

FRENCH ABSTRACT

Modèle thermo-hydro-chemo-mécanique du béton au jeune âge et son adaptation pour l'analyse numérique de la croissance des tumeurs cancéreuses.

Mots-clés: multi-physique, multiphasique, hydratation, retrait, fluage, cellules, division cellulaire, nécrose.

L'objectif du travail de thèse a été la mise en place de deux modélisations multi-physiques fondées sur des fondements théoriques communs mais appliquées à deux domaines de la recherche scientifique très différents: i) l'étude du comportement du béton au jeune âge pour la prévention de la fissuration précoce; ii) l'analyse des phénomènes physiques, chimiques et biologiques qui gouvernent la croissance et l'évolution de la tumeur cancéreuse.

Le développement d'un outil numérique pour la modélisation du béton au jeune âge est très important pour la conception de structures durables. Le modèle développé pendant la thèse doctorale a été implanté sur le code aux éléments finis Cast3M, puis validé expérimentalement. Il permet de multiples applications: étude des sollicitations et des phénomènes de fissuration au jeune âge, gradients thermiques et hydriques, prédiction du retrait endogène et de dessiccation, étude de l'inhibition de l'hydratation causée par le séchage, prédiction du fluage et de la redistribution des contraintes associées, étude des réparations.

Les équations qui gouvernent le comportement thermo-hydro-chemo-mécanique du béton au jeune âge ont plusieurs analogies formelles avec celles qui sont typiquement à la base de la modélisation de la croissance des tumeurs cancéreuses. L'élargissement de l'analyse numérique dans le domaine médical est d'un grand intérêt social en complément de l'intérêt scientifique. Les équations utilisées pour le béton ont été réadaptées, et le modèle mathématique obtenu a été implanté dans Cast3M. Les premiers résultats du modèle ont été satisfaisants et qualitativement très proches des données expérimentales de la littérature dans ce domaine.

ITALIAN ABSTRACT

Modello termo-igro-chemo-meccanico del calcestruzzo giovane e suo adeguamento per l'analisi numerica della crescita e dell'evoluzione del tumore.

Parole chiave: multi-fisico, multifase, idratazione, ritiro, deformazione differita, cellule, divisione cellulare, necrosi.

L'obiettivo del Dottorato è stato lo sviluppo di due modelli multifase basati su fondamenti teorici comuni ma applicati a due campi della ricerca scientifica molto diversi: i) lo studio del comportamento termo-igro-chemo-meccanico del calcestruzzo giovane; ii) l'analisi dei fenomeni fisici, chimici e biologici che regolano la crescita e lo sviluppo dei tumori.

La modellazione numerica del comportamento del calcestruzzo giovane è di grande importanza per la progettazione di strutture sostenibili e durevoli. Il modello sviluppato durante il Dottorato è stato implementato nel codice agli elementi finiti Cast3M e in seguito validato con la simulazione di casi sperimentali. Il modello numerico consente un'ampia gamma di applicazioni: studio delle sollecitazioni e dei fenomeni di fessurazione nel calcestruzzo durante i primi giorni dopo la posa in opera, analisi dei gradienti termici e igrometrici, valutazione del ritiro autogeno e di essiccazione, studio dell'inibizione dell'idratazione causata dall'essiccazione, ridistribuzione delle tensioni dovuta al ritiro e alle deformazioni differite, modellazione delle riparazioni.

Le equazioni che governano il comportamento termo-igro-chemo-meccanico del calcestruzzo hanno molte analogie formali con quelle che sono tipicamente alla base della modellazione della crescita dei tumori. L'allargamento dell'analisi numerica al campo medico è di grande interesse sociale oltre che scientifico, pertanto le equazioni utilizzate per il calcestruzzo sono state riadattate per la modellazione della crescita tumorale, e il modello matematico ottenuto è stato anch'esso introdotto in Cast3M. I primi risultati di questo modello sono stati soddisfacenti perché qualitativamente molto simili ai dati sperimentali della letteratura scientifica.

ABSTRACT

Keywords: multi-physics, multiphase, hydration, shrinkage, creep, cells, cell division, necrosis.

The aim of the PhD thesis is the development of two multiphase models from a common theoretical basis, applied to two very different research fields: i) the study of the behavior of concrete at early ages, essentially for the prevention of cracking and related issues; ii) the analysis of the physical, chemical and biological processes that govern the growth of cancer.

The modeling of concrete at early ages is very important and useful for the design of durable and sustainable structures. The model developed during the PhD thesis has been implemented on the finite element code Cast3M and then validated *via* the simulation of experimental cases. Nowadays this model allows for several applications: study of stresses and cracking in young concrete, analysis of thermal and hygral gradients, predictions of autogenous and drying shrinkage, creep strain, stress redistribution, study of the inhibition of hydration caused by drying, study of repairs, etc..

In the fight against cancer, the advance of medical strategies based on numerical analysis has a crucial scientific interest and can have a great social impact. The equations which govern the thermo-hygro-chemo-mechanical behavior of concrete at early ages have many formal analogies with those typically used to model tumor growth. Hence, these equations have been readapted and a novel mathematical model for tumor growth has been developed. This model has been implemented in Cast3M and the first numerical results are encouraging since qualitatively close to the experimental data present in the scientific bibliography.

CONTENTS

PREFACE AND ACKNOWLEDGMENTS

At the beginning of my PhD studies the title of my work was “Multiphysics modeling of concrete at early age” and concrete was the only subject of my investigation. I did my PhD in co-tutelage between the University of Padua and the Laboratory of Mechanics and Technology of Cachan (LMT-Cachan) and in both these places the analysis of concrete behavior is a fundamental topic. Indeed, I think in the LMT-Cachan sector Civil Engineering “béton” is the most said word of each day. In this context, with the scientific support of my PhD Directors Bernhard Schrefler, Professor at University of Padua, and Yves Berthaud, Professor at University Pierre et Marie Curie (UPMC), and of Farid Benboudjema and Caroline De Sa, Professors at ENS-Cachan, the research had a good evolution and after about 20 months (mostly spent in Cachan) I developed a thermo-hygro-chemo-mechanical model, afterward implemented in Cast3M (finite element code of the French atomic agency, CEA), and finally validated during *ConCrack*, a French international benchmark on control of cracking in concrete reinforced structures. Hence, I started writing my manuscript when one day my Italian Director Bernhard Schrefler told me that he wants to model tumor growth using a mathematical approach very close to that already developed for concrete during my PhD. I liked the idea and from that moment I started working also on tumor growth modeling.

I wish to express my gratitude to my PhD Directors, Bernhard Schrefler and Yves Berthaud to my French Supervisors Farid Benboudjema and Caroline de Sa and to my Italian Supervisor Francesco Pesavento, Professor at University of Padua, for their friendliness and scientific support during these three years. Also I acknowledge the technical support of Alain Millard, Research Engineer at CEA, in the implementation of the model in Cast3M, and the courtesy of Jean-Michael Torrenti, Professor at IFSTTAR (Institut Français des Sciences et Technologies des Transports, de l’Aménagement et des Réseaux) and Umberto Perego, Professor at Politectnico di Milano, who have agreed to examine my thesis. Finally, a Thanksgiving full of affection to my mother Filomena and my father Calogero for their support and encouragement throughout my studies.

LIST OF SYMBOLS AND ABBREVIATIONS

ABBREVIATIONS

CIT	Classical Irreversible Thermodynamics
eqn	equation
eqs	equations
FE	Finite Element
HMT	Hybrid Mixture Theory
ITZ	Interfacial Transition Zone
M	Mechanical
REV	Representative Elementary Volume
TCAT	Thermodynamically Constrained Averaging Theory
THC	Thermo-Hygro-Chemical

GENERAL AND TCAT SYMBOLS

Arabic numerals

$\mathbf{1}$	identity tensor

Greek letters

ε	porosity
ε^{α}	volume fraction of the phase α
θ^{α}	relative temperature
$\boldsymbol{\lambda}^{\alpha}$	thermal conductivity
μ^{α}	dynamic viscosity of the phase α
ρ^{α}	density of the phase α
$\sum_{\kappa \in \mathfrak{I}_{c\alpha}}$	sum over the set of entities connected to phase α
$\psi^{\bar{\alpha}}$	gravitational potential

Roman letters

C_p^{α}	specific heat of the phase α at constant pressure

$\mathbf{d}$ rate of strain tensor $\mathbf{d} = \frac{1}{2}\left[\nabla\mathbf{v} + (\nabla\mathbf{v})^T\right]$

$\overline{\overline{E^{\alpha}}}$ internal energy

$\overline{\mathbf{g}^{\alpha}}$ gravitational force

$\overline{\overline{K_E^{\alpha}}}$ kinetic energy due to microscale velocity fluctuations

$\overset{\kappa\to\alpha}{M}$ inter-phase mass transfer

$\overset{\kappa\to\alpha}{M_E}$ transfer of energy due to phase change

$\overline{\overline{\mathbf{q}^{\alpha}}}$ heat flow vector

$\overset{\kappa\to\alpha}{Q}$ transfer of energy due to heat transfer

$r^{i\alpha}$ intra-phase mass transfer

$\mathbf{R}^f$ resistance tensor

s^{α} heat source

$\overline{\overline{\mathbf{t}^{\alpha}}}$ stress tensor

$\overset{\kappa\to\alpha}{\mathbf{T}}$ inter-phase momentum transfer

$\overset{\kappa\to\alpha}{T_v}$ transfer of energy due to interfacial stress

$\overline{\mathbf{v}^{\alpha}}$ velocity vector

SYMBOLS IN THE CONCRETE SECTIONS (CHAPTERS 1, 2 AND 3)

Greek letters

$\bar{\alpha}$ Biot's coefficient

$\bar{\alpha}_{\infty}$ final Biot's coefficient

α_T thermal expansion coefficient

β function which depends on the relative humidity

β_{cr} constant coefficient which allows to couple damage with creep

β_{kl} constant coefficient in the function $\Psi(S^l)$

γ liquid-gas system surface tension

γ_E exponent in the function which regulates the evolution of E with hydration

γ_{FT} exponent in the function which regulates the evolution of f_t with hydration

Γ degree of reaction

Γ_i constant coefficient in the desorption isotherm function

Γ_p degree of reaction correspondent to the peak of affinity – constant in A(Γ)

Γ_0 percolation threshold

δ_{dc} constant coefficient which regulates the amplitude of the drying creep strain

ζ constant coefficient in A(Γ) – it regulates the deceleration phase of hydration

η_{bci} viscosity of the dashpot in the creep cell *i*

κ_0 maximal extension of concrete

ν Poisson's ratio

ν_∞ final value of the Poisson's ratio

ξ hydration degree

ξ_∞ final hydration degree

τ_{bci} characteristic time of the Kelvin-Voigt chain *i*

φ_h hygral convective coefficient

φ_t thermal convective coefficient

χ^α solid surface fraction in contact with the fluid phase α (i.e. Bishop's parameter)

Ψ function which allows to take into account the Klinkenberg's effect

Ω volume faction of the cement paste

Roman letters

a constant coefficient in the desorption isotherm function

a_h constant coefficient in the function β

a_ε constant coefficient in the porosity equation $\varepsilon(\Gamma)$

A chemical affinity equation which regulates the hydration reaction

A_i initial chemical affinity - constant coefficient in A(Γ)

A_p affinity peak value - constant coefficient in A(Γ)

A_k constant coefficient in the intrinsic permeability function $k(\Gamma)$

A_t constant coefficient in the damage model

b constant coefficient in the desorption isotherm function

B_t constant coefficient in the damage model

c mass of cement present in the mix

c_Γ constant coefficient in the desorption isotherm function

c_{hydr} mass of hydrated cement

$\mathbf{C}_{ij}$ non linear coefficient of the discretized capacity matrix

D mechanical damage

$D_0^{\overline{Wg}}$ diffusivity of water vapour in the gaseous phase

$D^{\overline{Wg}}$ effective diffusivity of water vapour in concrete

$\mathbf{e}$ total strain

$\mathbf{e}_{cr}$ creep strain

$\mathbf{e}_{th}$ thermal strain

$\mathbf{e}_{sh}$ shrinkage strain

$\mathbf{e}_{sh}^{inst}$ instantaneous shrinkage strain

$\mathbf{e}_{sh}^{visc}$ viscous shrinkage strain

$\widehat{e}$ equivalent strain (used in the damage model)

$e_{\mathrm{cr}i}$ scalar creep strain of the creep cell i

E_a activation energy

$\mathbf{E}$ tangent matrix

E_∞ final value of the Young's modulus

f_s in the effective diffusivity equation is the tortuosity function ($f_s = f_s(\Gamma)$)

f_t tensile strength

$f_{t\infty}$ final value of the tensile strength

$\mathbf{f}_i$ discretized source term associated with the primary variable i

g_{ft} density of the dissipated energy

G_{ft} fracture energy

h relative humidity

H_{hydr} specific enthalpy of hydration

H_{vap} specific enthalpy of vaporization

$k_{\mathrm{bc}i}$ stiffness of the spring in the creep cell *i*

$k_{\mathrm{bc}i\_\infty}$ final stiffness of the spring in the creep cell *i*

k_{∞} final intrinsic permeability

K^{T} Bulk's modulus of concrete

K_{∞}^{T} final Bulk's modulus of concrete

K^{S} Bulk's modulus of the solid phase

$\mathbf{K}_{ij}$ non linear coefficient of the discretized conduction matrix

l_c characteristic length

L_{hydr} latent heat of hydration

$\overset{l\rightarrow Hs}{m}$ mass of chemically combined water

$\overset{l\rightarrow Hs}{m_{\infty}}$ final mass of chemically combined water

M_{α} molar mass of the phase α

n_{∞}^{cp} final porosity of the cement paste

n^{As} porosity of the aggregate

p_{atm} atmospheric pressure

p_0 constant coefficient in the function $\Psi(S^l)$

$\mathbf{q}^{l}$ flow vector of the liquid phase

r averaged radius of the menisci

R gas constant in the ideal gas equation

s content of silica fume in the mix

$\overset{=}{\mathbf{t}}_{eff}^{s}$ effective stress tensor in the sense of porous media mechanics

$\tilde{\mathbf{t}}$ effective stress tensor in the sense of damage mechanics

$t_{\mathrm{sp}i}$ scalar stress in the spring in the creep cell *i*

$t_{\mathrm{ds}i}$ scalar stress in the dashpot in the creep cell *i*

T absolute temperature

$\mathbf{u}^{\alpha}$ displacement vector of the phase α

w content of water in the mix

$\mathbf{x}$ solution vector

Subscripts and superscripts

α phase indicator with α = *l*, *s* or *g*

Ag dry air

As aggregate

cp cement paste

Cs cement

g gaseous phase

Hs hydration products

l liquid water

s solid phase

Wg water vapour

SYMBOLS IN THE TUMOR SECTION (CHAPTER 4)

Greek letters

$\bar{\alpha}$ Biot's coefficient

β coefficient for the interpolation of the growth curve

γ^{t}_{growth} growth coefficient

$\gamma^{t}_{necrosis}$ necrosis coefficient

$\gamma^{\bar{nl}}_{growth}$ nutrient consumption coefficient related to growth

$\gamma^{\bar{nl}}_{0}$ nutrient consumption coefficient not related to growth

δ exponent in the effective diffusion function for the oxygen

δ^{t}_{a} additional necrosis induced by pressure excess

δ_{living} coefficient for the interpolation: thickness of the viable rim of tumor cells

σ_{c} coefficient in the pressure-saturations relationship

$\varsigma^{\bar{\alpha}}$ chemical potential

χ^{α} solid surface fraction in contact with the phase α

$\omega^{N\bar{t}}$ mass fraction of necrotic cells in the tumor cells phase

$\omega^{\bar{nl}}$ nutrient mass fraction in liquid.

$\omega^{\bar{nl}}_{crit}$ critical nutrient mass fraction in liquid for growth

$\omega_{env}^{\bar{nl}}$ reference nutrient mass fraction in the environment

Roman letters

$\mathbf{A}^{\alpha}$ fourth order tensor that accounts for the stress-rate of strain relationship

a coefficient for the interpolation of the growth curve

a_{α} adhesion of the phase α

b exponent in the pressure-saturations relationship

$\mathbf{C}_{ij}$ non linear coefficient of the discretized capacity matrix

$\mathbf{d}^{\bar{\alpha}}$ rate of strain tensor

$D_{eff}^{\bar{il}}$ diffusion coefficient for the species i dissolved in the phase l

$D_{eff}^{\bar{il}}$ effective diffusion coefficient for the species i dissolved in the phase l

$\mathbf{D}_s$ tangent matrix of the solid skeleton

$\mathbf{e}^s$ total strain tensor

$\mathbf{e}_{el}^s$ elastic strain tensor

$\mathbf{e}_{vp}^s$ visco-plastic strain tensor

$\mathbf{e}_{sw}^s$ swelling strain tensor

$\mathbf{f}_i$ discretized source term associated with the primary variable i

H Heaviside step function

$\mathbf{k}^{\alpha s}$ absolute permeability tensor of the phase α

k_{rel}^{α} relative permeability of the phase α

$\mathbf{K}_{ij}$ non linear coefficient of the discretized conduction matrix

$\mathbf{N}_v$ vector of shape functions related to the primary variable v

p^{α} pressure in the phase α

p_{crit}^t tumor pressure above which growth is inhibited

p_{necr}^t tumor pressure above which stress causes an increase of the death rate

r_{∞} tumor radius at sufficiently large time

r^{sph} radius of the spheroid

r^{nc} radius of the necrotic core

$\mathbf{R}^{\alpha}$	resistance tensor
S^{α}	saturation degree of the phase α
$\mathbf{t}^{\overline{=}s}_{eff}$	effective stress tensor of the solid phase *s*
$\mathbf{t}^{\overline{=}s}_{tot}$	total stress tensor of the solid phase *s*
$\mathbf{u}^{s}$	displacement vector of the solid phase *s*
$\mathbf{x}$	solution vector

Subscripts and superscripts

α	phase indicator with α=*t*,*h*,*l*, or *s*
crit	critical value for growth
h	host cell phase
l	interstitial fluid
n	nutrient
necr	critical value for the effect of pressure on the cell death rate
s	solid
t	tumor cell phase

GENERAL INTRODUCTION

Porous media mechanics is a major branch of continuum mechanics since it is of interest for a lot of engineering applications. A porous medium consist of a solid porous matrix saturated by one or more fluids phases. In geomechanics depending on the saturation degree of the liquid water, complete or partial, we distinguish between saturated and partially saturated porous media respectively. In the following list the main features of porous media are indicated.

i. Each phase can consist of several species. For instance, in the concrete model presented here, the gas in the pores consists of dry air and water vapour.
ii. There are interactions and momentum exchanges between the fluid phases and between these and the solid skeleton. Hence, part of strains is associated with the fluids-solid mechanical interactions.
iii. If the porous medium is not in hygral equilibrium (internal and with the external environment), mass transport of the different fluid phases and species occurs.
iv. Mass exchanges between the different phases of the system may arise. For instance vaporization of the liquid water and/or dissolution of the solid phase in the liquid one may happen.
v. In non-isothermal conditions, temperature variation impacts on mass exchanges; also mass transport is actually coupled with temperature and thermal gradients.
vi. The macroscopic behavior of a porous medium is significantly connected with the microstructure of the solid matrix and with the micro-scale physics. Hence, to achieve a meaningful set of macroscopic equations, these must be obtained taking into account the pore scale thermodynamics.

According with the previous list, porous media modeling should be multiphase and multiphysics, and must take into account phenomena also at scales different than the macroscopic one (microscale and mesoscale). These aspects are the basis of the Thermodynamically Constrained Averaging Theory (TCAT) developed by Gray and Miller in this last decade (Gray and Miller, 2005). In the TCAT procedure the balance equations are initially written at the microscale and then upscaled by averaging theorems to obtain the macroscopic balance equations. The main difference between the TCAT and its “big sister” i.e. the Hybrid Mixture Theory (HMT) (Hassanizadeh and Gray, 1979a,

1979b and 1980), is that in the HMT the respect of entropy inequality is guaranteed only at the macroscale (so not assured at the microscale), whilst in the TCAT balance equations for entropy of each phase are written at the microscale, and then upscaled similarly to the other balance equations; this assures that thermodynamic restrictions are respected at both the microscopic and the macroscopic scales, and gives the advantage that closure relationships exploiting the entropy inequality can be obtained and introduced also at the microscale. Sometimes the macroscopic behaviour cannot be explained exhaustively at the macroscale but depends on well-known microscopic phenomena; in that case the introduction of closure relationships at the microscale can be helpful. The ***rigorous connection between the microscale and the macroscale*** given by the TCAT procedure allows to take into account also pore scale properties of the phases which typically do not appear in classical models of flow where the balance equations are directly written at the macroscale. An example of this situation is fluid wettability as measured by the contact angle between fluid interfaces and the solid phase at the pore scale; wettability is well known to affect drastically multiphase flow at the macroscale, but does not appear in classical models of flow at that scale.
The main features of the TCAT procedure are reported and discussed in ***Paragraph 1.2***. However the mathematical procedure employed for upscaling is not fully shown because it has not be developed during the PhD thesis; the mathematical framework is presented in detail in the papers of Gray and Miller (2005 and subsequent papers).

The contents of the thesis and its structure reflect the research during the three year of PhD studies (2010-2012). Most of this time has been spent on the analysis of concrete behavior and on the development of a numerical tool capable to model strains of concrete at early age and prevent the related issues (early age cracking which may reduce the service life of the structure). Hence, three chapters of the thesis are dedicated to this part of the research (see ***Figure 1***). In ***Chapter 1*** TCAT is used as the rigorous theoretical base from which the mathematical formulation of the model of concrete at early age is fully developed. All the governing balance equations and constitutive equations are reported together to the relationships between the main properties of concrete and its hydration degree. The model is mainly inspired to the approach of Gawin, Pesavento and Schrefler (2006a and 2006b); however there are some differences between this reference formulation and the presented model and these are indicated in the text. In ***Chapter 2*** the experimental behavior of concrete is presented by means of the analysis of experimental

results taken from bibliography. A number of numerical examples are also shown and discussed to evidence the potentialities of the numerical model in terms of quantity (temperature, relative humidity, saturation degree, gas pressure, hydration degree, thermal strains, autogenous and drying shrinkage, creep, damage), and quality of the results by means of comparison with experimental ones. Cement hydration, drying, shrinkage and creep are the themes of this chapter. Within this chapter some aspects of the model are discussed in detail and compared with other approaches present in literature.

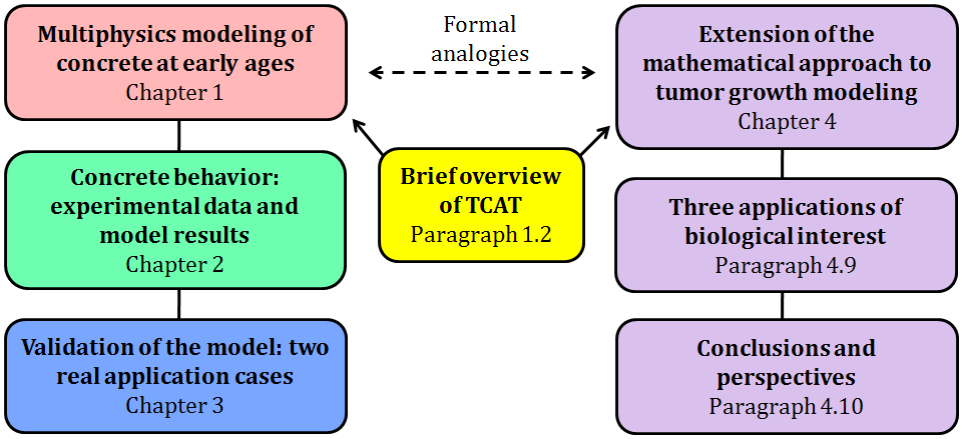

Figure 1 - Structure of the thesis

In ***Chapter 3*** the numerical model is validated through its application to two real cases. The first application case is one of the experiments performed during the French international benchmark on control of cracking in reinforced concrete structures *ConCrack*[1]. The second case is the repair of two beams using an ordinary concrete and a fiber reinforced ultra-high-performance concrete. A good agreement is shown between the experimental results and the numerical ones. In the last paragraph of the chapter other application perspectives (for instance the analysis of prestress losses in pretensioned concrete structures) of such a model are indicated.

Chapter 4 is the last one of the thesis and deals with the other theme of the PhD research, i.e. tumor growth modeling. After a brief introduction of the research context and a short bibliographic analysis of the models present in literature, the TCAT procedure is followed to develop the mathematical model. The governing equations and the introduced constitutive relationships are presented and explained. Numerical results for

[1] This benchmark has been organized within the French project CEOS (*Comportement et Evaluation des Ouvrages Speciaux vis-à-vis de la fissuration et du retrait*) a national French project on behaviour and assessment of special construction works concerning cracking and shrinkage.

three cases of biological interest as tumor spheroids and tumor cords are also shown. This research is still in progress very actively and the last part of the chapter illustrates the short term improvements and the perspectives of the model.

REFERENCES

Gawin D, Pesavento F and Schrefler B A 2006a Hygro-thermo-chemo-mechanical modelling of concrete at early ages and beyond. Part I: Hydration and hygro-thermal phenomena *International Journal for Numerical Method in Engineering* **67**(3) 299-331.

Gawin D, Pesavento F and Schrefler B A 2006b Hygro-thermo-chemo-mechanical modelling of concrete at early ages and beyond. Part II: Shrinkage and creep of concrete *International Journal for Numerical Method in Engineering* **67**(3) 332-363.

Gray W G and Miller C T 2005 Thermodynamically constrained averaging theory approach for modeling flow and transport phenomena in porous medium systems: 1. Motivation and overview *Advances in Water Resources* **28** 161–180.

Hassanizadeh S M and Gray W G 1979a General conservation equations for multi-phase systems: 1. Averaging procedure *Advances in Water Resources* **2** 131-144.

Hassanizadeh S M and Gray W G 1979b General conservation equations for multi-phase systems: 2. Mass, momenta, energy and entropy equations *Advances in Water Resources* **2** 191-203.

Hassanizadeh S M Gray W G 1980 General conservation equations for multi-phase systems: 3. Constitutive theory for porous media flow *Advances in Water Resources* **3** 25-40.

1 MULTIPHYSICS MODELING OF CONCRETE AT EARLY AGES

1.1 INTRODUCTION

The behavior of cementitious materials is very complex especially during the first hours after the casting, when various physical and chemical phenomena determine thermal, hygral and chemical strains. The hydration reaction is associated with the production of heat that in some cases, depending on the geometry of the structure and/or on the type of concrete, can be very critical. This is the case for instance of massive structures which are typically concerned by relevant thermal gradients that can induce cracking due to differential and restrained strains. Hence, thermo-chemo-mechanical models (TCM) are usually used for massive structures because during the first days their behavior and related issues depend mainly on hydration and on related thermal strains. On the other hand, in repairs and in thin structures in general the increase of temperature due to hydration is not too high and this time the behavior is governed mostly by drying and self-desiccation, consequently hygro-chemo-mechanical models (HCM) are the most appropriated. Between these two border class of cases (massive and thin structures) there are a number of concrete structures whose behavior is governed by both thermal and hygral phenomena. One could think that the resulting behavior of these structures can be estimated sufficiently summing the results of a TCM and a HCM models but this is false essentially for two reasons: the first one is that there is a coupling between thermo-chemical and the hygral phenomena; the second one is that concrete is not a linear elastic

material and so the actual solution cannot be obtained summing two solutions obtained by two different models. Therefore the choice is to develop a thermo-hygro-chemo-mechanical model, based on the Thermodynamically Constrained Averaging Theory (TCAT), which can predict correctly the complex behavior of concrete at early age and beyond.

1.2 BRIEF OVERVIEW OF TCAT

Thermodynamically constrained averaging theory provides a rigorous yet flexible method for developing multiphase, continuum models at any scale of interest. An important feature of the procedure is that it explicitly defines larger scale variables in terms of smaller scale variables. When modeling flow and transport in systems involving more than one phase, the length scale of the model impacts the form and parameterization of the relevant conservation equations.

1.2.1 Microscale

The smallest scale at which the continuum hypothesis holds is called the microscale or pore scale. At the microscale, a single (continuum) point contains a large number of molecules so that properties such as density, temperature, and pressure of a phase can all be defined. A single point will be in only one phase, so at every location in the domain, the type and state of the phase occupying that location is considered. At the microscale, well-known, classical "point" conservation equations and thermodynamic expressions can be written. However, the domains of many problems of interest are too large and the phase distributions are too complex for the system to be modeled at the microscale. The level of detail required to account for geometric structure and the variability of variables at the microscale precludes simulation of any but the smallest of problems. To overcome this challenge, many porous media models are formulated at a larger scale, called the macroscale, that is adequate for describing system behavior while filtering out the high frequency spatial variability.

1.2.2 Macroscale and concept of representative elementary volume REV

The macroscale depends on the concept of the representative elementary volume (REV), an averaging volume that can be centered at each point in the system and is large enough to include all phases present such that values of averages are independent of the size of the REV.

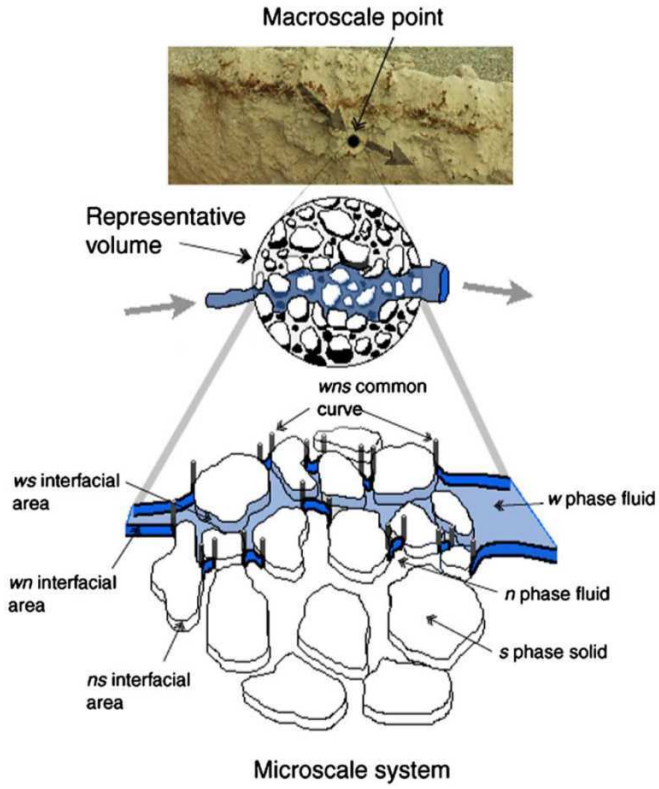

Figure 1.1 - Physical components of an example three-phase microscale system (Gray, 1999).

The volume must also be much smaller than the length scale of the entire system (known as the megascale), so that quantities such as gradients are meaningful. TCAT uses averaging theorems to formally and consistently transform microscale conservation and thermodynamic equations to the larger macroscale. These averaging theorems convert averages of microscale derivatives into derivatives of macroscale average quantities, and they share some features of the better known transport and divergence theorems. The description of a multiphase system must include equations for all entities of importance, where the term entities is used to designate collectively phases, interfaces (where two phases meet), common curves (where three interfaces meet), and common points (where four common curves meet). Averaging theorems are available for transforming equations describing processes in these entities from the microscale to the macroscale (Gray *et al.*, 1993).

1.2.3 Closure techniques

To close the conservation equations of mass, momentum, and energy for the entities of interest, additional model parameters and constitutive relations must be specified. Simplifications and modifications of the general equations that are appropriate to reach a system of equations that is more easily solvable can be obtained by a variety of methods

including elimination of unimportant terms and addition of approximate supplementary relations. Many existing models have been closed through ad hoc selection or formulation of equations, but TCAT employs averaged thermodynamic relations in the context of an entropy inequality to guide closure of the system equations. The microscale thermodynamic formalism that is chosen for averaging is classical irreversible thermodynamics (CIT). This seems adequate for the modeling goals here, but more complex thermodynamic formalisms can be employed if desired. The essential element of TCAT is that regardless of the formalism selected, it is posed at the microscale and averaged to the macroscale such that consistent definitions of intensive variables are maintained.

1.2.4 The TCAT procedure

The TCAT approach consists of the following steps (Gray and Miller, 2005):

i. formulate conservation equations of mass, momentum, energy, along with an entropy inequality for all relevant entities (volumes, interfaces, common curves, and common points);
ii. make a consistent set of thermodynamic postulates for all microscale entities;
iii. employ theorems that allow for a rigorous change in scale of universal relations that preserve relations among variables across scales;
iv. constrain entropy inequality (EI) using the products of Lagrange multipliers with conservation equations and with differential, consistent-scale thermodynamic equations;
v. determine values for the set of Lagrange multipliers that are consistent with the detail at which the system will be modeled that lead to an entropy generation rate that is expressed, essentially, in terms of products of forces and fluxes;
vi. employ geometric identities and approximations to assist in simplifying the entropy generation term to a form that is only in terms of macroscale forces and fluxes;
vii. use the resultant simplified EI to guide the formulation of general forms of closure approximations consistent with conservation laws and the second law of thermodynamics;
viii. compare microscale and macroscale modeling and experimentation to assist in improving the forms and parameterizations of the closure relations;
ix. develop needed additional constraints that may arise due to the scale of modeling.

1.2.5 Advantages of the TCAT approach

The benefits of using a TCAT approach are as follows. First, the model derivation proceeds systematically from known microscale relations to mathematically and physically consistent larger scale relations. This is accomplished by use of averaging theorems. Closure approximations are inserted near the end of the formulation. So, there is an explicit path back to the exact (unclosed) system if closure approximations are deemed to be insufficient and need to be reconsidered. Other models that are formulated without this systematic procedure may not be as easily mutable. Second, the thermodynamic analysis is consistent between scales, in the definitions of variables at different scales, and in satisfying the entropy inequality. The interscale consistency and explicit definition of variables are achieved using a rational thermodynamic approach. Macroscale variables are precisely defined by the averaging theorems. Since they are precisely defined from microscale antecedents, there is no chance of inconsistent variable definitions among equations; and the macroscale variable maintains a clear connection to its microscale counterpart. Models based on conservation and/or constitutive equations postulated directly at the macroscale run the risk of being inconsistent with microscale physics. Clear variable definitions, which are inherent to TCAT, are vital to the ability to observe and measure macroscale parameters. Third, relations may be obtained for the evolution of the spaces occupied by phases and of the interfacial area density. These relations are based on the averaging theorems.

1.3 THE MULTIPHASE SYSTEM

Concrete is modeled as a multiphase material. The multiphase system consists of three phases: a solid phase *s*, a liquid phase *l* and a gaseous phase *g*.

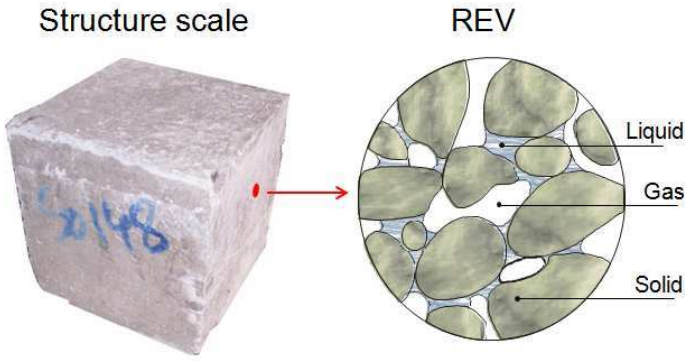

Figure 1.2 - The multiphase system

The solid phase contains several species: anhydrous grains of cement, aggregates, solid addiction and hydrates (CSH, etringite, etc.). The liquid phase *l* is liquid water whilst the gaseous phase *g*, is modeled as an ideal binary gas mixture of dry air and water vapour. The REV and its correlation with the structure scale are illustrated in ***Figure 1.2***.

1.4 GENERAL GOVERNING EQUATIONS

The model is inspired by the theoretical approach developed by Gawin *et al.* (2006a and 2006b); however, there are differences between this approach and the presented model: i) the model has been simplified in some aspects as for instance the partial uncoupling between the mechanical (M) and thermo-hygro-chemical (THC) parts (the M solution depends on the THC one but not *viceversa*); ii) a new flexible analytical expression for the chemical affinity is proposed and adopted; iii) the constitutive relationship of the desorption isotherm has been properly modified to take into account its dependence on the concrete hydration degree; iv) the autogenous shrinkage comes out mechanically without a dedicate additional constitutive equation, through the adoption of a relevant porosity function which respects stoichiometry; v) the mechanical damage is considered and coupled with creep; vi) 3D implementation.

The governing equations are derived by averaging from the microscale to the macroscale and then using closure techniques to parameterize the resultant equations. Only the macroscopic equations are reported here since their derivation from microscale is mathematically intensive such that providing it here in detail would distract from the main thrust of the thesis. These averaging techniques have been employed for transport and for multiphase systems elsewhere (Gray and Miller 2009, Jackson *et al.* 2009, and Shelton 2011) and the procedure is the same for the current system. An important feature of the approach is that the interphase contacts are explicitly accounted for.

1.4.1 Mass.

Concrete is treated as a porous solid and porosity is denoted by ε, so that the volume fraction occupied by the solid skeleton is $\varepsilon^s = 1 - \varepsilon$. The rest of the volume is occupied by the liquid water (ε^l); and the gaseous phase (ε^g). Indeed, the sum of the volume fractions for all phases has to be unit

$$\varepsilon^s + \varepsilon^l + \varepsilon^g = 1 \qquad (1.1)$$

The saturation degree of the phases is: $S^{\alpha}=\varepsilon^{\alpha}/\varepsilon$. Indeed, based on the definition of porosity ε and volume fraction ε^{α} in eqn (1.1) it follows that

$$S^{l}+S^{g}=1 \tag{1.2}$$

The mass balance equation for an arbitrary phase α based on application of the averaging theorems is written as

$$\frac{\partial\left(\varepsilon^{\alpha}\rho^{\alpha}\right)}{\partial t}+\nabla\cdot\left(\varepsilon^{\alpha}\rho^{\alpha}\mathbf{v}^{\bar{\alpha}}\right)-\sum_{\kappa\in\Im_{c\alpha}}\overset{\kappa\to\alpha}{M}=0 \tag{1.3}$$

where ρ^{α} is the density, $\mathbf{v}^{\bar{\alpha}}$ is the velocity vector, $\overset{\kappa\to\alpha}{M}$ are the mass exchange terms accounting for transport of mass at the interface between the phases κ and α, and $\sum_{\kappa\in\Im_{c\alpha}}$ is the summation over all the phases exchanging mass at the interfaces with the phase α.

An arbitrary species i dispersed within the phase α has to satisfy mass conservation too, and therefore the following equation is derived by averaging

$$\begin{aligned}&\frac{\partial\left(\varepsilon^{\alpha}\rho^{\alpha}\omega^{\overline{i\alpha}}\right)}{\partial t}+\nabla\cdot\left(\varepsilon^{\alpha}\rho^{\alpha}\omega^{\overline{i\alpha}}\mathbf{v}^{\bar{\alpha}}\right)+\nabla\cdot\left(\varepsilon^{\alpha}\rho^{\alpha}\omega^{\overline{i\alpha}}\mathbf{u}^{\overline{\overline{i\alpha}}}\right)+\\&-\varepsilon^{\alpha}r^{i\alpha}+\sum_{\kappa\in\Im_{c\alpha}}\overset{i\alpha\to i\kappa}{M}=0\end{aligned} \tag{1.4}$$

where $\omega^{\overline{i\alpha}}$ identifies the mass fraction of the species i dispersed with the phase α, $\varepsilon^{\alpha}r^{i\alpha}$ is a reaction term that allows to take into account the reactions between the species i and the other chemical species dispersed in the phase α, and $\mathbf{u}^{\overline{\overline{i\alpha}}}$ is the diffusive velocity of the species i. Differently than a mass exchange term between phases ($\overset{\kappa\to\alpha}{M}$), a reaction term $\varepsilon^{\alpha}r^{i\alpha}$ is an intra-phase exchange term.

The solid phase s comprises a portion of anhydrous cement with mass fraction $\omega^{\overline{Cs}}$ (the anhydrous cement fraction may contains also a percentage of anhydrous silica fume or other additions), a portion of aggregate with mass fraction $\omega^{\overline{As}}$, and hydrates with mass fraction $\omega^{\overline{Hs}}$. Thus the conservation equation for each fraction would be similar to eqn (1.4). Assuming that there is no diffusion of the different portions of the solid phase the mass conservation equations for hydrates, aggregate and the anhydrous cement read respectively

$$\frac{\partial\left(\varepsilon^s\rho^s\omega^{\overline{Hs}}\right)}{\partial t}+\nabla\cdot\left(\varepsilon^s\rho^s\omega^{\overline{Hs}}\mathbf{v}^{\bar{s}}\right)-\varepsilon^s r^{Hs}-\overset{l\to Hs}{M}=0 \tag{1.5}$$

$$\frac{\partial\left(\varepsilon^s\rho^s\omega^{\overline{As}}\right)}{\partial t}+\nabla\cdot\left(\varepsilon^s\rho^s\omega^{\overline{As}}\mathbf{v}^{\bar{s}}\right)=0 \tag{1.6}$$

$$\frac{\partial\left(\varepsilon^s\rho^s\omega^{\overline{Cs}}\right)}{\partial t}+\nabla\cdot\left(\varepsilon^s\rho^s\omega^{\overline{Cs}}\mathbf{v}^{\bar{s}}\right)+\varepsilon^s r^{Hs}=0 \tag{1.7}$$

where $\varepsilon^s r^{Hs}$ and $\overset{l\to Hs}{M}$ represent the hydrated cement and the combined water *per* second respectively. Summation of these three equations yields an overall mass conservation equation for the solid phase as

$$\frac{\partial\left(\varepsilon^s\rho^s\right)}{\partial t}+\nabla\cdot\left(\varepsilon^s\rho^s\mathbf{v}^{\bar{s}}\right)=\overset{l\to Hs}{M} \tag{1.8}$$

The mass balance equation for the liquid water *l* reads

$$\frac{\partial\left(\varepsilon^l\rho^l\right)}{\partial t}+\nabla\cdot\left(\varepsilon^l\rho^l\mathbf{v}^{\bar{l}}\right)=-\overset{l\to Hs}{M}-\overset{l\to Wg}{M} \tag{1.9}$$

where $\overset{l\to Wg}{M}$ is the vaporized water *per* second.

The gaseous phase consists of water vapor with mass fraction $\omega^{\overline{Wg}}$ and dry air with mass fraction $\omega^{\overline{Ag}}$. The mass conservation equations for these two species read

$$\frac{\partial\left(\varepsilon^g\rho^g\omega^{\overline{Wg}}\right)}{\partial t}+\nabla\cdot\left(\varepsilon^g\rho^g\omega^{\overline{Wg}}\mathbf{v}^{\bar{g}}\right)+\nabla\cdot\left(\varepsilon^g\rho^g\omega^{\overline{Wg}}\mathbf{u}^{\overline{\overline{Wg}}}\right)=\overset{l\to Wg}{M} \tag{1.10}$$

$$\frac{\partial\left(\varepsilon^g\rho^g\omega^{\overline{Ag}}\right)}{\partial t}+\nabla\cdot\left(\varepsilon^g\rho^g\omega^{\overline{Ag}}\mathbf{v}^{\bar{g}}\right)+\nabla\cdot\left(\varepsilon^g\rho^g\omega^{\overline{Ag}}\mathbf{u}^{\overline{\overline{Ag}}}\right)=0 \tag{1.11}$$

Being the gas phase an ideal binary gas mixture, the relationship between the diffusive fluxes of vapor water and dry air reads:

$$\nabla\cdot\left(\varepsilon^g\rho^g\omega^{\overline{Wg}}\mathbf{u}^{\overline{\overline{Wg}}}\right)=-\nabla\cdot\left(\varepsilon^g\rho^g\omega^{\overline{Ag}}\mathbf{u}^{\overline{\overline{Ag}}}\right) \tag{1.12}$$

Equation (1.12) allows to rewrite (1.11) as

$$\frac{\partial\left(\varepsilon^g\rho^g\omega^{\overline{Ag}}\right)}{\partial t}+\nabla\cdot\left(\varepsilon^g\rho^g\omega^{\overline{Ag}}\mathbf{v}^{\bar{g}}\right)-\nabla\cdot\left(\varepsilon^g\rho^g\omega^{\overline{Wg}}\mathbf{u}^{\overline{\bar{W}\bar{g}}}\right)=0 \tag{1.13}$$

Summing eqs (1.10, 1.13) gives the mass balance equation of the gaseous phase *g*

$$\frac{\partial\left(\varepsilon^g\rho^g\right)}{\partial t}+\nabla\cdot\left(\varepsilon^g\rho^g\mathbf{v}^{\bar{g}}\right)=\overset{l\to Wg}{M} \tag{1.14}$$

1.4.2 Momentum.

The momentum equation for the arbitrary phase α, including multiple species *i*, is

$$\begin{aligned}&\frac{\partial\left(\varepsilon^\alpha\rho^\alpha\mathbf{v}^{\bar{\alpha}}\right)}{\partial t}+\nabla\cdot\left(\varepsilon^\alpha\rho^\alpha\mathbf{v}^{\bar{\alpha}}\mathbf{v}^{\bar{\alpha}}\right)-\nabla\cdot\left(\varepsilon^\alpha\mathbf{t}^{\overline{\bar{\alpha}}}\right)+\\&-\varepsilon^\alpha\rho^\alpha\mathbf{g}^{\bar{\alpha}}-\sum_{\kappa\in\Im_{c\alpha}}\left(\sum_{i\in\Im_s}\overset{i\kappa\to i\alpha}{M_v}\mathbf{v}^{\bar{\alpha}}+\overset{\kappa\to\alpha}{\mathbf{T}}\right)=0\end{aligned} \tag{1.15}$$

where $\mathbf{g}^{\bar{\alpha}}$ is the body force, $\overset{i\kappa\to i\alpha}{M_v}\mathbf{v}^{\bar{\alpha}}$ represents the momentum exchange from the κ to the α phase due to mass exchange of species *i*, $\mathbf{t}^{\overline{\bar{\alpha}}}$ is the stress tensor and $\overset{\kappa\to\alpha}{\mathbf{T}}$ is the interaction force between phase α and the adjacent interfaces. When the interface properties are negligible, this last term is simply the force interaction between adjacent phases. Given the characteristic times scales (hours and days) of the problem and the small velocities, inertial forces as well as the force due to mass exchange are neglected so that the momentum equation simplifies to

$$-\nabla\cdot\left(\varepsilon^\alpha\mathbf{t}^{\overline{\bar{\alpha}}}\right)-\varepsilon^\alpha\rho^\alpha\mathbf{g}^{\bar{\alpha}}-\sum_{\kappa\in\Im_{c\alpha}}\overset{\kappa\to\alpha}{\mathbf{T}}=0 \tag{1.16}$$

From TCAT, see ***Appendix A***, it can be shown that the stress tensor for a fluid phase *f* is of the form $\mathbf{t}^{\overline{\bar{f}}}=-p^f\mathbf{1}$, with p^f being the averaged fluid pressure and **1** the unit tensor, and that the momentum balance equation can be simplified to

$$\varepsilon^f\nabla p^f-\varepsilon^f\rho^f\mathbf{g}^{\bar{f}}+\mathbf{R}^f\cdot\left(\mathbf{v}^{\bar{f}}-\mathbf{v}^{\bar{s}}\right)=0 \tag{1.17}$$

where $\mathbf{R}^\alpha$ is the resistance tensor.

1.4.3 Energy

A general macroscopic averaged equation for total energy conservation of the α phase is

$$\begin{aligned}&\frac{\partial}{\partial t}\left(\bar{\bar{E}}^{\alpha}+\frac{1}{2}\varepsilon^{\alpha}\rho^{\alpha}\bar{\mathbf{v}}^{\alpha}\cdot\bar{\mathbf{v}}^{\alpha}+\varepsilon^{\alpha}\rho^{\alpha}\bar{\bar{K}}_{E}^{\alpha}+\varepsilon^{\alpha}\rho^{\alpha}\bar{\psi}^{\alpha}\right)+\\&+\nabla\cdot\left[\left(\bar{\bar{E}}^{\alpha}+\frac{1}{2}\varepsilon^{\alpha}\rho^{\alpha}\bar{\mathbf{v}}^{\alpha}\cdot\bar{\mathbf{v}}^{\alpha}+\varepsilon^{\alpha}\rho^{\alpha}\bar{\bar{K}}_{E}^{\alpha}+\varepsilon^{\alpha}\rho^{\alpha}\bar{\psi}^{\alpha}\right)\bar{\mathbf{v}}^{\alpha}\right]\\&-\nabla\cdot\left(\varepsilon^{\alpha}\bar{\bar{\mathbf{t}}}^{\alpha}\cdot\bar{\mathbf{v}}^{\alpha}-\varepsilon^{\alpha}\bar{\bar{\mathbf{q}}}^{\alpha}\right)-\varepsilon^{\alpha}s^{\alpha}-\sum_{\kappa\in\Im_{c\alpha}}\left(\overset{\kappa\to\alpha}{M}_{E}+\overset{\kappa\to\alpha}{T}_{v}+\overset{\kappa\to\alpha}{Q}\right)=0\end{aligned}\qquad(1.18)$$

where $\bar{\bar{E}}^{\alpha}$ is the internal energy; $\bar{\bar{K}}_{E}^{\alpha}$ is the kinetic energy due to microscale velocity fluctuations; $\bar{\psi}^{\alpha}$ is the gravitational potential; $\bar{\bar{\mathbf{q}}}^{\alpha}$ is the heat flux vector; s^{α} is a heat source, $\overset{\kappa\to\alpha}{M}_{E}$, $\overset{\kappa\to\alpha}{T}_{v}$, and $\overset{\kappa\to\alpha}{Q}$ express the transfer of energy from the *κα* interface to the *α* phase due phase change, interfacial stress, and heat transfer. The $\bar{\bar{K}}_{E}^{\alpha}$ terms have traditionally been neglected or lumped in with other macroscale quantities, such as the internal energy. The heat flux vector is assumed proportional to the gradient of temperature $\bar{\bar{\mathbf{q}}}^{\alpha}=-\boldsymbol{\lambda}^{\alpha}\nabla\theta^{\alpha}$ (being $\boldsymbol{\lambda}^{\alpha}$ the thermal conductivity tensor of the phase α). Also not heat source terms $\varepsilon^{\alpha}s^{\alpha}$ are usually considered and these will be further omitted.

Due to the considered time scale it is assumed that phases are locally in a state of thermodynamic equilibrium. This means that the averaged temperatures of all phases are assumed equal:

$$\theta^{s}=\theta^{l}=\theta^{g}=\theta\qquad(1.19)$$

In eqn (1.18) terms related to viscous dissipation and mechanical work, caused by density variation due to temperature changes have been neglected as usually done in mechanics of geomaterials. Being the phases in thermal equilibrium also heat transfers between adjacent phases can be neglected, as well as the kinetic energy due to slow velocities. Using the general mass balance equation of the phase *α* (1.3), the linear momentum balance equation (1.15), through the definition of the material time derivative and expressing the energy balance by means of the specific phase enthalpy give the enthalpy balance equations of the solid, the liquid and the gaseous phases respectively

$$\varepsilon^{s}\rho^{s}C_{p}^{s}\frac{\partial\theta}{\partial t}-\nabla\cdot\left(\varepsilon^{s}\boldsymbol{\lambda}^{s}\nabla\theta\right)=\overset{l\to s}{M}_{E}\qquad(1.20)$$

$$\varepsilon^l \rho^l C_p^l \frac{\partial \theta}{\partial t} + \varepsilon^l \rho^l C_p^l \mathbf{v}^{\bar{l}} \cdot \nabla \theta - \nabla \cdot \left(\varepsilon^l \boldsymbol{\lambda}^l \nabla \theta \right) = \overset{s \to l}{M}_E + \overset{g \to l}{M}_E \tag{1.21}$$

$$\varepsilon^g \rho^g C_p^g \frac{\partial \theta}{\partial t} + \varepsilon^g \rho^g C_p^g \mathbf{v}^{\bar{g}} \cdot \nabla \theta - \nabla \cdot \left(\varepsilon^g \boldsymbol{\lambda}^g \nabla \theta \right) = \overset{l \to g}{M}_E \tag{1.22}$$

where the convective heat flux in the solid phase has been neglected since usually insignificant. C_p^{α} is the specific heat of the phase α at constant pressure.

The heat production due to hydration and the energy consumption due to vaporization are proportional to the mass of chemically combined and vaporized water respectively

$$\overset{l \to s}{M}_E + \overset{s \to l}{M}_E = H_{hydr} \overset{l \to Hs}{M} \qquad \overset{l \to g}{M}_E + \overset{g \to l}{M}_E = -H_{vap} \overset{l \to Wg}{M} \tag{1.23}$$

where H_{hydr} and H_{vap} are the specific enthalpies of hydration and vaporization respectively. Summing eqs (1.20-1.22) and introducing eqn (1.23) give

$$\begin{aligned} &\left(\rho C_p \right)_{\text{eff}} \frac{\partial \theta}{\partial t} + \left(\varepsilon^l \rho^l C_p^l \mathbf{v}^{\bar{l}} + \varepsilon^g \rho^g C_p^g \mathbf{v}^{\bar{g}} \right) \cdot \nabla \theta - \nabla \cdot \left(\boldsymbol{\lambda}_{\text{eff}} \nabla \theta \right) = \\ &= - \overset{l \to Wg}{M} H_{vap} + \overset{l \to Hs}{M} H_{hydr} \end{aligned} \tag{1.24}$$

where

$$\begin{aligned} \left(\rho C_p \right)_{\text{eff}} &= \varepsilon^s \rho^s C_p^s + \varepsilon^l \rho^l C_p^l + \varepsilon^g \rho^g C_p^g \\ \boldsymbol{\lambda}_{\text{eff}} &= \varepsilon^s \boldsymbol{\lambda}^s + \varepsilon^l \boldsymbol{\lambda}^l + \varepsilon^g \boldsymbol{\lambda}^g \end{aligned} \tag{1.25}$$

1.5 CONSTITUTIVE EQUATIONS

After the introduction of the general governing equations of the model several constitutive relationships are needed to obtain a solvable system of equations. In this section all the assumptions and additional equations introduced to close the mathematical model are reported and discussed.

1.5.1 The hydration model and averaged stoichiometry of the reaction

The hydration degree ξ is the percentage of hydrated cement, therefore the ratio between mass of hydrated cement, $c_{hydr}(t)$, and its total content in the mix, c

$$\xi(t) = \frac{c_{hydr}(t)}{c} \tag{1.26}$$

When the water to cement ratio is relatively low, as for high performance concretes, only a fraction of the cement present in the mix will be hydrated and the percentage of cement hydrated at sufficiently large time (nominally $t \to \infty$) is here indicated as ξ_∞. The degree of reaction Γ is the ratio between the amount of water chemically combined at time t, $m^{l \to Hs}(t)$, and that chemically combined for $t \to \infty$, (i.e. $m_\infty^{l \to Hs}$)

$$\Gamma(t) = \frac{m^{l \to Hs}(t)}{m_\infty^{l \to Hs}} \tag{1.27}$$

thence the relation between the hydration degree ξ(t) and the degree of reaction $\Gamma(t)$ reads

$$\xi(t) = \xi_\infty \Gamma(t) \tag{1.28}$$

$\Gamma(t) = 1$ doesn't mean *a priori* that all the cement has reacted, but that the hydration process is ended and the fraction of hydrated cement has reached ξ_∞. The degree of reaction Γ is the main internal variable of the mathematical model.

The cement hydration is a thermo-activated process. In the model this is taken into account through an Arrhenius type law (e.g. Regourd and Gauthier, 1980) which governs the reaction kinetic

$$\frac{\mathrm{d}\Gamma}{\mathrm{d}t} = A_{(\Gamma)} \beta_{(h)} \exp\left(-\frac{E_a}{RT}\right) \tag{1.29}$$

where T is the absolute temperature $A_{(\Gamma)}$ is the macroscopic volume-averaged chemical affinity, E_a is the hydration activation energy, R is the universal gas constant and $\beta_{(h)}$ is a function of the relative humidity (h) to take into account its effect on the hydration process. The function $\beta_{(h)}$ varies between 0 and 1 and reads

$$\beta_{(h)} = \left[1 + \left(a_h - a_h h\right)^4\right]^{-1} \tag{1.30}$$

where a_h is an empirical constant which has to be identified with test data ($a_h \approx 3 \div 6$). To compute the chemical affinity, a new analytical expression is proposed (Sciumè *et al.* 2012)

$$A_{(\Gamma)} = \frac{A_i + (A_P - A_i)\sin\left[\frac{\pi}{2}\left(1 - \left\langle \frac{\Gamma_p - \Gamma}{\Gamma_p} \right\rangle_+\right)\right]}{\left[1 + \zeta \left\langle \frac{\Gamma - \Gamma_P}{1 - \Gamma_p} \right\rangle_+^4\right]} - \left(\frac{A_p}{1+\zeta}\right)\left\langle \frac{\Gamma - \Gamma_P}{1 - \Gamma_p} \right\rangle_+ \qquad (1.31)$$

where A_i is the initial affinity, A_p is the maximum value of the affinity function reached for $\Gamma = \Gamma_p$, ζ governs the deceleration phase of the hydration process, and $< >_+$ is the positive part operator. ***Figure 1.3*** shows that eqn (1.31) is quite accurate to interpolate the experimental data of the affinity function. The parameters of such an equation govern the hydration reaction and even if they have not a physical interpretation their identification results very effortless since they have a "graphical connotation". Usually no more than two numerical tests are needed to reproduce the hydration kinetic.

To quantify the different phases present in the cement paste during hydration the model of Power (1960), subsequently improved by Jensen and Hansen (1996, 2001 and 2002) to take into account silica fume, is adopted. This averaging stoichiometric approach is governed by the following equations valid for an isolate system (i.e. without mass changes with the external environment):

$$\begin{aligned}
&\textit{Chemical shrinkage :} && \varepsilon^{cs} = k\cdot\left[0,20 + 0,69\cdot(s/c)\right]\cdot(1-p)\cdot\xi \\
&\textit{Capillary water :} && \varepsilon^{cw} = p - k\cdot\left[1,32 + 1,57\cdot(s/c)\right]\cdot(1-p)\cdot\xi \\
&\textit{Gel water :} && \varepsilon^{gw} = k\cdot\left[0,60 + 1,57\cdot(s/c)\right]\cdot(1-p)\cdot\xi \\
&\textit{Gel solid :} && \varepsilon^{gs} = k\cdot\left[1,52 + 0,74\cdot(s/c)\right]\cdot(1-p)\cdot\xi \\
&\textit{Cement :} && \varepsilon^{c} = k\cdot(1-p)\cdot(1-\xi) \\
&\textit{Silica fume :} && \varepsilon^{sf} = k\cdot\left[1,43\cdot(s/c)\right]\cdot(1-p)\cdot(1-\xi)
\end{aligned} \qquad (1.32)$$

with $\sum_i \varepsilon^i = 1$ and

$$p = \frac{w/c}{(w/c) + \left(\rho^w/\rho^c\right) + \left(\rho^w/\rho^{sf}\right)\cdot(s/c)}$$
$$k = \frac{1}{1 + \left(\rho^c/\rho^{sf}\right)\cdot(s/c)} \qquad (1.33)$$

w, *c* and *s* are respectively the masses of water, cement, silica fume. The following typical values are assumed as densities:

$$\rho^c = 3150\,kg/m^3; \quad \rho^{sf} = 2200\,kg/m^3; \quad \rho^w = 1000\,kg/m^3 \qquad (1.34)$$

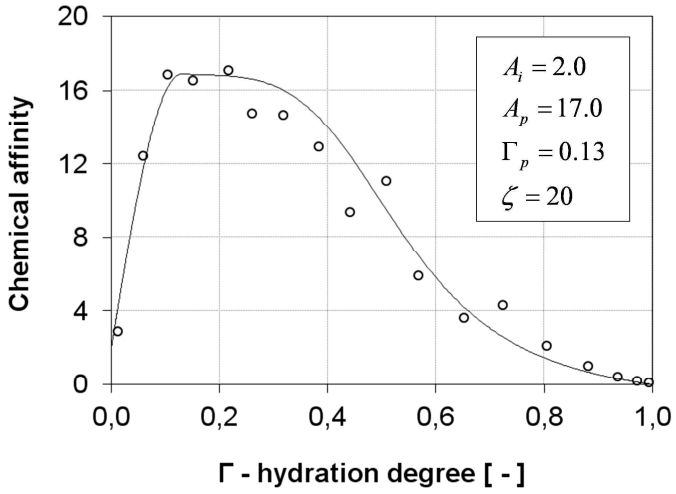

Figure 1.3 - Experimental data (open symbols) of the chemical affinity interpolated using eqn (1.31)

The cement's hydration is accompanied by a decrease in volume which is equal to about 8,7% of the formed hydrates volume, in other words the volume of the hydrates is smaller than the volume of the reacting water plus that of the anhydrous cement (LeChâtelier, 1900). In the set of eqs (1.32) this is expressed by the first equation (chemical shrinkage). Hence, in the capillary pores initially quasi-saturated by water, there is the development of a volume of gas that causes the self-dessiccation of the cement paste (Jensen, 1993).
The theoretic upper limit value for the fraction of hydrated cement $\bar{\xi}_\infty$, can be calculated imposing equal to zero the capillary water (second one in eqs (1.32))

$$\bar{\xi}_\infty = \min\left\{1 \quad \frac{p}{k\cdot\left[1{,}32+1{,}57\cdot(s/c)\right]\cdot(1-p)}\right. \tag{1.35}$$

It is worth to underline that the value $\bar{\xi}_\infty$, resulting from the approximated stoichiometry of the reaction and corresponding to perfect contact between water and cement grains, is always greater than the real one, ξ_∞. The final hydration degree, ξ_∞, depends upon the water/cement ratio and can be estimated using empirical equations as for instance those proposed by Mills (1966) and Waller (1999)

$$\xi_\infty^{Mills} = \frac{1.031(w/c)}{0.194+(w/c)} \qquad \xi_\infty^{Waller} = 1-\exp\left[-3.3(w/c)\right] \tag{1.36}$$

In ***Figure 1.4*** the differences between the theoretical value $\bar{\xi}_\infty$ (computed with eqn (1.35)) and that given by eqs (1.36) can be observed.

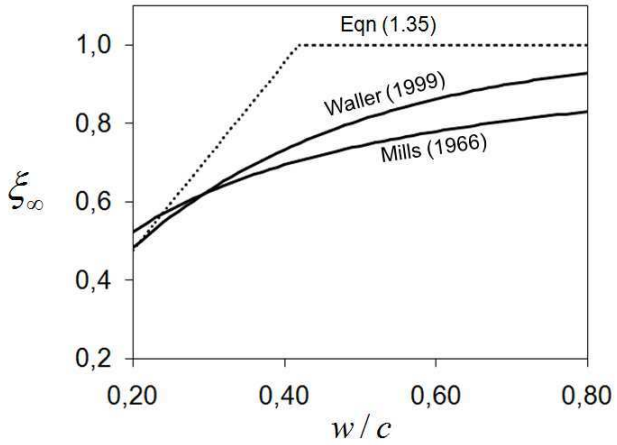

Figure 1.4 – Maximum hydration degree over the w/c ratio. Value given by eqn (1.35) and estimations obtained using eqs (1.36).

Once assumed ξ_∞, the total porosity of the cement paste can be expressed as function of the degree of reaction $\Gamma(t)$ summing the chemical shrinkage, the capillary and gel water volume fractions of eqs (1.32)

$$\varepsilon(\Gamma) = 1 - \varepsilon^s(\Gamma) \cong \left[n_\infty^{cp} + a_\varepsilon (1-\Gamma) \right] \Omega + n^{As} (1-\Omega) \tag{1.37}$$

where Ω is the volume of the cement paste, n^{As} is the averaged porosity of the aggregate (n^{As} can be usually neglected), n_∞^{cp} is the final value of the porosity of the cement paste (for $\Gamma = 1$) and a_ε is a constant coefficient. n_∞^{cp} and a_ε are given by

$$\begin{aligned} n_\infty^{cp} &= p - k \cdot \left[0.52 - 0.69 \cdot (s/c) \right] \cdot (1-p) \cdot \xi_\infty \\ a_\varepsilon &= k \cdot \left[0.52 - 0.69 \cdot (s/c) \right] \cdot (1-p) \end{aligned} \tag{1.38}$$

The porosity function (1.37) respecting stoichiometry and volume balance of the different phases during hydration (Jensen, 1993), allows to take into account the chemical shrinkage and then to estimate autogenous shrinkage by means of the governing balance equations and of the shrinkage constitutive model, without the introduction of additional constitutive equations or parameters.

From eqs (1.32) the total amount of chemically bound water (non-evaporable) for t→∞ can be obtained. This quantity does not depend on the silica fume content and reads

$$m_\infty^{l \to Hs} = 0.228 \cdot c \cdot \xi_\infty \tag{1.39}$$

Hence from eqs (1.27 and 1.39) the water consumed *per* second by hydration $\overset{l\to Hs}{M}$ (sink term in eqn (1.9)) reads:

$$\overset{l\to Hs}{M} = 0.228\cdot c\cdot \xi_{\infty}\frac{\mathrm{d}\Gamma}{\mathrm{d}t} \tag{1.40}$$

The heat release associated with hydration is taken into account of through the last term of equation (1.24). This source term ($\overset{l\to Hs}{M}\, H_{hydr}$) can be also expressed as

$$\overset{l\to Hs}{M}\, H_{hydr} = L_{hydr}\frac{\mathrm{d}\Gamma}{\mathrm{d}t} \tag{1.41}$$

where $L_{hydr} = 0.228\cdot c\cdot \xi_{\infty} H_{hydr}$ is the latent heat of hydration which usually can be estimated from adiabatic calorimetry.

1.5.2 Fluid phases velocities

$\mathbf{R}^{\alpha}$ of eqn (1.17) is the resistance tensor that accounts for the frictional interactions between phases. For example, porous medium flow of a single fluid encounters resistance to flow due to interaction of the fluid with the solid. If one has to model the flow at the microscale, a viscous stress tensor within the fluid phase would be employed. At the macroscale, the effects of the viscous interaction are accounted for as being related to the difference in velocities of the phases. In multiphase flow, resistance tensors must be developed that account for the velocity differences between each pair of phases. Eqn (1.15) contains the interaction vector $\overset{\kappa\to\alpha}{\mathbf{T}}$ that arises between each pair of phases. In the full implementation of the TCAT analysis, the simplest result is that this vector is proportional to the velocity difference between the two considered phases with the resistance tensor being the coefficient of proportionality. In the present version of the model, the interaction force $\overset{s\to\alpha}{\mathbf{T}}$ between the fluid phase α and the solid phase s (solid mineral skeleton) is explicitly taken into account while the macroscopic effect of the interaction forces between the liquid and the gaseous phases is taken care of through the relative permeabilities $k_{rel}^{\alpha s}$. The form of $\left(\mathbf{R}^{\alpha}\right)^{-1}$ is here assumed following the modeling of multiphase flow in porous media (Lewis and Schrefler, 1998), that is to say

$$\left(\mathbf{R}^{\alpha}\right)^{-1} = \frac{k_{rel}^{\alpha s}\mathbf{k}}{\mu^{\alpha}\left(\varepsilon^{\alpha}\right)^{2}} \qquad \left(\alpha = l, g\right) \tag{1.42}$$

Where **k** and μ^{α} are the intrinsic permeability tensor and the dynamic viscosity, respectively. The relative permeabilities of the liquid (wetting phase) and of the gas (non-wetting phase) are given by Van Genuchten (1980)

$$k_{rel}^{ls} = \left(S^{l}\right)^{0.5}\left\{1-\left[1-\left(S^{l}\right)^{b}\right]^{\frac{1}{b}}\right\}^{2} \tag{1.43}$$

$$k_{rel}^{gs} = \left(S^{g}\right)^{0.33}\left[1-\left(1-S^{g}\right)^{b}\right]^{\frac{2}{b}} \tag{1.44}$$

Introducing (1.42) in (1.17), and neglecting the effect of gravitational forces give the relative velocity of the fluid phase α

$$\mathbf{v}^{\bar{\alpha}} - \mathbf{v}^{\bar{s}} = -\frac{k_{rel}^{\alpha s}\mathbf{k}}{\mu^{\alpha}\varepsilon^{\alpha}}\nabla p^{\alpha} \qquad (\alpha = l, g) \tag{1.45}$$

The intrinsic permeability tensor **k** of the interstitial fluid is isotropic and depends on the degree of reaction Γ

$$\mathbf{k} = k_{\infty}10^{A_k(1-\Gamma)}\mathbf{1} \tag{1.46}$$

where k_{∞} is the intrinsic permeability when $\Gamma = 1$, A_k is a constant coefficient (A_k=4÷6) and **1** is the unit tensor.

1.5.3 Water vapour diffusion

To approximate the diffusive flux in eqs (1.10 and 1.13), the Fick's law is used ($\rho^{g}\omega^{\overline{Wg}}\mathbf{u}^{\overline{\overline{Wg}}} = -\rho^{g}D^{\overline{Wg}}\nabla\omega^{\overline{Wg}}$). Based on the work of Perre (1987) and Bažant *et al.* (1972), Gawin *et al.* (1999) proposed the following relationship for the effective diffusivity of vapour in concrete

$$D^{\overline{Wg}} = D_0^{\overline{Wg}}\left(\frac{T}{273.15}\right)^{1.667}\frac{p_{atm}}{p^{g}}\,\varepsilon^{g} f_s \tag{1.47}$$

where p_{atm} is the atmospheric pressure, $D_0^{\overline{Wg}} = 2.6\cdot10^{-5}\,\mathrm{m}^2/\mathrm{s}$, and the factor $f_s = 0.001\div0.01$ is a constant coefficient which allows to take into account tortuosity. Here $f_s = f_{s\infty}10^{A_k(1-\Gamma)}$ to consider the effect of hydration (A_k is the same of eqn (1.46)).

Dry air, water vapour and their mixture, are assumed to behave as perfect gases, following Dalton's law

$$p^{g} = p^{gA} + p^{gW} \tag{1.48}$$

and the Clapeyron equation of state:

$$\rho^{\alpha} = p^{\alpha} M_{\alpha} \big/ RT \qquad \left(\alpha = gA,\ gW,\ g\right) \tag{1.49}$$

where

$$\frac{1}{M_g} = \frac{\rho^{gW}}{\rho^g}\frac{1}{M_W} + \frac{\rho^{gA}}{\rho^g}\frac{1}{M_A} = \frac{\omega^{\overline{Wg}}}{M_W} + \frac{\omega^{\overline{Ag}}}{M_A} \tag{1.50}$$

The density of water vapour, ρ^{gW}, calculated by means of (1.49) differs slightly from the results of the experimental tests but may be used in the temperature range encountered usually in practical problems with sufficient accuracy. In these conditions the diffusive flow of the water vapour can be also expressed as

$$\rho^g \omega^{\overline{Wg}} \mathbf{u}^{\overline{\overline{Wg}}} = -\rho^g D^{\overline{Wg}} \nabla \omega^{\overline{Wg}} = -\frac{\rho^g}{\varepsilon^g}\frac{M_A M_W}{M_g^2} D^{\overline{Wg}} \nabla\left(\frac{p^{gW}}{p^g}\right) \tag{1.51}$$

1.5.4 A hydration-dependent desorption isotherm

The desorption isotherm is closely linked with the microstructure of the cement paste that shows important changes during hydration (refinement of the porous network). Hence the classical analytical expression proposed by Van Genuchten (1980) is properly adapted to take into account the degree of hydration (Sciumè *et al*., 2012)

$$S^l = \left\{1 + \left[\frac{p^c}{a}\left(\frac{\Gamma + \Gamma_i}{1 + \Gamma_i}\right)^{-c_\Gamma}\right]^{\frac{b}{b-1}}\right\}^{-\frac{1}{b}} \tag{1.52}$$

where a and b are the classical parameters of the equation of Van Genuchten, while c_Γ and Γ_i are the newly introduced parameters. The curves obtained at different degrees of reaction are shown in ***Figure 1.5.a***. The experimental evaluation of adsorption properties during hydration is hard to perform, thence the results in bibliography concern hydrated or almost completely hydrated concretes or cement pastes. Due to this reason eqn (1.52) has not been directly validated. However, if a parallelism between the w/c ratio and the hydration degree is considered, *via* the degree of refinement of the microstructure of the cement paste, to a lower w/c ratio corresponds a more refined microstructure and so an higher degree of reaction Γ.

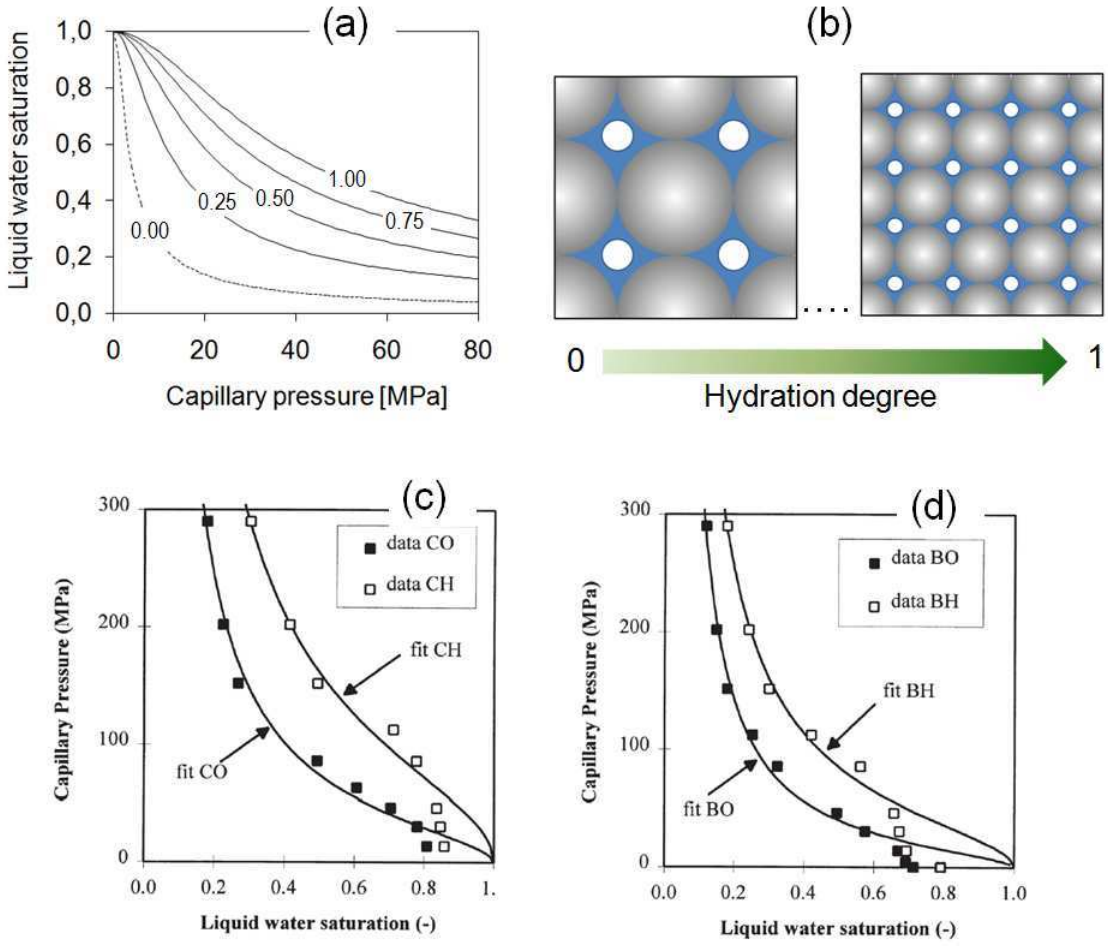

Figure 1.5 - Desorption isotherm function used in the model: the number in the lines is the degree of reaction (a); Two different refined porous networks with the same saturation degree (b). Results obtained by Baroghel-Bouny (1999): desorption isotherms for a high performance cement paste CH (w/c = 0.19, s/c = 0.10) and an ordinary one CO (w/c = 0.34) (c), and desorption isotherms for a high performance concrete BH (w/c = 0.26, s/c = 0.10) and an ordinary one BO (w/c = 0.48) (d);

With this parallelism in mind, the experimental results of Baroghel-Bouny (1999) are consistent with the proposed equation (***Figures 1.5.c-d***). Moreover, the curves represented in ***Figure 1.5.a*** are similar to those proposed by Tacke (2002) who also considers the effect of the hydration degree on the desorption isotherm. Also a physical justification can be given for eqn (1.52). In fact ***Figure 1.5.b*** shows that at two different hydration degrees (i.e. different degrees of refinement of the microstructure) the same saturation degree of liquid water does not correspond to the same capillary pressure, due to the different radii r of the interface between the wetting and the non-wetting phases, according with the Young-Laplace equation

$$p^c = \frac{2\gamma}{r} \tag{1.53}$$

where γ is the surface tension. For temperatures normally encountered in concrete structures (i.e. lower than the critical point of water, $T<T_{cr}$) the capillary pressure, p^c, is given by the difference between the pressures of the non wetting (gas) and wetting phase (liquid)

$$p^c = p^g - p^l \tag{1.54}$$

This equation is valid only at thermodynamic equilibrium and can be obtained from an exploitation of the entropy inequality as shown by Gray (2000) and Gray and Schrefler (2001). The Kelvin equation gives the relationship between the relative humidity h, and the capillary pressure p^c

$$h = \frac{p^{gw}}{p^{gws}} = \exp\left(-\frac{p^c}{\rho^w}\frac{M_w}{RT}\right) \tag{1.55}$$

where p^{gws} is the saturated vapour pressure which varies with temperature and is given by the classical Antoine equation

$$p^{gws} = b_1 \cdot 10^{b_2 - \frac{b_3}{b_4+\theta}} \tag{1.56}$$

Where b_1=133.322, b_2=8.07131, b_3=1730.63 and b_4=233.426.

1.5.5 The effective stress principle

The closure relation for the stress tensor acting on the solid phase according with the effective stress principle is

$$\mathbf{t}^{\bar{s}}_{eff} = \mathbf{t}^{\bar{s}} + \bar{\alpha} p^s \mathbf{1} \tag{1.57}$$

with $\mathbf{t}^{\bar{s}}_{eff}$ the effective stress tensor in the sense of porous media mechanics and the solid pressure p^s given as (Gray and Schrefler, 2007)

$$p^s = \chi^l p^l + \chi^g p^g \tag{1.58}$$

where χ^α is the solid surface fraction in contact with the respective fluid phase, known as the parameter of Bishop. This parameter is a function of the degree of saturation and is taken here equal to this last one (i.e. $\chi^\alpha = S^\alpha$).

1.5.6 Effective thermal conductivity and thermal capacity

The effect of hydration degree on thermal properties can be considered indirectly by accounting for changes of the volume fractions of the liquid water ε^l and the solid phase ε^s. More in detail the effective thermal conductivity of the moist material may be evaluated as

$$\boldsymbol{\lambda}_{\text{eff}} = \lambda_{dry}\left(1+4\frac{\rho^l\varepsilon^l}{\rho^s\varepsilon^s}\right) \tag{1.59}$$

The effect of the gaseous phase on the effective thermal capacity is not considered. Hence the first of eqs (1.25) simplifies to

$$\left(\rho C_p\right)_{\text{eff}} = \varepsilon^s\rho^s C_p^s + \varepsilon^l\rho^l C_p^l \tag{1.60}$$

1.5.7 Mechanical constitutive model

The mechanical behavior is governed by the macroscopic, volume-averaged linear momentum balance equation in a rate form (Lewis and Schrefler, 1998):

$$\nabla\cdot\left(\frac{\partial\mathbf{t}}{\partial t}\right)+\frac{\partial\rho}{\partial t}\mathbf{g}=0 \tag{1.61}$$

where ρ is the averaged concrete density:

$$\rho=\varepsilon^s\rho^s+\varepsilon^l\rho^l+\varepsilon^g\rho^g \tag{1.62}$$

The interaction between the solid and the two fluids (liquid water and gas), is accounted for through the effective stress principle (eqs (1.57-1.58)) and the related strains which are defined in the follow.

Concrete is modeled as a visco-elastic damageable material, whose mechanical properties depend on the hydration degree (De Schutter and Taerwe 1996). The relationship between apparent stresses **t**, effective stresses $\tilde{\mathbf{t}}$ (in the sense of damage mechanics), damage *D*, elastic stiffness matrix **E**, elastic strains $\mathbf{e}_{el}$, creep strains $\mathbf{e}_{cr}$, shrinkage strains $\mathbf{e}_{sh}$ (caused by the fluid pressures), thermal strains $\mathbf{e}_{th}$ and total strains **e** reads:

$$\mathbf{t}=\left(1-D\right)\tilde{\mathbf{t}} \tag{1.63}$$

$$\dot{\tilde{\mathbf{t}}}=\mathbf{E}_{(\Gamma)}\dot{\mathbf{e}}_{el}=\mathbf{E}_{(\Gamma)}\left(\dot{\mathbf{e}}-\dot{\mathbf{e}}_{cr}-\dot{\mathbf{e}}_{th}-\dot{\mathbf{e}}_{sh}\right) \tag{1.64}$$

The Young's modulus E, the tensile strength f_t and the Poisson's ratio ν vary due to hydration as follows (De Schutter and Taerwe 1996, De Schutter 2002)

$$E_{(\Gamma)} = E_{\infty} \left\langle \frac{\Gamma - \Gamma_0}{1 - \Gamma_0} \right\rangle_+^{\gamma_E} \tag{1.65}$$

$$f_{t(\Gamma)} = f_{t\infty} \left\langle \frac{\Gamma - \Gamma_0}{1 - \Gamma_0} \right\rangle_+^{\gamma_{FT}} \tag{1.66}$$

$$\nu_{(\Gamma)} = \left[\nu_{\infty} - 0.49\exp(-10)\right]\sin\left(\frac{\pi}{2}\Gamma\right) + 0.49\exp(-10\Gamma) \tag{1.67}$$

in which Γ_0 is the mechanical percolation threshold that corresponds to the degree of reaction below which the concrete has negligible mechanical properties (Young's modulus, strength, etc.), E_{∞} is the final value of the Young's modulus, $f_{t\infty}$ and ν_{∞} are the final values of the tensile strength and Poisson's ratio respectively, and γ_E and γ_{ft} are constants obtained from experiments. Equation (1.67) is a readapted version of the equation proposed by De Schutter (2002). The mechanical percolation threshold depends in general on the aggregate content, type of cement and water to cement ratio (Torrenti and Benboudjema, 2005), however for ordinary concretes Γ_0 can be taken equal to 0.1.

1.5.8 Creep rheological model

In the reference model of Gawin *et al*. (2006b), creep is modeled by means of the solidification theory (Bažant and Prasannan, 1989a and 1989b) for the description of the basic creep, and microprestress theory (Bažant *et al*., 1997) for the description of the long-term creep and the drying induced creep (the so called drying creep); both the solidification and the microprestress theories had been properly adapted for a multiphase porous material by Gawin *et al*. (2006b). The thermodynamic consistency of the aging visco-elasticity theory has been shown by Pesavento *et al*. (2008). Here, a rearranged version of the reference model is adopted to compute the creep deformation: the separate effects of aging elasticity, non-aging creep and microprestress developments are reunified through the definition of a rheological model made of a Kelvin-Voigt chain and two dashpots combined in serial way (see ***Figure 1.6***). The first two cells (aging Kelvin-Voigt chain and one single dashpot) are used to compute the basic creep and the last cell (single dashpot) is dedicated to the drying creep strain.

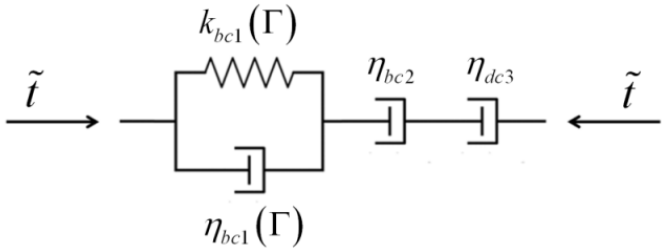

Figure 1.6 - Creep rheological model

In the first creep cell an incremental constitutive relation for an aging spring is used:

$$\dot{\tilde{t}} = \dot{t}_{sp1} + \dot{t}_{ds1} \tag{1.68}$$

in which t_{ds1} and t_{sp1} are the stresses acting on the dashpot and the spring of the Kelvin-Voigt chain. The behaviour law of the spring reads:

$$k_{bc1}(\Gamma)\dot{e}_{cr1} = \dot{t}_{sp1} \tag{1.69}$$

where e_{cr1} is the basic creep strain of the first cell and k_{bc1} is the stiffness of the spring. The behaviour law of the dashpot reads:

$$\eta_{bc1}(\Gamma)\dot{e}_{cr1} = t_{ds1} \tag{1.70}$$

in which η_{bc1} is the viscosity of the dashpot.

The effect of age on basic creep is taken into account by relating the material parameters to the degree of reaction Γ. The relationships proposed by De Schutter (1999) are slightly modified by Benboudjema and Torrenti (2008):

$$k_{bc1}(\Gamma) = k_{bc1\_\infty}\left[0.473\left(2.081-1.608\left\langle\frac{\Gamma-\Gamma_0}{1-\Gamma_0}\right\rangle_+\right)^{-1}\right]\left\langle\frac{\Gamma-\Gamma_0}{1-\Gamma_0}\right\rangle_+^{0.62} \tag{1.71}$$

$$\tau_{bc1} = \frac{\eta_{bc1}(\Gamma)}{k_{bc1}(\Gamma)} \tag{1.72}$$

in which k_{bc1_∞} is the final stiffness (i.e. when $\Gamma=1$) of the spring. The retardation time τ_{bc1} is assumed to be constant. Therefore combining the previous equations (1.68-1.72), the behavior of the first creep cell is governed by the following non-linear second-order differential equation:

$$\frac{\dot{\tilde{t}}}{\bar{k}_{bc1}} = \tau_{bc1}\ddot{e}_{cr1} + \left(\tau_{bc1}\frac{\dot{\bar{k}}_{bc1}}{\bar{k}_{bc1}} + 1 \right)\dot{e}_{cr1} \tag{1.73}$$

For the creep cells *2* and *3* the constitutive relationships are:

$$\tilde{t} = \eta_{bc2}\dot{e}_{cr2} \tag{1.74}$$

$$\tilde{t} = \frac{1}{\delta_{dc}\left|\mathbf{q}^{l}\right|}\dot{e}_{cr3} \tag{1.75}$$

in which δ_{dc} is the coefficient that governs the drying creep response of the model, and $\mathbf{q}^{l}$ is the liquid water flux in the porous medium.

For the time integration of the equations (1.73-1.75) and their extension to the three-dimensional case see the ***Appendix B***.

1.5.9 Thermal and hygral strains

The thermal strain $\mathbf{e_{th}}$ is related to the temperature variation:

$$\dot{\mathbf{e}}_{th} = \alpha_T \dot{\theta}\mathbf{1} \tag{1.76}$$

in which α_t is the thermal dilatation coefficient (kept constant) and **1** is the unit tensor.
To compute the shrinkage, the instantaneous elastic part and the viscous one must be considered:

$$\mathbf{e}_{sh} = \mathbf{e}_{sh}^{inst} + \mathbf{e}_{sh}^{visc} \tag{1.77}$$

For a porous medium the hygral strain is proportional to the Biot's coefficient $\bar{\alpha}$:

$$\bar{\alpha}_{(\Gamma)} = 1 - \left(\frac{K^T}{K^S} \right)_{(\Gamma)} \tag{1.78}$$

where K^T is the Bulk modulus of the skeleton and K^S is the Bulk modulus of the solid phase (grain). The Bulk modulus of the skeleton changes with hydration and conforming with equations (1.65) and (1.67) can be estimated as:

$$K_{(\Gamma)}^{T} = \max\left\{ \begin{array}{l} 2.2\ GPa \\ \dfrac{E_{(\Gamma)}}{3\left(1-2\nu_{(\Gamma)}\right)} \end{array} \right. \tag{1.79}$$

where 2.2 GPa is the water compressibility assumed as minimum Bulk modulus for the skeleton. During hydration also the Bulk modulus of the solid phase K^S varies since the relative volume fractions of the different solid constituents change due to the chemical reactions. However the variation of K^S is relatively negligible compared to evolution of K^T during hydration. Hence the Bulk modulus of the solid phase is here assumed to be constant and equal to its final value (i.e. $K^S(\Gamma) \approx K^S_\infty = const$). With respect to this hypothesis and to eqs (1.78, 1.79), assuming as input parameter the final value $\bar{\alpha}_\infty$(Biot coefficient when Γ = 1), the evolution of the Biot coefficient with hydration reads

$$\bar{\alpha}(\Gamma) = 1 - \frac{1-\bar{\alpha}_\infty}{K^T_\infty} K^T(\Gamma) \tag{1.80}$$

where K^T_∞ is the final Bulk modulus of the solid skeleton (when Γ = 1). Note that setting $\bar{\alpha}_\infty$ as input parameter is equivalent to assume $K^S_\infty = K^T_\infty \left(1-\bar{\alpha}_\infty\right)^{-1}$. Shrinkage and autogenous shrinkage are strongly governed by the Biot coefficient and its final value $\bar{\alpha}_\infty$ should to be evaluated experimentally.

In ***Figure 1.7*** the evolutions of the most important mechanical properties during hydration are represented.

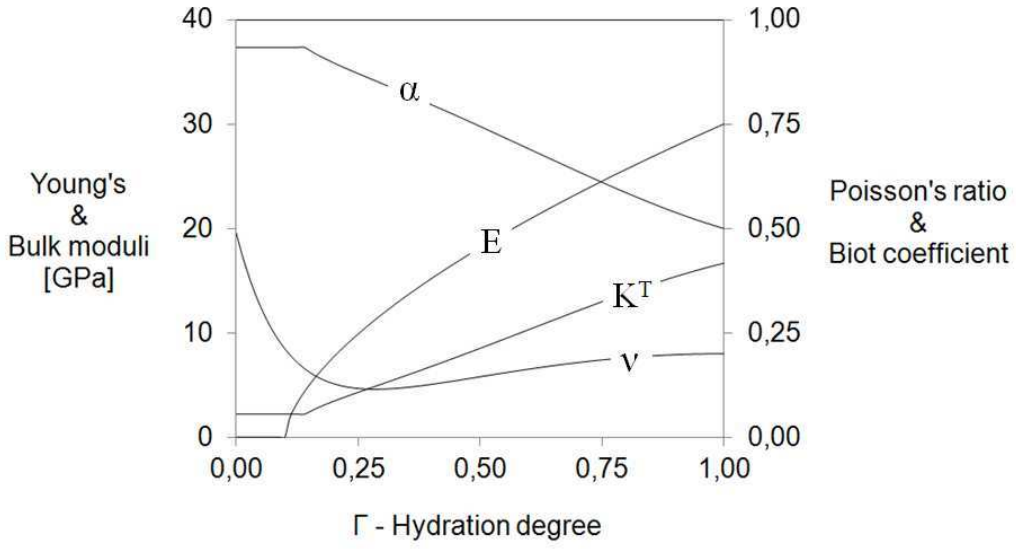

Figure 1.7 - Evolution of the main mechanical properties with hydration

Defining the solid pressure $p^s = p^g - S^l p^c$, the constitutive model used to compute the instantaneous shrinkage reads

$$\dot{\mathbf{e}}_{sh}^{inst} = \frac{\mathbf{1}}{3K_{(\Gamma)}^{T}} \frac{\partial\left(\bar{\alpha}_{(\Gamma)} p_s\right)}{\partial t} \tag{1.81}$$

Finally the viscous part of the shrinkage strain $\dot{\mathbf{e}}_{sh}^{visc}$ is computed using the creep rheological model (eqs (1.68-1.75)) in which the stress tensor is now $\bar{\alpha}_{(\Gamma)} p^s \mathbf{1}$.

For the time integration of eqs (1.76-1.81) see the ***Appendix B***.

1.5.10 Damage model

The damage D is linked to the elastic equivalent tensile strain $\hat{e}$. To take into account the coupling between creep and cracking, the expression of $\hat{e}$ proposed by Mazars (1986) is modified by Mazzotti and Savoia (2003), and reads

$$\hat{e} = \sqrt{\left\langle \mathbf{e}_{el} \right\rangle_+ : \left\langle \mathbf{e}_{el} \right\rangle_+ + \beta_{cr} \left\langle \mathbf{e}_{cr} \right\rangle_+ : \left\langle \mathbf{e}_{cr} \right\rangle_+} \tag{1.82}$$

where β_{cr} is a coefficient calibrated experimentally, which allows to consider that often cracking may occur even at lower tensile stress than the expected tensile strength since caused by the excess of strain. The damage criterion is given by:

$$f = \hat{e} - \kappa_0(\Gamma) \tag{1.83}$$

where $\kappa_0(\Gamma)$ is the tensile strain threshold, which is computed from the evolution of tensile strength (1.66) and the Young's modulus (1.65)

$$\kappa_0(\Gamma) = \frac{f_t(\Gamma)}{E(\Gamma)} = \frac{f_{t\infty}}{E_\infty} \left\langle \frac{\Gamma - \Gamma_0}{1 - \Gamma_0} \right\rangle_+^{\gamma_{FT} - \gamma_E} \tag{1.84}$$

Considering the equivalent tensile strain $\hat{e}$ eqn (1.82) and with respect to criterion (1.83), the damage *D* is given by the equations proposed by Benboudjema and Torrenti (2008).

Strain softening may induce mesh dependency because of the local damage formulation (Pijaudier-Cabot and Bažant, 1987). To overcome this problem the model is regularized in tension with the introduction of a characteristic length, l_c, related to the size of each finite element (Rots, 1988, Cervera and Chiumenti, 2006). After cracking strains localize in one row of finite elements but thanks to this characteristic length the same amount of energy is dissipated even if different meshes are used. The dissipated energy density g_{ft} (for tension failure) reads

$$g_{ft}(\Gamma)=\frac{f_t(\Gamma)\left(1+A_t/2\right)}{B_t\left(\Gamma\right)}=\frac{G_{ft}(\Gamma)}{l_c} \tag{1.85}$$

where G_{ft} is the fracture energy and l_{c} is the characteristic length; A_{t} and B_{t} are constant material parameters which control the softening part in the stress–strain curve in tension. To take into account the dependence of fracture energy on the degree of reaction Γ, the expression proposed by De Schutter and Taerwe (1997) is used:

$$G_{ft}(\Gamma)=G_{ft\infty}\left\langle\frac{\Gamma-\Gamma_0}{1-\Gamma_0}\right\rangle_+^{\gamma_G} \tag{1.86}$$

in with γ_{G} is a constant which have to be estimated experimentally (if experiments are not available it can be taken equal to 0.46).

1.6 FINAL SYSTEM OF EQUATIONS

Introducing some of the constitutive relationships presented in the previous paragraph the governing equations can be rewritten as follows:

Mass balance equation of the solid phase

$$\frac{\partial\left(\varepsilon^s\rho^s\right)}{\partial t}+\nabla\cdot\left(\varepsilon^s\rho^s\frac{\partial\mathbf{u}^s}{\partial t}\right)=0.228\cdot c\cdot\xi_{\max}^{hydr}\frac{\mathrm{d}\Gamma}{\mathrm{d}t} \tag{1.87}$$

Mass balance equation of the liquid phase

$$\begin{aligned}&\frac{\partial\left(\varepsilon^l\rho^l\right)}{\partial t}+\nabla\cdot\left(\varepsilon^l\rho^l\frac{\partial\mathbf{u}^s}{\partial t}\right)-\nabla\cdot\left[\rho^l\frac{k_{rel}^l\mathbf{k}}{\mu^l}\nabla\left(p^g-p^c\right)\right]=\\&=-0.228c\xi_{\max}^{hydr}\frac{\mathrm{d}\Gamma}{\mathrm{d}t}-\overset{l\to Wg}{M}\end{aligned} \tag{1.88}$$

Mass balance equation of the water vapour (species in the gaseous phase)

$$\begin{aligned}&\frac{\partial\left(\varepsilon^g\rho^g\omega^{\overline{Wg}}\right)}{\partial t}+\nabla\cdot\left(\varepsilon^g\rho^g\omega^{\overline{Wg}}\frac{\partial\mathbf{u}^s}{\partial t}\right)-\nabla\cdot\left(\rho^{gW}\frac{k_{rel}^g\mathbf{k}}{\mu^g}\nabla p^g\right)\\&-\nabla\cdot\left[\rho^g\frac{M_AM_W}{M_g^2}D^{\overline{Wg}}\nabla\left(\frac{p^{gW}}{p^g}\right)\right]=\overset{l\to Wg}{M}\end{aligned} \tag{1.89}$$

Mass balance equation of the dry air (species in the gaseous phase)

$$\frac{\partial\left(\varepsilon^g \rho^g \omega^{\overline{Ag}}\right)}{\partial t} + \nabla\cdot\left(\varepsilon^g \rho^g \omega^{\overline{Ag}} \frac{\partial \mathbf{u}^s}{\partial t}\right) - \nabla\cdot\left(\rho^{gA} \frac{k_{rel}^g \mathbf{k}}{\mu^g} \nabla p^g\right) + \nabla\cdot\left[\rho^g \frac{M_A M_W}{M_g^2} D^{\overline{Wg}} \nabla\left(\frac{p^{gW}}{p^g}\right)\right] = 0 \tag{1.90}$$

Enthalpy balance equation

$$\left(\rho C_p\right)_{\text{eff}} \frac{\partial \theta}{\partial t} + \left(\varepsilon^l \rho^l C_p^l \mathbf{v}^{\bar{l}} + \varepsilon^g \rho^g C_p^g \mathbf{v}^{\bar{g}}\right)\cdot\nabla\theta - \nabla\cdot\left(\boldsymbol{\lambda}_{\text{eff}} \nabla\theta\right) = = -\overset{l\to Wg}{M}\, H_{vap} + L_{hydr} \frac{\mathrm{d}\Gamma}{\mathrm{d}t} \tag{1.91}$$

Linear momentum balance equation

$$\nabla\cdot\left(\frac{\partial \mathbf{t}}{\partial t}\right) + \frac{\partial \rho}{\partial t}\mathbf{g} = 0 \tag{1.92}$$

To simplify the general reference formulation of Gawin *et al.* (2006a and 2006b) the following hypotheses are introduced:

i) the concrete is always partially saturated by liquid water ($S^l < 1$);
ii) the velocity of the solid skeleton is negligible compared to those of the fluid phases;
iii) the advective heat transport is insignificant because the heat transport is dominated by conduction;
iv) the parameters governing the thermo-hygro-chemical phenomena (THC) do not depend on mechanics (strains, cracking etc.).

i), ii), iii) and iv) allow to partially uncouple the problem in the sense that the mechanical solution depend on the THC one but not *viceversa*. These assumptions are admissible for not extreme thermal and/or hygral load conditions and small cracks opening (less than 100μm, Bažant *et al.*, 1986) as is generally the case of concrete at early age. The assumption of small deformation regime together with i) and ii) lead to the equivalent hypothesis that the impact of mechanical strains on porosity and on the fluid pressures is negligible.

Hence, taking into account these assumptions eqn (1.90) simplifies to

$$\frac{\partial\left(\varepsilon^g \rho^g \omega^{\overline{Ag}}\right)}{\partial t} - \nabla\cdot\left(\rho^{gA}\frac{k_{rel}^g \mathbf{k}}{\mu^g}\nabla p^g\right) + \nabla\cdot\left[\rho^g \frac{M_A M_W}{M_g^2} D^{\overline{Wg}} \nabla\left(\frac{p^{gW}}{p^g}\right)\right] = 0 \quad (1.93)$$

also adding (1.88) and (1.89) eliminates $\overset{l\to Wg}{M}$ and gives:

$$\begin{aligned} &\frac{\partial\left(\varepsilon^l \rho^l\right)}{\partial t} + \frac{\partial\left(\varepsilon^g \rho^g \omega^{\overline{Wg}}\right)}{\partial t} - \nabla\cdot\left[\rho^l \frac{k_{rel}^l \mathbf{k}}{\mu^l}\nabla\left(p^g - p^c\right)\right] + \\ &-\nabla\cdot\left(\rho^{gW}\frac{k_{rel}^g \mathbf{k}}{\mu^g}\nabla p^g\right) - \nabla\cdot\left[\rho^g \frac{M_A M_W}{M_g^2} D^{\overline{Wg}} \nabla\left(\frac{p^{gW}}{p^g}\right)\right] = \\ &= -0.228 c \xi_\infty \frac{\mathrm{d}\Gamma}{\mathrm{d}t} \end{aligned} \quad (1.94)$$

using (1.88) to eliminate $\overset{l\to Wg}{M}$ from (1.91) and passing from the relative temperature θ to the absolute one T give:

$$\begin{aligned} &\left(\rho C_p\right)_{\text{eff}} \frac{\partial T}{\partial t} - \nabla\cdot\left(\boldsymbol{\lambda}_{\text{eff}}\nabla T\right) = L_{hydr}\frac{\mathrm{d}\Gamma}{\mathrm{d}t} + H_{vap}\frac{\partial\left(\varepsilon^l \rho^l\right)}{\partial t} + \\ &+H_{vap} 0.228 c \xi_\infty \frac{\mathrm{d}\Gamma}{\mathrm{d}t} - \nabla\cdot\left[H_{vap}\rho^l \frac{k_{rel}^l \mathbf{k}}{\mu^l}\nabla\left(p^g - p^c\right)\right] + \\ &+\nabla H_{vap}\cdot\left[\rho^l \frac{k_{rel}^l \mathbf{k}}{\mu^l}\nabla\left(p^g - p^c\right)\right] \end{aligned} \quad (1.95)$$

1.7 NUMERICAL SOLUTION AND COMPUTATIONAL PROCEDURE

The primary variables of the model are: the gas pressure p^g, the capillary pressure p^c, the absolute temperature T and the displacements vector **u**. The hydration degree Γ and the mechanical damage D are internal variables. With reference to these primary variables the weak form of eqs (1.93-1.95) and (1.92) is obtained by means of the standard Galerkin procedure and is then discretized using the finite element method (Lewis and Schrelfer, 1998). The integration in the time domain is carried out using the θ-Wilson Method in which θ is set equal to 0.52. Within each time step the equations are linearized by means of the Newton-Raphson method.

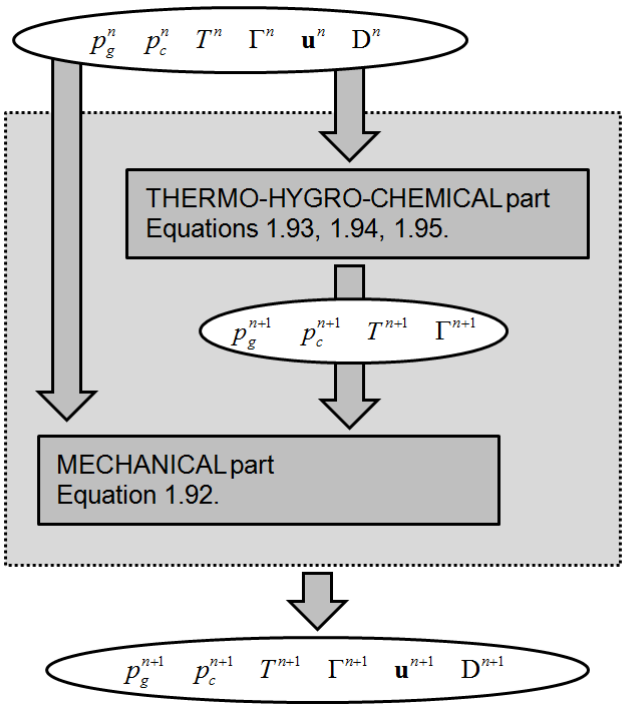

Figure 1.8 - Computational procedure: step n + 1

For the FE discretization the primary variables are expressed in terms of their nodal values as

$$\begin{aligned} p^g(t) &\cong \mathbf{N}_{\mathrm{p}}\bar{\mathbf{p}}^g(t) & p^c(t) &\cong \mathbf{N}_{\mathrm{p}}\bar{\mathbf{p}}^c(t) \\ T(t) &\cong \mathbf{N}_{\mathrm{T}}\bar{\mathbf{T}}(t) & \mathbf{u}(t) &\cong \mathbf{N}_{\mathrm{u}}\bar{\mathbf{u}}(t) \end{aligned} \tag{1.96}$$

where $\bar{\mathbf{p}}^g(t)$, $\bar{\mathbf{p}}^c(t)$, $\bar{\mathbf{T}}(t)$ and $\bar{\mathbf{u}}(t)$ are vectors of the nodal values of the primary variables at the time instant *t*, and $\mathbf{N}_{\mathrm{p}}$, $\mathbf{N}_{\mathrm{T}}$ and $\mathbf{N}_{\mathrm{u}}$ are vectors of shape functions related to these variables. After the FE discretization, the final system of equations can be expressed in a matrix form, eqs (1.97 and 1.98).

$$\mathbf{C}_{ij}(\mathbf{x})\frac{\partial \mathbf{x}}{\partial t} + \mathbf{K}_{ij}(\mathbf{x})\mathbf{x} = \mathbf{f}_i(\mathbf{x}) \tag{1.97}$$

with

$$\mathbf{C}_{ij} = \begin{pmatrix} \mathbf{C}_{gg} & \mathbf{C}_{gc} & \mathbf{C}_{gt} & 0 \\ \mathbf{C}_{cg} & \mathbf{C}_{cc} & \mathbf{C}_{ct} & 0 \\ \mathbf{C}_{tg} & \mathbf{C}_{tc} & \mathbf{C}_{tt} & 0 \\ 0 & 0 & 0 & \mathbf{C}_{uu} \end{pmatrix} \quad \mathbf{K}_{ij} = \begin{pmatrix} \mathbf{K}_{gg} & \mathbf{K}_{gc} & \mathbf{K}_{gt} & 0 \\ \mathbf{K}_{cg} & \mathbf{K}_{cc} & \mathbf{K}_{ct} & 0 \\ \mathbf{K}_{tg} & \mathbf{K}_{tc} & \mathbf{K}_{tt} & 0 \\ 0 & 0 & 0 & 0 \end{pmatrix} \quad \mathbf{f}_i = \begin{pmatrix} \mathbf{f}_g \\ \mathbf{f}_c \\ \mathbf{f}_t \\ \mathbf{f}_u \end{pmatrix} \tag{1.98}$$

where $\mathbf{x}^{\mathrm{T}} = \left\{ \overline{\mathbf{p}}^{g}, \overline{\mathbf{p}}^{c}, \overline{\mathbf{T}}, \overline{\mathbf{u}} \right\}$ is the approximated solution. The nonlinear coefficients of the matrices $\mathbf{C}_{ij}(\mathbf{x})$ and $\mathbf{K}_{ij}(\mathbf{x})$, and the source terms in the vector $\mathbf{f}_i(\mathbf{x})$ are given in the ***Appendix C***.

The solution of the system of equations (1.93-1.95) is obtained by a monolithic approach (fully coupled) in which the internal variable Γ (degree of reaction) is updated at each iteration *via* the hydration model presented in the *sub-paragraph 1.5.1*. After the thermo-hygro-chemical (THC) step, the new computed THC solution is used to compute the mechanical solution (M) (i.e. displacements and damage). The computational procedure is represented in ***Figure 1.8***. The degree of reaction, Γ, and the hydration rate (results of the THC computation), are given to the M part of the model as input variables. The effect of the THC results on the M solution is taken care through the introduction of the thermal and shrinkage strains in the source term in eqn (1.97). Similarly, creep strains (basic and drying creep) are introduced in this source term but these are updated at each iteration within the time step, because they depend on the rate of the effective stress tensor and on its averaged value in the time step. Also damage, *D*, being related to stresses and strains, is updated at each iteration within the time step of the M calculation. This model has been implemented in the code Cast3M of the French Atomic Energy Commission (*http://www-cast3m.cea.fr*).

REFERENCES OF CHAPTER 1

Baroghel-Bouny V, Mainguy M and Coussy O 1999 Characterization and identification of equilibrium and transfer moisture properties for ordinary and high-performance cementitious materials *Cement and Concrete Research* **29**(8) 1225–1238.

Bažant Z P and Najjar L J 1972 Nonlinear water diffusion in non-saturated concrete *Materials and Structures* **5** 3-20.

Bažant Z P, Sener S and Kim J K 1986 Effect of cracking on drying permeability and diffusivity of concrete *ACI Materials Journal* **84** 351-357.

Bažant Z P and Prasannan S 1989 Solidification theory for concrete creep. I: formulation *Journal of Engineering Mechanics (ASCE)* **115** 1691-1703.

Bažant Z P and Prasannan S 1989 Solidification theory for concrete creep. II. Verification and application *Journal of Engineering Mechanics (ASCE)* **115** 1704-1725.

Bažant Z P, Hauggaard A B, Baweja S and Ulm F J 1997 Microprestress-solidification theory for concrete creep. I: aging and drying effects *Journal of Engineering Mechanics (ASCE)* **123**(11) 1188-1194.

Benboudjema F and Torrenti J M 2008 Early-age behaviour of concrete nuclear containments *Nuclear Engineering and Design* **238**(10) 2495-2506.

Cast3M: FE code developed by the French Atomic Agency (CEA) - www-cast3m.cea.fr.

Cervera M and Chiumenti M 2006 Mesh objective tensile cracking via a local continuum damage model and a crack tracking technique *Computat. Methods Appl. Mech. Eng.* **196** 304-320.

De Schutter G and Taerwe L 1996 Degree of hydration based description of mechanical properties of early-age concrete *Materials and Structures* **29**(6) 335-344.

De Schutter G 2002 Finite element simulation of thermal cracking in massive hardening concrete elements using degree of hydration based material laws *Computers and Structures* **80** 2035-2042.

De Schutter G 1999 Degree of hydration based Kelvin model for the basic creep of early age concrete *Materials and Structures* **32** 260-265.

De Schutter G and Taerwe L 1997 Fracture energy of concrete at early ages *Materials and Structures* **30** 67-71.

Gawin D, Majorana C E and Schrefler B A 1999 Numerical analysis of hygro-thermal behaviour and damage of concrete at high temperatures *Mechanics of Cohesive-Frictional Materials* **4** 47-74.

Gawin D, Pesavento F, Schrefler B A 2006a Hygro-thermo-chemo-mechanical modelling of concrete at early ages and beyond. Part I: Hydration and hygro-thermal phenomena *International Journal for Numerical Method in Engineering* **67**(3) 299-331.

Gawin D, Pesavento F, Schrefler B A 2006b Hygro-thermo-chemo-mechanical modelling of concrete at early ages and beyond. Part II: Shrinkage and creep of concrete *International Journal for Numerical Method in Engineering* **67**(3) 332-363.

Gray W G, Leijnse A, Kolar R L and Blain C A 1993 Mathematical tools for changing scales in the analysis of physical systems *Boca Raton FL: CRC Press Inc*.

Gray W G 1999 Thermodynamics and constitutive theory for multiphase porous-media flow considering internal geometric constraints *Adv Water Resources* **22**(5) 521–47.

Gray W G 2000 Macroscale equilibrium conditions for two-phase flow in porous media. *International Journal of Multiphase Flow* **26** 467–500.

Gray W G and Miller C T 2005 Thermodynamically constrained averaging theory approach for modeling flow and transport phenomena in porous medium systems: 1. Motivation and overview *Advances in Water Resources* **28** 161–180.

Gray W G and Miller C T 2009 Thermodynamically constrained averaging theory approach for modeling flow and transport phenomena in porous medium systems: 5. Single-fluid-phase transport *Advances in Water Resources* **32** 681–711.

Gray W G, Schrefler B A 2001 Thermodynamic approach to effective stress in partially saturated porous media.*European Journal of Mechanics – A/Solids* **20** 521–538.

Gray W G and Schrefler B A 2007 Analysis of the solid stress tensor in multiphase porous media *IJ Num. Anal. Meth. Geomechanics* **31** 541-581.

Hansen T C 1986 Physical structure of hardened cement paste. A classical approach *Mater. Struct.* **19**(114) 423-436.

Hassanizadeh S M and Gray W G 1979a General conservation equations for multi-phase systems: 1. Averaging procedure *Advances in Water Resources* **2** 131-144.

Hassanizadeh S M and Gray W G 1979b General conservation equations for multi-phase systems: 2. Mass, momenta, energy and entropy equations *Advances in Water Resources* **2** 191-203.

Hassanizadeh S M Gray W G 1980 General conservation equations for multi-phase systems: 3. Constitutive theory for porous media flow *Advances in Water Resources* **3** 25-40.

Jackson A S, Miller C T and Gray W G 2009 Thermodynamically constrained averaging theory approach for modelling flow and transport phenomena in porous medium systems: 6. Two-fluid-phase flow *Advances in Water Resources* **32** 779-795.

Jensen O M 1993 Autogenous deformation and RH-change, self-desiccation and self-desiccation shrinkage. *PhD thesis*. Building Materials Laboratory, Technical University of Denmark.

Jensen O M and Hansen P F 1996 Autogenous deformation and change of the relative humidity in silica fume-modified cement paste *ACI Mat J* **93**(6) 539-543.

Jensen O M and Hansen P F 2001 Water-entrained cement-based materials: I. Principles and theoretical background *Cement and Concrete Research* **31**(4) 647-654.

Jensen O M and Hansen P F 2002 Water-entrained cement-based materials: II. Experimental observations *Cement and Concrete Research* **32**(6) 973-978.

Lewis R W and Schrefler B A 1998 The Finite Element Method in the Static and Dynamic Deformation and Consolidation of Porous Media, Wiley, Chichester.

Mazars J 1986 A description of micro and macroscale damage of concrete structures *Engineering Fracture Mechanics* **25**(5-6) 729-737.

Mazzotti C and Savoia M 2003 Nonlinear Creep Damage Model for Concrete under Uniaxial Compression *Journal of Engineering Mechanics* **129**(9) 1065-1075.

Mills R H 1966 *ACI – SP 60*, Washington.

Perre P 1987 Measurements of softwoods' permeability to air: importance upon the drying model. *Int. Comm. Heat Mass Transfer* **14** 519-529.

Pesavento F, Gawin D and Schrefler BA 2008 Modeling cementitious materials as multiphase porous media: theoretical framework and applications *Acta Mechanica* **201**(1-4) 313–339.

Pijaudier-Cabot G and Bažant Z P 1987 Nonlocal damage theory *J. of Engrg Mech.* **113** 1512-1533.

Powers T C and Brownyard T L 1948 Studies of the Physical Properties of Hardened Portland Cement Paste *Bulletin 22, Research Laboratories of the Portland Cement Association,* Chicago.

Powers T C 1947 A Discussion of Cement Hydration in Relation to the Curing of Concrete *Bulletin 25, Research Laboratories of the Portland Cement Association,* Chicago.

Powers T C 1960 Physical properties of cement paste. *Proceedings of the Fourth International Symposium on the Chemistry of Cement, Washington, DC* **V**-1 577-613.

Regourd M and Gauthier E 1980 Comportement des ciments soumis au durcissement acceleré *Annales de I'ITBTP* **179** 65-96.

Rots J G 1988 Computational modeling of concrete fracture *PhD Thesis* Delft University of Technology.

Schrefler B A 2002 Mechanics and thermodynamics of saturated-unsaturated porous materials and quantitative solutions *Applied Mechanics Reviews (ASME)* **55**(4) 351-388.

Sciumè G, Benboudjema F, De Sa C, Pesavento F, Berthaud Y and Schrefler B A 2012 A multiphysics model for concrete at early age applied to repairs problems *Engineering Structures* (in preparation).

Shelton S 2011 Mechanistic modelling of cancer tumor growth using a porous media approach. *PhD Thesis*. University of North Carolina at Chapel Hill, Chapel Hill (USA).

Tacke R 2002 Feuchte- und Festigkeitsentwicklung hydratisierenden Betons - Modellierung und numerische Analyse *PhD Thesis* TU Braunschweig, Institut für Statik.

Torrenti J M and Benboudjema F 2002 *Mechanical threshold of cementitious materials at early age* Materials and Structures **277**(38) 299-304.

Van Genuchten M-Th 1980 A closed-form equation for predicting the hydraulic conductivity of unsaturated soils *Soil Science Society of America Journal* **44**(5) 892-898.

Waller V 1999 Relations entre la composition des bétons, exothermie en cours de prise et résistance en compression *PhD Thesis* Ecole Nationale des Ponts et Chaussées, Paris.

2 CONCRETE BEHAVIOR: EXPERIMENTAL DATA AND MODEL RESULTS

2.1 INTRODUCTION

Concrete is a highly heterogeneous material. Due to the complexity of its micro and meso structures its behavior is strongly non-linear and very hard to predict. Concrete can be considered as a composite material consisting of cement paste and aggregates (in special concretes other phases may be present). The cement paste is a cohesive matrix which gives to concrete stiffness and strength; its percentage in volume normally varies between 25% and 45% of the total volume of concrete. Most of the volume of concrete (up to 75%) is occupied by aggregates. Originally aggregates were viewed as inert materials dispersed throughout the cement paste largely for economic reasons. However economy is not the only reason for using aggregates since they confer considerable technical advantages to concrete, such as higher volume stability and better durability than hydrated cement paste alone. Aggregates are connected by means of the cement paste, in a manner similar to masonry construction. The interface area between cement paste and aggregates, commonly called the interfacial transition zone (ITZ), is often the weak point of concrete where cracks start. Both cement paste and aggregates are porous solids phases. The pores are saturated by liquid water and gas (mixture of water vapour and dry air) which can flow within the porous network. At early ages, the largest and surface pores of aggregates are filled by the fresh cement paste and even if the residual porosity of aggregates contributes to the overall porosity of concrete, the liquid and gaseous

transfers occur essentially within the cement paste (except in special cases as for instance aggregates with entrained water, Hansen and Jensen, 2001). Due to this heterogeneity and to the presence of water and gas in the pores, the global behavior of concrete is the consequence of the coupling of several chemical, hygral, thermal and mechanical phenomena at different scales, from the nano to the macroscopic level.

This chapter deals about concrete hydration, its mechanical properties, shrinkage and creep. Each of these aspects is presented separately by means of simple tests analyzed together with the results obtained numerically *via* the developed model.

2.2 HYDRATION PROCESS AND RELATED PHENOMENA

Portland Cements consist essentially of four compounds reported in ***Table 2.1***.

Table 2.1. – Main compounds of Portland Cement (Neville, 1996).

Name of compound	*Oxide composition*	*Abbreviation*
Tricalcium silicate	$3CaO.SiO_2$	C_3S
Dicalcium silicate	$2CaO.SiO_2$	C_2S
Tricalcium aluminate	$3CaO.Al_2O_3$	C_3A
Tetracalcium aluminoferrite	$4CaO.Al_2O_3.Fe_2O_3$	C_4AF

Cement chemists use abbreviated symbols which describes each oxide by one letter: CaO = C; SiO_2 = S; Al_2O_3=A; and Fe_2O_3=F. Similarly H_2O in hydrated cement is denoted by H, and SO_3 by S. The compounds listed in the previous table react with water forming the solid hydrated cement paste. The two calcium silicates are the main constituents of cements and so the physical behaviour of cement during hydration is similar to that of these two compounds alone. The mechanics of hydration is not yet perfectly known but probably hydration proceeds by a gradual reduction of the size of the anhydrous grain of cement. For instance, Giertz-Hedstrom (1938) found that after 28 days in contact with water only a depth of 4 μm of cement grains is hydrated and 8 μm after a year. Furthermore Powers (1949) calculated that complete hydration is possible only for cement particles smaller than 50 μm since in greater particles water cannot reach the core. The main hydrates are the calcium silicate hydrates $C_3S_2H_3$ (the so called C-S-H) and the tricalcium aluminate hydrate C_3AH_6. $C_3S_2H_3$ consists of fibrous particles with a very irregular shape (see ***Figure 2.1***).

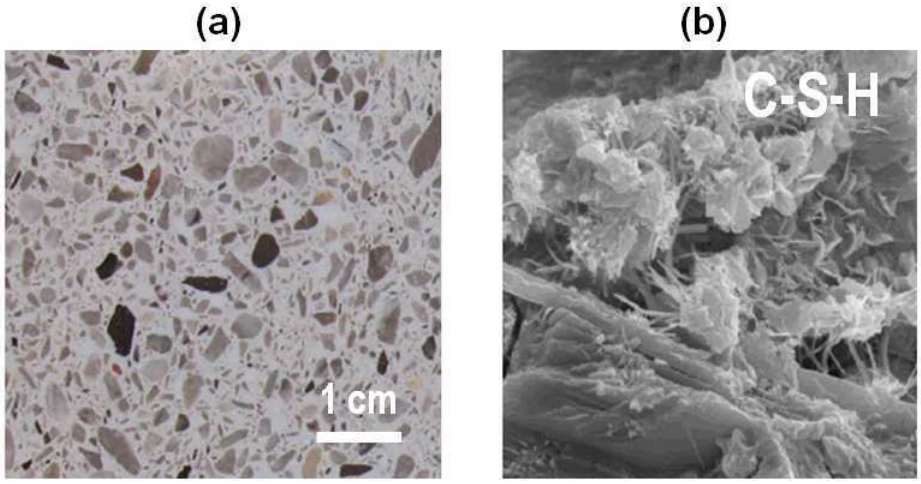

Figure 2.1 – Mesoscopic scale: aggregates within cement paste (a); gel pores scale: Calcium Silicate Hydrates (C-S-H) (b).

Assuming that $C_3S_2H_3$ is the final product of hydration of both C_3S and C_2S, the reaction of the two calcium silicates and of the tricalcium aluminate with water is given by

$$\begin{aligned} 2C_3S+6H &\rightarrow C_3S_2H_3+3Ca(OH)_2 \\ 2C_2S+4H &\rightarrow C_3S_2H_3+Ca(OH)_2 \\ C_3A+6H &\rightarrow C_3AH_6 \end{aligned} \qquad (2.1)$$

These equations are approximations since the knowledge of the exact stoichiometry of cement hydration is not yet exhaustive; also the stoichiometric approach of Power (1960) presented in the following pages (and used in the mathematical model) is based on approximated equations. In other word stoichiometry of hydration should be understood here as approximate stoichiometry.

The kinetic of cement hydration results from the different hydration rates of its compounds and their interactions. Being the hydration of cement an exothermic reaction the heat production is a direct indicator of the hydration rate. ***Figure 2.2*** shows the evolution of the heat production with respect to time. The first peak corresponds to the initial hydration of the surface of the cement particles, largely involving the C_3A; in fact when the cement grain ‘meets’ water, a quasi-instantaneous hydration of its surface happens and the formed layer of hydrates impedes further hydration; consequently concrete passes through a *dormant* phase during which the hydration rate is very low and concrete is workable. Following this dormant phase (one or two hours) there is an important increase of the hydration rate until a second peak is achieved typically between eight and twelve hours of age.

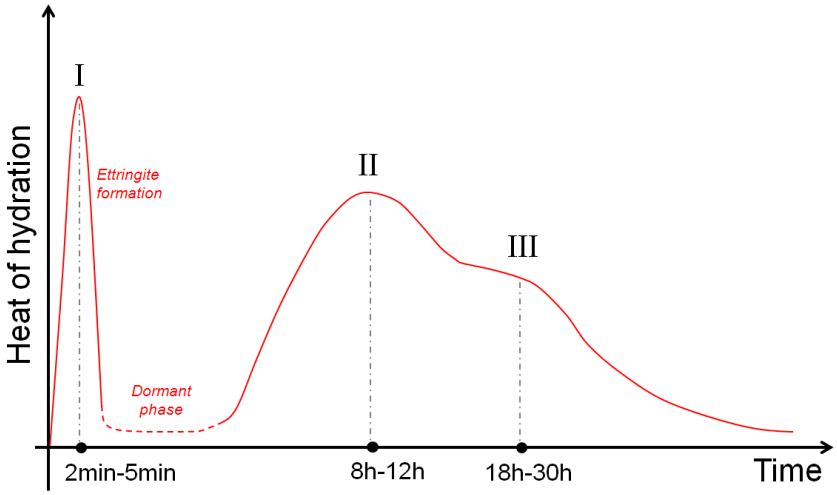

Figure 2.2 – Heat of hydration, evolution with respect to time. The first part of the time axis is not in scale.

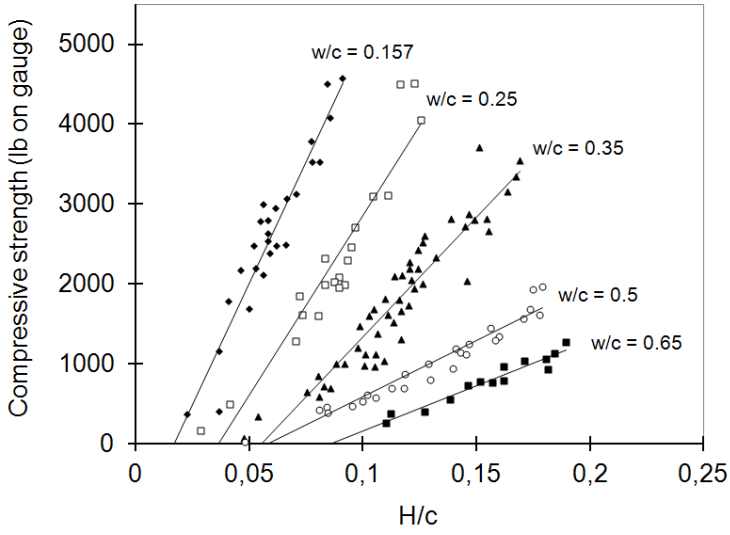

Figure 2.3 - Compressive strength of cement pastes with different w/c ratios. H/C is the amount of hydration products per gram of cement (readapted from Taplin, 1957).

After this peak the hydration rate decreases during a long period. In some cements there is also a third peak related to a renewed reaction of C_3A, due to the exhaustion of gypsum. The hydration rate of C_3A is very high and leads to an immediate stiffening of the cement paste, the so called flash set. For this reason, gypsum is added[2] to the cement to control the reaction of C_3A: gypsum and C_3A react to form insoluble ettringite crystals retarding and weakening the reaction of C_3A. However gypsum needs a few minutes to exert its retardation effect and consequently we observe a very important peak within the first five minutes after the contact with water, probably connected with the reaction of pure C_3A with water.

[2] Gypsum, which reacts with C_3A and C_4AF, partially modifies the last reaction in eqn (2.1).

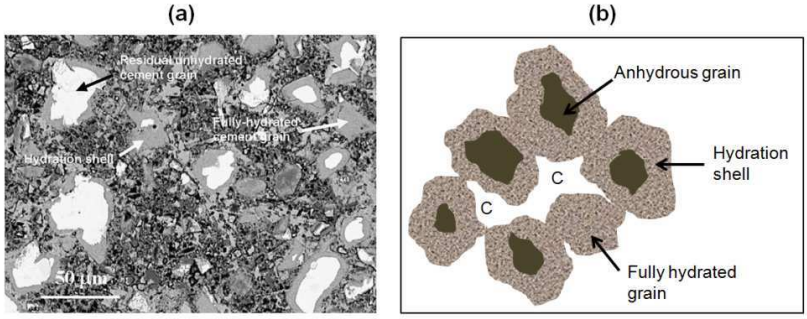

Figure 2.4 – Microscopic image of the cement paste (Diamond, 2004) (a), and a model for its solid microstructure (b). C indicates the capillary pores.

During the first hours of hydration the change from the semi-liquid to the solid stage occurs; this is the so called *setting*. Setting is the consequence of the mutual coagulation of the components of the paste thanks to the cohesive hydration products. For cement pastes the amount of hydrates which allows setting depends strictly on the water/cement ratio. ***Figure 2.3*** shows that for cement pastes more elevated is the water/cement ratio more hydrates are needed to have a not negligible value of compressive strength. However for concrete due to the presence of aggregates a lower amount of hydrates is sufficient to set the material (Taplin, 1957).

2.2.1 Microstructure of the cement paste

The microstructure of the cement paste consists of the hydration products (essentially C-S-H gel and $Ca(OH)_2$), anhydrous cement grains and capillary pores which are partially saturated by water (see ***Figure 2.4***). Actually also hydrates are porous but their pores are very small compared to the capillary ones (from one to two orders of magnitude smaller), and for the relative humidities higher than the 50% are completely water-filled.

The porosity of hydrates is approximately equal to 0.28 and the order of magnitude of the pores size is about 2 nm. The mass of non-evaporable water (chemically combined) has been estimated as 23% of the mass of the anhydrous cement. The volume of the solid part of hydrates is smaller than the sum of the volumes of the anhydrous cement and the chemically bound water by about 0.254 of the volume of the latter. These averaged relationships have been obtained experimentally by Power (1947 and 1960) and are the basis for the equations proposed by Jensen and Hansen (1996, 2001 and 2002) where silica fume is also considered (eqs (1.32) of ***Chapter 1***). These equations are valid for an isolated system (i.e. without mass exchanges with the external environment) and give the evolution with hydration of the volume fractions of chemical shrinkage, capillary water, gel water, gel solid, anhydrous cement and silica fume.

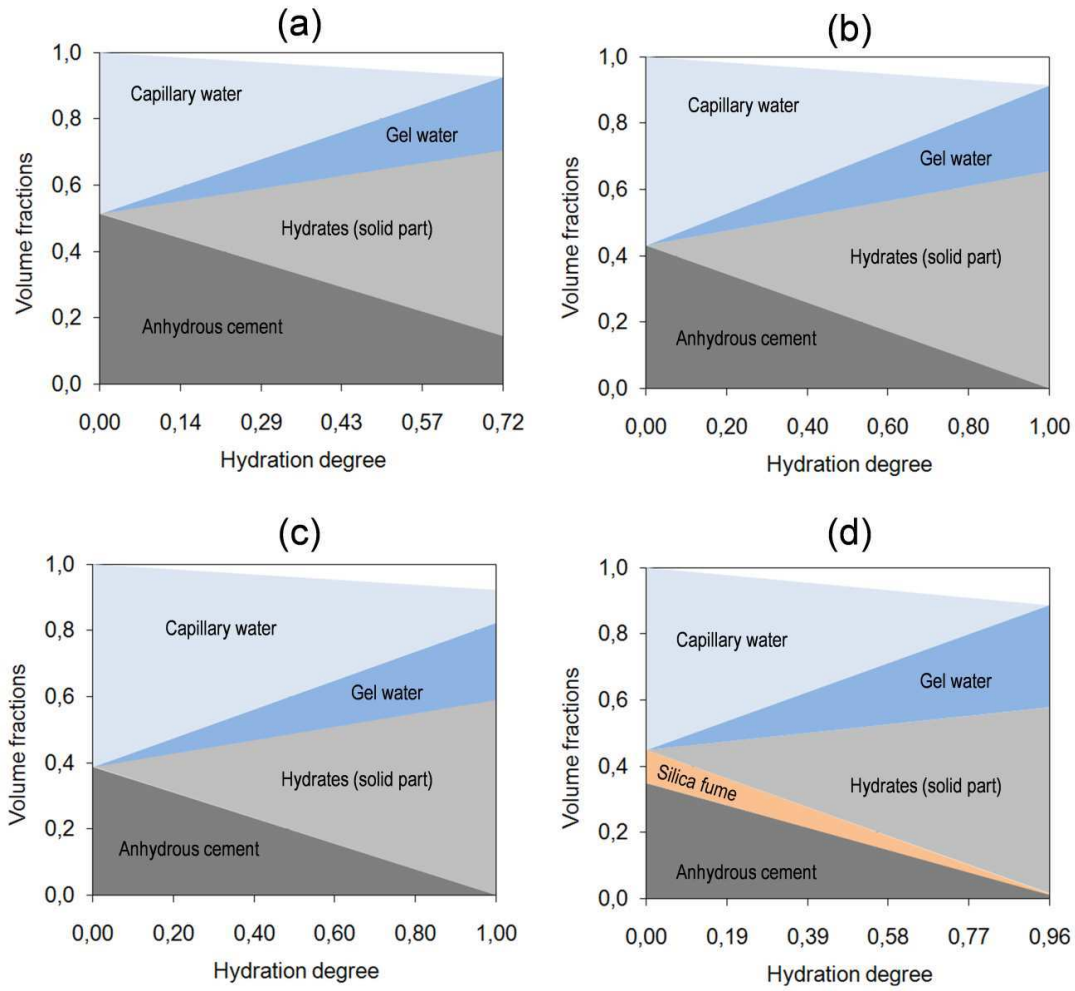

Figure 2.5 – Volume fractions over hydration of unhydrated cement, silica fume, capillary water, gel water and hydrates (solid part) for four cement pastes: w/c=0.30 (a); w/c =0.42 (b); w/c = 0.5 (c); w/c = 0.5 and s/c = 0.2 (d).

The chemical shrinkage has been firstly observed and quantified by LeChâtelier in 1900. The development of a volume of gas caused by this phenomenon leads to the self-desiccation of the cement paste (Jensen, 1993). From this averaging stoichiometric model, the smallest water/cement ratio that allows the hydration of all the cement is 0.42. ***Figure 2.5.a-c*** shows the volume fractions of the different phases in three cement pastes with w/c = 0.30, w/c = 0.42 and w/c = 0.50. In the case represented in ***Figure 2.5.d*** also silica fume is considered (w/c=0.5, s/c=0.2). The capillary porosity, at any stage of hydration, represents that part of the volume which has not been filled by the hydration products; the total volume of capillary pores decreases with the progress of hydration and can be estimated from ***Figure 2.5*** as the sum of capillary water and chemical shrinkage (white area in the diagrams).

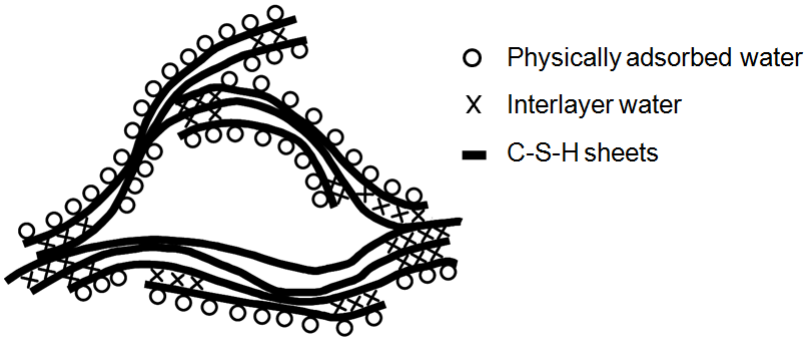

Figure 2.6 – Idealized structure of hydrated silicates (Feldman *et al.*,1968).

The order of magnitude of the size of capillary pores was estimated to be about 1 μm, however the size of pores varies widely and Glasser's studies (1992) indicate that in mature cement pastes few pores are larger than 1 μm, with most pores being smaller than 100 nm. The capillary pores are partially filled by water which is commonly called "free water"; due to their size, very large compared to that of the gel pores, capillary pores are usually empty for relative humidities lower than the 45%. The distribution of the capillary pores and their connection grade are the main factors which affect concrete permeability. With water/cement ratios greater than 0.7 even after the complete hydration the volume of hydrates is not sufficient to fill all the interconnections between capillaries, hence the permeability of concrete may become very important. In ***Figure 2.5*** the volume fraction of the gel water is also reported. Being the gel pores water filled, the volume fraction of gel water in the figure represents also the volume of the gel porosity. Water in gel pores is typically classified as evaporable water but is much less "free" than water in capillary pores, because gel water is physically adsorbed on the surfaces of C-S-H sheets (see ***Figure 2.6***).

2.2.2 Heat of hydration of cement

The hydration reaction is exothermic, energy of up to 500 J *per* gram of cement being liberated. Consequently in massive structures hydration can result in a large rise in temperature and also in large thermal gradients which may induce diffuse or localized cracking. This behavior modified by creep and autogenous shrinkage can be very difficult to predict. Moreover, especially in the summer months (depending evidently on the geographic region) also solar radiation on the surfaces must be taken into account since it has a not negligible effect (Sciumè *et al.* 2012a). The knowledge of the heat production of cement is then critical especially in mass concrete.

Table 2.2. –Indicative values of the heat of hydration of the cement compounds (Lerch *et al.* 1934).

Compound	*Heat of hydration (J/kg)*
C_3S	502×10^3
C_2S	260×10^3
C_3A	867×10^3
C_4AF	419×10^3

The measured heat of hydration consists of the chemical heat of the reactions of the compounds and the heat of adsorption of water on the surface of the formed gel, this last part is almost a quarter of the total heat of hydration. The factors that impact on the heat release of concrete during hydration are essentially four.

i. *The quantity of cement in the mix*. The cement content can be varied in order to control the heat development.

ii. *The cement type and its chemical composition*. The heat of hydration depends on the chemical composition of cement, and can be calculated with good degree of accuracy summing the heats of hydration of the individual compounds when hydrated separately. Typical values of the heat of hydration of pure compounds are given in ***Table 2.2***. From this table follows that by reducing the proportion of the compounds that hydrate most rapidly (C_3A and C_3S) the high rate of heat release at early ages can be controlled.

iii. *The fineness of cement*. The increase in fineness speeds up the reaction of hydration and consequently the heat release rate increases. It is realistic to assume that the initial hydration rate is proportional to the surface area of cement. However, at later stages, the total amount of released heat is not affected significantly by the fineness of cement.

iv. *Curing temperature*. The temperature at which hydration occurs has an important effect on the development of the rate of heat. However, similarly the fineness of cement, the curing temperature has no substantial effect on the long term value of the heat of hydration.

The hydration degree ξ has been defined as the ratio between the mass of reacted cement at time t, $c_{hydr}(t)$, and the initial mass of anhydrous cement present in the mix c

$$\xi(t) = \frac{c_{hydr}(t)}{c} \tag{2.2}$$

However the experimental quantification of the mass of the hydrated cement is not easy. For this reason indirect methods based on the evaluation of the consequences of hydration have been developed. These methods are based on the definition of the degree of reaction, (already introduced, and briefly explained in ***Chapter 1***) which varies from 0 to 1. The hydration degree ξ, is the degree of reaction Γ times the final hydration degree ξ_∞, which depends essentially on the water/binder ratio of the cement paste.

$$\xi(t) = \xi_\infty \Gamma(t) \tag{2.3}$$

Actually for most of frequently used concretes the amount of water is not sufficient to hydrate all the cement present in the mix and so the final hydration degree will be lower than 1. Hence, to estimate the hydration degree in time ξ(t), the evolution of the degree of reaction Γ(t) and the final value of the hydration degree ξ_∞ are needed. The final hydration degree ξ_∞ can be obtained using the averaged stoichiometric equations presented in ***Chapter 1*** (eqs 1.32), imposing the volume of the capillary water equal to zero

$$\xi_\infty = \min\left\{1 \quad \frac{p}{k\cdot\left[1{,}32+1{,}57\cdot(s/c)\right]\cdot(1-p)}\right. \tag{2.4}$$

However, the obtained value of ξ_∞ is very often an overestimation of the real final hydration degree; indeed after a certain degree of hydration the formed hydrates obstruct the contact of water with the not hydrated core of the cement grain. Then empirical equations based on experiments (Mills 1966, and Waller, 1999) are commonly used to estimate ξ_∞. (see eqs (1.36) and ***Figure 1.4*** of ***Chapter1***).

In the presented model the degree of reaction has been defined as the ratio between the amount of water chemically combined at time *t*, $m_{bw}(t)$, and that chemically combined at time $t = \infty$, $m_{bw}(t=\infty)$

$$\Gamma(t) = \frac{m_{bw}(t)}{m_{bw}(t=\infty)} \tag{2.5}$$

The mass of chemically combined water m_{bw} is also indicated as bound water. The degree of reaction can also be defined from the amount of heat released until time *t*, $Q_{hydr}(t)$, and the total heat released $Q_{hydr}(t=\infty)$, when the reaction is finished

$$\Gamma(t) = \frac{Q_{hydr}(t)}{Q_{hydr}(t=\infty)} \tag{2.6}$$

Hydration is not only exothermic but also a thermo-activated reaction. For this reason in mass concrete the important increase of temperature gives an acceleration of the hydration process. Therefore time dependent hydration laws are not adequate in particular when the temperature of concrete varies a lot during hydration. The effect of temperature can be integrated by means of an Arrhenius type law (e.g. Regourd and Gauthier, 1980)

$$\frac{\mathrm{d}\Gamma}{\mathrm{d}t} = A_{(\Gamma)} \exp\left(-\frac{E_a}{RT}\right) \tag{2.7}$$

where T is the absolute temperature $A_{(\Gamma)}$ is the macroscopic volume-averaged chemical affinity, E_a is the hydration activation energy and R is the universal gas constant (8.314 $J.mol^{-1}.K^{-1}$). In eqn (2.7), which is used in the parameters identification process, the effect of relative humidity is not explicitly taken into account as done in eqn (1.29) of ***Chapter 1*** where the function $\beta_{(h)}$ is introduced. In fact the effect of self-desiccation on hydration kinetic is intrinsic on the affinity function, $A_{(\Gamma)}$, and $\beta_{(h)}$ has essentially no impact in sealed condition but only in drying condition.

Similarly to the heat of hydration the activation energy depends on the chemical composition of cement (Kishi & Maekawa, 1994). Recently an empirical equation based on the percentage of C_3A and C_4AF and on the specific surface of cement has been proposed by Schindler (2004)

$$E_a = 22100 \cdot \left(P_{C_3A}\right)^{0.3} \cdot \left(P_{C_4AF}\right)^{0.3} \cdot Blaine^{0.35} \tag{2.8}$$

where P_{C_3A} and P_{C_4AF} are the weight ratios of C_3A and C_4AF respectively (in term of total cement content) and *Blaine* is the Blaine value[3].

The chemical affinity is a hydration dependent function which allows describing the hydration kinetic; its evolution with hydration can be obtained by means of the adiabatic calorimetry test: the concrete is placed in an adiabatic calorimeter and assuming the appropriate activation energy E_a, from the evolution of the concrete temperature the averaged chemical affinity can be evaluated.

[3] The Blaine value is the specific surface area of cement (m^2/kg).

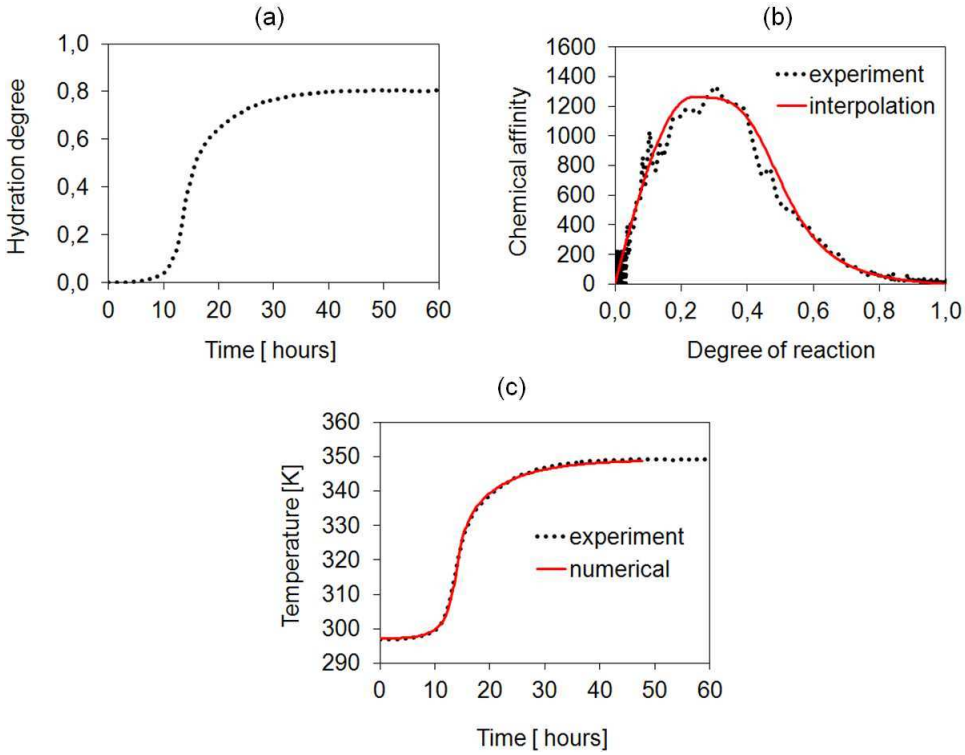

Figure 2.7 – Hydration degree over time estimated from the measured temperatures in adiabatic condition (a); experimental averaged chemical affinity and its interpolation *via* eqn (1.31) (b); measured temperature and numerical one computed after the identification of the averaged chemical affinity (c).

The system is thermally governed by the following equation

$$(\rho C)_{eff}\frac{\mathrm{dT}}{\mathrm{d}t}=Q_{\infty}\frac{\mathrm{d}\Gamma}{\mathrm{d}t} \tag{2.9}$$

where Q_{∞} is the total heat released during hydration which can simply be estimated as $Q_{\infty}=(\rho C)_{eff}\left(\mathrm{T}_{fin}-\hat{\mathrm{T}}_0\right)$. From the n measured temperatures $\hat{\mathrm{T}}_0,\hat{\mathrm{T}}_1,\ldots..\,\hat{\mathrm{T}}_n$, at the correspondent times the degree of reaction $\hat{\Gamma}$ can be computed as

$$\hat{\Gamma}_0=0\ ,\qquad \hat{\Gamma}_{i+1}=\hat{\Gamma}_i+\frac{(\rho C)_{eff}}{Q_{\infty}}\left(\hat{\mathrm{T}}_{i+1}-\hat{\mathrm{T}}_i\right)\qquad i=0,1,..,(n-1) \tag{2.10}$$

Once computed the degrees of reaction $\hat{\Gamma}_0,\hat{\Gamma}_1,\ldots..\,\hat{\Gamma}_n$, eqn (2.7) allows to calculate approximately the chemical affinity as

$$A\left(\hat{\Gamma}_{i+1}\right)=\frac{\hat{\Gamma}_{i+1}-\hat{\Gamma}_i}{t_{i+1}-t_i}\left[\exp\left(-\frac{E_a}{R\hat{\mathrm{T}}_{i+1}}\right)\right]^{-1}\qquad i=0,1,..,(n-1) \tag{2.11}$$

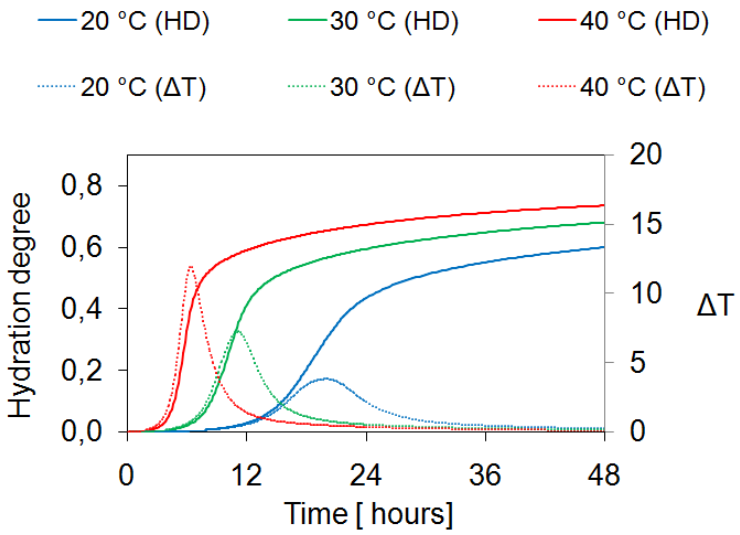

Figure 2.8 – Evolution of the hydration degree (HD) and increase of temperature (ΔT) in non-thermally-isolated conditions considering three external temperatures (20°C, 30°C and 40°C).

The following example is considered for an ordinary concrete (w/c = 0.46) with E_a/R = 5369 K. ***Figure 2.7.a-b*** shows the evolution of the hydration degree (corresponding to the measured temperatures), the experimental affinity and its interpolation by means of eqn (1.31) in ***Chapter 1***. Once the affinity has been evaluated by means of eqs (2.11 and 2.12) the numerical simulation of the experiment can be performed and the comparison between the numerical results and the experimental ones is shown in ***Figure 2.7.c*** for temperature.

Considering a cylindrical specimen with a radius of 37 mm and assuming a convective exchange of heat at the lateral surfaces only ($h_{conv} = 10 \mathrm{W \cdot K^{-1} \cdot m^{-2}}$), the model is able to reproduce the effect of the curing temperature on the hydration process. Three curing temperatures are considered: 20 °C, 30 °C and 40 °C. In ***Figure 2.8*** the numerical results are reported: a reduction of the dormant phase, an increase of the hydration rate and of the rise in temperature can be observed at higher curing temperature.

The identification of the affinity function is strictly related to the activation energy E_a of concrete, in other word the assumed activation energy determines the chemical affinity curve obtained *via* the parameters identification process. With reference to the previous considered concrete, ***Figure 2.9*** shows the affinity curves obtained with E_a/R = *4500*, E_a/R = *5000* and E_a/R = *5369*; these three values represent almost the range of the common value of E_a/R (Schindler, 2004). The effect of temperature depending on the assumed ratio E_a/R is shown in ***Figure 2.10***.

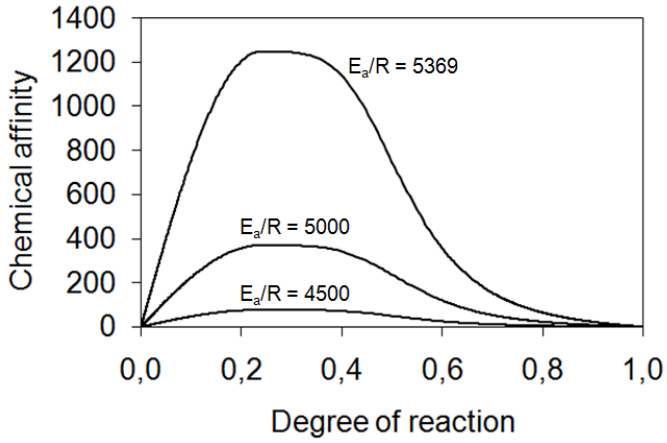

Figure 2.9 - Affinity curves obtained from the identification procedure (based on the adiabatic calorimetry test) assuming three different values of the activation energy.

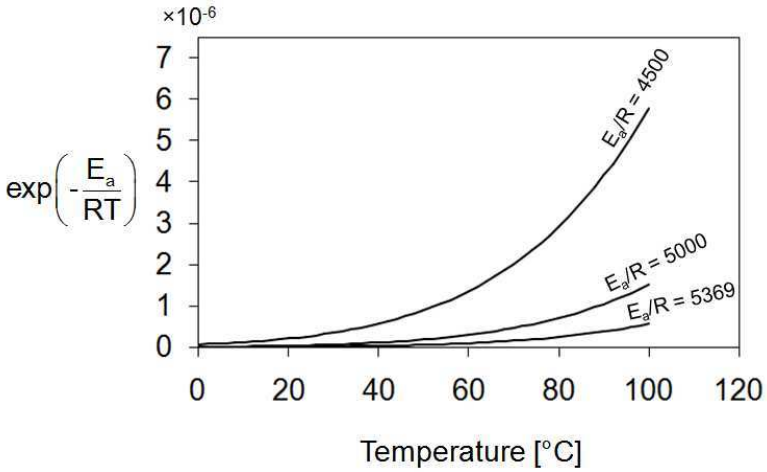

Figure 2.10 – Effect of temperature for three assumed values of the activation energy.

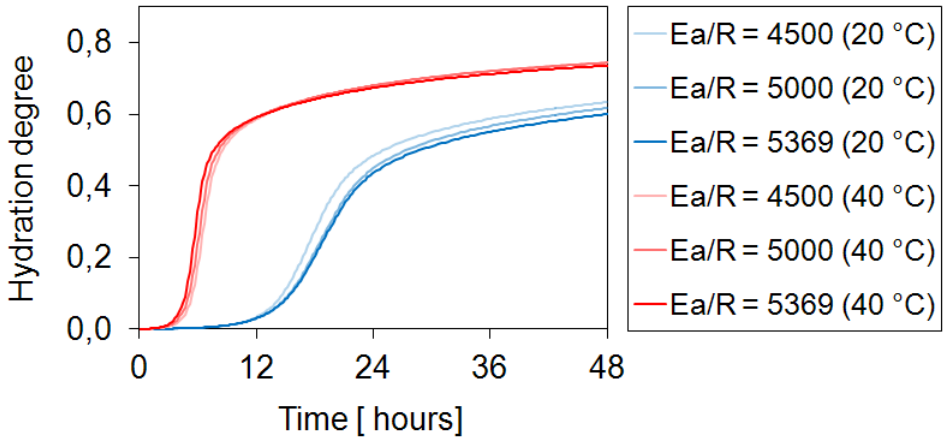

Figure 2.11 – Hydration degree during 48 hours for the three considered values of the activation energy. Two curing temperatures are considered: 20 °C (blue lines) and 40 °C (red lines).

The results in terms of adiabatic temperatures are identical for the three cases, but this is obvious since the identification procedure is based on the adiabatic calorimeter test. The interesting results is that in non-adiabatic conditions the results are also similar and this is shown in ***Figure 2.11***. Of course this does not mean that the use of the correct activation energy E_a is not important, but even if its knowledge is not adequate, a small error in the activation energy, assumed to identify the averaged affinity function, has no great impact on the results of the model. A similar result have been obtained by Briffaut *et al*. (2012).

2.3 MECHANICAL PROPERTIES

Concrete can be considered as a composite material which consists of aggregates within the cement paste. Therefore the mechanical properties of concrete depend on the properties of aggregate, cement paste and on the quality of their bond zone, also called interfacial transition zone (ITZ). ***Figure 2.12*** shows the typical stress-strain curves (in compression) of net cement paste, aggregate and concrete. Interesting is to note that aggregate and hydrated cement paste, when individually considered, exhibit a linear stress-strain relation, although for cement paste this relation becomes non linear for high stress level. The curve relative to concrete is placed between those of cement paste and aggregate; the stress-strain relationship is linear only in its first part, then the curve continues to bend over with an apparent pseudo-plastic behavior until a peak of stress is reached.

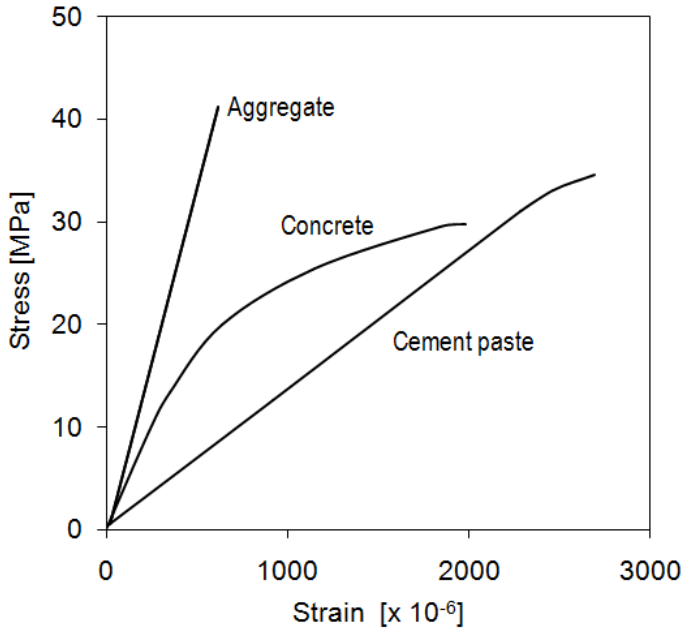

Figure 2.12 – Stress-strain relation for cement paste, aggregate and concrete (Neville, 1996)

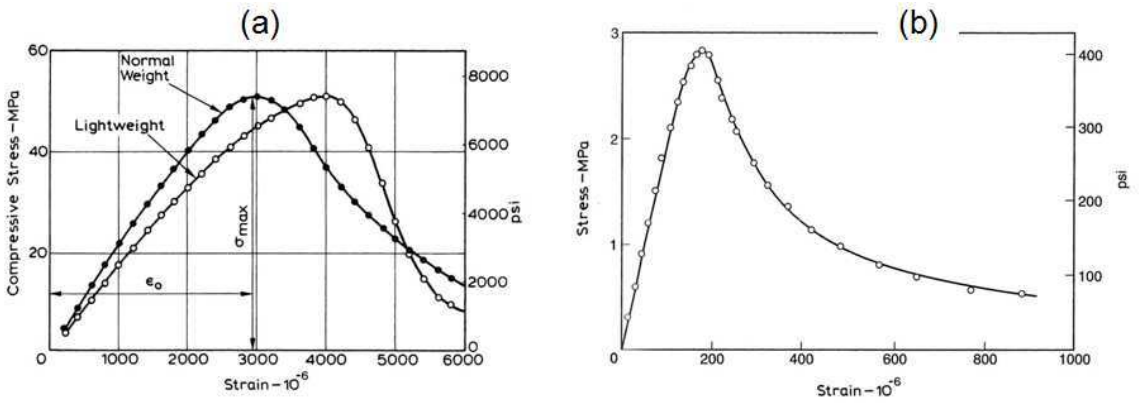

Figure 2.13 – Stress-strain relation of concretes tested in compression at a constant rate of strain (Wang *et al.*, 1978) (a); Example of the stress-strain relation in direct tension (Guo *et al*., 1987) (b).

The reason of this non-linear relationship in concrete is the development of bond microcracks at the interfaces between the cement paste and the aggregate. These microcracks lead to the reduction of the effective area resisting the applied load, so that the local stress is higher than the nominal stress based on the total cross-section of the specimen and strain increases at a faster rate than the nominal applied stress until the ultimate strength of the specimen is reached. If the test is performed at controlled rate of strain also the post-peak part of the stress-strain curve can be obtained: the strain continues to increase with a decrease of the nominal applied stress; this is the typical strain softening of concrete (see ***Figure 2.13.a***). High strength concretes and lightweight aggregate concretes have a more brittle behavior than normal concretes and consequently exhibit a steeper descending part of the stress-strain curve (see ***Figure 2.13.a***). The stress-strain curve in tension is similar to that in compression but the peak stress is considerably lower than in compression since the cracks (perpendicular to the strain rate) cause a brutal reduction of the effective area resisting stress. Also the stress-strain curve ends more abruptly at the peak than in compression because tensile failure is usually not ductile. ***Figure 2.13.b*** shows an example of stress-strain relation in direct tension.

The elastic modulus E_c and the tensile strength f_t can be estimated from the compressive strength f_c. In general a concrete with a high compressive strength has also high elastic modulus and tensile strength, and an increase of the compressive strength for instance due to hydration corresponds to an increase of the elastic modulus and of the tensile strength. For the modulus of elasticity this relationship with the compressive strength is recommended by ACI 318-02

$$E_c = 4.73\left(f_c\right)^{0.5} \qquad (2.12)$$

with E_c expressed in GPa and f_c the cylindrical compressive strength expressed in MPa. The Eurocode 2 suggests a similar equation

$$E_c = 22\left(\frac{f_{cm}}{10}\right)^{0.3} \tag{2.13}$$

where f_{cm} is the mean value of the compressive strength. Also for the tensile strength a number of empirical formulae are proposed, and most of them have the form

$$f_t = k_t \left(f_c\right)^n \tag{2.14}$$

In the Eurocode 2 k_t = 0.3 and n = 2/3, but depending on the type of aggregate other values of these coefficients may be used. In the case of fiber reinforced concretes the tensile strength depends also on the amount and type of fibers.

When a uniaxial load is applied to a concrete specimen, in addition to the longitudinal strain in the direction of the applied load it produces a lateral strain of opposite sign. Strictly speaking a uniaxial tensile load in the direction *z*, results in an extension in this direction and in a contraction in the directions *x* and *y*, this contraction being governed by the Poisson's ratio. For a fully hydrated concrete the Poisson's ratio is approximately constant and depending on the properties of the used aggregate it varies in the range of 0.15 to 0.22. No differences have been found between the Poisson's ratio in compression and that in tension. On the other hand the Poisson's ratio varies during hydration but this is discussed on the following of the paragraph.

Concrete properties are very variable and depend on the concrete mix. Nowadays a number of concretes and mortars are used and for this reason it is hard to state general laws or values for the material properties. Hence several authors have studied the influence of the mix on the properties of concrete. Taking into account fully compacted concretes (in which the presence of air voids is about the 1% of the total volume), the water/cement ratio has been found to be one of the most important features, but also other factors have critical effect on the material properties. With reference to the mechanical properties, concrete strength is inversely proportional to the water/cement ratio and various laws have been proposed from the end of the XIX century and can be found in the literature. However ***Figure 2.14.a*** shows that the range of the validity of these laws is limited. In fact for low values of the water/cement ratio these laws are generally not correct and the mean of compaction of the fresh concrete has a crucial impact.

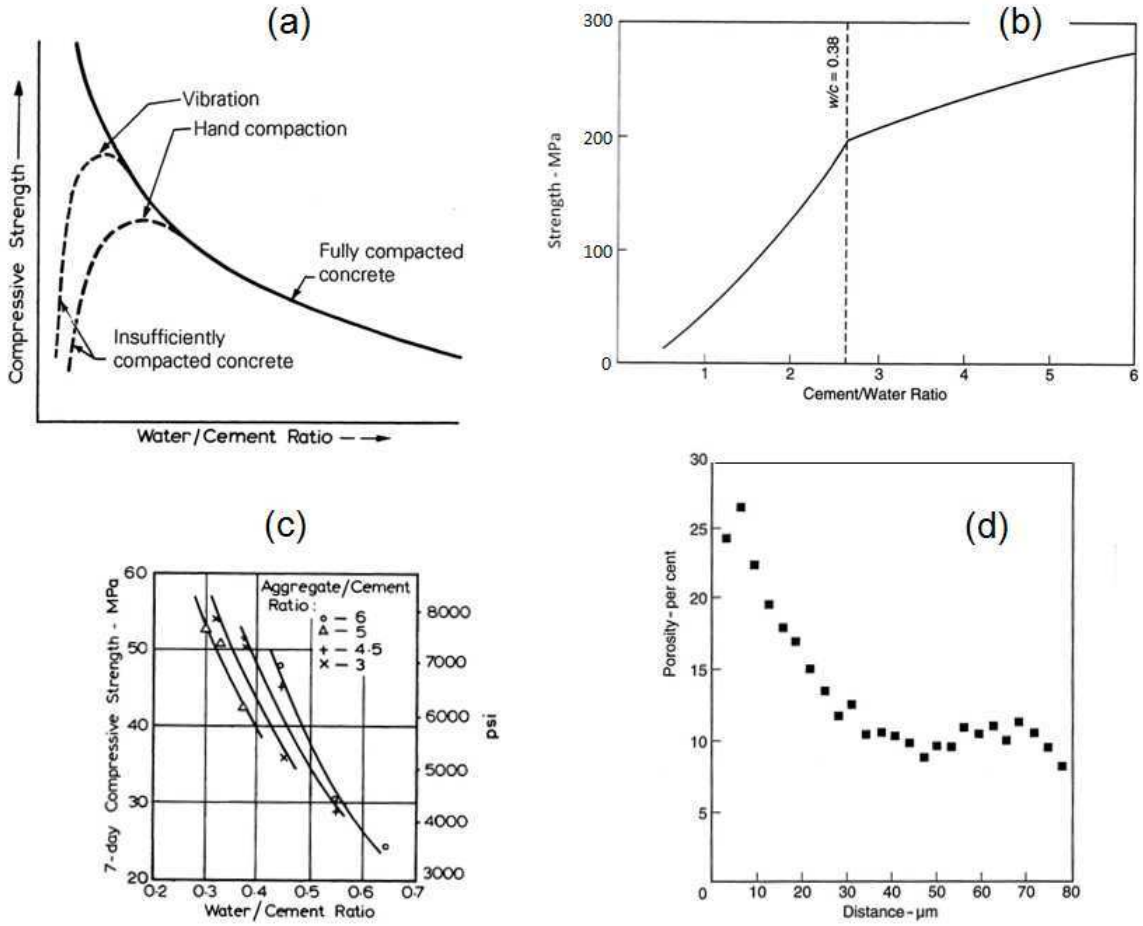

Figure 2.14 – Relation between strength and water/cement ratio of concrete (Neville, 1996) (a). Relation between the calculated strength of neat cement paste and cement/water ratio (Nielsen, 1993) (b); maximum possible hydration is assumed to have taken place. Influence of aggregate/cement ratio on strength of concrete (Singh, 1958) (c). Variation in the local porosity of the hydrated cement paste with the distance from the surface of an aggregate particle (Scrivener & Gariner, 1988) (d).

As suggested by Gilkey (1961) the strength of concrete and its mechanical properties in general are influenced by: i) ratio of cement to mixing water; ii) ratio of cement to aggregate; iii) grading, surface texture, shape, size, strength, and stiffness of aggregate particles.

Ratio of cement to mixing water. For cement pastes cured in water (achieving the maximum possible hydration), from 1.2 until a cement/water ratio to almost 2.6 (corresponding to w/c = 0.38), the relation between the strength and the c/w ratio is approximately linear. For cement/water ratios larger than 2.6 there exists a different but also linear relation with strength. These results have been obtained by Nielsen (1993) and are shown in ***Figure 2.14.b***. According to the model of Power (1960) for w/c ratios

lower than about 0.38 the maximum possible hydration is less than 100% and with high probability this is the reason of the change of the slope of the curve.

Ratio of cement to aggregate. The impact of the aggregate/cement ratio is difficult to be quantified since it is related also to the hygral state of the particles which may modify the effective water content of the mix. For constant water/cement ratio higher strength and modulus of elasticity have been measured with the increase of the aggregate/cement ratio (see ***Figure 2.14.c*** by Singh, 1958). This tendency in some cases may depend on the water absorbed by the aggregate which reduces the effective water/cement ratio of the cement paste and/or on the lower shrinkage of concrete which produces less damage at the bond between the aggregate and the cement paste (shrinkage is proportional to the volume of cement paste). Furthermore for constant water/cement ratio the overall porosity and the total content of water in concrete are proportional to the volume of cement paste. Consequently in a leaner mix the volume of voids is lower and this has a positive effect on strength. Indeed, capillary porosity is a primary factor influencing the strength of cement paste and concrete.

Grading, surface texture, shape, size, strength, and stiffness of aggregate particles. The meso-structure of concrete (at the level of the aggregate particles) has an important effect on the strength which is also affected by the capacity of the material to resist crack propagation. In a loaded specimen, peaks of stress occur at the interfaces between the coarse aggregate and the mortar arising from the difference in the modulus of elasticity and the Poisson's ratio of the two materials. Mechanics of bond is influenced by the surface properties and the shape of the coarse aggregate; in fact microcracking starts at the interface between coarse aggregate and the surrounding mortar, and also at failure macrocracks mostly include interface areas. Therefore improving the mechanical properties of the interface zone leads to higher strength of concrete. During mixing of fresh concrete, unhydrated cement particles are unable to become closely packed against large particles of aggregate. Hence, in the proximity of coarse aggregate the water/cement ratio is higher than the averaged value of the mix and so in this zone porosity is much higher than in the hydrated cement paste further away from the coarse aggregate (see ***Figure 2.14.d***). The influence of porosity on strength is relevant and this explains the weakness of the interface zone. Thus, the ability to resist crack propagation depends on the quality of the interface between the coarse aggregate and the surrounding mortar and on the surface properties of the particles: smooth gravel leads to cracking at lower stresses than rough and angular crushed rock.

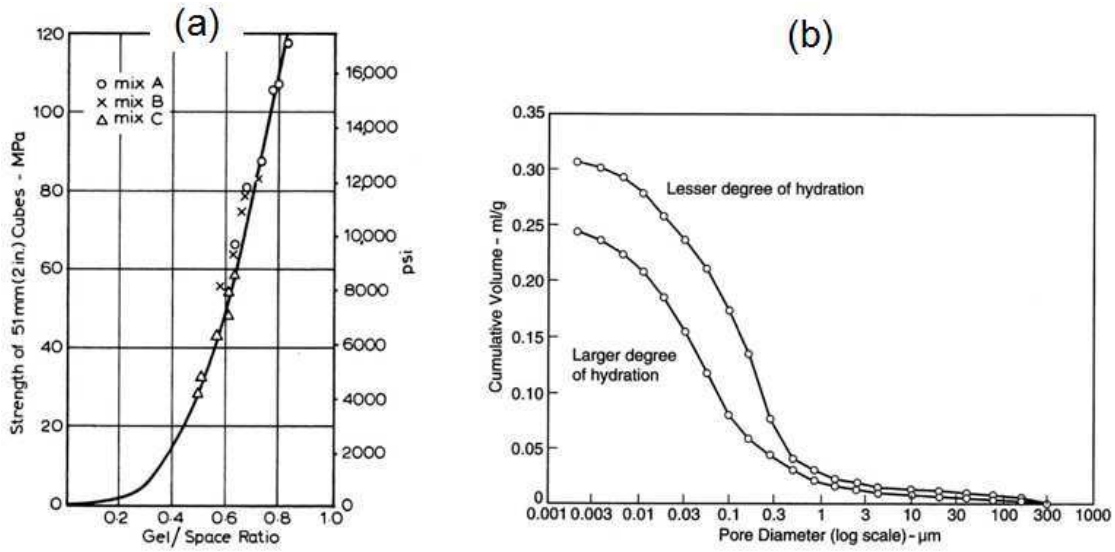

Figure 2.15 – Relation between the compressive strength of mortar and gel/space ratio (Power, 1958) (a). Cumulative volume of pores larger than the indicated ore diameter in concrete with a water/cement ratio of 0.45 (Winslow *et al*., 1990) (b).

The quality of bond is often enhanced by the addition of silica fume with is very much finer than cement particles and leads to a more dense interface zone; also aggregates with a porous outer layer improves mechanical interlocking of the aggregate particles and the hydrated cement paste.

Until this point only the final mechanical properties of concrete have been considered and discussed. However it is clear that mechanical properties, as well as physical and chemical ones, vary with hydration. In such a scenario, very interesting is the correlation between the strength of cement paste and the gel/space ratio proposed by Powers (1958) (see ***Figure 2.15.a***). In fact the microstructure of the cement paste has an important impact on the mechanical properties of the concrete. During hydration with the refinement of the porous microstructure the strength of concrete increases; in ***Figure 2.15.b*** the distribution of pores at two different degrees of hydration is represented. The gel/space ratio, according with Powers' model, depends on the hydration degree and reads

$$\frac{gel}{space} = \frac{0.657\xi}{0.319\xi + (w/c)} \tag{2.15}$$

The strength versus the gel/space ratio has a more general application than relationships based on the water-cement ratio because the amount of gel and the volume of voids depend on the cement type, on the mix of the cement paste (w/c ratio, silica fume, admixtures etc.), but also on the degree of hydration.

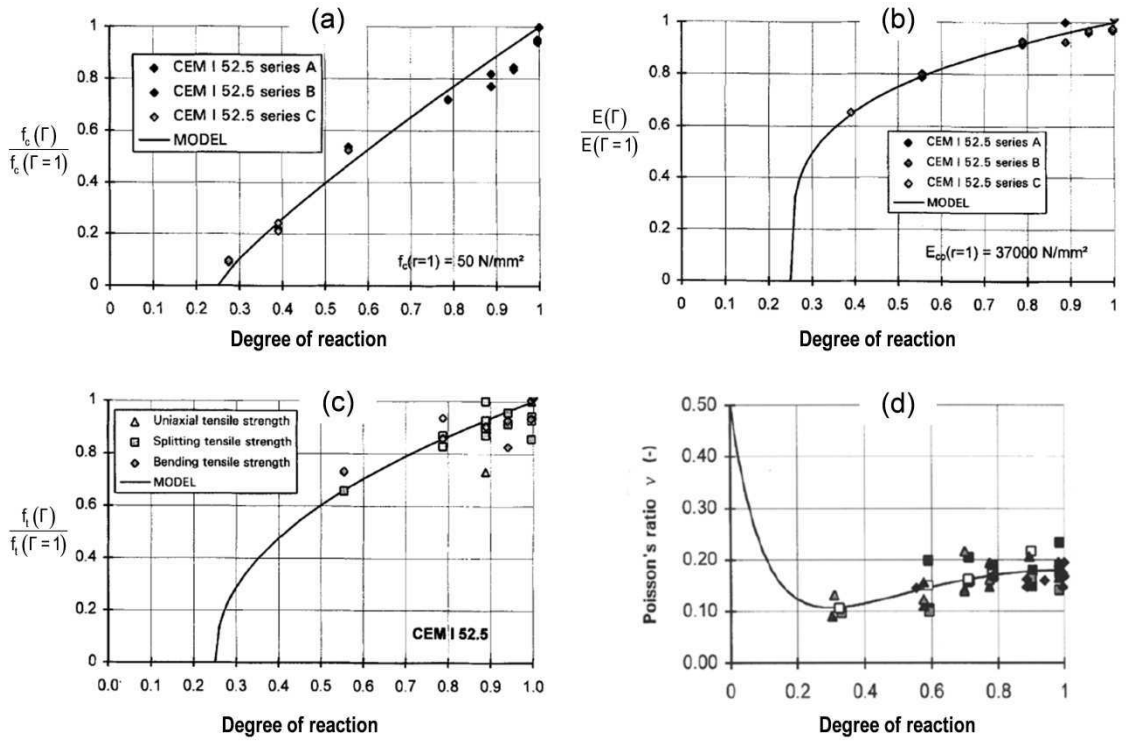

Figure 2.16 – Relationships between the degree of reaction and the compressive strength (a), Young's modulus (b), tensile strength (c) and Poisson's ratio (d). Readapted from De Schutter & Taerwe (1996).

If the evolution of the hydration degree is known, the development of the mechanical properties with time can be predicted. The knowledge of the strength-time relation is important to state when the structure can be put into use, to remove formwork or in other situations as for example prestressed concrete. The relationships proposed by De Schutter and Taerwe (1996) give the mechanical properties (Young's modulus, tensile strength and compressive strength) from the degree of reaction (eqn (2.5). These equations can be summarized in the following form

$$M(\Gamma) = M(\Gamma=1)\left\langle \frac{\Gamma(t)-\Gamma_0}{1-\Gamma_0} \right\rangle_+^{\alpha_M} \tag{2.16}$$

where M is the considered mechanical property, $M(\Gamma=1)$ is the final value of M, and a_M is the exponent (associated with M) which has to be calibrated experimentally. An empirical relationship between the Poisson's ratio ν, and the degree of reaction has been also proposed by De Schutter (2002)

$$\nu(\Gamma) = 0.18\sin\frac{\pi}{2}\Gamma + 0.5\exp(-10\Gamma) \tag{2.17}$$

Eqn (2.17) gives $\nu = 0.5$ when $\Gamma = 0$; 0.5 is the characteristic value of the Poisson's ratio for non compressible fluids. Eqn (2.16) and a modified version of eqn (2.17) are used in the mathematical model to relate the hydration degree with the mechanical properties of concrete.

2.4 SELF-DESICCATION AND AUTOGENOUS SHRINKAGE

After setting, with the progress of hydration the volume changes of the different phases present in the cement paste have as consequence the development of a volume of gas which leads to the self-desiccation of the cement paste (Jensen, 1993). The self-desiccation is very important in high performance concretes and cement pastes with a low water/binder ratio. In ***Figure 2.17*** the internal relative humidity measured in an ordinary concrete (OC) and in a high-performance concrete (HPC) is plotted over time (the specimen are sealed). A strong self-desiccation for the high-performance concrete is shown. Being the self-desiccation related to the hydration process the decrease of relative humidity is very important during the first 3 weeks after the casting.

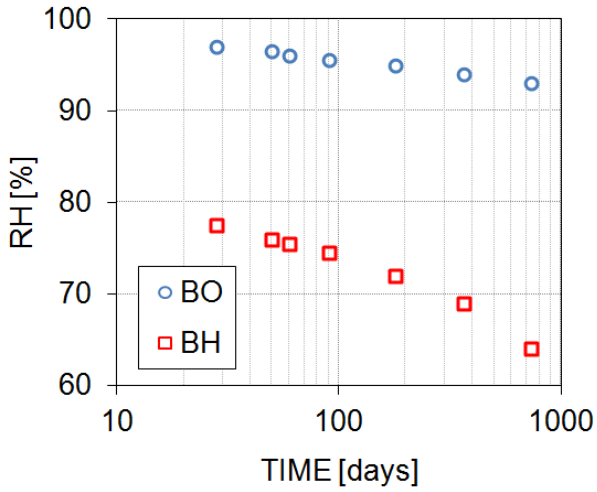

Figure 2.17 - Internal RH measured in sealed conditions by RH-sensors at T = 20°C. Readapted from Baroughel-Bouny and Mounanga (2005).

However the first couple of data-points in ***Figure 2.17*** is relative to 28 days; this depends probably to the fact that RH-sensors often don't work properly at early age since water condensation inside the protection 'head' of the sensor occurs. This problem has been observed by our research team using a type of sensors which during the first 5 days of hydration stay at RH = 100%. Due to self-desiccation the capillary pressure in the pore increases inducing an autogenous contraction commonly called autogenous shrinkage.

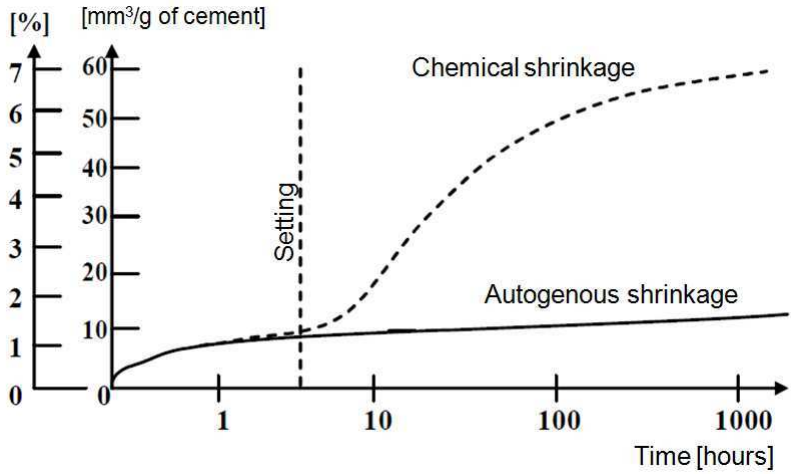

Figure 2.18 – Chemical shrinkage and autogenous shrinkage for a cement paste (Jensen, 2005).

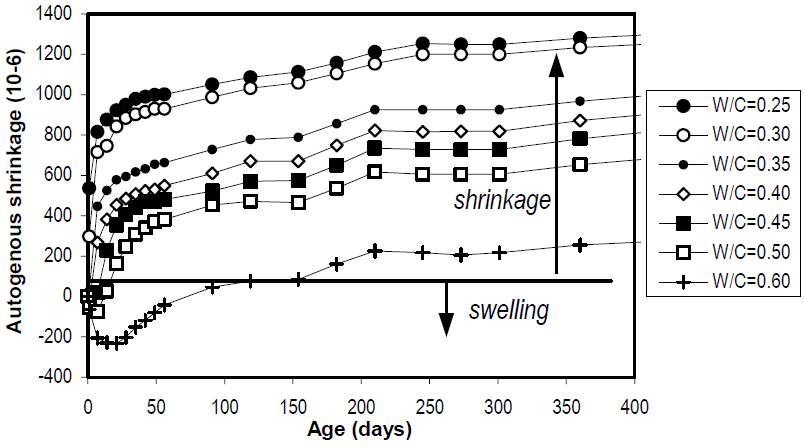

Figure 2.19 - 1-D autogenous deformation (length changes) versus age, measured from setting up to 1 year on Ø20x160-mm sealed samples of cement pastes cast with cement 1 and various w/c, at T = 20 °C. From Baroughel-Bouny and Mounanga (2005).

In concretes, autogenous shrinkage is partially restrained by the aggregate particles and then is an order of magnitude smaller than in neat cement paste. Before setting the autogenous shrinkage corresponds to the chemical shrinkage since capillary effects are negligible at this stage (pores remain almost saturated). After setting, which for concretes corresponds to a degree of reaction $\Gamma \approx 0.1$, the chemical shrinkage results in a diminution of the liquid saturation degree and the autogenous shrinkage is produced mainly by capillary forces. The volumetric amplitudes of chemical and autogenous shrinkage for a cement paste are represented in ***Figure 2.18***. Autogenous shrinkage depends on the water/cement ratio of the mix and in concretes is inversely proportional to the volume of aggregate. In ***Figure 2.19*** the autogenous shrinkage of seven cement pastes is plotted; the influence of the water/cement ratio is clear and is evidenced also in ***Figure 2.20***.

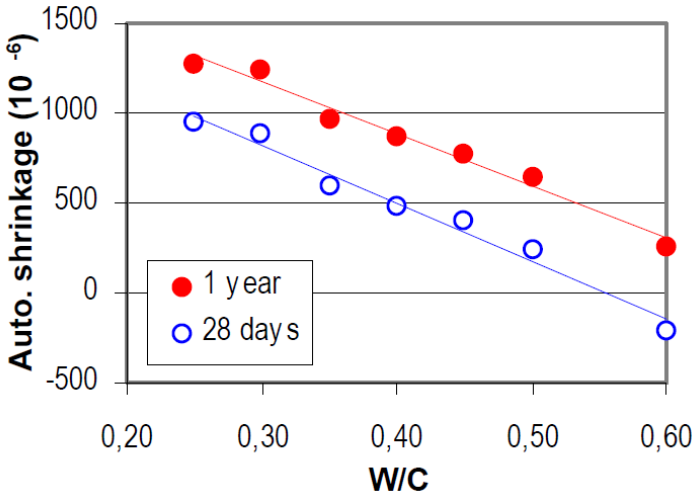

Figure 2.20 – 28-days and 1-year autogenous deformation versus the water/cement ratio (no silica fume is present in the considered cement pastes). From Baroughel-Bouny and Mounanga (2005).

Autogenous shrinkage can be modeled with different approaches which are mainly based on the degree of hydration of concrete.

When the hygral aspects are not explicitly considered the autogenous contraction, $\mathbf{e}_{ash}$, can be assumed proportional to the degree of reaction

$$\dot{\mathbf{e}}_{ash} = e_{ash}\left(\Gamma = 1\right)\mathbf{1}\frac{\partial \Gamma}{\partial t} \tag{2.18}$$

where $e_{ash}\left(\Gamma = 1\right)$ is the final isotropic contraction. Using this constitutive model the autogenous shrinkage stops to increase when hydration is ended. Also the viscous part of the contraction cannot be correctly taken into account. In fact after setting the autogenous shrinkage is governed by capillary forces which impact on the effective stress tensor and cause elastic and viscous strain.

Another method is based on the evolution of porosity and liquid saturation degree during hydration. The volume of pores and the pore size distribution with hydration are predicted using empirical models based on experiments. Hence, porosity and the decrease of the saturation degree, S^l, (given by stoichiometry), allow to calculate the averaged radius of liquid menisci (at the pore level), and so the capillary pressure, p^c, by means of the Laplace's equation

$$p^c = p^g - p^l = \frac{2\gamma}{r} \tag{2.19}$$

where γ is the surface tension of water. Assuming the impact of gas pressure negligible the autogenous shrinkage can be computed by means of the effective stress principle as

$$\dot{\mathbf{e}}_{ash} = \frac{\mathbf{1}}{3K^T}\frac{\partial}{\partial t}\left(\bar{\alpha} p^s\right) \tag{2.20}$$

where K^T is the Bulk modulus of concrete, $\bar{\alpha}$ is the Biot's coefficient and p^s is the solid pressure, given by

$$p^s = -S^l p^c \tag{2.21}$$

An example of this approach is that of Michaud *et al.* (2006); in such a model concrete viscosity is taken into account and so the viscous strain originated by the solid pressure p^s is computed and added to the elastic part of autogenous shrinkage (eqn (2.20)). For this type of model we can summarize that the relationship between the saturation degree and the capillary pressure is given through the volume of pores and the pore size distribution.
In the presented model the pore size distribution is not modeled, however the capillary pressure p^c is a primary variable of the model and is governed essentially by the mass balance equation of the liquid phase. In sealed condition the evolution of the saturation degree depends only on the volume balance of the different phases in the mix, and is given fundamentally by the averaged stoichiometry of the hydration reaction (Power, 1960); on the other hand the evolution of capillary pressure results from the assumed desorption isotherm and its evolution with hydration (eqn (1.52)). In other words changing the desorption isotherm gives different capillary pressure but the results in terms of saturation degree S^l do not change. The hygral solution (capillary pressure and saturation degree) is used to compute the autogenous visco-elastic contraction with respect to the effective stress principle similarly to the previous presented method (for more details see *Paragraph 1.5.9*). To conclude the features and the parameters of the developed model which govern autogenous shrinkage can be summarized in the following list:

a) *Volume balance of the phases during hydration*. It depends on the concrete mix according with the model of Powers (1960). No parameters have to be identified.
b) *Advance of the hydration degree.* The evolution of the autogenous shrinkage depends on concrete hydration. The parameters that govern the hydration process are effortlessly identified by means of adiabatic calorimetry.
c) *Desorption isotherm function*. The capillary pressure is related to the assumed desorption isotherm which can be calibrated using experimental results of the evolution of relative humidity during hydration in a sealed specimen.

d) *Biot's coefficient*. The contraction is proportional to the Biot's coefficient which can be estimated from the autogenous shrinkage test. Only the final value of the Biot's coefficient $\bar{\alpha}_\infty$ is needed (see eqn (1.80)); the evolution of the Biot's coefficient with hydration is represented in ***Figure 1.7***.

e) *Bulk's modulus and creep properties.* The Bulk's modulus and creep have a primary impact on autogenous shrinkage. However in the model calibration procedure, when autogenous shrinkage is analyzed, Bulk's modulus and the parameters which govern creep are already known since previously identified from the experimental measurements of Young's modulus and Poisson's ratio at different age and by means of the basic creep test.

Hence, to reproduce correctly the autogenous deformation the final Biot's coefficient of concrete and the desorption isotherm are the key points of the presented model. The desorption isotherm is evaluated from the evolution of relative humidity in sealed condition while for the identification of the Biot's coefficient the autogenous shrinkage measured experimentally is considered.

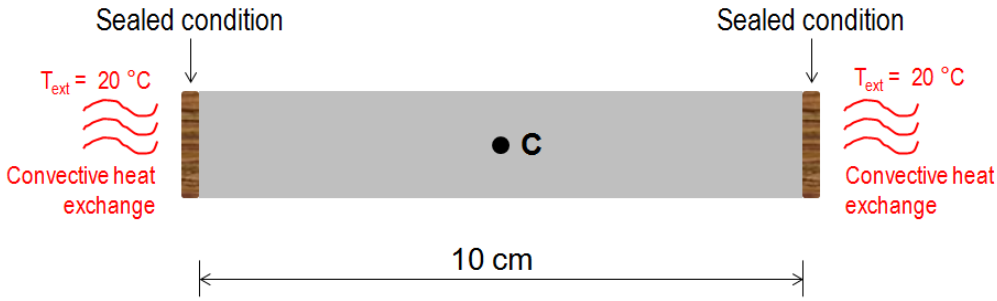

Figure 2.21 – Geometry and boundary conditions of the simulated case.

A numerical example is presented for three different concretes: two ordinary concretes (OC1 and OC2) and an ultra-high-performance concrete (UHPC) (see ***Table 2.3***). The geometry and the boundary conditions of the modeled 1D case are represented in ***Figure 2.21***. The specimens are supposed to be in perfectly sealed condition. A convective heat exchange at the surface is assumed

$$\mathbf{q}_t = \varphi_t \left(T_s - T_{ext} \right) \mathbf{n} \qquad (2.22)$$

where φ_t = 10 W.m^{-2}.K^{-1} is the thermal convective coefficient, T_s is the temperature on the surface, T_{ext} is the imposed ambient temperature (20 °C), and $\mathbf{n}$ is the unit vector normal to the surface (oriented towards the exterior).

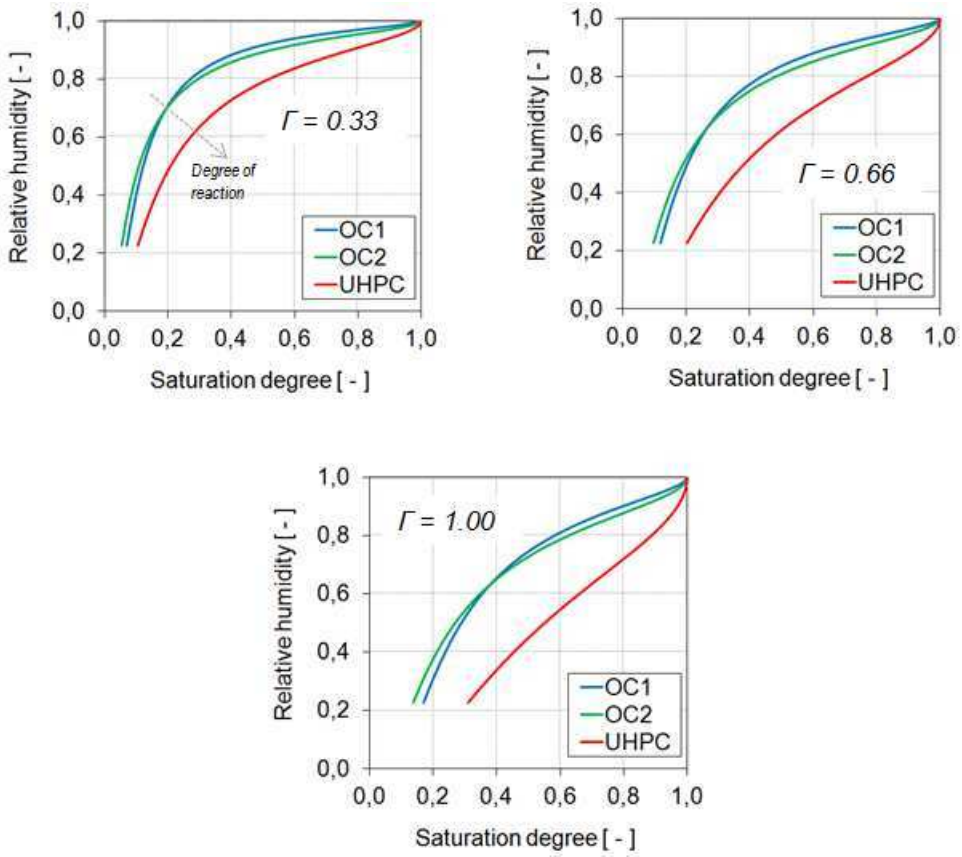

Figure 2.22 – Desorption isotherms of the three concretes at different degrees of reaction.

The evolution of the degree of reaction Γ, saturation degree S^l, relative humidity h, gas pressure p^g and temperature θ are reported in ***Figures 2.23-28*** for the point C represented in ***Figure 2.21***. The assumed desorption isotherm for the three considered concretes are shown in ***Figure 2.22***. ***Figure 2.23*** and ***Figure 2.25*** show the decrease of relative humidity h and saturation degree S^l due to self-desiccation for OC1 and OC2. For ordinary concretes, in sealed condition typically the relative humidity doesn't decrease below 90-85%, also the saturation degree S^l stays generally below the relative humidity h; these facts can be observed in the numerical results of OC1 and OC2. On the other hand for high-performance concretes the decrease of relative humidity is more important and relative humidity can fall below the saturation degree as in the case of UHPC (see ***Figure 2.27)***.

Table 2.3 – Mix data of the three concretes modeled in the 1D case in Figure 2.21

	water/cem.	Silica fume/cem.	water/binder
OC1	0.67	0.10	0.62
OC2	0.46	0.00	0.46
UHPC	0.27	0.25	0.21

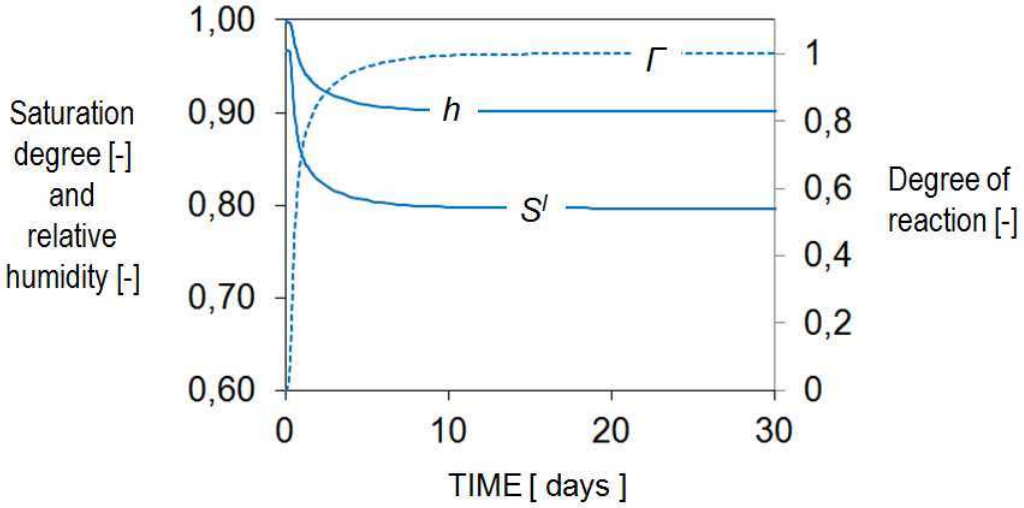

Figure 2.23 - Degree of reaction Γ, saturation degree S^l and relative humidity h for OC1. Specimen in perfectly sealed condition (numerical results).

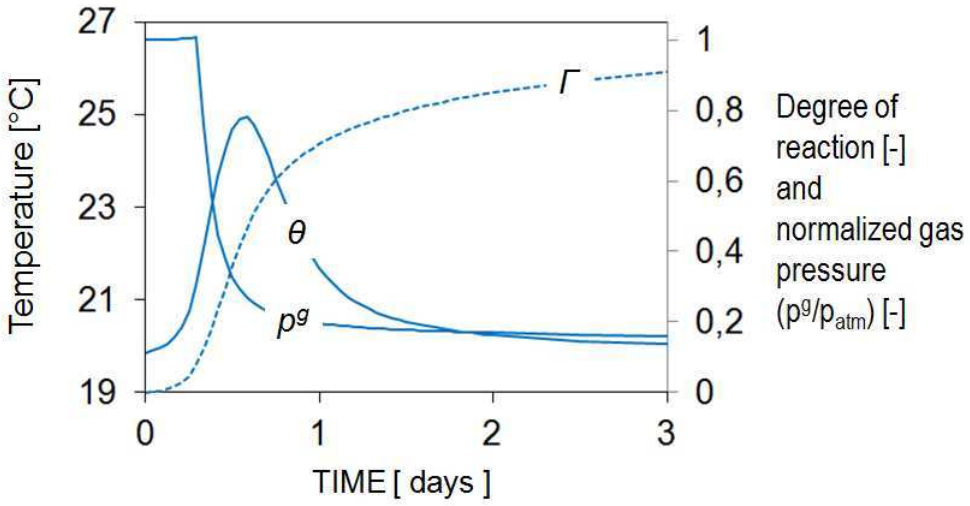

Figure 2.24 - Degree of reaction Γ, gas pressure p^g and temperature θ for OC1. Specimen in perfectly sealed condition (numerical results).

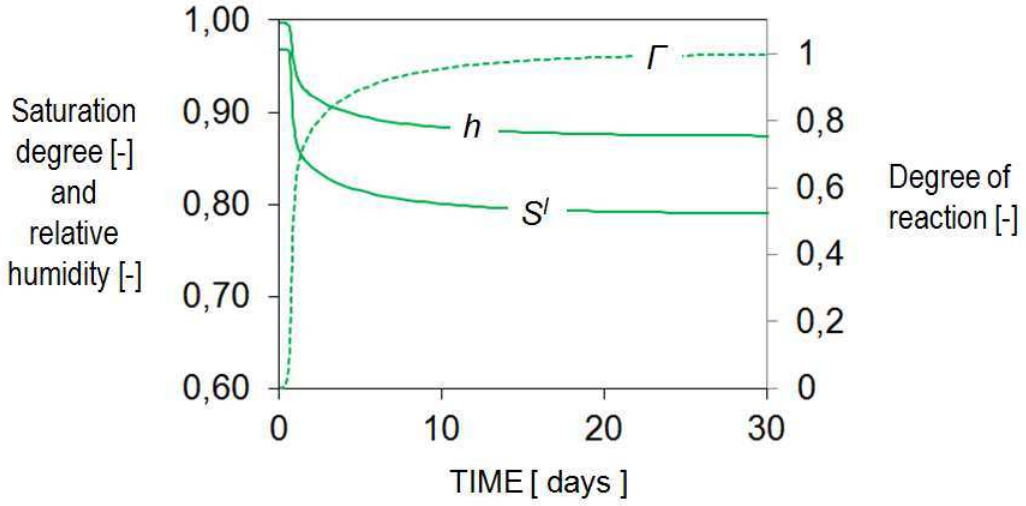

Figure 2.25 – Degree of reaction Γ, saturation degree S^l and relative humidity h for OC2. Specimen in perfectly sealed condition (numerical results).

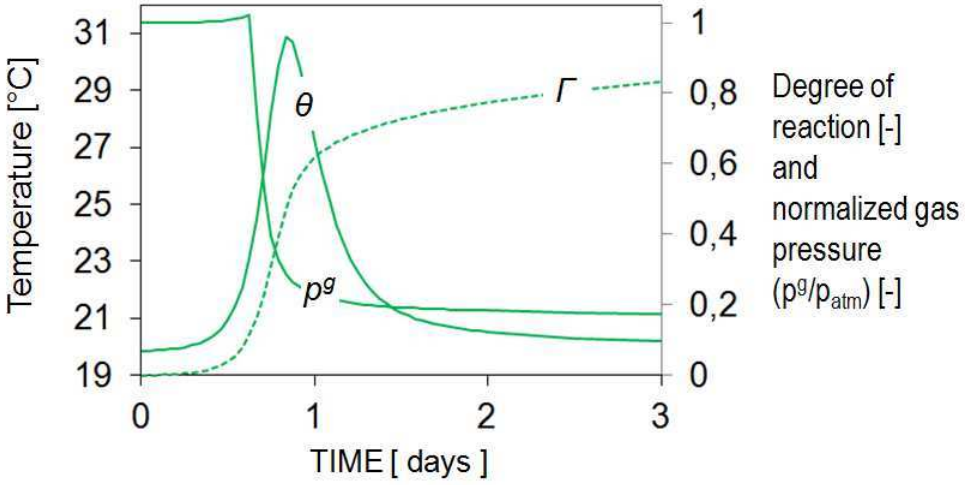

Figure 2.26 - Degree of reaction Γ, gas pressure p^g and temperature θ for OC2. Specimen in perfectly sealed condition (numerical results).

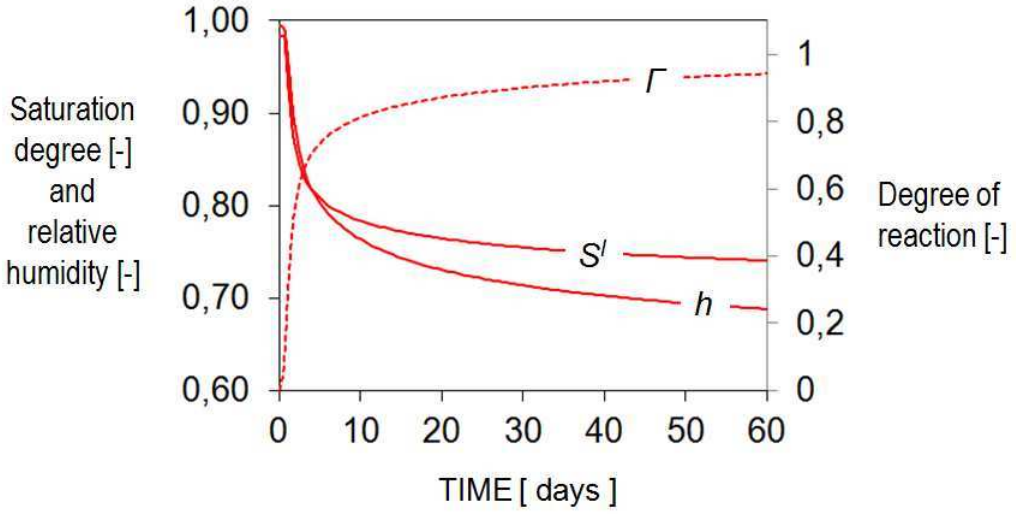

Figure 2.27 - Degree of reaction Γ, saturation degree S^l and relative humidity h for UHPC. Specimen in perfectly sealed condition (numerical results).

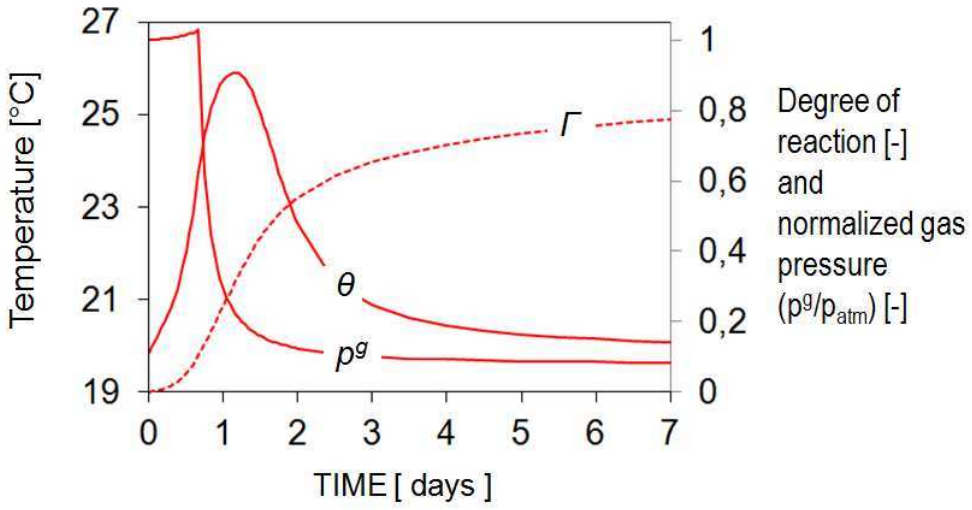

Figure 2.28 - Degree of reaction Γ, gas pressure p^g and temperature θ for UHPC. Specimen in perfectly sealed condition (numerical results).

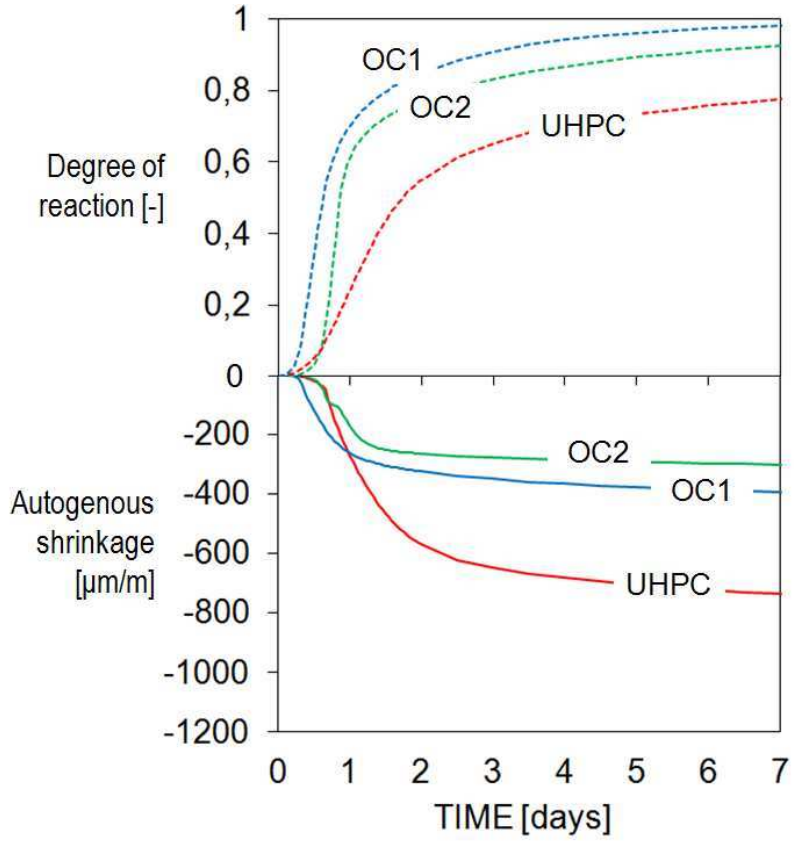

Figure 2.29 – Degree of reaction and autogenous contraction during the first week.

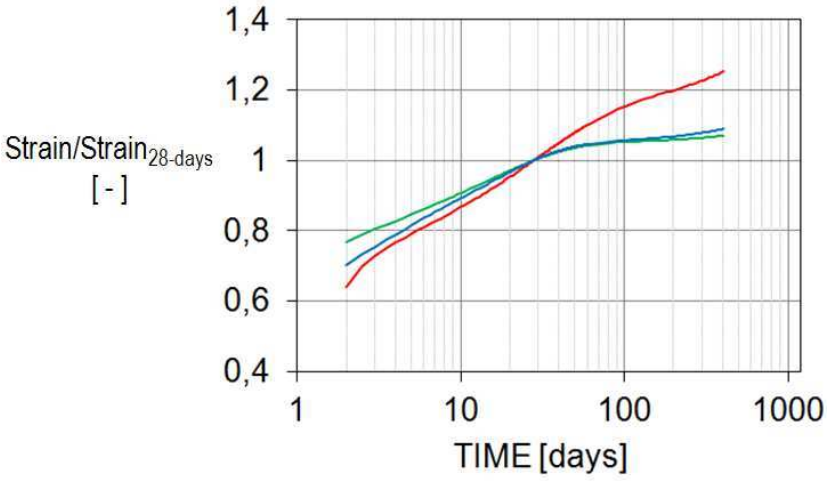

Figure 2.30 – Ratio between the autogenous shrinkage strain and that obtained after 28 days.

These differences between the two ordinary concretes (OC1 and OC2) and the considered ultra-high-performance concrete (UHPC) depend also on the desorption isotherm functions (see ***Figure 2.22***). A relatively important decrease of the gas pressure can be observed for each of the three concretes (see ***Figure 2.24***, ***Figure 2.26*** and ***Figure 2.28***). This internal depressurization is due to the LeChatelier contraction which leads to an increase of the volume of gas.

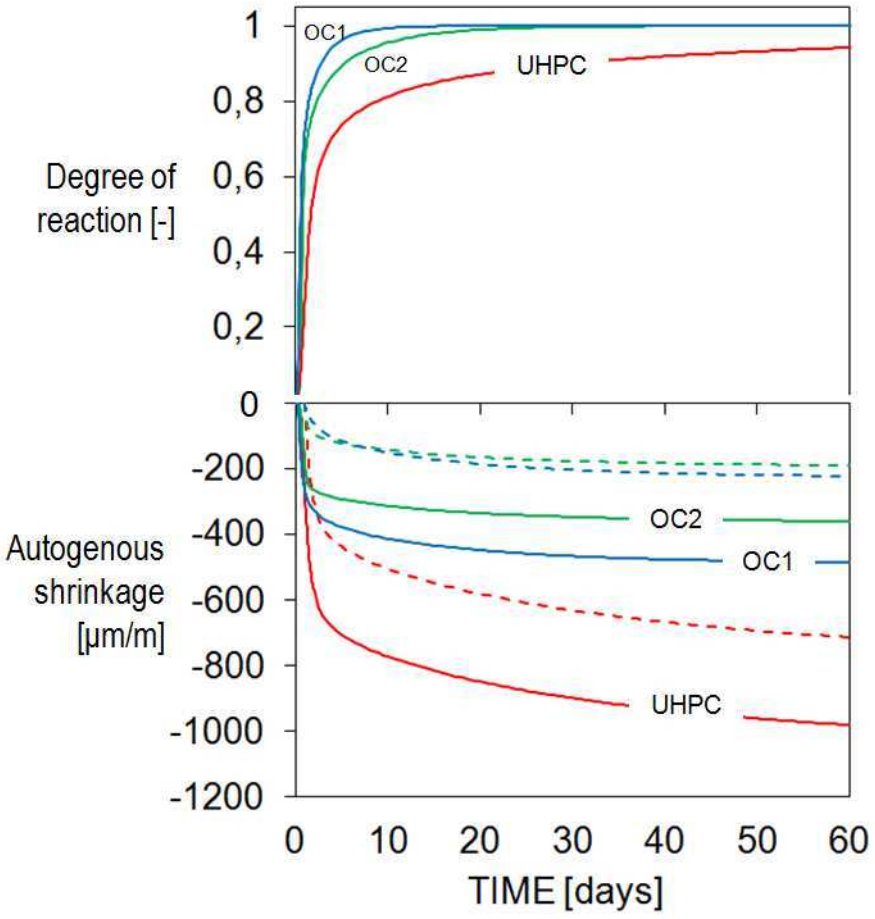

Figure 2.31 - Degree of reaction and autogenous shrinkage during 60 days. The solid line are the strains computed from the beginning whilst the dashed lines are the strains computed from 1 day after the casting.

Figure 2.29 shows the degree of reaction and the autogenous shrinkage versus time for the three concretes. The hydration kinetics are quite different, in particular the progress of hydration for UHPC is slower than those of the two ordinary concretes OC1 and OC2. After seven days the amplitude of the autogenous shrinkage of UHPC is almost two times that of OC1 and more than two times larger than that of OC2. In ***Figure 2.30*** is interesting to observe that for the ordinary concretes after 1 year the autogenous shrinkage is only 8% larger than that obtained at 28 days, in contrast for UHPC the 1-year-strain is almost 30% larger than that obtained after 28 days; these differences in terms of strain evolution are the reflections of the different hydration kinetic between the two ordinary concretes, OC1 and OC2, and the high-performance concrete, UHPC.

The experimental measurement of autogenous shrinkage at very early age is difficult to perform because the specimen has low mechanical properties and its manipulation is delicate. Thus, very frequently the autogenous shrinkage is not measured from the beginning but from a time that varies between 12h and 24h after the casting.

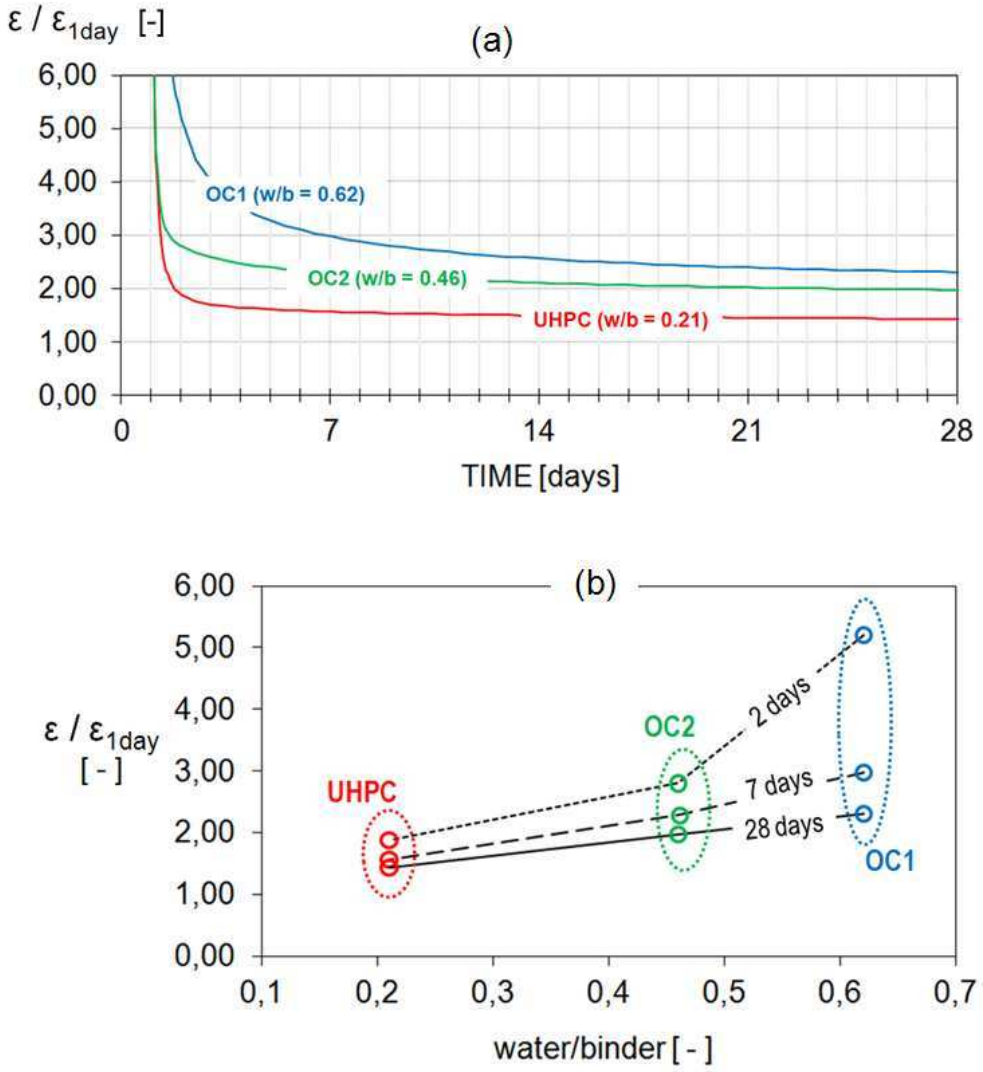

Figure 2.32 – Ratio between the autogenous shrinkage (considered from the beginning) and that considered from 24 hours, when typically the experimental measurement starts. Numerical results over the time (a); numerical results over the water/binder ratio (b).

Figure 2.31 shows the autogenous shrinkage considered from the time "zero", when the degree of reaction for the three concretes is $\Gamma = 0$ (solid lines), together with the autogenous shrinkage considered from 1 day after the casting (dashed lines). From this figure and from ***Figures 2.32.a-b*** we can realistically presume that the shrinkage measured from 1 day is an underestimation of the real shrinkage of the material especially for ordinary concretes. Of course autogenous strains are larger in high-performace concretes with low water/cement ratio, however, when sometimes in literature is stated that for concretes with relatively big water/cement ratio the autogenous shrinkage is not relevant it must be added that a non-negligible amount of strain occurs before the start of experimental measurement, and if this fact is not taken into account in the design process it can results in early age cracking.

2.5 HYGRAL TRANSPORT AND DRYING SHRINKAGE

In the previous paragraph the self-desiccation of concrete and its consequences have been discussed, and numerical examples have been presented. When the material is hygrally isolated from the environment, if not important thermal gradients are established during the hydration process, the hydration degree increases homogenously and so also the self-desiccation is homogenous. This means that in sealed conditions hygral gradients are negligible and then no mass transport of water occurs; nonetheless it is important to remember that for mass concrete this statement is not valid because in that case serious thermal gradients leads to non homogenous hydration advancement, and so also to a non homogenous self-desiccation of the material which induces a weak hygral transport from the colder border to the hydrated core of the structure; an example is presented in the following pages.

After the exposure of concrete to the environment, as happens in civil engineering structures when the formworks are removed, if the environmental relative humidity is lower than that of the material, a movement of the internal water from the concrete structure to the environment occurs. Taking into account this phenomenon in concrete structure design is of critical significance because drying is the cause of shrinkage and has effect on creep strain. Moreover hygral gradient induces gradient of strain which can produce cracks due to the self-restrained shrinkage.

In the present model liquid transport, gas transport and diffusion of vapour water and dry air are considered. The equations have been presented in ***Chapter 1***. The fluxes are computed with a generalized form of the Darcy's law in which the relative permeabilities of the liquid and of the gas are introduced (k_{rel}^{ls} and k_{rel}^{gs}). As typically done for geomaterials other than concrete, the darcian gas permeability of concrete is assumed equal to the liquid one according with the concept of intrinsic permeability of a porous medium, which is independent from the nature of the considered fluid. Several authors, as for instance Gawin *et al*. 2006, follow the philosophy of an unique intrinsic permeability of concrete for both the liquid and the gaseous phases. However recent experimental measurements (Baroghel-Bouny *et al*., 2002) demonstrate that the intrinsic gas permeability k^{gs}, may be two or three order of magnitude larger than the intrinsic water permeability k^{ls}. In addition, for high-performance concretes the Klinkenberg's effect may become important. This effect is due to the slip flow of gas at pore walls which enhances gas flow when pore sizes are very small. Therefore, the liquid flow is only laminar whilst

the gas flow, following the approach of Klinkenberg (1941), consist of two parts: i) one is the viscous flow; ii) the second one is the slip flow due to the slippage velocity of the gas molecules at pore walls. The Klinkenberg's effect is taken into account by Thiery *et al.* (2007) who considers also two different intrinsic permeabilities for the gaseous and the liquid phases (i.e. $\mathbf{k}^{gs}$ and $\mathbf{k}^{ls}$). These aspects can be easily incorporated in the present model modifying the relative velocity of gas (eqn (1.45)) which becomes

$$\mathbf{v}^{\bar{g}} - \mathbf{v}^{\bar{s}} = -\frac{\mathbf{k}^{gs}}{\mu^g \varepsilon^g}\left(k_{rel}^{gs} + \frac{\Psi}{p^g}\right)\nabla p^g \tag{2.23}$$

where $\mathbf{k}^{gs}$ is the intrinsic gas permeability and Ψ allows to take into account the Klinkenberg's effect. The other symbols have been explained in ***Chapter 1***. The coefficient Ψ is not constant and depends on the saturation degree of concrete. It can be estimated using the following equation

$$\Psi = \Psi\left(S^l\right) = p_0 \exp\left(-\beta_{kl} S^l\right) \tag{2.24}$$

where β_{kl} and p_0 are constant parameters. ***Figure 2.33*** shows experimental curves of $\Psi(S^l)$ interpolated using eqn (2.24).

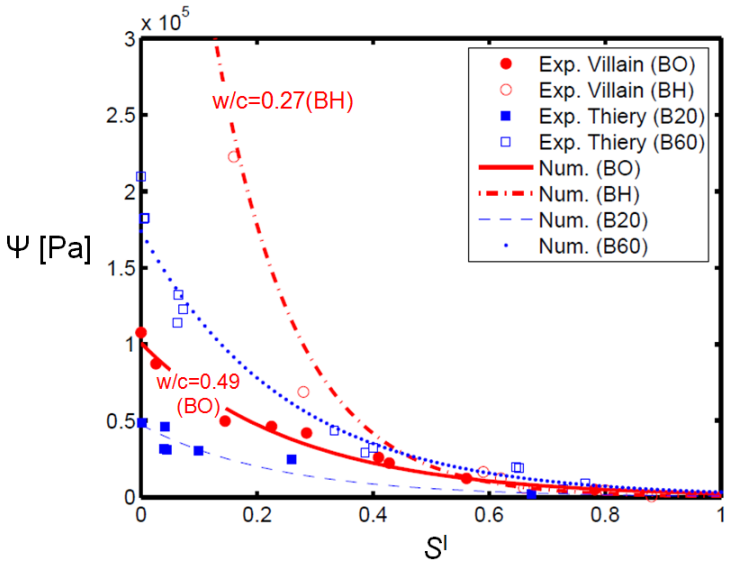

Figure 2.33 – Experimental estimation (symbols) of the function $\Psi(S^l)$ (Klinkenberg effect) for several concretes (Villain *et al.*, 2001, and Thiery, 2000). The experimental results are interpolated using eqn (2.24) (solid lines). The used coefficients are: i) p_0 = 47334 and β_{kl} = 4.28 for B20; ii) p_0 = 100604 and β_{kl} = 3.77 for BO; iii) p_0 = 173862 and β_{kl} = 4.01 for B60; iv) p_0 = 758336 and β_{kl} = 7.26 for BH.

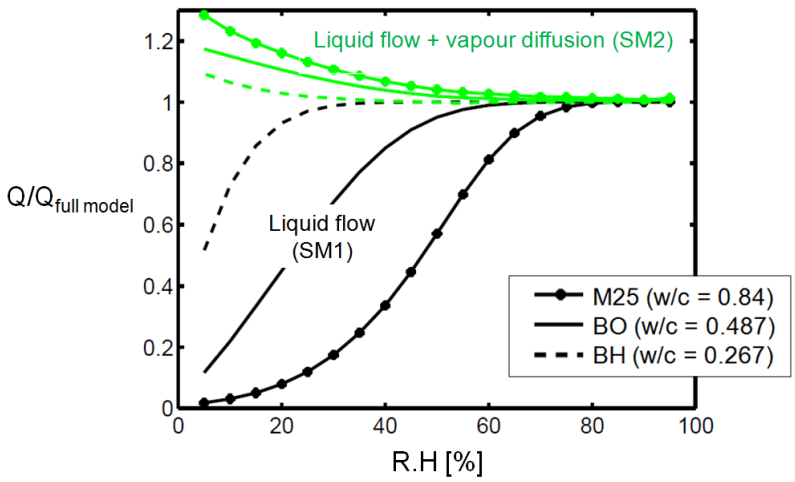

Figure 2.34 – Ratio between the loss of mass after 1000 days of drying calculated using the two simplified models (SM1 and SM2) and that calculated using the full model (FM). Three concretes have been considered (M25, BO and BH). The initial relative humidity has been set equal to h_0 = 99% and the resulting ratios are plotted as functions of the imposed external relative humidity h_{ext}. Image readapted from Thiery *et al*. (2007).

Figure 2.33 is taken from the paper of Thiery *et al*. (2007), where also the results of simplified models for hygral transport are studied in detail. Two simplified approaches are analyzed: in the first one the drying is modeled only taking into account the darcian flow of liquid water (this simplified version is indicated as SM1 in the sequel), in the second one transport is modeled considering liquid flow and vapour water diffusion with the gas pressure assumed to be constant and equal to 1 atm (this simplified version is indicated as SM2 in the sequel). The conclusion of this comparative study is summarized in ***Figure 2.34*** where the ratio between the loss of mass after 1000 days of drying obtained with the two simplified models and that obtained with the full model are plotted for several external values of relative humidity, in isothermal condition (θ = 20°C). The water/cement ratio of the three concretes considered in this study are: w/c = 0.84 for M25, w/c = 0.487 for BO and w/c = 0.267 for BH. If the maximum admissible relative error is 0.1, from ***Figure 2.34*** can be learned that SM2 is always adequate for BH, while for BO and M25 can be used respectively for h_{ext}>20% and h_{ext}>30%. Concerning SM1, the ranges of validity are more restrictive: h_{ext} >20% for BH, h_{ext} >45% for BO and h_{ext} >65% for M25. Thus, from this interesting comparative study, it may be deduced that it is sufficient (at ordinary thermal and hygral environmental conditions) to take into account the liquid flow and vapour diffusion (SM2) to model drying; in addition this may be valid for all concretes since the considered materials cover almost the whole range of usual water/cement ratios. In other words, one can affirm that the darcian flow of gas has no

significant effect on the final results in terms of loss of mass. Moreover, from these results we can suppose that probably gas pressure has also no impact on the evolution of the saturation degree and on its spatial distribution; these last hypotheses are confirmed in the same paper by Thiery *et al.* (2007). In spite of these numerical results, it is important to underline that this negligible impact of gas pressure, in the general solution of a drying case, has been demonstrated only in isothermal conditions and at 20°C. Furthermore, sometime it may be very interesting to know qualitative and quantitative numerical data about the gas flow, for instance in the analysis of the infiltration in concrete of unwanted gases (carbon dioxide is an example). Also is important to remember that at high temperatures the gas pressure together with concrete dehydration is the main cause of spalling. Hence, as already shown in ***Chapter 1*** the choice is to include the gas pressure p^g between the primary variables of the model, together with the capillary pressure p^c, temperature T and the displacement vector $\mathbf{u}$ in order to have a flexible mathematical model which from early age can be easily extended to modeling of other aspects. In fact this general mathematical model has been already used for concrete at high temperature (Gawin *et al.*, 2003), leaching (Gawin *et al.*, 2008) and for the analysis of concrete degradation due to alkali-silica reaction (Pesavento *et al.*, 2012).

On the other hand, even if experimental measurements (Baroghel-Bouny *et al.*, 2002) apparently demonstrate that the intrinsic gas permeability $\mathbf{k}^{gs}$ is different from the liquid one $\mathbf{k}^{ls}$, and also suggest the existence of the Klinkenberg's effect (especially in concretes with relatively low water/cement ratio), in the developed model the choice is to neglect the Klinkenberg's effect and to use a unique intrinsic permeability for both the gaseous and liquid phases according to the concept of intrinsic permeability and to the reference paper of Gawin *et al.* (2006). The main reason of these preferences is essentially the absence of certain experimental results of the gas pressure distribution and evolution in a drying specimen. A small number of data are currently available in literature, these are mostly numerical results, frequently in contrast with each other. Also experimental techniques for the measurement of concretes' gas permeability seem still not consolidated: the intrinsic gas permeability is measured in completely dried specimens and it cannot be excluded that the micro-cracking due to the specimen desiccation process (caused by strain incompatibilities at meso and micro-level) leads to an increase of the measured value. This opinion is also supported by the paper of Hearn and Morley (1997) where the water permeability of concrete was measured in two sets of concrete specimens: the first set consists of virgin samples, (i.e. never-dried), while the second one

consists of dried and resaturated samples. In the second set an important increase (two order of magnitude) of the water permeability has been measured and this is explained as caused by the previous drying of the specimens and the consequent micro-cracking which enhances the water flow within the porous network of concrete. In this paragraph it has been shown that the effect of Klinkenberg can be easily incorporated in the model together with the adoption of a different permeability for gas; these aspects may be implemented in a future version of the code when more experimental results will be available.

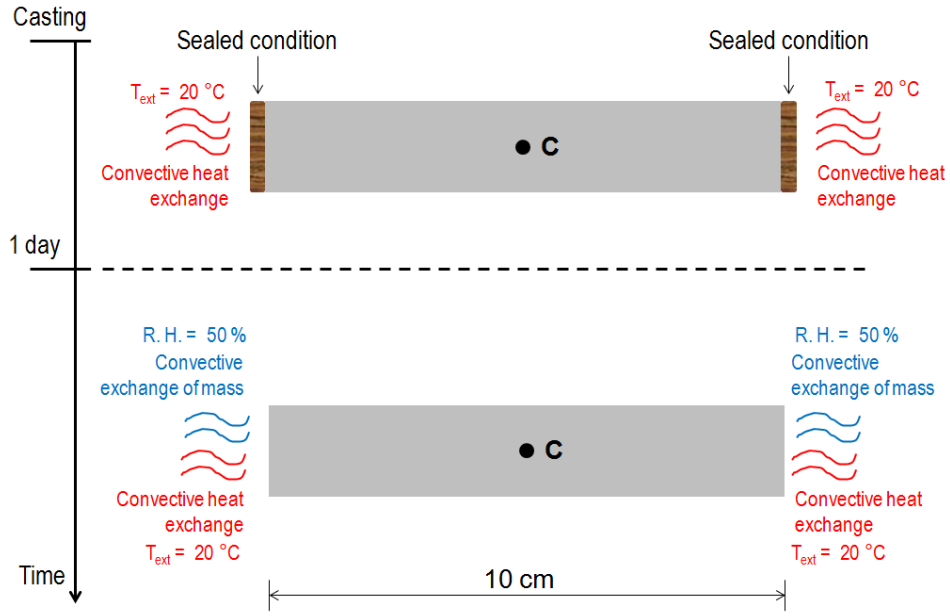

Figure 2.35 - Geometry and boundary conditions (before and after 1 day) of the simulated 1D case.

For the 1D case considered in the previous paragraph, we assume now drying condition at the lateral surface from 1 day after casting, (see ***Figure 2.35***). This time for sake of brevity only the OC2 is considered (w/c = 0.46). The hygral boundary conditions are assumed to be of convective type similarly to the thermal boundary ones. Thus, the convective water mass flux $\mathbf{q}_h$ (kg s^{-1} m^{-2}) is given by

$$\mathbf{q}_h = \varphi_h \left(p_s^c - p_{ext*}^c \right) \mathbf{n} \qquad (2.25)$$

where φ_h is the hygral convective coefficient; p_s^c is the capillary pressure at the surface in contact with the environment and p_{ext*}^c is a fictitious capillary pressure related to the ambient relative humidity and temperature (calculated using the Kelvin equation eqn (1.55) in ***Chapter 1***). The gas pressure p^g is imposed equal to the atmospheric one since 1 day after the casting

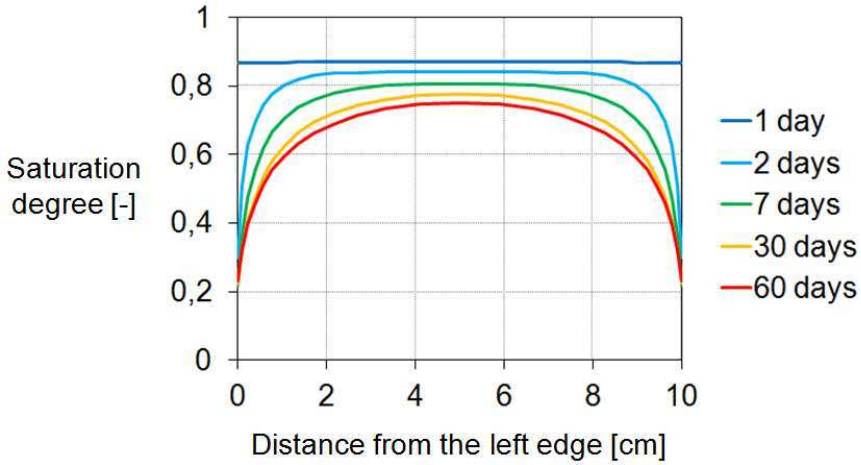

Figure 2.36 – Saturation degree at different times (numerical results). The indicated time is considered since the casting of the specimen.

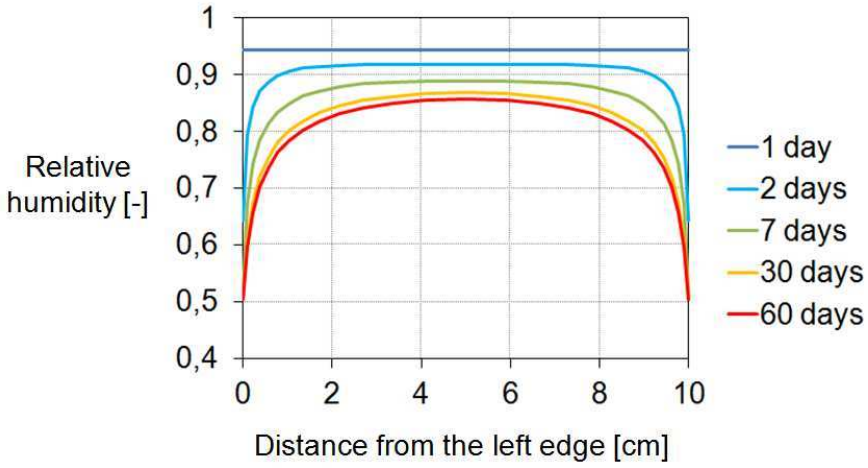

Figure 2.37 - Relative humidity at different times (numerical results). The indicated time is considered since the casting of the specimen.

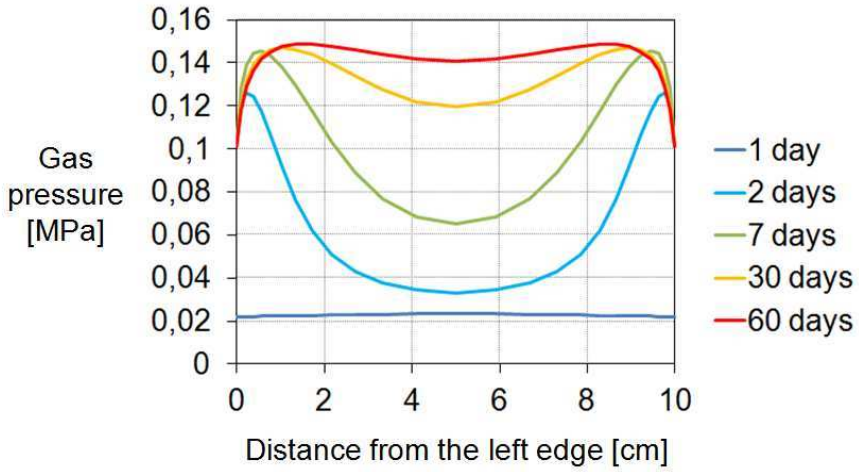

Figure 2.38 – Spatial distribution of the gas pressure at different times (numerical results). The indicated time is considered since the casting of the specimen.

Figures 2.36-37 shows the saturation degree and relative humidity at different time within the structure. The spatial distribution and temporal evolution of the gas pressure shown in ***Figure 2.38*** is qualitatively consistent with that obtained for a similar case by Mainguy *et al*. (2001) (see ***Figure 2.39***). In this interesting article is also shown that when a higher permeability of the gaseous phase is used (10^3 times greater than the intrinsic permeability to water) the magnitude of the obtained overpressure decreases notably and the transport of water vapour is enhanced. Consequently to obtain the same experimental results numerically (evolution and spatial distribution of the liquid saturation degree), the intrinsic permeability of the liquid phase has to be re-identified: the value found is 60% lower than that identified using the model with a unique intrinsic permeability: 4×10^{-22} m^2 instead of 10^{-21} m^2 (Mainguy *et al*., 2001).

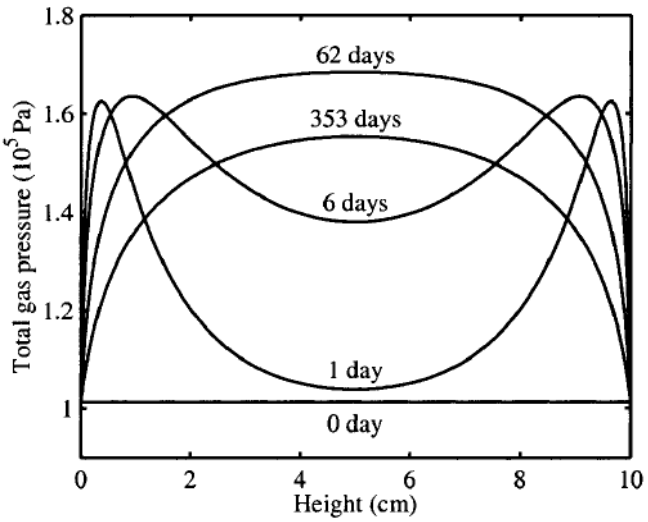

Figure 2.39 - Predicted gas pressure at different times in an ordinary cement paste (Mainguy *et al*., 2001).

The following example is a massive wall with a thickness of 150 cm. The geometry of the wall is represented in ***Figure 2.40.a***. As in the previous example for sake of brevity only the OC2 is considered (w/c = 0.46). Half of the structure is analyzed (see ***Figure 2.40.b***). The thermal and hygral boundary conditions at the external faces are assumed to be of convective type similarly to the previous case; at the *axis y* the symmetry of the problem is respected. The structure is assumed in sealed condition during the first 24 hours after the casting, then a convective water flow (liquid and water vapour) is imposed at the external surfaces. The gas pressure p^g is imposed equal to the atmospheric one since 1 day after the casting. For the first week, the numerical results at different times over the line joining the points C and B (L_{CB}) are shown in ***Figure 2.41***.

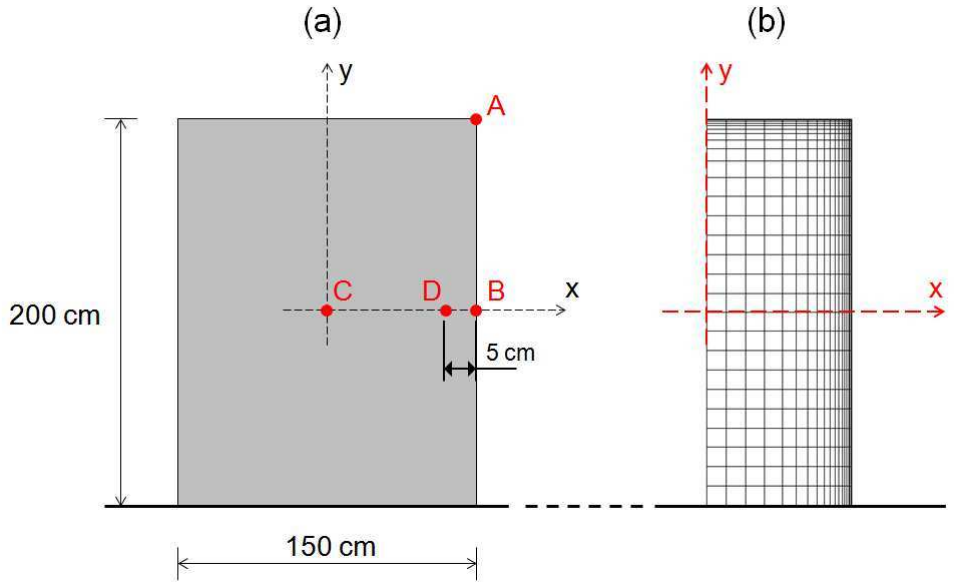

Figure 2.40 – Geometry of the massive wall (a). Finite element mesh of half of the wall (b).

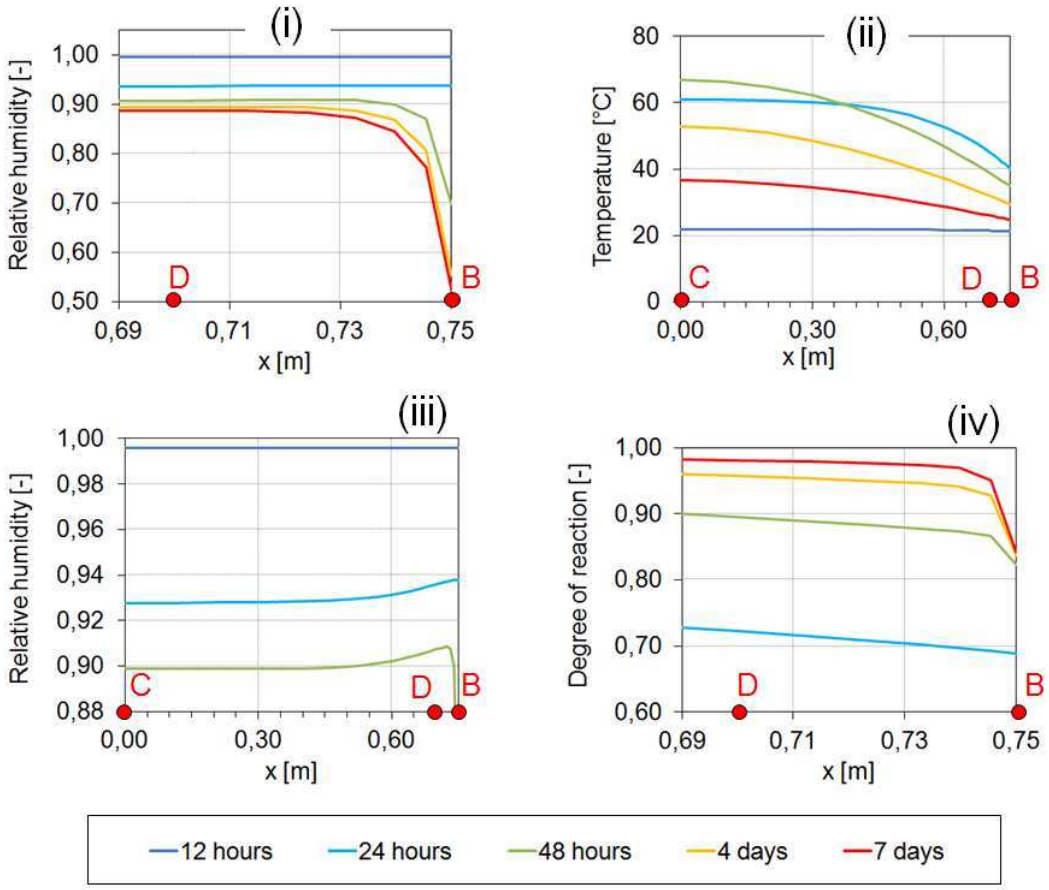

Figure 2.41 – Numerical results over the line L_{CB} at different times (12 hours, 24 hours, 48 hours, 4 days and 7 days). Relative humidity near the edge (i); temperature over the full L_{CB} (ii); relative humidity over the full L_{CB} (iii); degree of reaction near the edge (iv).

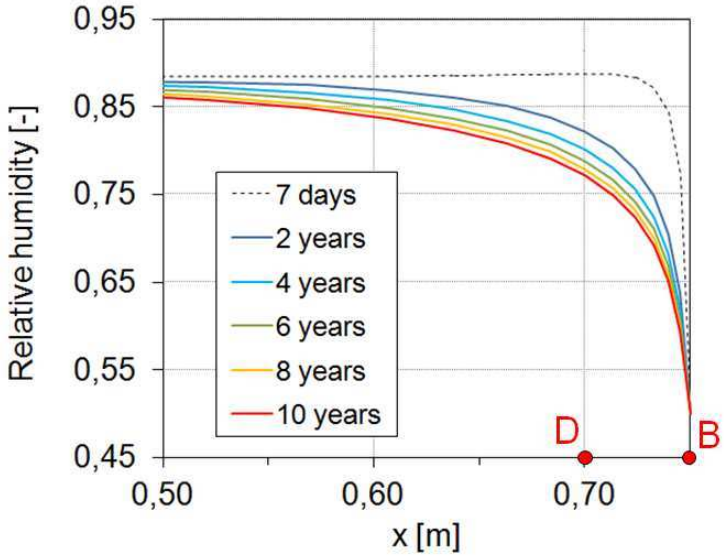

Figure 2.42 – Relative humidity over the line L_{CD} at different times: 7 days, 2 years, 4 years, 2 years, 8 years, 10 years (results are plotted from x=0.5 m to the edge of the structure).

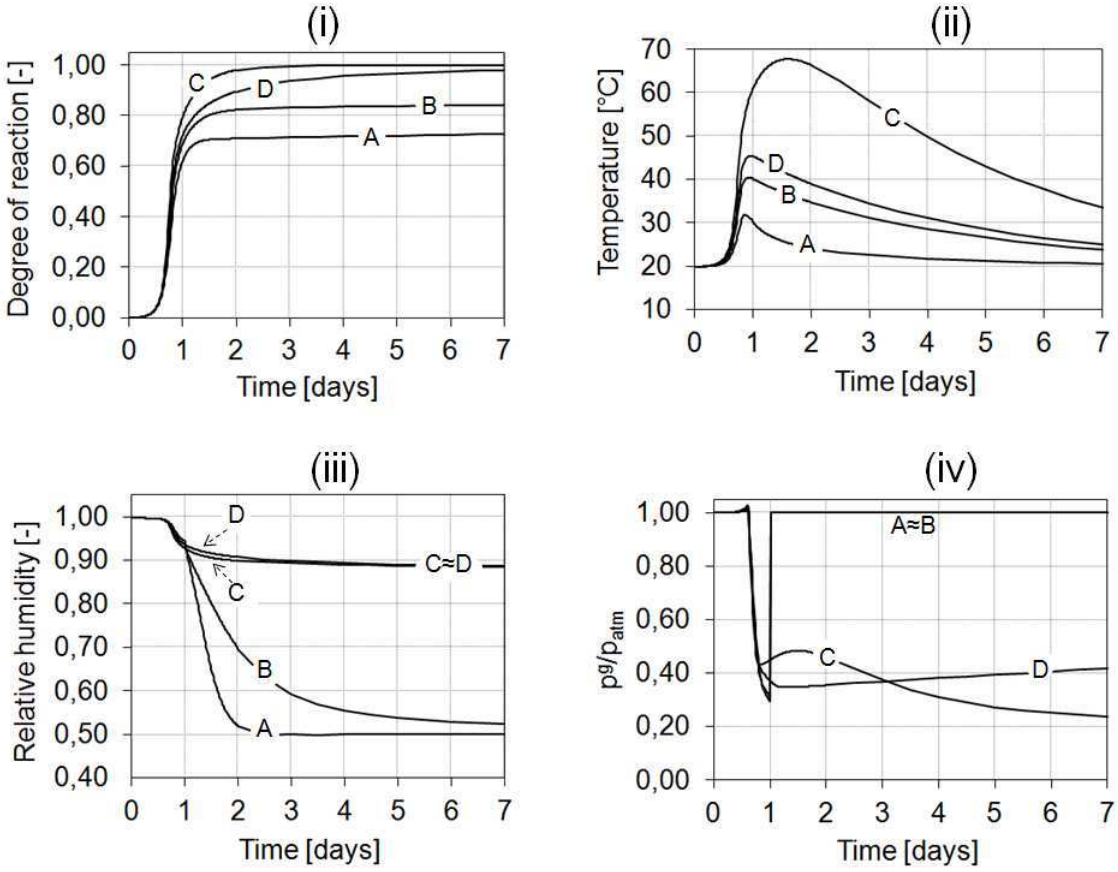

Figure 2.43 – Numerical results from 0 to 7 days for the points A, B, C and D: degree of reaction (i); temperature (ii); relative humidity (iii); normalized gas pressure (iv).

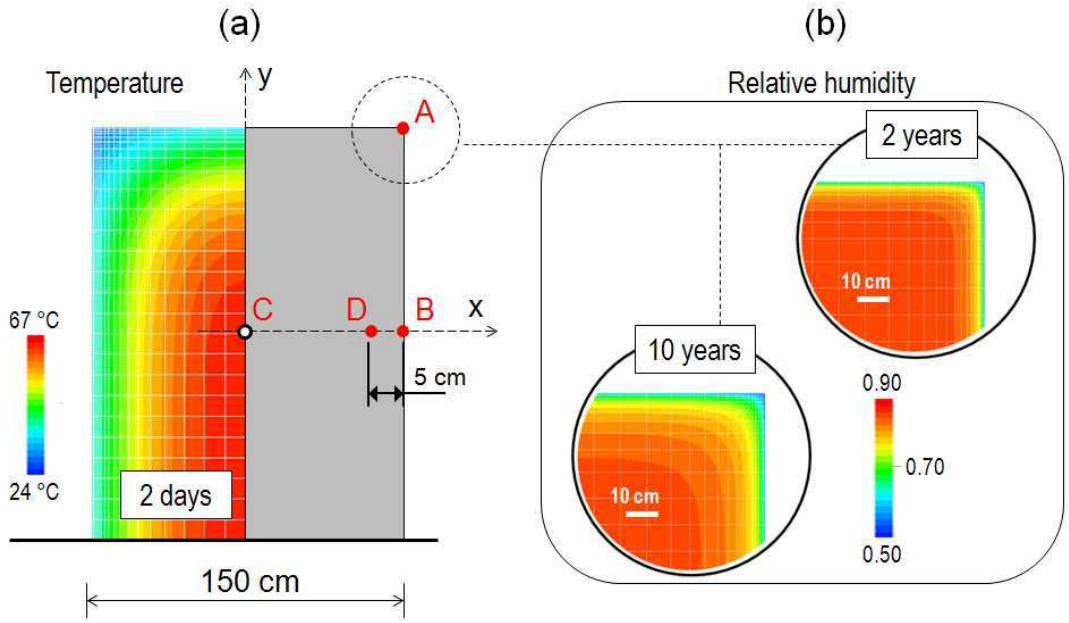

Figure 2.44 – Temperature in the massive wall at 2 days after the casting (a); Relative humidity at 2 and 10 years in the proximity of point A (b).

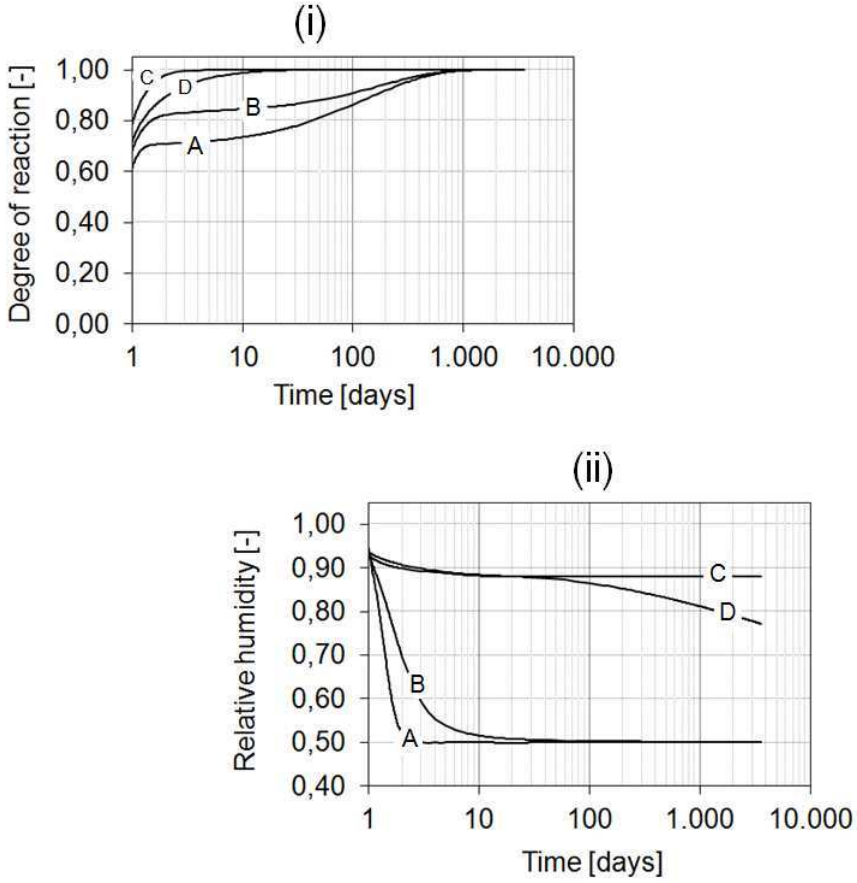

Figure 2.45 - Numerical results during 10 years for the points A, B, C and D: degree of reaction (i); relative humidity (ii).

Figure 2.42 shows the relative humidity over L_{CB} at 7 days, 2 years, 4 years, 2 years, 8 years and 10 years; from this figure is confirmed that hygral phenomena are very slow compared to thermal ones. In ***Figure 2.43*** the obtained results are also plotted over the time (from 0 to 7 days after the casting) for the four point represented in ***Figure 2.40.a***. In ***Figure 2.44.a*** the severe thermal gradient established at two days after the casting of the wall can be clearly observed. ***Figure 2.44.b*** shows the relative humidity after 2 and 10 years of drying in the proximity of the point A. Due to drying the hydration in A and B is inhibited and retarded. This can be seen in ***Figure 2.45.i*** where the evolution with time of the degree of reaction from 1 to 10 years is plotted for the considered points (A, B, C and D). In ***Figure 2.45.ii*** the relative humidity is plotted for the same period.

The decrease of relative humidity and the loss of water in consequence of drying cause the drying shrinkage which in the model is computed by means of the same constitutive model already presented for autogenous shrinkage. The change in the volume of the drying concrete is not equal to the volume of water removed since drying results essentially in the decrease of the saturation degree of the porous medium. The reduction of concrete porosity due to the autogenous and drying shrinkage is of a lower order of magnitude (the same of concrete contraction) and so can be neglected in the governing equation of the thermo-hygro-chemical part of the developed model[4].

Shrinkage is larger the higher the water/cement ratio because the latter determines the amount of evaporable water in the cement paste and the material permeability and consequently also the rate at which water can move towards the surface of the specimen. Brooks (1989) demonstrated that shrinkage of cement pastes is proportional to the water/cement ratio between the values of about 0.2 and 0.6. At higher water/cement ratios the additional water is removed upon drying without resulting in shrinkage. Passing from cement paste to mortar and concrete experimental evidences have demonstrated that the content of aggregate has a critical impact on shrinkage since aggregate particles restrain the shrinkage contraction; the degree of restraint offered depends on the mechanical properties of aggregate. In the system aggregate + cement paste, being in general the cement paste much more involved by drying and shrinkage than the aggregates, the resulting contraction in concrete is larger the higher is the volume of cement paste. Also, shrinkage consists of an elastic part and a viscous part and so its magnitude depends primarily on concrete compressibility and on its creep potential.

[4] This is another way to enunciate the simplification *hypothesis ii* in Paragraph 1.6.

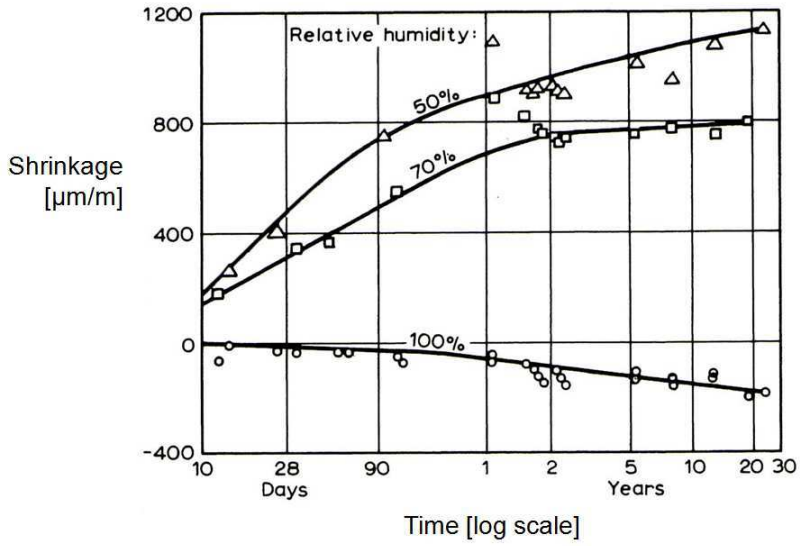

Figure 2.46 – Relation between shrinkage and time for concretes stored at different relative humidities (Troxell, 1958). Time reckoned since end of wet curing at the age of 28 days.

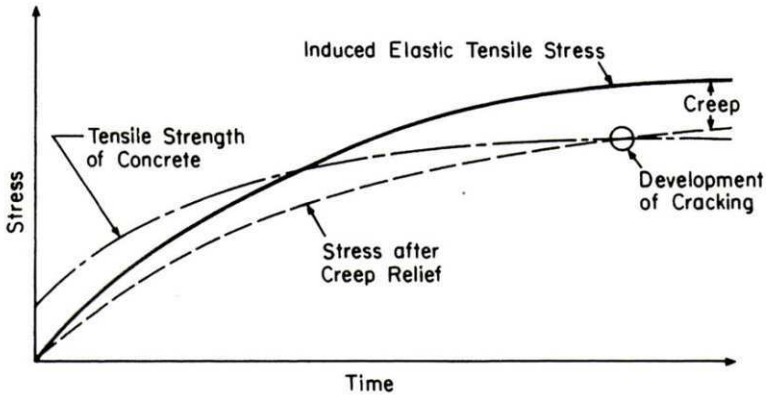

Figure 2.47 – Schematic pattern of crack development when tensile strain due to restrained shrinkage is relieved by creep (Neville, 1996).

Clearly the environmental relative humidity is the external factor which mainly affects the magnitude of shrinkage as shown in ***Figure 2.46***; this figure illustrates also swelling of concrete in water (curve with r.h. = 100%): the absolute magnitude of swelling is very lower than that of shrinkage.

Experimentally, the magnitude of the measured shrinkage varies considerably with the size and the shape of the specimen and depends on the surface/volume ratio. In fact moisture loss takes place at the surfaces in contact with the environment. The established gradient of relative humidity induces fluid flow from the core of the structure to the external surfaces, and produces a non-homogenous shrinkage: the contraction is more important at the dryer external surfaces than in the core of the structure. In addition to

drying shrinkage, the surface zone of concrete undergoes carbonation and the associated contraction. Hence, even if drying and carbonation are quite distinct phenomena, often experimental data on drying shrinkage include also the effect of carbonation. At the dried surfaces, the differential shrinkage induces tensile stresses partially relaxed by creep in tension; this latter, if drying in not too rapid, may prevent the development of cracking. Therefore the cracking tendency depends not only on the magnitude of shrinkage but also on the rate of the contraction, on tensile strength and on the extensibility of concrete (of course in concrete structures cracking tendency depends also on the mechanical boundary conditions which may restrain shrinkage). At early age concrete properties vary with time and so ***cracking prevention*** is very hard to be generalized in a number of design specifications because cracking tendency depends on several factors. ***Figure 2.47*** shows the schematic pattern of crack development due to restrained shrinkage with the induced stress relaxed by creep. Nowadays self-restrained shrinkage and cracking tendency of concretes are often studied experimentally by means of a ring-shaped concrete specimen restrained by an internal steel ring. This test is also useful for the analysis of cracking due to thermal shrinkage and autogenous shrinkage in massive structures: a thermo-activated ring reproduces the increase of temperature due to the hydration process and restrains the contraction due to autogenous shrinkage and to the decrease of temperature which occurs when the hydration rate decreases and the reaction goes towards its end (see ***Figure 2.48*** taken from the paper of Briffaut *et al.* 2011).

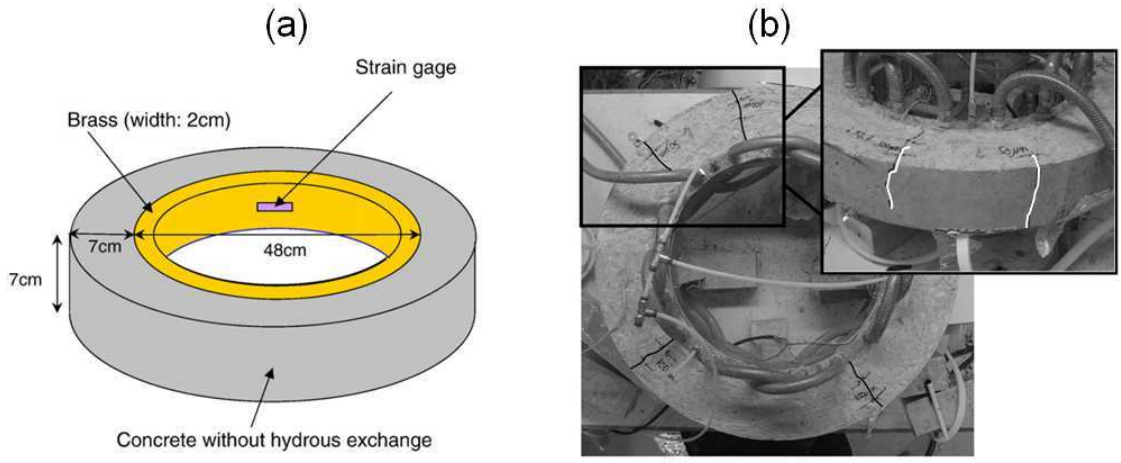

Figure 2.48 – Geometry of the thermo-activated ring test (a); Cracks due to the restrained autogenous contraction (b) (readapted from Briffaut *et al.* 2011).

In such a scenario is clear that numerical modeling may be crucial in the prevention of cracking caused by restrained or self-restrained shrinkage.

The first set of numerical results deals with a typical cylindrical specimen sealed during the first 24 hours and then drying at the lateral surfaces only (different environmental conditions are tested). The geometry of the modeled specimen and the FE mesh are shown in ***Figure 2.49***. Half of the cylinder is considered and the case is solved in axial symmetry (*y* is the vertical axis of the cylinder).

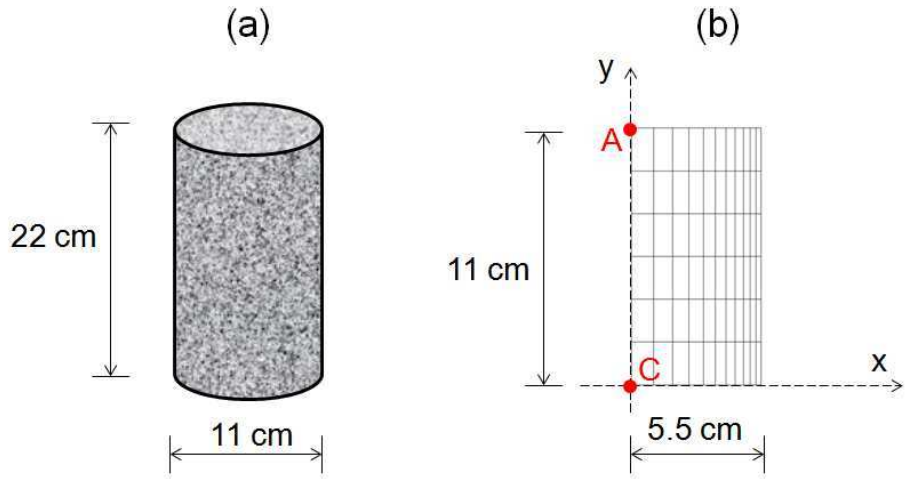

Figure 2.49 – Geometry (a), and FE mesh (b), of the considered cylinder. The specimen is sealed during the first 24 hours, then it dries at the lateral surface only.

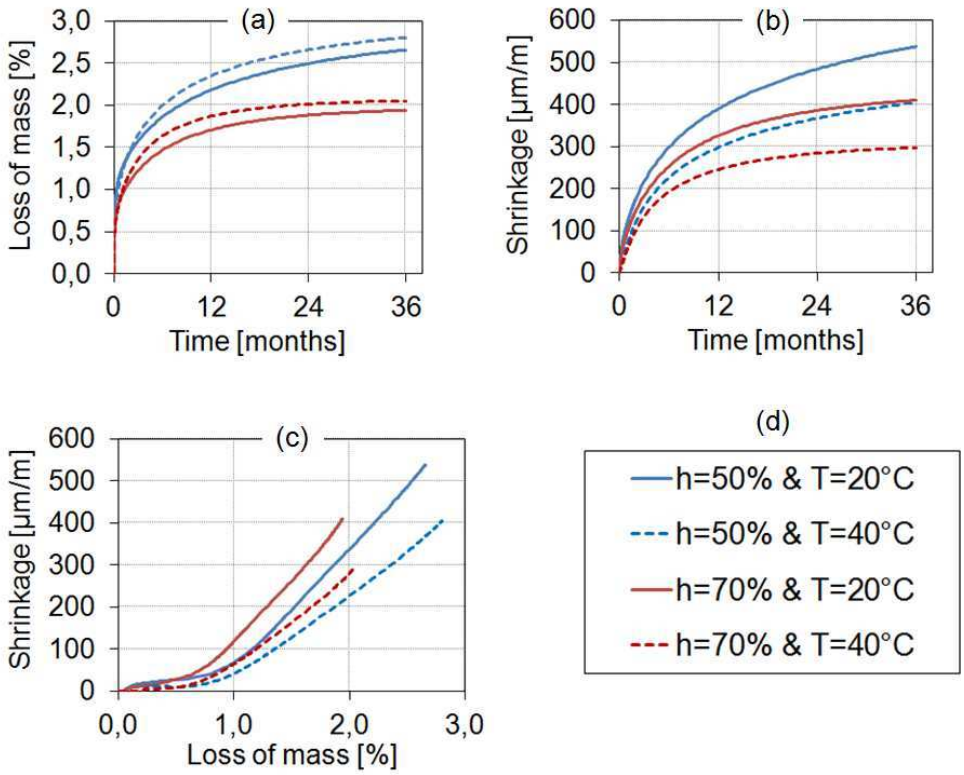

Figure 2.50 – Predicted results during 36 months: loss of mass (a), drying shrinkage (b), loss of mass *versus* drying shrinkage curves (c), legend of the graphs (d).

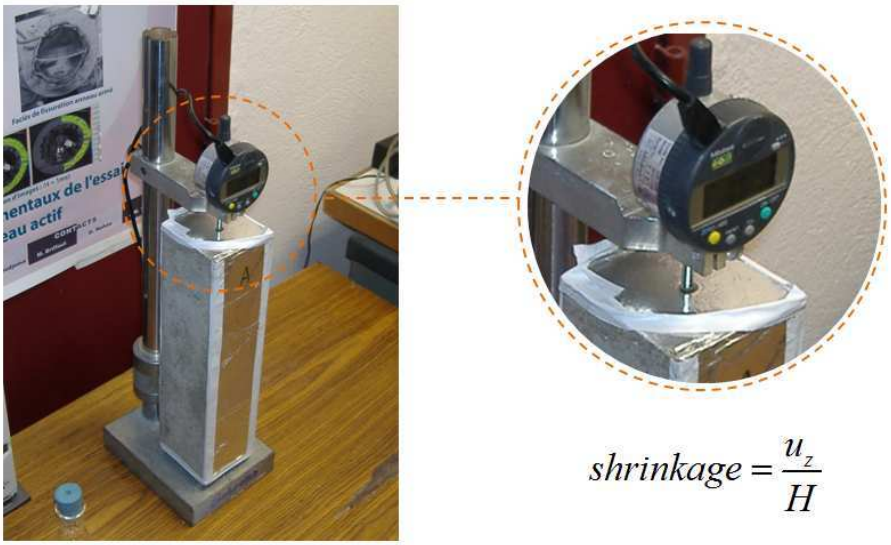

Figure 2.51 – Shrinkage measured on the vertical axis of the specimen.

Figures 2.50.a-c show the numerical results during 36 months after the casting of the specimen. Four environmental situations are considered varying the external temperature, T_{ext}, and relative humidity, h_{ext}: i) T_{ext} = 20°C and h_{ext}=50%; ii) T_{ext} = 40°C and h_{ext}=50%; iii) T_{ext} = 20°C and h_{ext}=70%; iv) T_{ext} = 40°C and h_{ext}=70%.

The averaged shrinkage is estimated from vertical displacement of points A in ***Figure 2.49*** (the point C doesn't move according to the symmetry of the problem). This is consistent with the experimental measuring method represented in ***Figure 2.51***. However shrinkage sometimes is measured at the surface of the specimen. The autogenous shrinkage is removed from the total contraction in order to obtain the sole drying shrinkage.

As expected, with the same external temperature, loss of mass and shrinkage are higher the lower the external relative humidity is (i.e. for h_{ext}=50%). Interesting is the effect of temperature. A higher external temperature has as consequence an higher loss of mass and this means that the mass transport of water is enhanced the higher the temperature. On the other hand shrinkage is smaller when the external temperature is set equal to 40 °C. Actually at 24 hours, when the concrete is exposed to the external environment, the specimen cured at 20°C is much less hydrated than that cured at 40 °C and therefore in this last one the amplitude of drying shrinkage is smaller. The loss-of-mass *versus* drying-shrinkage curves represented in ***Figure 2.50.c*** are in agreement with literature (Neville 1996), in fact the loss of free water causes initially a modest contraction, then as drying continues the absorbed water begins to be removed and more substantial shrinkage occurs.

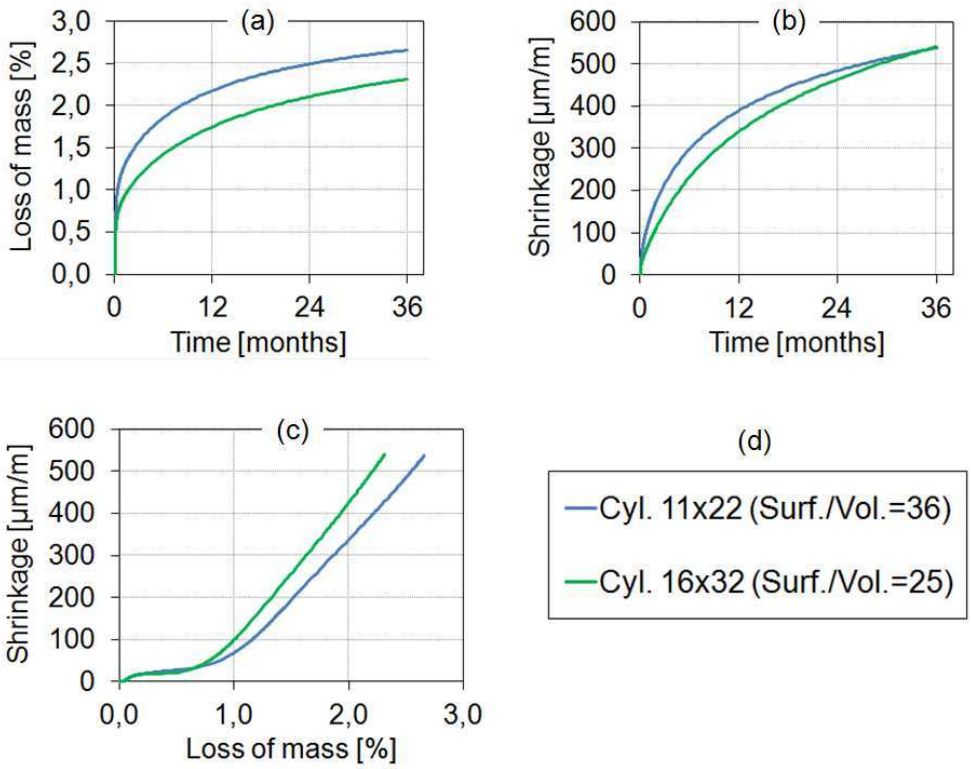

Figure 2.52 - Predicted results during 36 months for the reference cylinder (11Ø×22) and the bigger one (16Ø×32): loss of mass (a), drying shrinkage (b), loss of mass *versus* drying shrinkage curves (c), legend of the graphs (d).

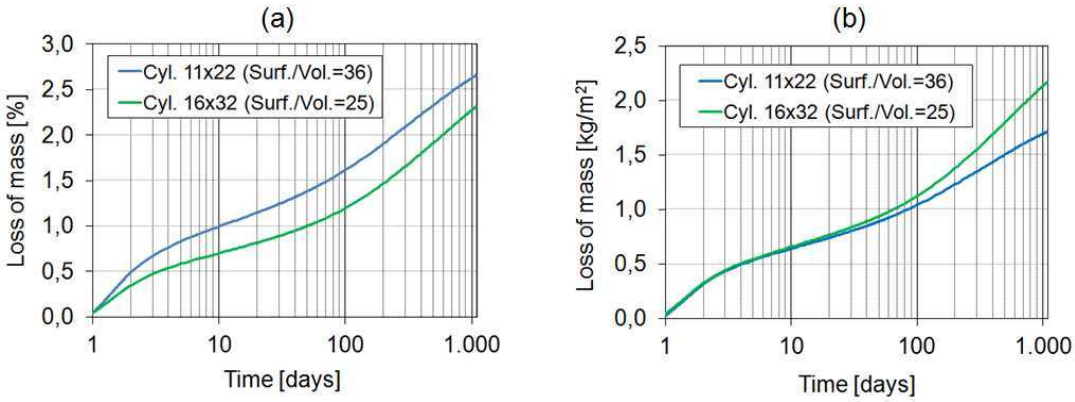

Figure 2.53 - Predicted results during 1080 days for the reference cylinder (11Ø×22) and the bigger one (16Ø×32): loss of mass [% of the initial weight] (a), loss of mass[kg/m^2] (b).

The effect of the surface/volume ratio can be observed in ***Figure 2.52.a-c*** where the results obtained with a cylinder 16Ø×32 are compared with those obtained with the cylinder 11Ø×22 (for both cases T_{ext} = 20°C and h_{ext}=50%). Even if the loss of mass is more important in the smaller specimen (see ***Figure 2.52.a***), shrinkage after a certain time tends to the same value (see ***Figure 2.52.b***). On the other hand in ***Figure 2.52.a*** the loss of mass is expressed in terms of percentage of the initial mass of the cylinder.

Being the initial mass of the two cylinders very different (m_0 = 4.9 kg for the cylinder 11Ø×22 and m_0 = 15.1 kg for the cylinder 16Ø×32) it is interesting to plot the loss of mass *per* m^2 of drying surface [kg/m^2] to understand better the drying process in the two cases. This plot is shown in ***Figure 2.53.b*** over a logarithmic time scale; the graph in percentage (i.e. ***Figure 2.52.a***) is re-plotted over a logarithmic time scale in ***Figure 2.53.a*** to facilitate the comparison with the previous one. We can clearly observe that in the two cases the loss of mass *per* square meter of drying surface is not influenced by the size of the cylinder until one month; then the drying rate decreases in the cylinder 11Ø×22.

To test the effect of the shape, a prismatic specimen is also modeled. When the specimens dry only from the lateral faces, a cylinder and a square prism have the same surface/volume ratio if the edge of the square base is equal to the diameter of the cylinder. The geometry of the prism and the 3D finite element mesh are represented in ***Figure 2.54***. The specimen has three planes of symmetry, hence only an octave is modeled. The external temperature and relative humidity are respectively T_{ext} = 20°C and h_{ext}=50%. ***Figure 2.55*** shows damage and stresses at 36 months in 1/8 of the prismatic specimen.

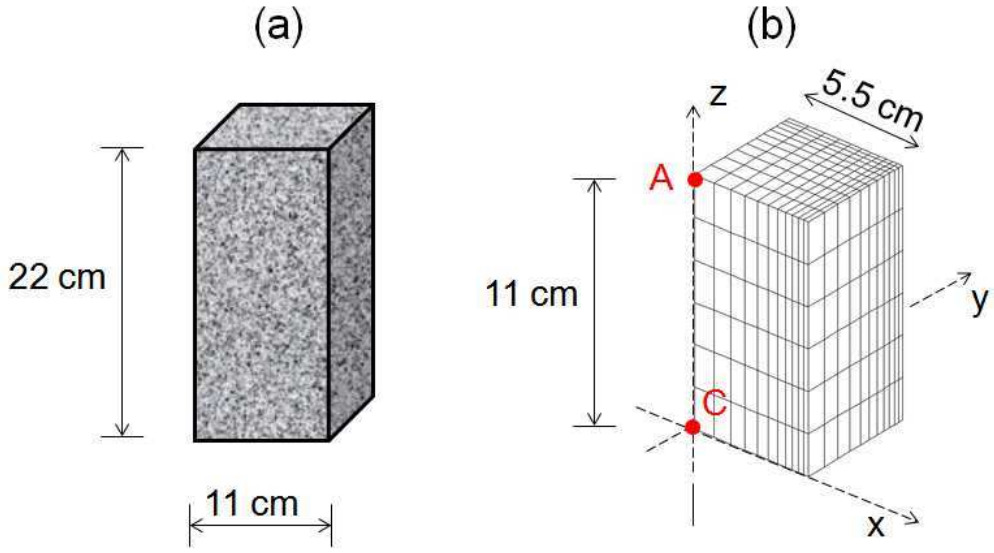

Figure 2.54 - Geometry (a), and FE mesh (b), of the considered square prism. The specimen is sealed during the first 24 hours, then it dries at the lateral surfaces only .

In ***Figure 2.56.a-b*** the obtained results are compared with that of the cylinder having the same surface/volume ratio: the differences between the two cases is not remarkable and this means that the loss of mass and the amplitude of drying shrinkage depend essentially on the surface/volume ratio and not on the shape of the specimen.

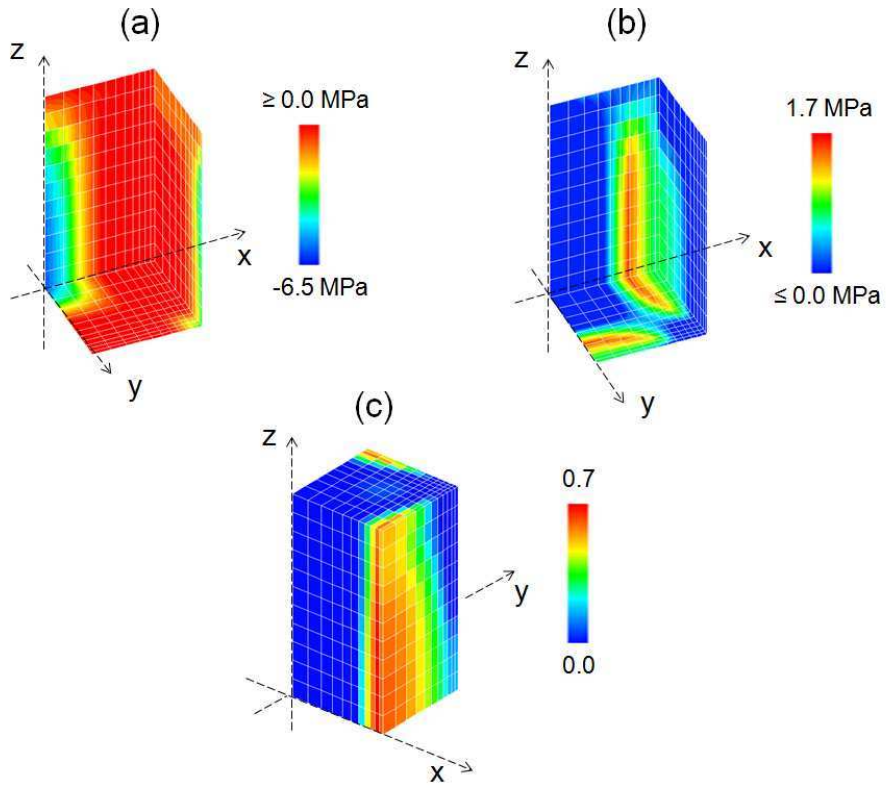

Figure 2.55 – Negative stresses t_{zz} (a), positive stresses t_{zz} (b), and damage (c) in the prismatic specimen at 36 months.

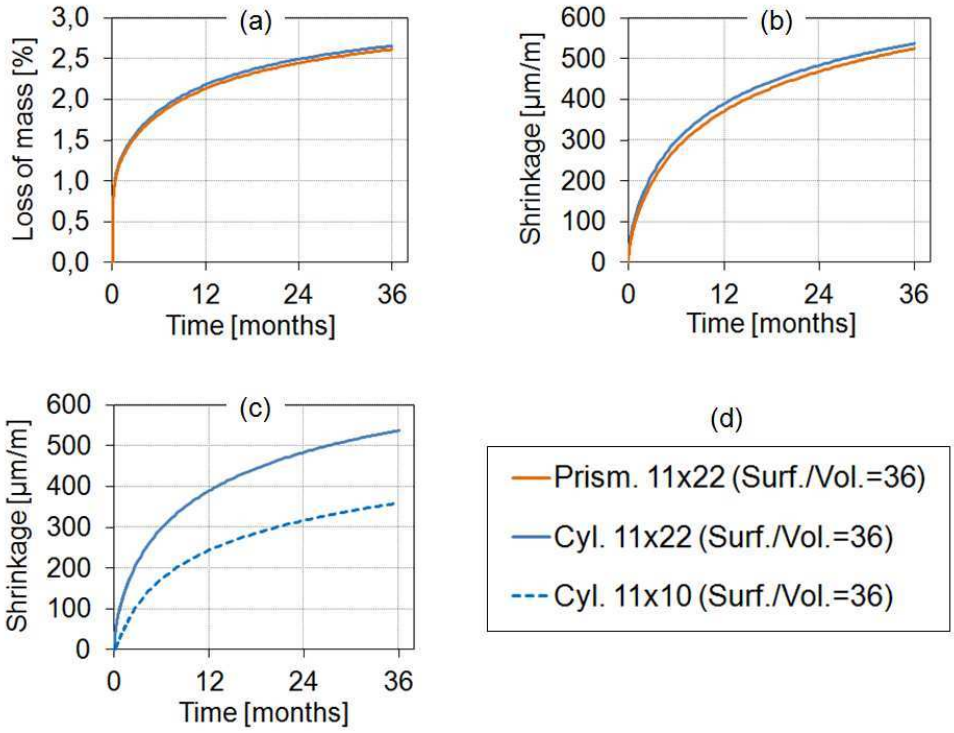

Figure 2.56 - Predicted results during 36 months for the reference cylinder (11Ø×22) and the prismatic one (11×11×22): loss of mass (a), drying shrinkage (b). Predicted drying shrinkage for the reference cylinder (11Ø×22) and a cylinder 11Ø×10 (c), legend of the graphs (d).

Concerning the loss of mass, being the difference between the two cases irrelevant when this is expressed in percentage of the initial weight (***Figure 2.56.a***), if this is expressed in kg *per* m^2 of drying surface the difference between the two cases is also irrelevant because the specimens have the same surface/volume ratio.
To conclude this group of numerical tests, a cylinder 11Ø×10 is modeled. In this case even at constant surface/volume ratio the estimated shrinkage is lower than in the cylinder 11Ø×22 because the structural effect is significantly reduced (see ***Figure 2.56.c***).

The numerical results presented and discussed within this paragraph are in agreement with the experimental data of concrete's bibliography regarding drying and drying shrinkage. It can be summarized that the external relative humidity together with the external temperature and the surface/volume ratio[5] of the specimen are the key factors which control the loss of mass and drying shrinkage. In addition, when the ratio between the height of the specimen and the characteristic length of the base[6] is lower than 2, the drying shrinkage can be underestimated if measured using the method shown in ***Figure 2.51***.

2.6 BASIC AND DRYING CREEP

The total strain of concrete can be expressed as summation of several components: elastic strain, thermal and hygral strains (autogenous and drying shrinkage) and viscous strain which is usually is indicated as creep. Creep can be defined as the increase in strain under a sustained stress. From another point of view creep has also the effect of relaxation: if a concrete specimen is subjected to a constant strain, the consequence of creep is the conversion of the elastic strain in a viscous deformation which leads to the decrease of stress. Being the final creep strain almost two or three times the instantaneous elastic strain obviously it cannot be neglected in design of concrete structures. The mechanism of creep has not yet been fully elucidated, but a number of aspects have been understood with time and are explained in the following pages. The ***basic creep*** is the strain of a concrete specimen loaded in sealed condition. However this definition is not completely exhaustive. In effect the specimen must been in sealed condition but also in internal hygral equilibrium (not necessary saturated or at a specific relative humidity but water transport must not occur).

[5] The surface is the drying surface of the analyzed specimen.
[6] The characteristic length of the base is the diameter for a cylinder and the edge for a square prism.

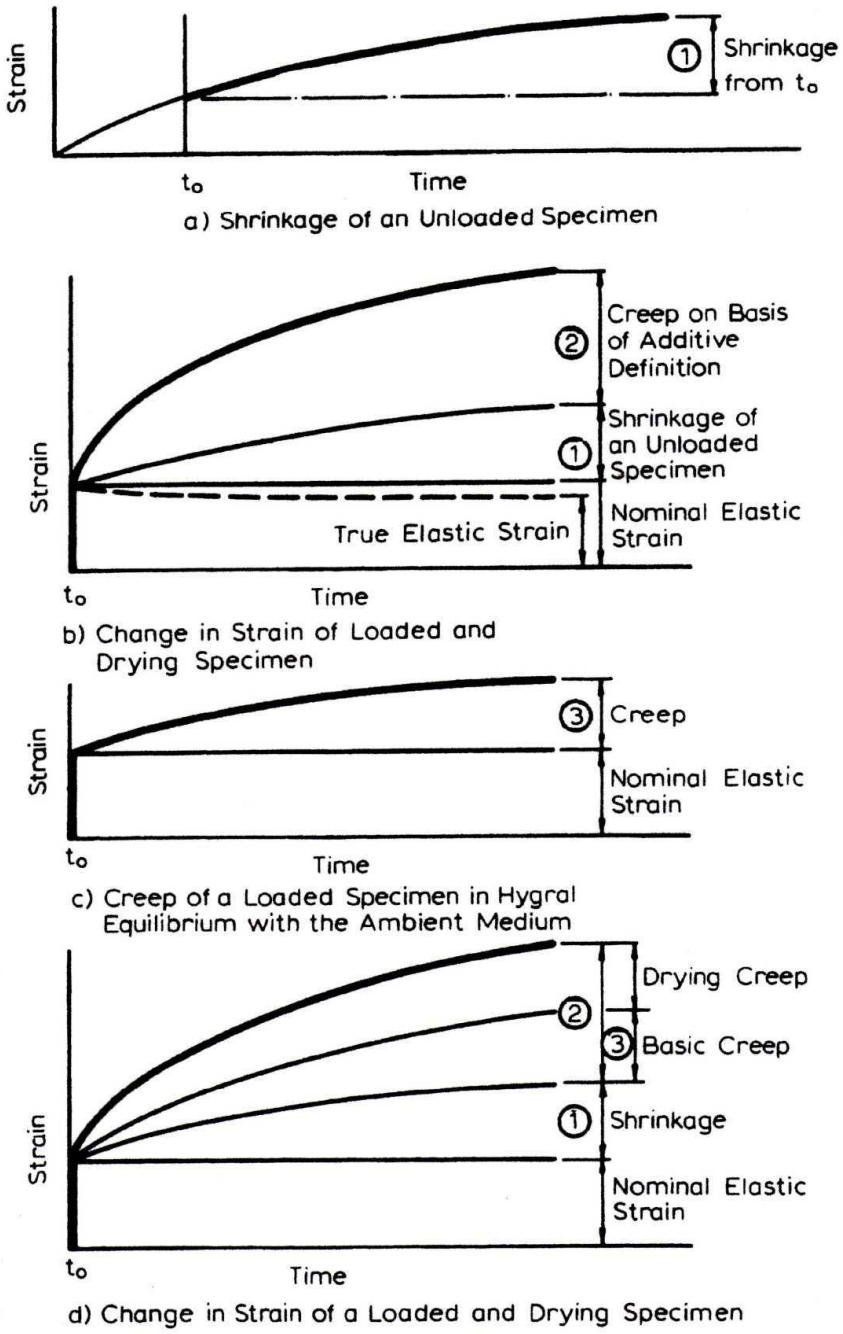

Figure 2.57 – Time dependent deformation in concrete subjected to a sustained load (Neville, 1996)

If a specimen is drying while under load another component of strain called ***drying creep*** is induced (in addition to shrinkage). This additional deformation has been discovered by Pickett (1942). In other word the summation of the basic creep strain of a sealed specimen, and the shrinkage of the same drying specimen (not loaded), is lower than the total strain of a third identical specimen drying and loaded at the same time.

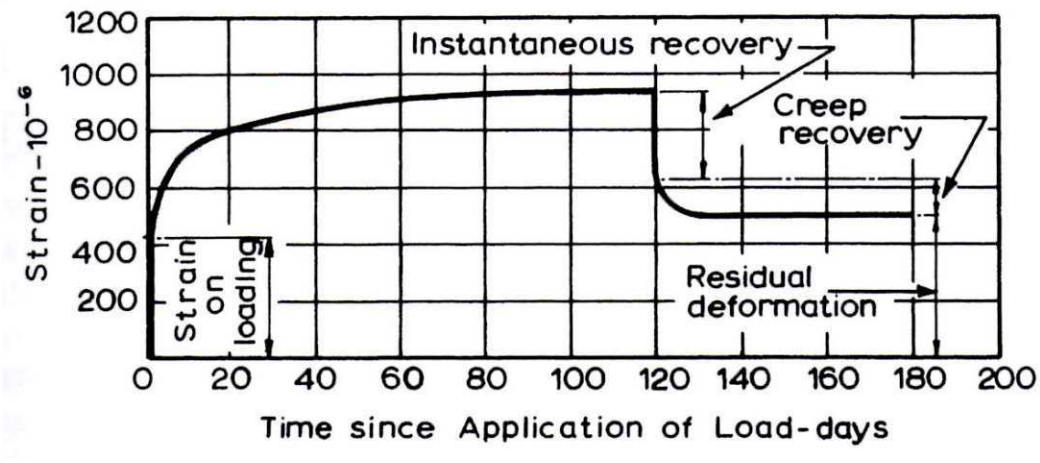

Figure 2.58 – Creep and creep recovery of a mortar specimen loaded with a stress of 14.8 MPa and then unloaded after 120 days (Neville, 1959).

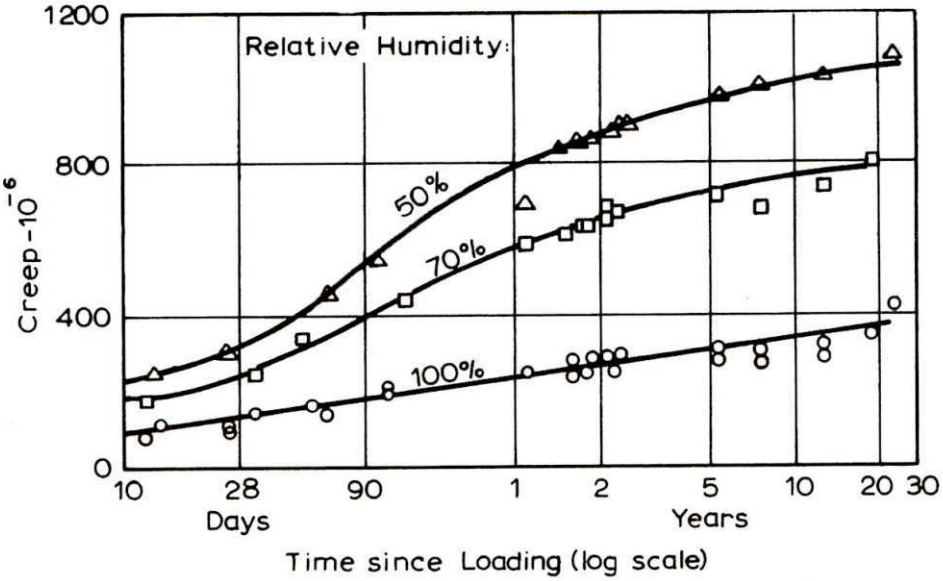

Figure 2.59 – Creep of concrete cured at r.h=100% for 28 days, then loaded and stored at different relative humidities (Troxell, 1958).

This means that creep and shrinkage are not independent phenomena and that their associated strains are not additive (see ***Figure 2.57***). Hence distinction will be made between creep of concrete under conditions of no moisture movement to or from the ambient medium (basic creep) and the additional creep caused by drying (drying creep).

When the load is removed the instantaneous elastic recovery is followed by the creep recovery, however part of strain remains unrecovered not being creep completely reversible (residual deformation in ***Figure 2.58***). The main significant property of creep is its proportionality with the applied stress when the loading stress is less than 1/2 of the concrete strength (this limit may vary depending on the type of concrete). After this limit

value for the applied stress, creep loses the proportionality with stress because of the development of severe micro-cracking.

The factors that influence creep are essentially the same which impact on shrinkage strain. This is due almost certainly to the intrinsic connection of both creep and shrinkage with cement paste micro-structure and concrete mix. For example, similarly to shrinkage, creep is function of the volumetric content of cement paste in concrete. Also, creep is inversely proportional to the strength of concrete at the time of application of the load. The relation between creep and the stress/strength ratio has been demonstrated to be approximately linear (Neville, 1959).

If the specimen is not sealed, the environmental relative humidity has an important effect on creep: generally creep is higher the lower the relative humidity (see ***Figure 2.59***). However, this figure is just indicative, because the importance of the effect of relative humidity depends also on the size and on the shape of the considered specimen. Also, the influence of relative humidity is much smaller in the case of specimens which have reached the hygral equilibrium with the surrounding environment prior to the application of the load. Hence it is not the relative humidity that influences creep but the process of drying which induces the drying creep strain. A number of hypotheses, more or less plausible, have been proposed to explain the drying creep but up to now its mechanism has not been fully understood. Surely drying creep cannot be connected with a sort of consolidation: Maney (1941) had shown experimentally that the mechanical load does not increase the drying rate of a specimen. A probable explication is given by Bažant *et al*. (1997) who suggest that drying creep is a stress induced shrinkage caused by local movement of water between capillary pores and gel pores; the rheological model proposed by Bažant is one of the most used for modeling drying creep. In this model creep is explained with the microprestress-solidification theory. More in detail basic and drying creep are associated with the microprestress generated as a reaction to the disjoining pressure at the micro level. This microprestress depends on relative humidity and changes with time; in brief with a constant relative humidity, $\frac{\partial h}{\partial t} = 0$, this model gives the basic creep, while with $\frac{\partial h}{\partial t} < 0$ and additional strain is computed (i.e. the drying creep). This model works for the current experimental cases, but even if is clear that drying creep is associated with drying, experiments have not clarified if this additional

strain is related to moisture movement (vapor and liquid water flows) or to the specimen desiccation (decrease of the internal relative humidity). In fact in some situations we can have moisture movement without decrease of relative humidity. An example of such a situation is illustrated in ***Figure 2.60***: with the represented boundary conditions (constant with time) the hygral equilibrium is achieved after a certain time t_{equ}, which depends on the thickness of the concrete structure. In this case the hygral equilibrium does not correspond to a homogenous relative humidity but to the establishment of a hygral gradient which determines a stationary water flow. Hence if drying creep is only connected to changes of relative humidity (as in the model proposed by Bažant *et al.*, 1997) drying creep is exhausted when the hygral equilibrium is achieved. On the other hand if drying creep is the consequence of the moisture transport, it persists even after the hygral equilibrium is reached, because of the stationary water flow. However, similar cases have not yet been analyzed experimentally and so the question remains still open.

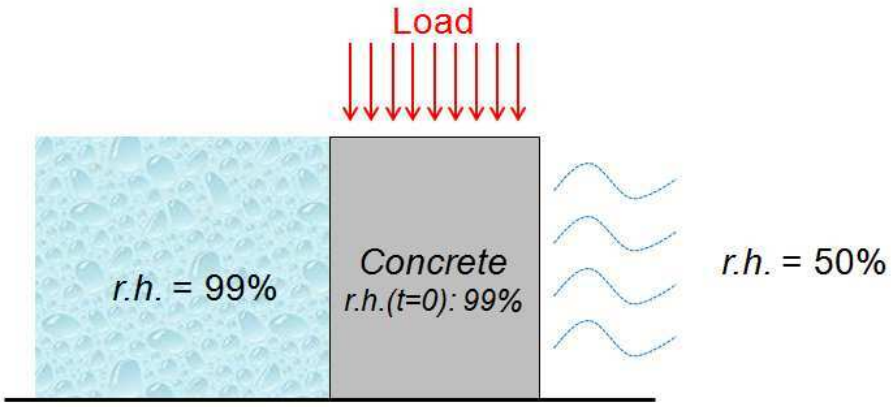

Figure 2.60 – Example of mass transport under hygral equilibrium.

As already pointed out, the physical mechanisms of basic and drying creep seem not sufficiently understood until now. For instance, in completely dried specimen creep is negligible or absent, but the intrinsic effect of the water content on creep has not been quantified.

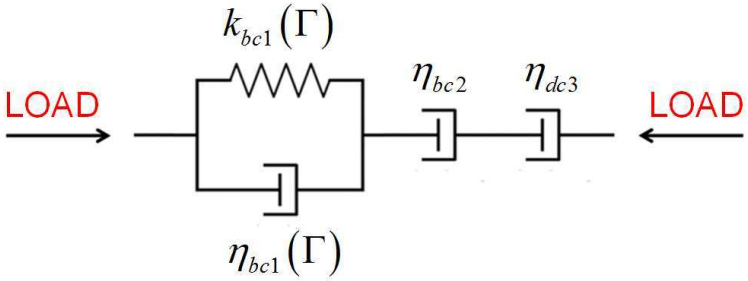

Figure 2.61 - Creep rheological model

In the present model creep is modeled by means of a Kelvin-Voigt chain and two dashpots combined in serial way (see ***Figure 2.61***). The first two cells (aging Kelvin-Voigt chain and one single dashpot) are used to compute the basic creep and the last cell (single dashpot) is dedicated to the drying creep strain. The effect of hydration is taken care by relating the material parameters to the degree of reaction Γ. The relationship is similar to that proposed by De Schutter (1999). In the model is hypothesized that drying creep is directly associated with the liquid flow within the porous medium (see eqn (1.75)). Details about the adopted rheological model are given in the *section 1.5.8* of ***Chapter 1***. The intrinsic impact of temperature is not negligible (see for instance ***Figure 2.62*** which represents experimental results from Arthanari and Yu (1967)). Temperature increases creep strains due to the two following factors (Hauggaard *et al.*, 1999): i) at constant temperature, creep strain rate increases the higher the temperature and this is due to the decrease of water viscosity with temperature; ii) transient temperature history increases also creep strains. The obtained deformation is called transient thermal creep or load induced thermal strains.

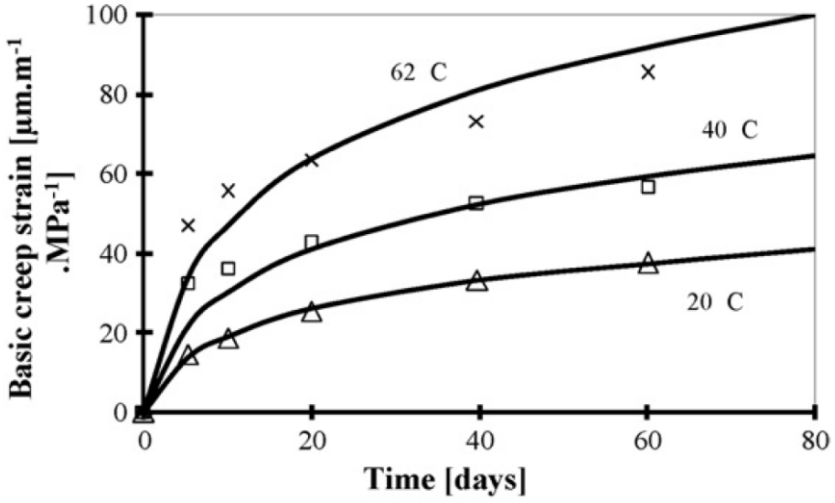

Figure 2.62 - Basic creep strain evolution for different constant temperatures (experimental results are from Arthanari and Yu, 1967).

Such kind of strain is also observed at very high temperature (above 100 °C). Bažant *et al.* (1997) suggest that this strain correspond to drying creep. The effect of temperature and its correlation with the progression of the hydration degree of concrete is broadly discussed in the work of Benboudjema and Torrenti (2008), where a way to integrate the intrinsic effect of temperature in creep modeling is also proposed.

In the first numerical example the cylinder 11Ø×22 modeled in the previous paragraph is loaded in compression at 7 days with 10 MPa. The geometry and the mechanical boundary conditions are represented in ***Figure 2.63.a***. The concrete is the same used for the numerical analyses of shrinkage (OC2, w/c = 0.46).

Three situations are considered: i) the cylinder is sealed; ii) the cylinder dries with h_{ext} = 50%; iii) the cylinder dries with h_{ext} = 70%. The sole creep strains (shrinkage and autogenous shrinkage are removed) are plotted in ***Figure 2.63.b***. In case i) the strain is only the elastic one + basic creep while in the cases ii) and iii) also drying creep occurs, since the material is drying while loaded. As expected when the specimen is exposed to h_{ext} = 50% creep strain is more important.

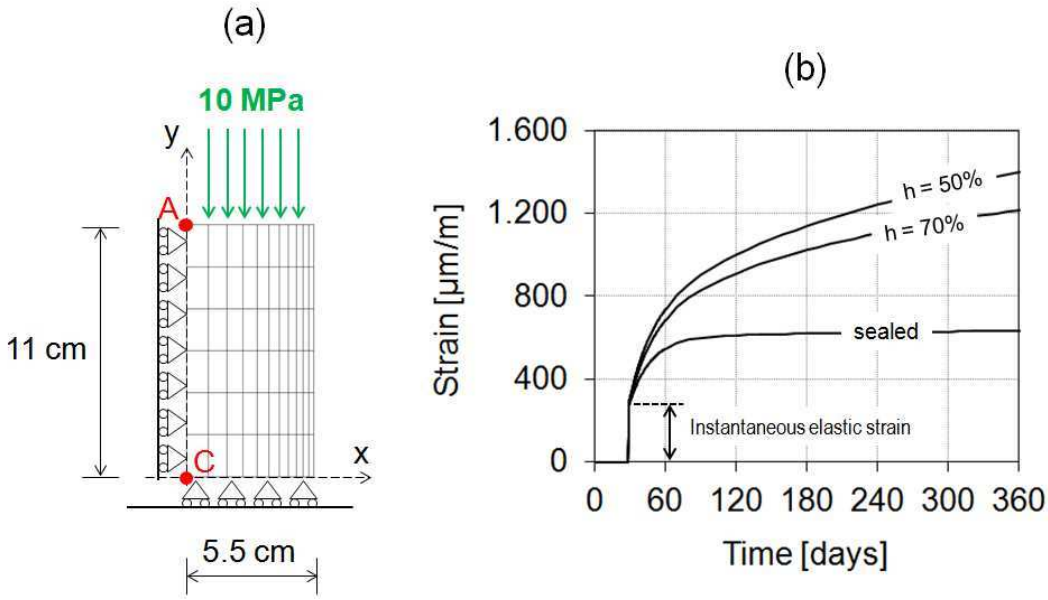

Figure 2.63 – Geometry and boundary condition of the modeled case (a); Creep strains in the three considered conditions (b).

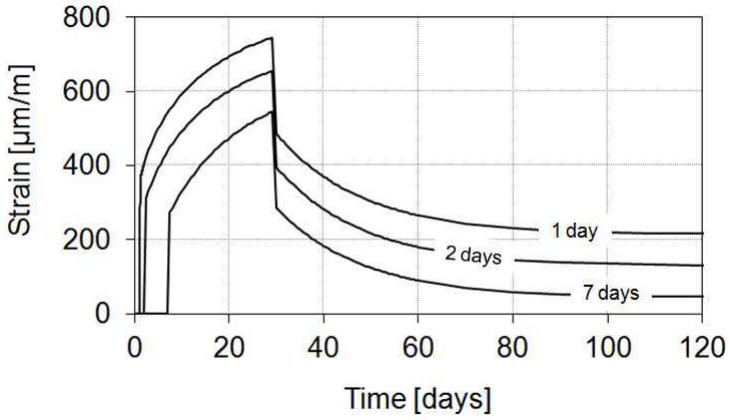

Figure 2.64 – Basic creep of three specimens loaded at 1 day, 2 days and 7 days respectively. The three specimens have been unloaded at 30 days.

In the second example three numerical analyses are performed: the three cylinders are loaded at 1 day, 2 days and 7 days respectively, and then unloaded at 30 days. This example is useful to evidence the effect of the degree of reaction and creep recovery. The specimens are assumed to be in sealed condition. ***Figure 2.64*** shows that the residual strain is more important when the cylinder is loaded at early age (1 day and 2 days).

In the actual version of the model the effect of temperature on creep is not considered but will be introduced in a future development of the model. Also the effect of aging on the creep properties of concrete must be investigated more in detail and taken into account in the definition of rheological model. Therefore, the present model needs to be enhanced regarding these two aspects of creep.

REFERENCES OF CHAPTER 2

Arthanari S and Yu C W 1967 Creep of concrete under uniaxial and biaxial stresses at elevated temperatures. *Mag. Concrete Res.* **19**(60) 149–156.

Baroghel-Bouny V, Chaussadent T, Croquette G, Divet L, Gawsewitch J, Godin J, Henry D, Platret G and Villain G 2002 Méthodes d'essai N±58. Caractéristiques microstructurales et propriétés relatives à la durabilité des bétons : Méthodes de mesure et d'essai de laboratoire *Coll. Techniques et Méthodes des Laboratoires des Ponts et Chaussées-LCPC.*

Baronghel-Bouny V and Mounanga P 2005 Effect of self-desiccation on autogenous deformation, microstructure and long-term hygral behaviour *Proceeding of the 4th Int. Seminar of Self-desication and its importance in concrete technology 20 June 2005 Gaithersburg, Maryland, USA* 21-48.

Bažant Z P, Hauggaard A B, Bawela S and Ulm F J 1997 Microprestress-solidification theory for concrete creep. I: aging and drying effect *Journal of Engineering Mechanics* **123**(11) 1188–1194.

Benboudjema F and Torrenti J M 2008 Early-age behaviour of concrete nuclear containments *Nuclear Engineering and Design* **238**(10) 2495-2506.

Briffaut M, Benboudjema F, Torrenti J-M and Nahas G 2011 A thermal active restrained shrinkage ring test to study the early age concrete behavior of massive structures *Cem. Conc. Res.* **41** 56-63.

Briffaut M, Benboudjema F, Torrenti J-M and Nahas G 2012 Analysis of semi-adiabiatic tests for the prediction of early-age behavior of massive concrete structures *Cement and Concrete Composites* **34**(5) 634-641.

Brooks J J 1989 Influence of mix proportions, plasticizers and superplasticizer on creep and drying shrinkage of concrete *Mag. Concr. Res.* **41**(148) 145-154.

De Schutter G and Taerwe L 1996 Degree of hydration based description of mechanical properties of early-age concrete *Materials and Structures* **29**(6) 335-344.

De Schutter G 2002 Finite element simulation of thermal cracking in massive hardening concrete elements using degree of hydration based material laws *Computers and Structures* **80** 2035-2042.

Diamond S 2004 The microstructure of cement paste and concrete - a visual primer *Cement and Concrete Research* **26**(8) 919-933.

Feldman R F and Sereda P J 1968 A model for hydrated Portland cement paste as deduced from sorption-length change and mechanical properties *Materials and Structures* **6** 509-519.

Gawin D, Pesavento F and Schrefler B A 2003 Modelling of hygro-thermal behaviour of concrete at high temperature with thermo-chemical and mechanical material degradation *Computer Methods in Applied Mechanics and Engineering* **192**(13–14) 1731-1771.

Gawin D, Pesavento F and Schrefler B A 2006 Hygro-thermo-chemo-mechanical modelling of concrete at early ages and beyond. Part I: Hydration and hygro-thermal phenomena. International *Journal for Numerical Method in Engineering* **67**(3) 299-331.

Gawin D, Pesavento F and Schrefler B A 2008 Modeling of cementitious materials exposed to isothermal calcium leaching, considering process kinetics and advective water flow. Part 1: Theoretical model International *Journal of Solids and Structures* **45**(25-26) 6221-6240.

Giertz-Hedstrom S 1938 The Physical Structure of Hydrated Cements *Proc. 2nd Int. Symp. Chem. Cements, Stockholm,* 505-534.

Gilkey - Discussion of paper by Gilkey H J 1961 Water/cement ratio versus strength – another look *J. Amer. Concr. Inst. - Part 2* **58** 1851-1878.

Glasser F P 1992 Progress in the immobilization of radioactive wastes in cement *Cement and Concrete Research* **22**(2-3) 201-216.

Guo Z H and Zhang X Q 1987 Investigation of complete stress-deformation curves for concrete in tension *ACI Material Journal* **86**(4) 278-285.

Hauggaard A B, Damkilde L and Hansen P F 1999 Transitional thermal creep of early age concrete *J. Eng. Mech.* **125**(4) 465-468.

Hearn N and Morley C T 1997 Self sealing property of concrete - experimental evidence *Materials and structures* **30** 404-411.

Jensen O M 1993 Autogenous deformation and RH-change, self-desiccation and self-desiccation shrinkage. *PhD thesis*. Building Materials Laboratory, Technical University of Denmark.

Jensen O M and Hansen P F 1996 Autogenous deformation and change of the relative humidity in silica fume-modified cement paste *ACI Mat J* **93**(6) 539-543.

Jensen O M and Hansen P F 2001 Water-entrained cement-based materials: I. Principles and theoretical background *Cement and Concrete Research* **31**(4) 647-654.

Jensen O M and Hansen P F 2002 Water-entrained cement-based materials: II. Experimental observations *Cement and Concrete Research* **32**(6) 973-978.

Jensen O M 2005 Autogenous phenomena in cement-based materials. University of Denmark.

Kishi T and Maekawa K 1994 Thermal and mechanical modelling of young concrete based on hydration process of multi-component cement materials *Thermal cracking in concrete at early age, Rilem Proceeding* **25** 11-19.

Klinkenberg L 1941 The permeability of porous media to liquids and gases *Am. Pet.Inst. Drilling and Production Practices* 200-213.

Lerch W and Bogue R H 1934 Heat of hydration of Portland cement pastes *J. Res. Nat. Bur. Stand.* **12**(5) 645-664.

Mainguy M, Coussy O and Boroghel-Bouny V 2001 Role of air pressure in drying of weakly permeable materials *Journal of Engineering Mechanics* **127**(6) 582-592.

Maney G A 1941 Concrete under sustained working loads: evidence that shrinkage dominates time yield *Proc. ASTM* **41** 1021-1030.

Mills R H 1966 *ACI – SP 60*, Washington.

Michaud P M, Georgin J F, Bissonnette B, Marchand J, Lory F, Perez F and Reynouard JM 2005 Importance de la distribution poreuse dans une approche milieu poreux de la prediction des deformations endogenes des betons *Septième édition des Journées scientifiques du Regroupement francophone pour la recherche et la formation sur le béton (RF)2B Toulouse, France 19-20 Juin 2006*.

Neville A M 1996 Properties of Concrete – Fouth Edition. Pearson, Edinburgh.

Neville A M 1959 Creep recovery of mortars made with different cements *J. Amer. Concr. Inst.* **56** 167-174.

Nielsen L F 1993 Strength development in hardened cement paste: examination of some empirical equations *Materials and Structures* **26**(159) 255-260.

Pesavento F, Gawin D, Wyrzykowski M, Schrefler B A, Simoni L 2012 Modeling alkali–silica reaction in non-isothermal, partially saturated cement based materials *Computer Methods in Applied Mechanics and Engineering*, **225**/**228** (June 15, 2012) 95-115.

Pickett G 1942 The effect of change in moisture content on the creep of concrete under a sustained load *ACI J.* **38** 333-355.

Powers T C 1947 A Discussion of Cement Hydration in Relation to the Curing of Concrete *Bulletin 25, Research Laboratories of the Portland Cement Association*, Chicago.

Powers T C 1949 The non-evaporable water content of hardened Portland cement paste: its significance for concrete research and its method of determination *ASTM Bul. May 1949* **158** 68-76.

Powers T C 1958 Structure and physical properties of hardened portland cement paste *J. Amer. Ceramic Soc.* **41** 1-6.

Powers T C 1960 Physical properties of cement paste. *Proceedings of the Fourth International Symposium on the Chemistry of Cement, Washington, DC* **V**-1 577-613.

Regourd M and Gauthier E 1980 Comportement des ciments soumis au durcissement acceleré *Annales de I'ITBTP* **179** 65-96.

Schindler A K 2004 Effect of temperature on hydration of cementitious materials *ACI Materials Journal* **101**(1) 72-81.

Scrivener K L and Gariner E R 1988 Microstructural gradients in cement paste around aggregate particles *Materials Research Symposium Proc.* **114** 77-85.

Sciumè G Schrefler B A and Pesavento F 2012a Thermo-hygro-chemo-mechanical modeling of the behavior of a massive beam with restrained shrinkage *Proceedings of RILEM-JCI international workshop on crack control of mass concrete and related issues concerning early-age of concrete structures* 133-144.

Sciumè G, Benboudjema F, De Sa C, Pesavento F, Berthaud Y and Schrefler B A 2012b A multiphysics model for concrete at early age applied to repairs problems *Engineering Structures*.

Singh B G 1958 Specific surface of aggregates related to compressive and flexural strength of concrete *J. Amer. Concr. Inst.* **54** 897-907.

Taplin J M 1957 A method of following the hydration reaction in Portland cement paste *Australian Journal of Applied Science* **10** (3) 329-345.

Thiery M, Baroghel-Bouny V, Bourneton N, Villain G and Stefani C 2007 Modélisation du séchage des bétons: analyses des différent modes de transfert hydrique *Revue Européenne de Genie Civil* **11**(5) 541-577.

Thiery M 2000 Etude de la durabilité liée aux transferts gazeux pour deux bétons très différents *Rapport de recherche* Division bétons et composites cimentaires, Laboratoire Central des Ponts et Chaussées.

Troxell G E, Raphael J M and Davis R E 1958 Long-time creep and shrinkage tests of plain and reinforced concrete *Proc. ASTM* **58** 1101-1120.

Villain G, Baroghel-Bouny V, Kounkou C and Hua C 2001 Mesure de la perméabilité aux gaz en fonction du taux de saturation des bétons *Revue Française de Génie Civil* **5**(2-3) 251-268.

Waller V 1999 Relations entre la composition des bétons, exothermie en cours de prise et résistance en compression *PhD Thesis* Ecole Nationale des Ponts et Chaussées, Paris.

Wang P T, Shah S P and Naaman A E 1978 Stress-strain curves of normal and lightweight concrete in compression *J. Amer. Concr. Inst.* **75** 603-611.

Winslow D and Ding Liu 1990 The pore structure of paste in concrete *Cement and Concrete Research* **20**(2) 227-284.

3 VALIDATION OF THE MODEL: TWO REAL APPLICATION CASES

3.1 INTRODUCTION

In the first chapter the mathematical model of concrete at early age, the associated constitutive equations, and its numerical solution have been presented. Then, in the second chapter the complex behavior of concrete has been analyzed more in detail. Also, the developed model is used to perform numerical analyses of simple cases and the obtained results are commented and compared qualitatively with the experimental data of literature[7].

Within this third chapter the model is validated through its application to two real cases: a massive beam specimen with restrained shrinkage, and two repaired beams (one repaired using an ordinary concrete, OC, the other using a fiber reinforced ultra-high-performance concrete, UHPC).

3.2 THE CONCRACK BENCHMARK

ConCrack has been an international benchmark for Control of Cracking in reinforced concrete structures. This benchmark is part of the national French project CEOS (*Comportement et Evaluation des Ouvrages Speciaux vis-à-vis de la fissuration et du retrait*) dedicated to the analysis of the behaviour of special construction works concerning cracking and shrinkage. The modeled structure is a large beam specimen with

[7] The experimental results of Chapter 2 are principally taken from Neville (1996).

restrained shrinkage (***Figures 3.1, 3.2*** and ***3.3***). This test deals with the cracking occurring at early age under THM loading and its influence on the mechanical behavior of the structure. The massive structure has a special form and the contraction of the central part is restrained by two metallic struts which induce cracking at early age.

We can divide the test in three phases.

i) During two days after the casting the structure is protected from drying and thermally isolated. Therefore, the structure is first subjected to a THM loading (self-desiccation and temperature elevation due to hydration).

ii) After these two days the isolation and the formwork are removed and the structure is conserved during 2 months in the environment. During these 2 months environmental temperature and relative humidity have been measured.

iii) Finally, subsequent to this THM test, the structure has been submitted to a static bending test.

During the hardening stage (phases i) and ii)) the beam was instrumented by: temperature sensors, vibrating cord sensors for local internal and external deformation, internal and external optical fibre sensor, electrical strain gauges placed on reinforcement bars. Moreover, during the bending test (phase iii)), also load and displacement sensors, acoustic sensors and an image correlation technique on a lateral face have been used.

Figure 3.1 - 3D specimen model (a). Photo of the specimen after the removal of formwork and thermal isolation (b). Images from ConCrack home page

The test process has followed this schedule:

- 07 April 2010, 10:30: beginning of the casting (T_{ini} concrete = 17°C);
- 07 April 2010, 12:00: end of the casting;
- 09 April 2010, 9:00: prestressing of the “heads” of the structure;
- 09 April 2010, 10:00: removing of the isolation and the formwork on all the faces;
- 06 June 2010: static bending test;

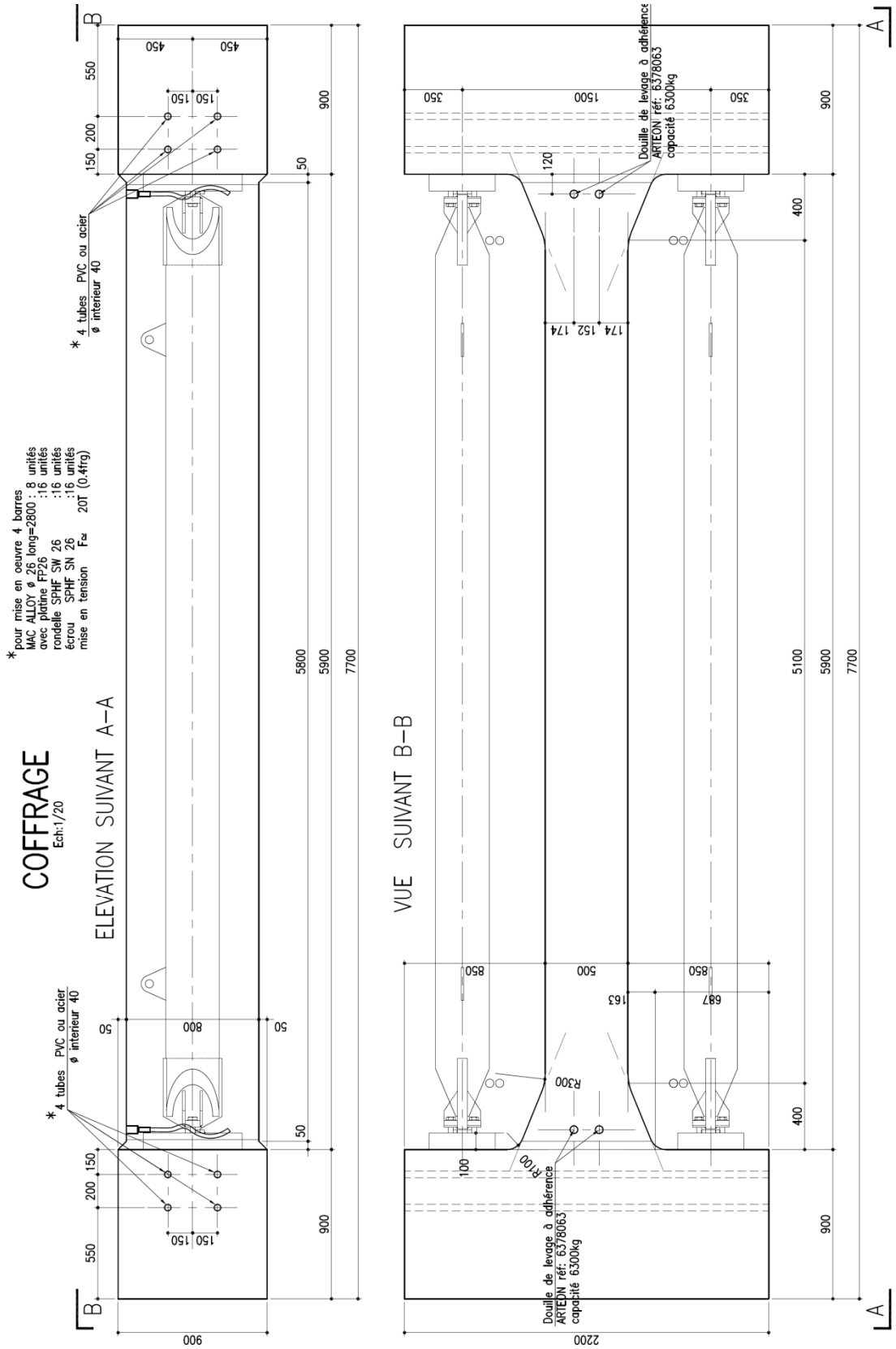

Figure 3.2 - Geometry of the specimen (ConCrack website 2010)

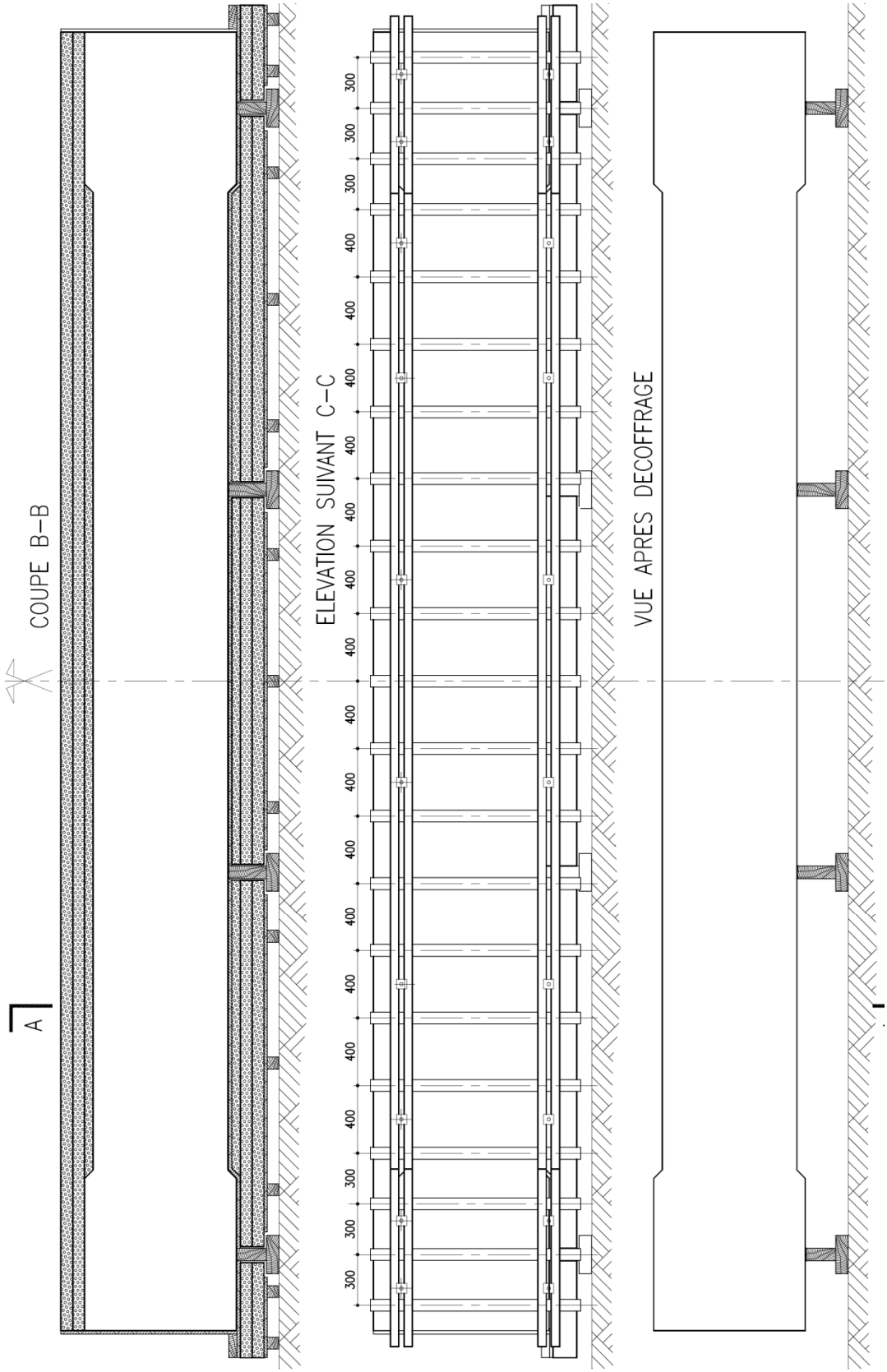

Figure 3.3 - Formwork and thermal isolation (ConCrack website 2010)

3.2.1 Identification of the model parameters

The concrete used in the analyzed structure is a C50/60 concrete cast with a CEM I 52.5N cement. The composition is given in the following table:

Table 3.1 - Mix design of the concrete used in the calculation

CONSTITUENTS	**Quantities (kg/m3)**
CEM I 52,5N CE CP2 NF Couvrot	400
Sand 0/4 GSM LGP	785
Gravel 4/20 GSM LGP	980
Superplastifiant Axim 4019	5.4
Total water	185

Several tests have been performed by the benchmark organizers[8] to characterize the concrete used to cast the beam. These tests are used to identify the input parameters of the numerical model.

Hydration adiabatic test. The hydration adiabatic test has the objective to follow the concrete's temperature during the cast and maturation phase. The fresh concrete has been placed in a 300 mm sealed cubic container, thermally isolated (adiabatic conditions).

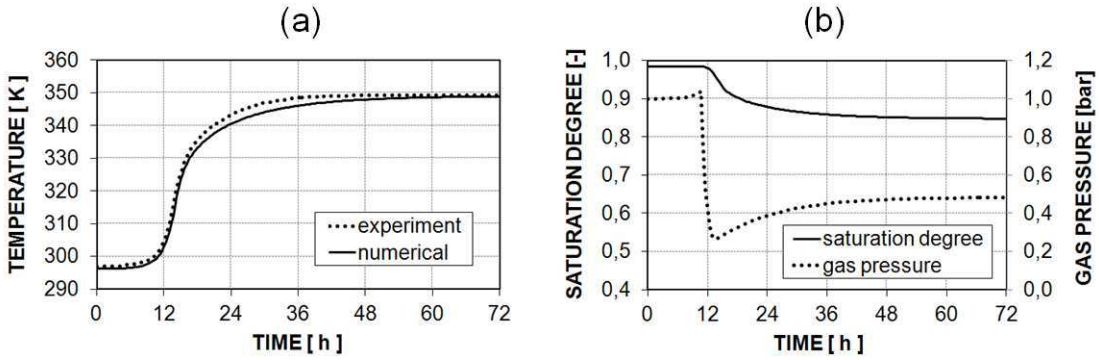

Figure 3.4 - Results of the hydration adiabatic test. Adiabatic temperature (a). Numerical results for the gas pressure and the saturation degree (b)

There is good agreement between the experimentally measured temperature and the numerical one (see ***Figure 3.4.a***). The only available experimental result is the temperature, but the numerical simulation gives also the expected evolution of the saturation degree and of the gas pressure during the adiabatic test. The cement's hydration is accompanied by a decrease in volume which is equal to about 8,7% of the formed

[8] All the experimental results shown within this paragraph have been obtained by the organizers of ConCrack.

hydrates volume (LeChâtelier, 1900). Before the development of a rigid mineral skeleton, this contraction produces only a small decrease in the external volume of cement paste. After the transition from semi-fluid state to semi-solid state ($\Gamma > \Gamma_0$), the decrease in volume due to hydration is incompatible with the admissible deformation of the solid skeleton. Therefore in the capillary pores initially almost saturated by water, the volume of gas increases and consequently the gas pressure shuts down (see ***Figure 3.4.b***). The decrease of the saturation degree causes the autogenous shrinkage. The stoichiometric approach used in the mathematical formulation of the hydration model allows to compute the autogenous shrinkage mechanically without the introduction of additional constitutive equations.

Loss of mass and shrinkage test. Autogenous and total shrinkage are determined by a refractometer with 70x70x280 mm specimens. Three specimens have been made up for each kind of shrinkage.

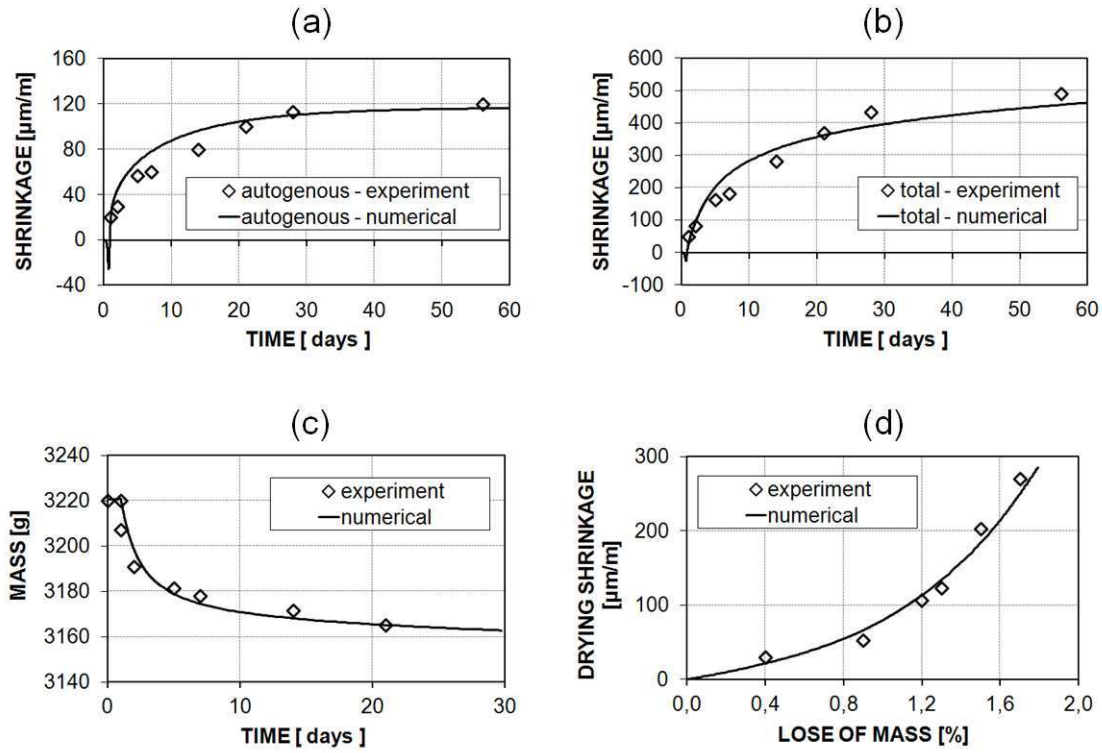

Figure 3.5 - Comparison of the simulation results with the experimental data for: autogenous shrinkage (a); total shrinkage (b); loss of mass (c); loss-of-mass *versus* drying-shrinkage curve (d).

After the cast, the specimens have been protected by a plastic film and kept at 20° for the first 24 hours. Then the specimens have been removed of their form and transported to the laboratory. The autogenous shrinkage has been measured without water exchange

between the specimen and the environment. For the total shrinkage, the specimens are subjected to the environmental conditions of the laboratory (20°C and 50±5% RH). For the specimen subjected to the desiccation, the loss of water mass has also been measured. Experimental and numerical results are shown in ***Figure 3.5***.

Mechanical properties during hydration. The mechanical properties of concrete have been measured at several ages in order to investigate their variation during hydration. ***Figures 3.6-a-b*** show the good agreement between experimental measures and numerical results.

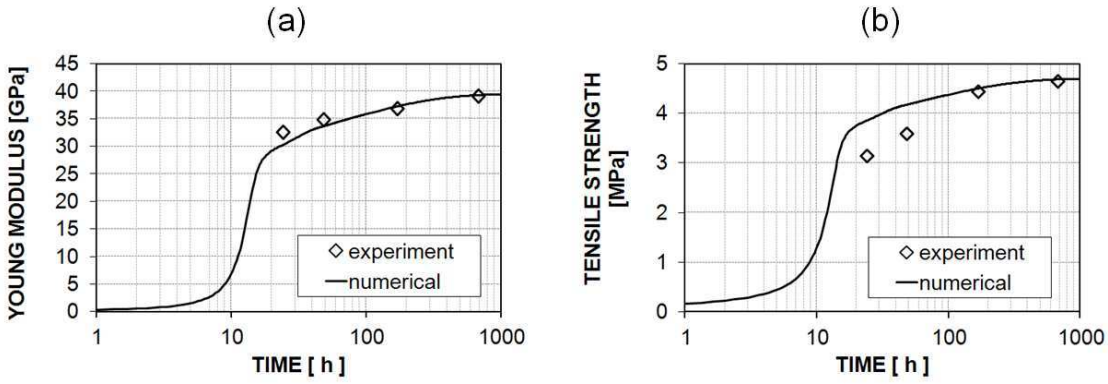

Figure 3.6 - Evolution of Young's modulus (a), and tensile strength (b) during hydration

Viscous properties. To investigate the delayed behaviour of concrete some cylindrical 110x220 mm specimens were cast in the laboratory (initial temperature 17.3°C) and saved at 20°C.

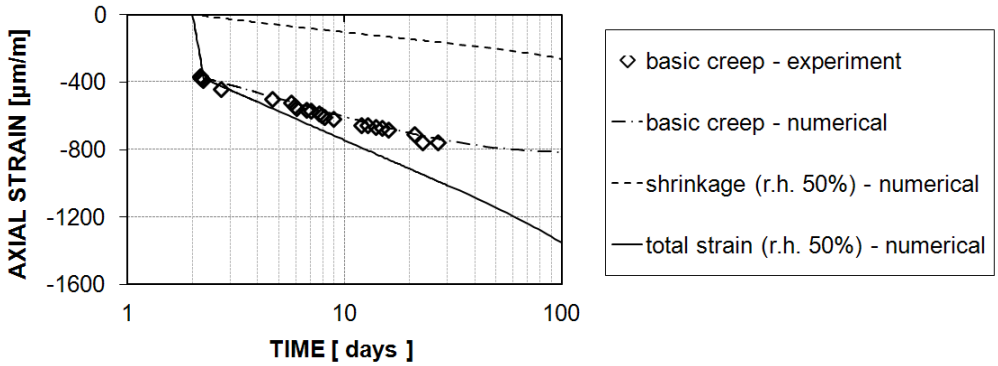

Figure 3.7 - Comparison of the simulation results with the experimental data for the creep test

After 48 hours, they have been loaded at 60% of the compressive strength measured on the specimens (Rc = 20.3 MPa => load = 12.2MPa). The test was performed without water interchange between the specimen and the environment (basic creep). The delayed

creep deformation has been calculated by deduction of the instantaneous elastic strain from the total strain measured. The experimental and numerical results are shown in ***Figure 3.7***.

A lot of parameters are needed to model the beam. Some of these are given by the literature, others, as for instance those of the porosity function are given by stoichiometry, and the remains parameters are identified *via* the previous presented experiments. In the following table the main identified parameters are reported.

Table 3.2 - Main input parameters

PARAMETERS	**SYMBOL**	**UNIT**	**CEOS$_{concrete}$**
Thermal conductivity (dry)	λ_{eff}	[W/mK]	1.5
Heat of hydration	L_{hydr}	[MJ/m^3]	117
Activation energy	E_a/R	[K]	5369
Parameter A_i in Equ. (1.31)	A_i	[1/s]	0.15
Parameter A_P in Equ. (1.31)	A_P	[1/s]	1350
Parameter Γ_P in Equ. (1.31)	Γ_P	[-]	0.215
Parameter ζ in Equ. (1.31)	ζ	[-]	71
Mechanical percolation threshold	Γ_0	[-]	0.1
Porosity (final i.e. for Γ= 1)	n_∞	[-]	0.13
Biot's coefficient (final i.e. for Γ= 1)	$\bar{\alpha}_\infty$	[-]	0.33
Intrinsic permeability (final i.e. for Γ= 1)	K_∞	[m^2]	$6 \cdot 10^{-22}$
Parameter a in Equ. (1.52)	a	[MPa]	23
Parameter b in Equ. (1.52)	b	[-]	2.1
Parameter c_Γ in Equ. (1.52)	c_Γ	[-]	1.1
Parameter Γi in Equ. (1.52)	Γ_i	[-]	0.1
Young modulus (final i.e. for Γ= 1)	E_∞	[GPa]	39.4
Tensile strength (final i.e. for Γ= 1)	$f_{t\infty}$	[MPa]	4.65
Poisson ratio (final i.e. for Γ= 1)	ν_∞	[-]	0.19
Creep cell 1: spring (final i.e. for Γ= 1)	$k_{bc1\infty}$	[GPa]	24
Creep cell 1: retardation time	τ_{bc1}	days	20
Creep cell 3: drying creep coeff.	δ_{dc}	[m^2/(Pa·kg)]	1.0×10^{-10}

3.2.2 Finite element mesh of the structure and boundary conditions

The mesh of concrete consists of 3D elements (***Figure 3.8***). To model the steel, truss elements rigidly linked with the concrete 3D mesh are used. Two truss elements are also used to model the two struts that contrast shrinkage. The boundary conditions are

assumed to be of convective type for both heat and mass exchange. Thus, the convective heat flux $\boldsymbol{q}_t$ (Wm^{-2}) and convective water mass flux $\boldsymbol{q}_h$ ($kg\ s^{-1}\ m^{-2}$) are defined as:

$$\mathbf{q}_t = \varphi_t \left(T_s - T_{ext}\right)\mathbf{n} \qquad \mathbf{q}_h = \varphi_h \left(p_s^c - p_{ext*}^c\right)\mathbf{n} \tag{3.1}$$

where φ_t and φ_h are the thermal and hygral convective coefficients, T_s is the temperature on the surface, T_{ext} is the ambient temperature, $p^c{}_s$ is the capillary pressure on the surface, $p^c{}_{ext*}$ is a fictitious capillary pressure related to the ambient relative humidity and temperature (calculated using the Kelvin equation), and **n** is the unit vector normal to the surface (oriented towards the exterior).

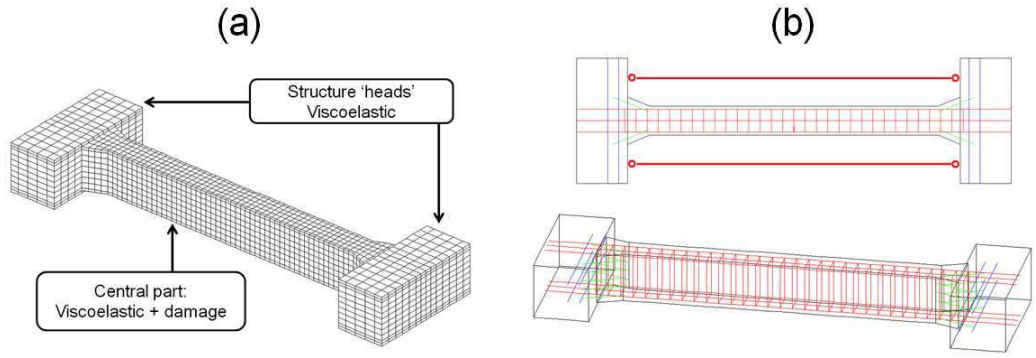

Figure 3.8 - Finite elements mesh of concrete (a). Mesh of reinforcement bars (b)

According with the real conditions of the test three phases are considered:

Phase1: structure isolated. For the thermal part, we use two different equivalent convective coefficients (0,73 W $K^{-1}m^{-2}$ and 3,9 W $K^{-1}m^{-2}$), in this way we can take into account the thermal bridge of the lateral isolation (see ***Figure 3.9***). For the hygral part, we assume sealed conditions.

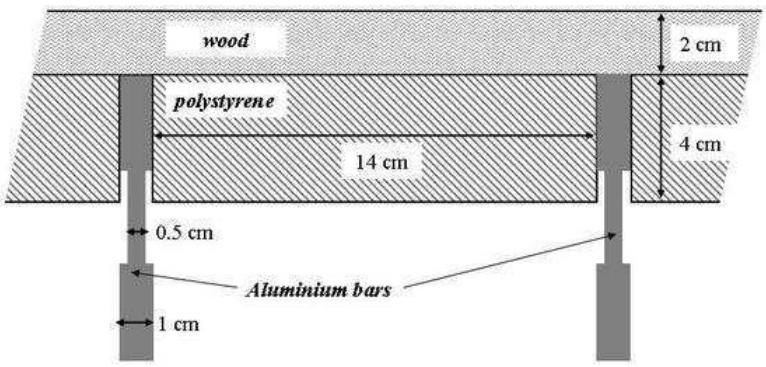

Figure 3.9 - Drawing of lateral isolation interrupted by formwork reinforcements (ConCrack website 2010).

Phase2: structure in the environment. For the thermal part, we pass at a uniform thermal convective coefficient (10,0 W $K^{-1}m^{-2}$) and we take into account also solar irradiation. For the hygral part, we use a hygral convective coefficient set to 5.e-14 kg s^{-1} m^{-2} Pa^{-1}.

Phase3: four point bending test. After 60 days the structure is submitted to a four points bending test.

3.2.3 Thermo-hygro-chemical results

During the test, the temperature has been measured in several point of the specimen. For the first phase (structure isolated) to take into account the thermal bridge of the lateral isolation, two different equivalent convective coefficients (0,73 W $K^{-1}m^{-2}$ and 3,9 W $K^{-1}m^{-2}$) are used. For the hygral part sealed conditions are assumed.

For the second phase a uniform thermal convective coefficient (10 W $K^{-1}m^{-2}$) is used and solar radiation is taken into account. To compute the convective water mass flux the hygral convective coefficient is set equal to 5e-14 kg s^{-1} m^{-2} Pa^{-1}.

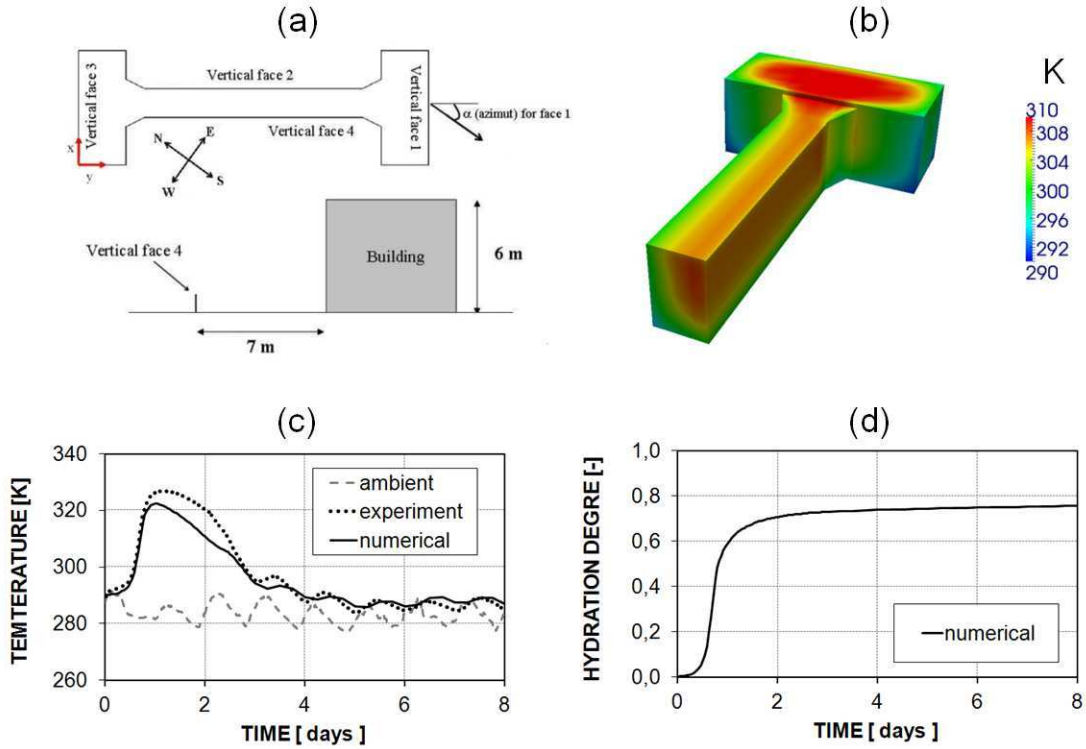

Figure 3.10 - Specimen orientation and surrounding (a). Temperature after 2,25 days (b). Temperature in the central point of the beam (c). Hydration degree in the central point of the beam (d)

3.2.4 Mechanical results and four point bending test

During the first and second phases the longitudinal displacements of the specimen are globally restrained by the two metallic struts. During hydration the thermal extension of

concrete is restrained and so in this phase the beam is axially compressed. Then, when hydration is ended the thermal and hygral contractions of the beam, due to the decrease of temperature and to autogenous and drying shrinkage, are contrasted and this generates tensile stresses and localized and diffuse cracks. In ***Figure 3.11.b*** the relative displacement between the points C and D is shown (see ***Figure 3.11.a***, for the position of the two points).

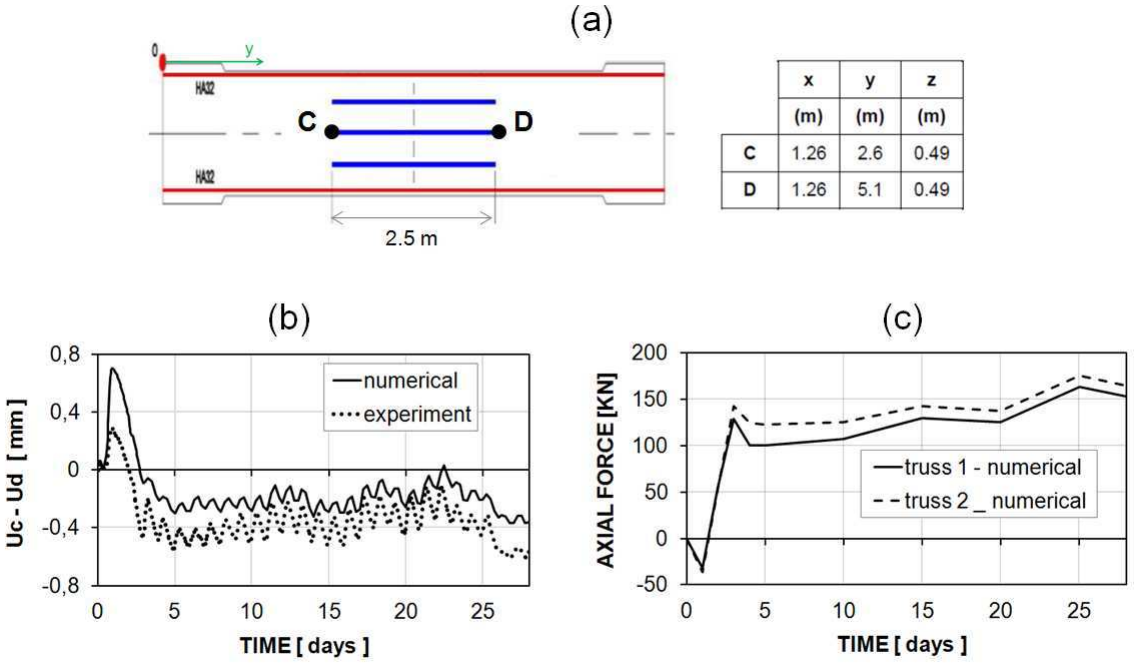

	x (m)	y (m)	z (m)
C	1.26	2.6	0.49
D	1.26	5.1	0.49

Figure 3.11 - Position of the points C and D where the relative displacement is measured (a); Relative displacement between the point C and D (b). Numerical results for the axial force in the two metallic truss which restrain shrinkage (positive values indicate compression) (c).

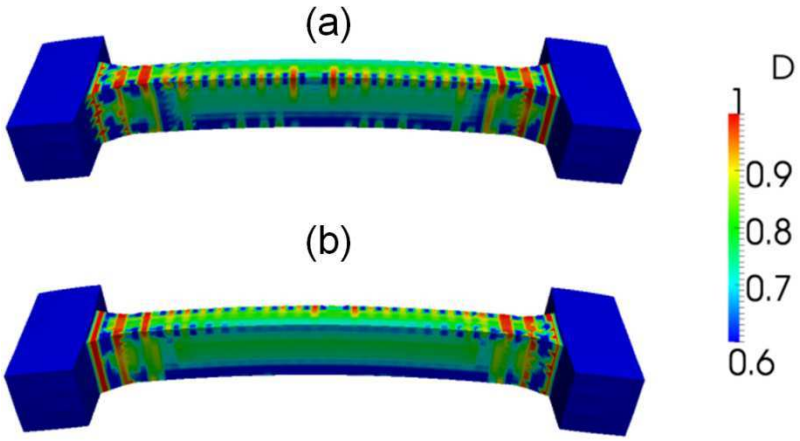

Figure 3.12 - Deformed configuration (× 500) and damage after 60 days. Face exposed to the sun (a) and face not exposed to the sun (b)

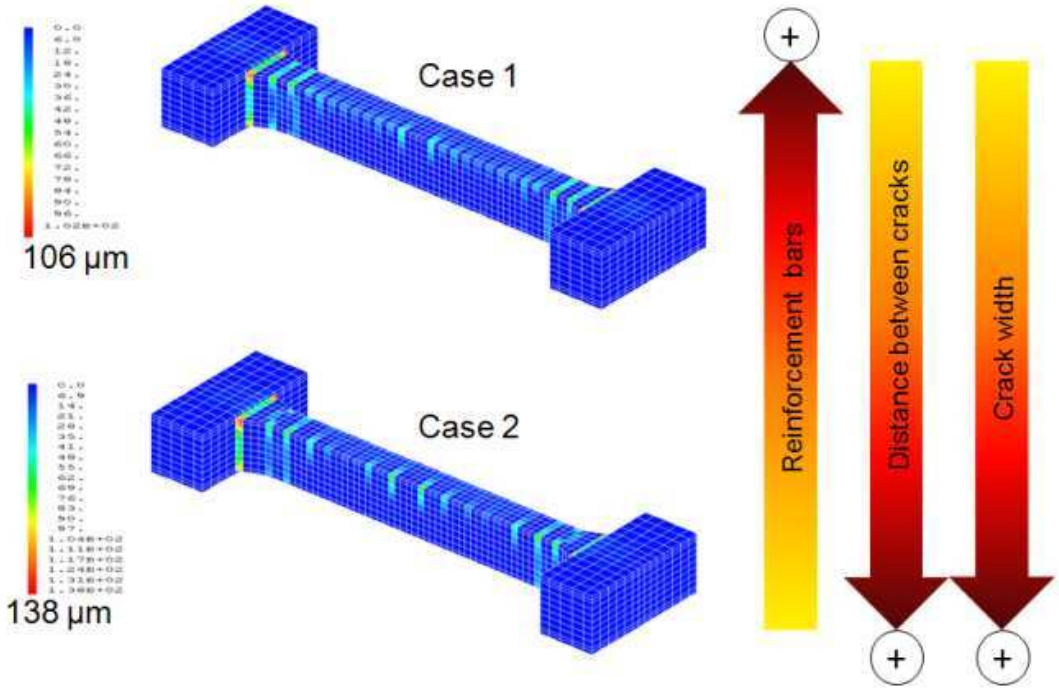

Figure 3.13 - Estimation of cracks width two months after the cast for two specimens with different amount of longitudinal bars reinforcement. Specimen 1 more reinforced than specimen 2.

In ***Figure 3.11.c*** the axial forces obtained numerically in the two metallic struts are shown over time; these forces are different because the boundary conditions are not symmetric due to the solar radiation. This asymmetry of the solution is clearly visible also in ***Figure 3.12*** where damage after 60 days is depicted.

Figure 3.13 shows the cracks' width two months after the cast for two specimens with different amount of longitudinal bars reinforcement. When the structure is more reinforced, case 1 in ***Figure 3.13***, the distance between the cracks is smaller but also the cracks widths are generally smaller than in case 2.

After two months a static four point bending test until rupture has been carried out. Compression will be assured by eight jacks and live controlled by a pressure sensor with an independent data registration system. The load is applied with increments of 50kN and each loading step is kept during 20 min. For more details on the analyzed test see the reference web page of the benchmark (Concrack website, 2010). In ***Figure 3.14.a*** the experimental crack pattern is compared with that obtained numerically; a good agreement can be observed especially in the central part of the beam.

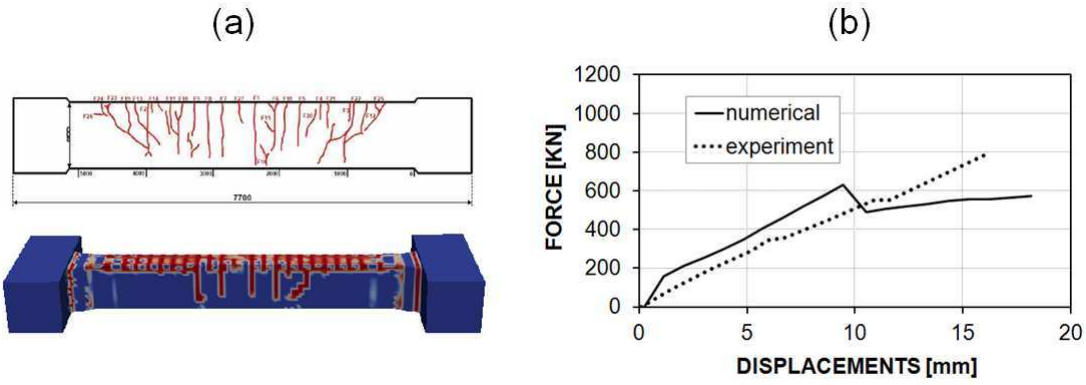

Figure 3.14 - Comparison between the numerical and experimental crack pattern (a). Curve force vs displacements during the bending test (b).

3.3 APPLICATION TO REPAIRS OF CONCRETE STRUCTURES

Concrete, even if exposed to aggressive environments, can have a service life of 50 years or longer. However, due to workmanship or design errors and to the current fast construction methods, some concrete structures being built in the past and today may require repairs after as few as 5 years of service; also change of environmental conditions, not taken into account during the dimensioning process, may induce extensive cracking. For example, the total cost for repair, strengthening, and protection of the concrete structures in the U.S. represents $18 to $21 billion a year (Emmons and Sordyl, 2006).

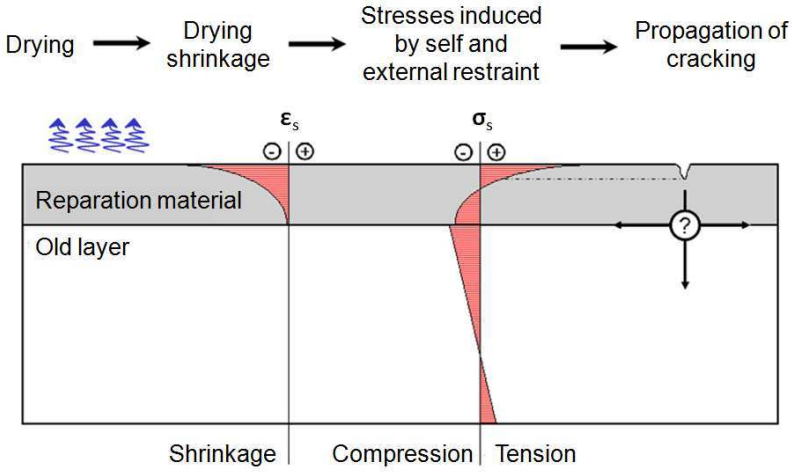

Figure 3.15 - Drying cracking due to self and external restraint in a reparation (adapted from Molez, 2003)

During the last twenty years great progress has been achieved in the study and development of special mortars and concretes for the repairs of damaged concrete structures. The main modes of failure in repair/substrate systems are tensile cracking

through the thickness and peeling or shearing at the interface between both materials (Mauroux *et al.* 2012, Molez L. 2003, Emmons *et al.* 1994, Cusson *et al.* 1996, Saucier *et al.* 1997): internal stresses and cracking may be induced by the differential shrinkage between the reparation layer and the repaired material. Indeed, the development at early age of the aforementioned stress state is very complex and heterogeneous in the mortar thickness (***Figure 3.15***) due to the combination of several phenomena, such as hydration, drying, evolution of mechanical properties, creep. Therefore, a good compatibility between both materials has to be achieved for a durable repair: low shrinkage and Young's modulus, great tensile strength and creep strains in tension, especially.

Lots of experimental studies can be found in the literature on the durability of repairs regarding: i) characterization of material properties involved in cracking process by differential shrinkage: autogeneous and drying shrinkage, basic and drying creep (in particular in tension), Young's modulus and tensile strength evolutions, influence of fibers, quality of adhesion (Bissonnette *et al*., 1995 and 1999); ii) development of devices to analyze the behavior of repaired systems. One example is the ring-test, which consists in casting a mortar ring around a metallic ring (modeling the substrate rigidity) for the determination of stresses induced by strain incompatibilities during hardening in the reparation material (Hossain *et al.* 2006, Bentur *et al*. 2003, Briffaut *et al.* 2011). Besides, several authors designed "real" systems (beams for instance). Experiments are performed in laboratory conditions (temperature and relative humidity, mechanical boundary conditions) which may be controlled or not. Since, all phenomena involved in cracking by differential shrinkages are strongly dependent on these conditions, but also on specimen size, such approaches and results cannot be easily transposed to any other conditions. Hence the experimental approaches can typically introduce errors when changing from laboratory specimens to real repairs cases. A predictive (numerical) model, which takes into account all complex phenomena involved (hydration, drying, shrinkages, creeps, cracking, etc.) needs to be used for such a goal.

The purpose is to show that the developed numerical model is useful for the analysis of the thermo-hygro-chemo-mechanical behaviour of repairs, taking into account the history of the repaired material (drying, hydration, shrinkages, creeps, cracking), realistic casting and environmental conditions. A numerical tool to predict the expected behavior of the repairs would be of great help for the industry allowing it to improve repair materials and to design optimal and durable repair solutions.

Two repaired beams analyzed experimentally by Bastien Masse (2010) are modeled. The experimental data are used to identify the material parameters; most of these have been measured, and all tests have been performed in well controlled conditions.

3.3.1 Identification of the model parameters

The beams were repaired using two different concretes: an ordinary concrete (OC) and an ultra-high performance fiber reinforced concrete (UHPC). The mix of the two concretes used for the repairs is reported in ***Table 3.3***.

Table 3.3 - Formwork and thermal isolation data

CONSTITUENT	UNIT	OC	UHPC
Cement	[kg/m^3]	276	1007
Silica fume	[kg/m^3]	24	252
Gravel	[kg/m^3]	980	-
Sand	[kg/m^3]	875	600
Water	[L/m^3]	184	225
Superplasticizer	[L/m^3]	2.50	42
Steel fibers (10 mm)	[% vol.]	-	4

To predict correctly the behavior of a concrete structural repair the knowledge of the material properties, in particular those of the restoration materials is essential. An exhaustive experimental analysis to identify the properties of the two repair concretes (shrinkage, Young's modulus, tensile strength, creep, etc.) has been carried out by Bastien Masse (2010). On the other hand for the concrete used to cast the beams only the mechanical properties have been measured. Being this concrete very similar (in term of mix design) to the ordinary concrete (OC), the choice is to assume the unknown properties equal to those of OC.

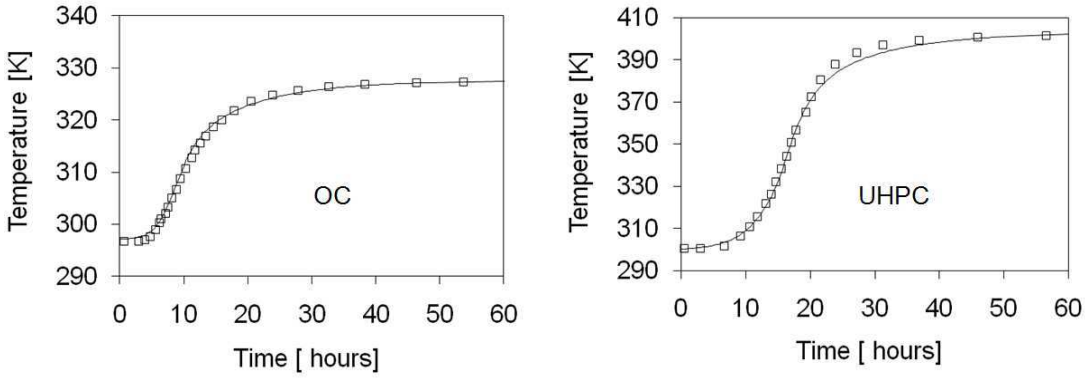

Figure 3.16 - Adiabatic calorimetry test for the two repair concretes. Experimental (open symbols) and numerical results (solid lines)

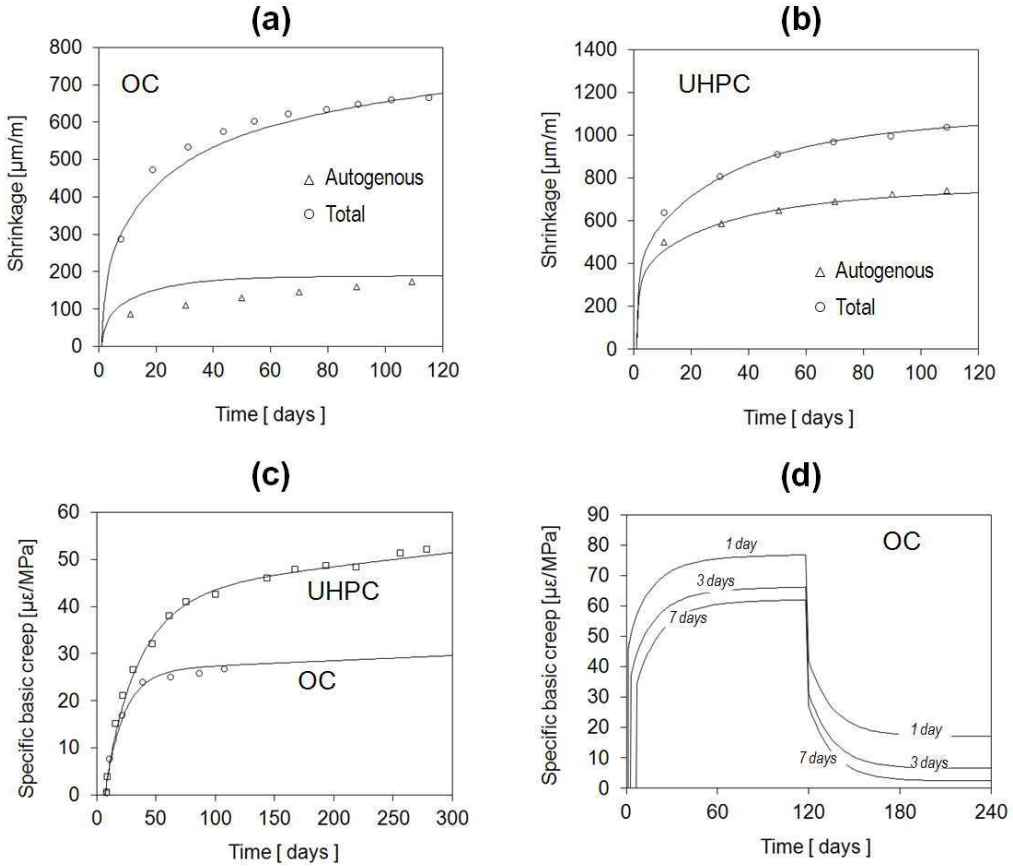

Figure 3.17 - Shrinkage (a,b) and creep tests (c,d): experimental (open symbols) and numerical results (solid lines) for the two repair concretes

The hydration parameters are identified via semi-adiabatic calorimetry: the fresh concrete is placed in a quasi-adiabatic calorimeter and during six days the evolution of the temperature is measured (the temperature of the laboratory is 23°C ± 1°C). From the measured temperatures, knowing the calorimeter heat loss, it is possible to compute the adiabatic temperature (open symbols in ***Figure 3.16***). ***Figure 3.16*** shows also the numerical results (solid lines) of the adiabatic calorimetry for the two repair concretes, and their fine agreement with the experiments.

Measuring shrinkage is very important because it is the first cause of repairs' cracking (which reduce the service life). The total shrinkage and the autogenous shrinkage have been measured in for both the repair concretes (open symbols in ***Figures 3.17.a-b***). Concerning the UHPC, due to the low water/cement ratio and its high cement content, ***Figure 3.17.b*** shows that the autogenous shrinkage is relevant and is larger than the drying shrinkage (difference between the total shrinkage and autogenous one). Globally the UHPC has a total shrinkage potential (autogenous + drying shrinkage) almost 1.5 times bigger than the OC.

Table 3.4 - Parameters of the two concretes used for the repairs.

PARAMETERS	**SYMBOL**	**UNIT**	**OC_{repair}**	**$UHPC_{repair}$**
Thermal conductivity (dry)	λ_{eff}	[W/mK]	1.5	1.95
Heat of hydration	L_{hydr}	[MJ/m^3]	64	230
Activation energy	E_a/R	[K]	5000	4500
Parameter A_i in Equ. (1.31)	A_i	[1/s]	10	2.0
Parameter A_P in Equ. (1.31)	A_P	[1/s]	340	17.5
Parameter Γ_P in Equ. (1.31)	Γ_P	[-]	0.16	0.13
Parameter ζ in Equ. (1.31)	ζ	[-]	16	18
Mechanical percolation threshold	Γ_0	[-]	0.1	0.1
Porosity (when Γ= 1)	n_∞	[-]	0.1439	0.2071
Intrinsic permeability (when Γ= 1)	K_∞	[m^2]	8×10^{-21}	2.8×10^{-22}
Parameter a in Equ. (1.52)	a	[MPa]	17.00	58.04
Parameter b in Equ. (1.52)	b	[-]	2.4	2.11
Parameter c_Γ in Equ. (1.52)	c_Γ	[-]	1.50	1.50
Parameter Γi in Equ. (1.52)	Γ_i	[-]	0.20	0.20
Biot coefficient (when Γ= 1)	$\overline{\alpha}_\infty$	[-]	0.68	0.36
Young modulus (when Γ= 1)	E_∞	[GPa]	30	36
Tensile strength (when Γ= 1)	$f_{t\infty}$	[MPa]	3.0	11.0
Poisson ratio (when Γ= 1)	ν_∞	[-]	0.20	0.25
Parameter β_{cr} in Equ. (1.82)	β_{cr}	[-]	0.35	0.35
Creep cell 1: spring (when Γ= 1)	$k_{bc1\infty}$	[GPa]	38	37
Creep cell 1: retardation time	τ_{bc1}	days	16	35
Creep cell 2: dashpot (when Γ= 1)	η_{bc2}	[GPa·days]	9.3×10^4	3.5×10^4
Creep cell 3: drying creep coeff.	δ_{dc}	[m^2/(Pa·kg)]	3×10^{-11}	1×10^{-12}

In ***Figures 3.17.a-b*** the numerical results are also reported (solid lines). ***Figures 3.17.c*** shows the results of the basic creep test for the OC and the UHPC. The specimens have been charged in compression at 7 days with two different loads; to simplify the comparison the experimental and numerical results are shown in ***Figure 3.17.c*** in term of specific creep. Also ***Figures 3.17.d*** shows the numerical results for three OC specimens charged at 1, 3 and 7 days and discharged at 120 days. The specific creep potential and the residual strains (after unloading) are higher when the specimen is charged at 1 and 3 days as clearly shown in the figure. This typical behavior due to the evolution of the main mechanical properties during hydration is taken care in the model via the evolution of the Young's modulus $E(\Gamma)$(eqn (1.65)) and of the stiffness of the spring of the first creep cell $k_{bc1}(\Gamma)$ (eqn (1.71)).

The described experiments test are used to calibrate the numerical model and the identified input parameters are summarized in ***Table 3.4***.

3.3.2 Modeling of the two repaired beam and of the reference one

Once the model parameters have been identified, the numerical simulation of the thermo-hygro-mechanical behavior of the two repaired beams can be performed. The geometry of the beams is represented in ***Figure 3.18***.

For the experiment, three identical reinforced beams were cast. Two of these beams, after the hydrodemolition of 30 mm of the upper part, had been repaired: one using the ordinary concrete (OC) and the other using the ultra-high performance fiber reinforced concrete (UHPC). The third beam is the reference specimen. Two fiber-optic sensors (FO-h and FO-b) were placed inside the beams.

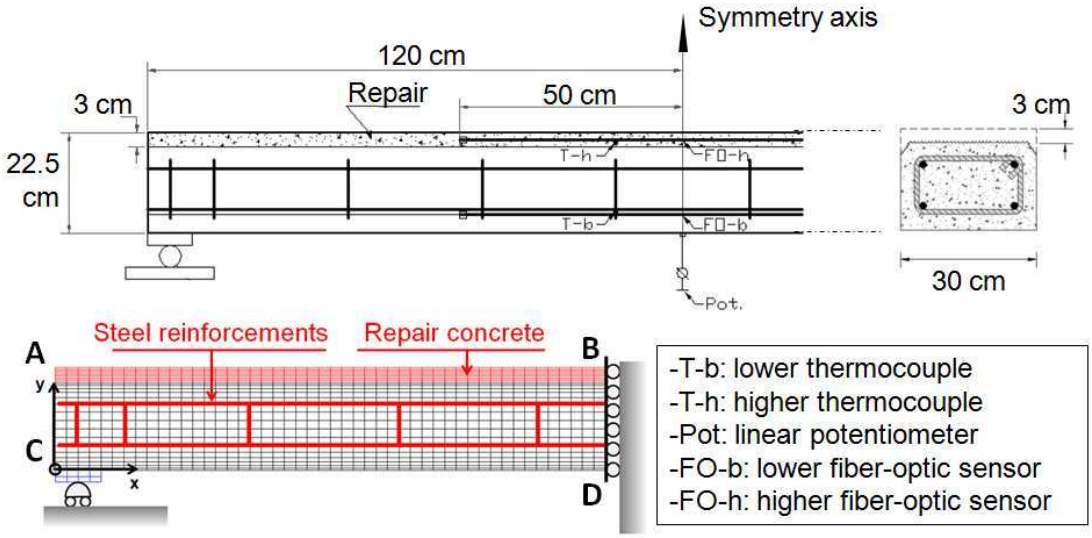

Figure 3.18 - Geometry of the repaired beams (readapted from Bastien Masse, 2010) and associate finite element mesh

The experiment was realized in a laboratory with controlled environmental conditions (22 ± 2 °C and 50 ± 5 % of relative humidity). The fresh concrete of the repairs has been cured and protected from drying during the first 90 hours. The lateral surfaces of the beams had been covered using a resin so that the case can be analyzed in 2D plane stress (the lateral surfaces were not thermally isolated, but the thermal aspect has not a critical impact on thin repairs). The 2D F.E. mesh of the concrete consists of 1200 plate elements. To model the reinforcements, beam elements rigidly linked with the concrete mesh are used. The nodes of the mesh of the reinforcement bars have the same spatial position of those of the concrete mesh.

For temperature T and capillary pressure p^c the boundary conditions are assumed to be of convective type. The convective heat flux $\mathbf{q_t}$ (Wm^{-2}) and convective water mass flux $\mathbf{q_h}$ ($kg\ s^{-1}\ m^{-2}$) are:

$$\mathbf{q}_t = \varphi_t \left(T_s - T_{ext}\right)\mathbf{n} \qquad \mathbf{q}_h = \varphi_h \left(p_s^c - p_{ext*}^c\right)\mathbf{n} \tag{3.2}$$

where the meaning of symbols is the same of eqn (3.1). The gas pressure p^g is assumed equal to the atmospheric one at the surface of the specimens. The environmental conditions of the laboratory and the initial conditions for the two repairs are summarized in ***Table 3.5***.

Table 3.5 - Environmental and initial conditions for the repairs.

	T	R.H	Γ
Environment	22 °C (± 2 °C)	0.50 (± 0.05)	-
Repair concretes (initial values)	22 °C	0.99	0.00

The full THCM history of the reference beam and of the two repaired beams, and the wetting procedure for the preparation of the substrate are also taken into account; in other words the numerical simulations start from the casting of the three beams. ***Figure 3.19*** shows the boundary conditions of the three beams before and after the repair time which is indicated in the following as the time "zero".

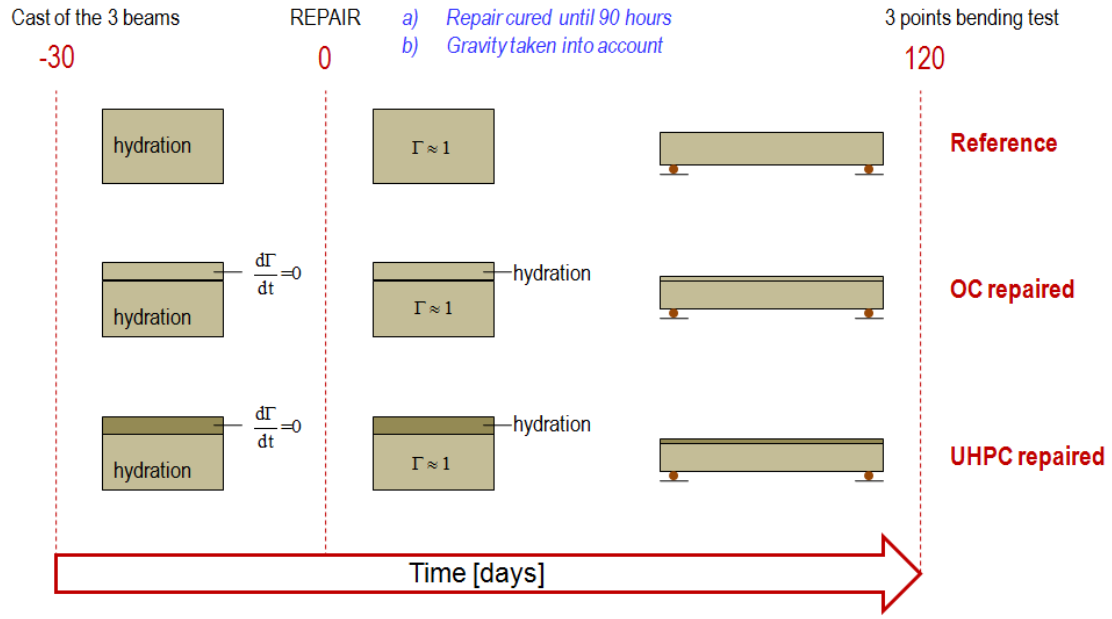

Figure 3.19 - Boundary conditions for the reference beam and the two repaired beams before and after the repair of the beams. The repair time is the time zero.

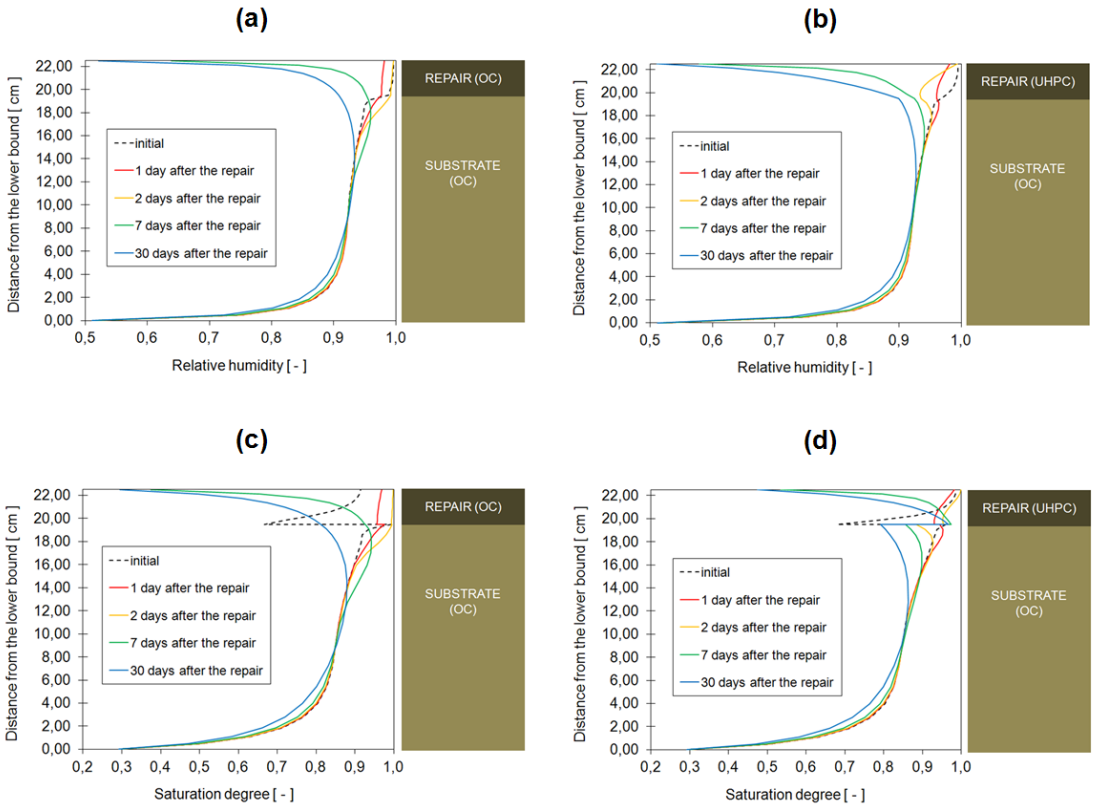

Figure 3.20 - Relative humidity (a) and (b), and saturation degree (c) and (d), for the two repair cases.

Because of the two types of repair concretes, the global and local behaviour of the repaired beams will be very different. For both cases the relative humidity is continuous at the interface (see ***Figures 3.20.a-b***), but there are discontinuities for the liquid phase saturation degree (see ***Figures 3.20.c-d***). This discontinuity depends on the different porous micro-structures (and associated desorption isotherms) of the new material of restoration and the substrate. When the repair material is the same of the substrate this discontinuity decreases due to hydration and becomes imperceptible after 1 month (see blue line ***Figure 3.20.c***). If the repair material is different from that of the substrate, this discontinuity of the saturation degree persists even after the hydration of the restoration material. Concerning the analyzed case, ***Figure 3.20.d*** shows that at the beginning (dashed and red line) at the interface the substrate is more saturated than the repair, but after the first hours the discontinuity inverts since the solid skeleton of the UHPC has a more refined porous micro-structure.

Figures 3.21 shows the numerical and the experimental results for the vertical displacement of the three beams measured using the linear potentiometer placed in the lower middle point of the beams (Pot. in ***Figure 3.18***).

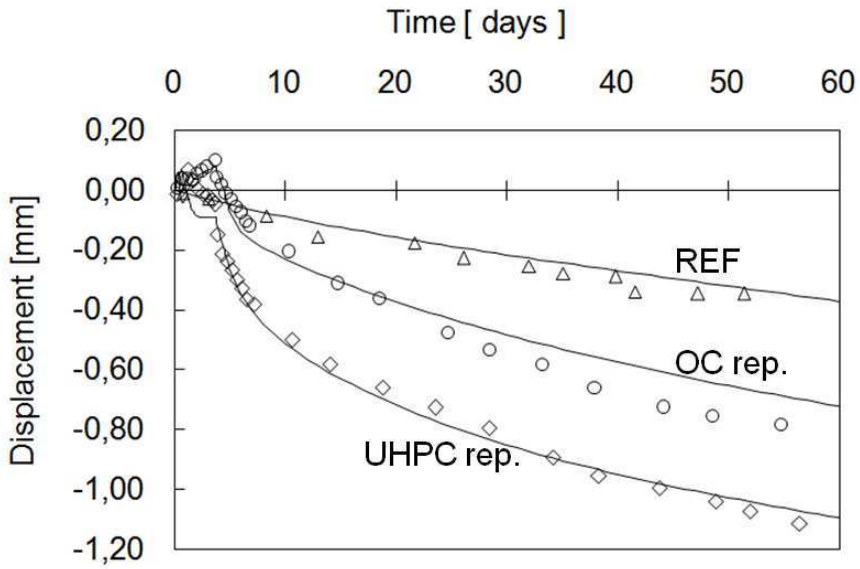

Figure 3.21 - Experimental (open symbols) and numerical results (solid lines) for the vertical displacement of the middle points of the three beams. The time "zero" corresponds to the application of the repairs

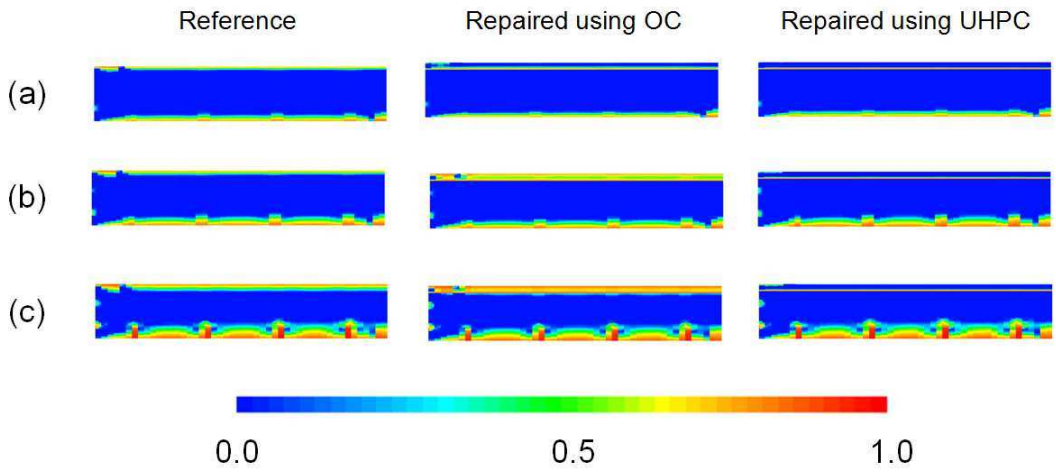

Figure 3.22 - Damage at 5 days (a), at 30 days (b) and at 120 days (c) after the repair of two of the beams (numerical results for a half beam).

In ***Figure 3.21*** a good agreement between the experimental results and the numerical ones can be observed. The deflection of the reference beam is mainly due to its weight and also to the not symmetric position of the steel reinforcements: in other words the shrinkage of the upper and lower part of the beam generates an eccentric force which increases the deflection of the beam. In the repaired beams the deflections are accentuated by the autogenous and drying shrinkage of the fresh restoration materials. ***Figure 3.22*** shows the damage at 5 days (first line), 30 days (second line) and at 120 days (third line) after the repair of two of the beams.

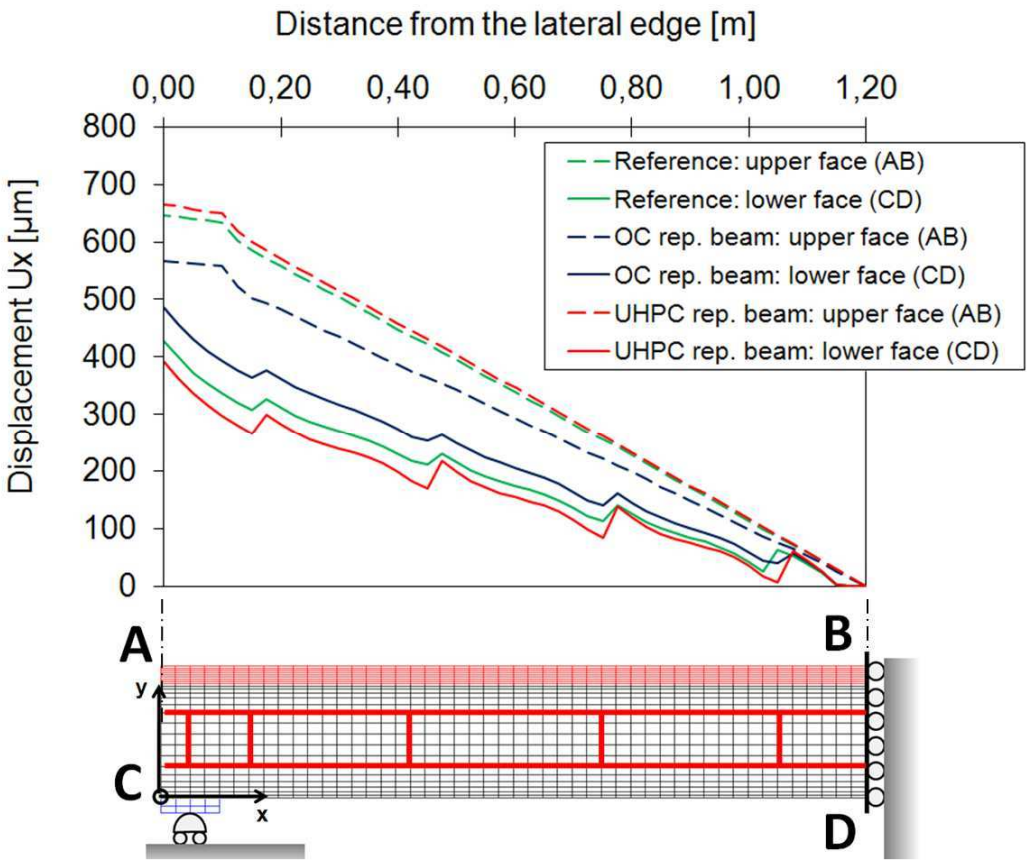

Figure 3.23 - Horizontal displacements u_x at 120 days along the upper face (AB) and lower face (CD) of the three beams.

These beams had been repaired 30 days after their casting, hence 5 days after the repair means also 35 days after the casting of the beams. Concerning the beam repaired using the OC (second column), ***Figure 3.22.a*** shows that after 5 days there is damage only at the interface between the restoration material and the substrate, although after 30 days the whole thickness of the restoration concrete is damaged due to the contrasted shrinkage. Differently the third column of ***Figure 3.22*** shows that for the UHPC repaired beam up to 120 days the damage is localized only at the interface with the substrate. The horizontal displacements u_x at 120 days along the upper face (from A to B) and the lower face (from C to D) are reported in ***Figure 3.23***. For each of the three beams the lack of evident discontinuities in the horizontal displacements of the upper face indicates that only diffuse micro-cracks caused by the contrasted shrinkage are present. On the other hand in the lower face, four macro-cracks are clearly observable from the horizontal displacements discontinuities. For the reference beam and the OC repaired beam the maximum cracks' width is of about 18 µm while for the UHPC repaired beam is of about 45 µm.

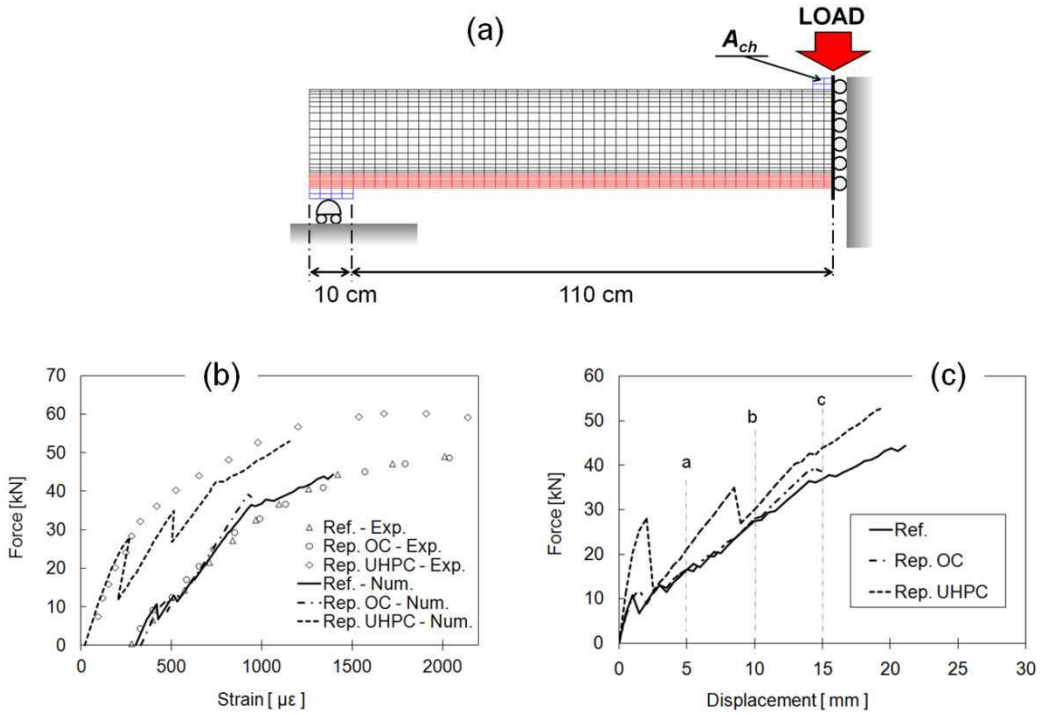

Figure 3.24 - Mechanical boundary conditions and geometrical configuration for the three points bending test (a); Force versus averaged strain of the compressed fiber optic sensor (b); Force versus displacement curves (numerical results) (c)

After 120 days from the repair, the repaired beams and the reference one are first submitted to a fatigue test and then to a three point bending test until failure. Here only the bending test is simulated and the imposed boundary conditions are represented in ***Figure 3.24.a***. A controlled vertical displacement has been imposed in the charged area (surface A_{ch} in ***Figure 3.24.a***). ***Figure 3.24.b*** shows that experimentally the global response (in term of force-strain curve) of the reference beam is very similar to that of the OC repaired beam, and this is confirmed by the numerical simulations. Also the results in terms of damage for the reference and the OC repaired beams are very similar (see ***Figure 3.25***). The analogous bending behavior of these two beams is due mainly to the fact that the OC repaired beam had been repaired only 30 days after its casting, hence the substrate was yet saturated (see ***Figure 3.20.c***) and the differential shrinkage is not too relevant. In other words when the three point bending test was performed (120 days after the repair) no relevant differences can be observed between the reference and the OC repaired beams in terms of damage and stresses. Concerning the UHPC repaired beam the increase of the initial flexural stiffness and of the limit load observed during the experiment is qualitatively obtained by the numerical model as shown in ***Figure 3.24.b***.

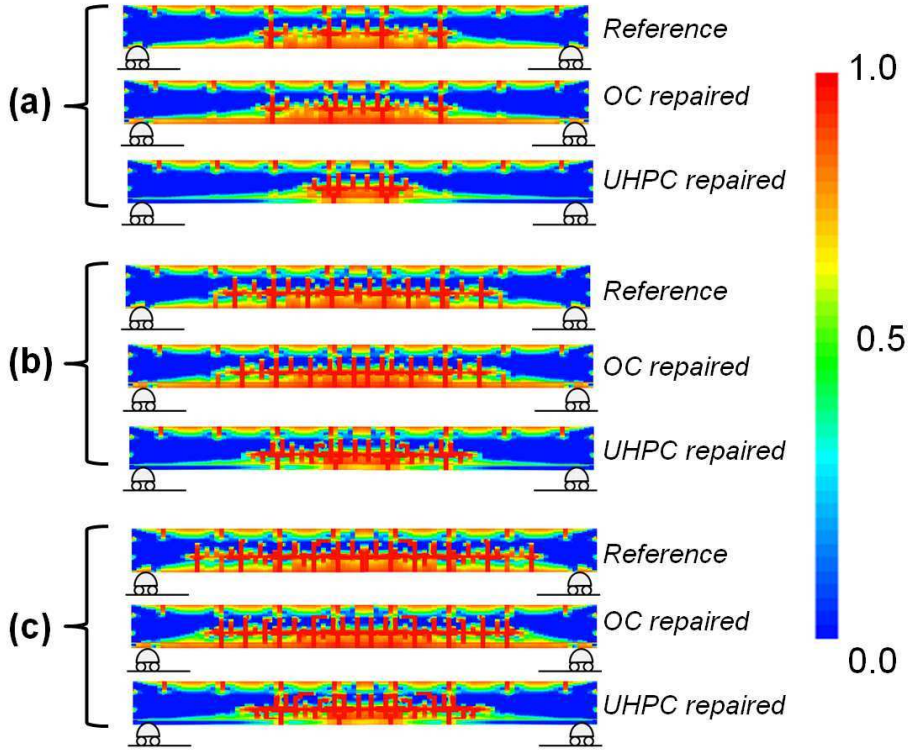

Figure 3.25 - Damage of the three beams at different imposed displacements: 5mm (a), 10 mm (b), 15 mm (c). Numerical results for the entire beam obtained by symmetry

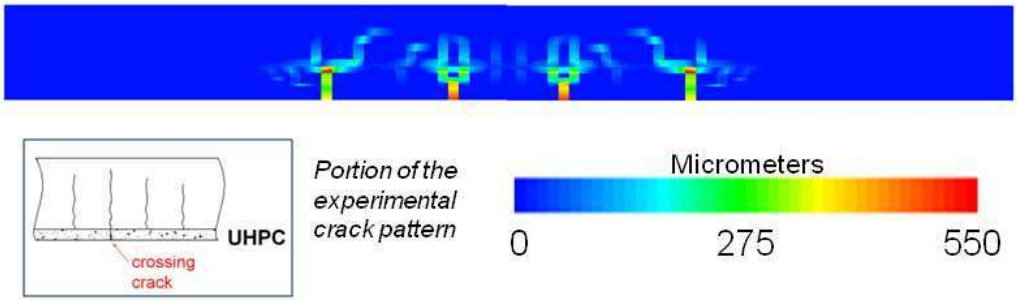

Figure 3.26 - Cracks width of the UHPC repaired beam at 15 mm of imposed vertical displacement. Numerical results for the entire beam obtained by symmetry

Indeed UHPC has greater mechanical performance than OC. Similarly to the experimental crack pattern (insert in ***Figure 3.26***), ***Figure 3.26*** shows that not all the cracks obtained numerically cross the UHPC repaired thickness.

As shown within this section, the numerical model is able to capture the most significant physical phenomena governing the behavior of concrete structural repairs. The experimental results have been successfully reproduced by the model which is useful for completely general repair cases, when experiments can be not representative of the real environmental and casting conditions.

3.4 CONCLUSIONS

In the first application is shown that the 3D implementation in Cast3M allows to model properly reinforced concrete structures (Sciumè *et al.*, 2012). Moreover the tests performed by the benchmark organizers to characterize the CEOS concrete allowed the model validation.

In the second application the model is used to simulate the behavior of two repaired beams analyzed experimentally by Bastien Masse (2010). These beams had been repaired using two wholly different concretes: an ordinary concrete (w/b = 0.62) and an ultra high performance fiber reinforced concrete (w/b = 0.22). The model is able to simulate accurately the thermo-hygro-mechanical behavior of the two considered concretes: hydration evolution, autogenous and drying shrinkage, creep. Going from the material scale (experimental tests used to identify the parameters of the model) to the structure one (modeling of the reference and repaired beams), an agreement between the numerical and experimental results is achieved qualitatively and quantitatively. The analyzed cases confirm that the factors influencing mainly the behaviour of repairs are: installation and environmental conditions, the repair's geometry and the materials' properties. Concerning the repair material, elastic modulus, tensile strength and creep potential impact critically on the success of a repair. The creep has a very important role because it relaxes the tensile stress and moderates crack phenomena.

To succeed in simulating the behaviour of concrete at early age many parameters are needed and the model must be calibrated accurately. However to identify the main input parameters only four classical experiments are needed: i) adiabatic calorimetry, ii) measuring shrinkage and loss of mass, iii) Young modulus and tensile strength values (possibly also their evolution during hydration), iv) creep test. Therefore even if the model is quite sophisticated it can be reasonably applied to real cases of interest. This multiphase THCM model can be applied to very different situations such as massive structures, repairs, losses analysis in pre-stressed concrete structures, and reinforced structures in general. Examples of model application to practical engineering problems have been presented, showing the effectiveness of such a kind of approach.

REFERENCES OF CHAPTER 3

Al-Gadhib A H, Rahman M K and Baluch M H 1999 Prediction of shrinkage and creep stresses in concrete repair systems *ACI Mater. J.* **96** 542-551.

Bastien Masse M. 2010 Étude du comportement déformationnel des bétons de réparation. *Master Thesis*. Université de Montréal.

Bentur A and Kovler K 2003 Evaluation of early age cracking characteristics in cementitious systems *Mater. Struct.* **36** 183-190.

Bissonnette B and Pigeon M 1995 Tensile creep at early ages of ordinary, silica fume and fiber reinforced concretes *Cement and Concrete Research* **25(**5) 1075-1085.

Bissonnette B, Pascale P and Pigeon M 1999 Influence of key parameters on drying shrinkage of cementitious materials *Cement and Concrete Research* **29**(10) 1655-1662.

Briffaut M, Benboudjema F, Torrenti JM and Nahas G 2011 A thermal active restrained shrinkage ring test to study the early age concrete behavior of massive structures *Cem. Conc. Res.* **41** 56-63.

Cast3M: FE code developed by the French Atomic Agency (CEA) - www-cast3m.cea.fr.

Concrack - international benchmark for Control of Cracking in reinforced concrete structures – Organized within the national French project CEOS - www.concrack.org.

Cusson D and Mailvaganarn V 1996 Durability of repair materials *Conc. Int.* **18** 34-38.

Emmons P H and Vaysburd 1994 A Factors affecting the durability of concrete repair: the contractor's viewpoint *Const. Build. Mat.* **8** 5-16.

Emmons P H and Sordyl D J 2006 The State of the Concrete Repair Industry, and a Vision for Its Future *Concrete Repair Bulletin July/August* 7-14.

Hossain A B and Weiss J 2006 The role of specimen geometry and boundary conditions on stress development and cracking in the restrained ring test *Cem. Conc. Res.* **36** 189-199.

Mauroux T, Benboudjema F, Turcry P, Aït-Mokhtar A and Deves O 2012 Study of cracking due to drying in coating mortars by digital image correlation *Cement and Concrete Research* **42**(7) 1014-1023.

Molez L 2003 Comportement des réparations structurales en beton : couplage des effets hydriques et mécaniques. *PhD thesis*. ENS Cachan.

Neville A M 1996 Properties of Concrete – Fouth Edition. Pearson, Edinburgh.

Saucier F, Claireaux F, Cusson D and Pigeon M 1997 The challenge of numerical modeling of strains and stresses in concrete repairs *Cem. Conc. Res.* **27** 1261-1270.

Sciumè G Schrefler B A and Pesavento F 2012 Thermo-hygro-chemo-mechanical modeling of the behavior of a massive beam with restrained shrinkage *Proceedings of RILEM-JCI international workshop on crack control of mass concrete and related issues concerning early-age of concrete structures* 133-144.

4 EXTENSION OF THE MATHEMATICAL APPROACH TO TUMOR GROWTH MODELING

4.1 INTRODUCTION

Several mathematical formulations have analyzed the time-dependent behaviour of a tumor mass. However, most of these propose simplifications that compromise the physical soundness of the model. Here, multiphase porous media mechanics is extended to model tumor evolution, using governing equations obtained via the Thermodynamically Constrained Averaging Theory (TCAT). A tumor mass is treated as a multiphase medium composed of an extracellular matrix (ECM); tumor cells (TCs), which may become necrotic depending on the nutrient concentration and tumor phase pressure; healthy cells (HCs); and an interstitial fluid (IF) for the transport of nutrients. The equations are solved by the Finite Element method to predict the growth rate of the tumor mass as a function of the initial tumor-to-healthy cell density ratio, nutrient concentration, mechanical strain, cell adhesion and geometry. Within the chapter results are shown for three cases of biological interest such as multicellular tumor spheroids (MTSs) and tumor cords. First, the model is validated by experimental data for time-dependent growth of an MTS in a culture medium. The tumor growth pattern follows a biphasic behaviour: initially, the rapidly growing tumor cells tend to saturate the volume available without any significant increase in overall tumor size; then, a classical

Gompertzian pattern is observed for the MTS radius variation with time. A core with necrotic cells appears for tumor sizes larger than 150 μm, surrounded by a shell of viable tumor cells whose thickness stays almost constant with time. A formula to estimate the size of the necrotic core is proposed. In the second case, the MTS is confined within a healthy tissue. The growth rate is reduced, as compared to the first case – mostly due to the relative adhesion of the tumor and healthy cells to the ECM, and the less favourable transport of nutrients. In particular, for host cells adhering less avidly to the ECM, the healthy tissue is progressively displaced as the malignant mass grows, whereas tumor cells infiltration is predicted for the opposite condition. Interestingly, the infiltration potential of the tumor mass is mostly driven by the relative cell adhesion to the ECM. In the third case, a tumor cord model is analyzed where the malignant cells grow around microvessels in a 3D geometry. It is shown that tumor cells tend to migrate among adjacent vessels seeking new oxygen and nutrient. This model can predict and optimize the efficacy of anticancer therapeutic strategies. It can be further developed to answer questions on tumor biophysics, related to the effects of ECM stiffness and cell adhesion on tumor cell proliferation.

4.2 TCAT PROCEDURE FOR BIOLOGICAL SYSTEM

Although TCAT has heretofore been employed primarily in hydrology, it can impact tumor modeling in that the underlying physics and mathematics needed to describe tumors are related. Biological growth also lends itself to modeling using mass conservation because cells require nutrient input to grow and divide into new cells. TCAT provides a framework in which the aspects that are unique to biological modeling can be incorporated directly, and the fundamental physical laws remain unchanged whether we are modeling a tumor or an aquifer. Additionally, if hybrid tumor models are to be developed in the future, it is essential that the relation between the smaller scale variables and continuum variables be known. TCAT ensures that these relations are known.

4.3 CONTEXT AND BIBLIOGRAPHIC REVIEW OF TUMOR GROWTH MODELS

With the aging world population, a surge in cancer incidence is anticipated in coming years, with major societal and economic impact. With such a scenario, the development

of novel therapeutic strategies is critical for improving the prognosis, outcome of intervention, quality of life, and minimizing economical impact. In this context, computational models for tumor growth and its response to different therapeutic regimens play a pivotal role. Over the past two decades, multiple models have been developed to tackle this problem. As discussed in the comprehensive works of Roose *et al*. (2007), Lowengrub *et al*. (2010), and Deisboeck *et al*. (2011), three major classes of models have been proposed: discrete, continuum, and hybrid models. *Discrete models* follow the fate of a single cell, or a small cohort of cells, over time. As such, they cannot capture tissue mechanics aspects, nor are the modelled subdomains representative of the whole tumor. However, they explain cell-to-cell cross signalling and cell response to therapeutic molecules (Perfahl *et al*. 2011). On the other hand, *continuum models* describe cancerous tissues as domains composed of multiple homogeneous fluid and solid phases interacting one with the other. Differential equations describe the spatiotemporal evolution of the system, but no direct information is provided at the single cell level (Roose *et al*. 2007). Finally, *hybrid models* incorporate different aspects of discrete and continuum models, depending on the problem of interest. For instance they represent cells individually and extracellular water as a continuum (Chaplain, 2000, Anderson, 2005, Bearer *et al*. 2009).

At very early stages, solid tumors are composed of a few abnormal cells growing within an otherwise healthy tissue. The vasculature is generally absent, and the tumor cells take all their nutrients by diffusion from the surrounding tissue. This is defined as the *avascular phase* for a solid tumor. As the mass of tumor cells increases, the extracellular matrix undergoes extensive rearrangements with increased deposition of collagen fibers, making the resulting tissue thicker and more difficult to trespass (Jain, 1999, Jain and Stylianopoulos, 2010). Also, since the tumor cells divide much faster than normal cells, the growing tumor mass exerts mechanical stresses on the surrounding healthy tissue, leading to the localized constriction and, at times, collapse of blood and lymphatic vessels. At this point, the tumor cells are already in millions and the malignant tissue has reached a characteristic size of hundreds of microns. A necrotic zone appears deep inside, far from the pre-existing vasculature, and the interstitial fluid pressure (IFP) builds up against the vascular hydrostatic pressure mainly due to the compression of the healthy tissue, obstruction of the lymphatic vessels and hyper-permeability of the new blood vessels. Using proper biochemical stimuli, the tumor cells recruit new blood vessels (angiogenesis) to support a continuous transport of nutrients and oxygen. This is defined the *vascular phase* of a solid tumor.

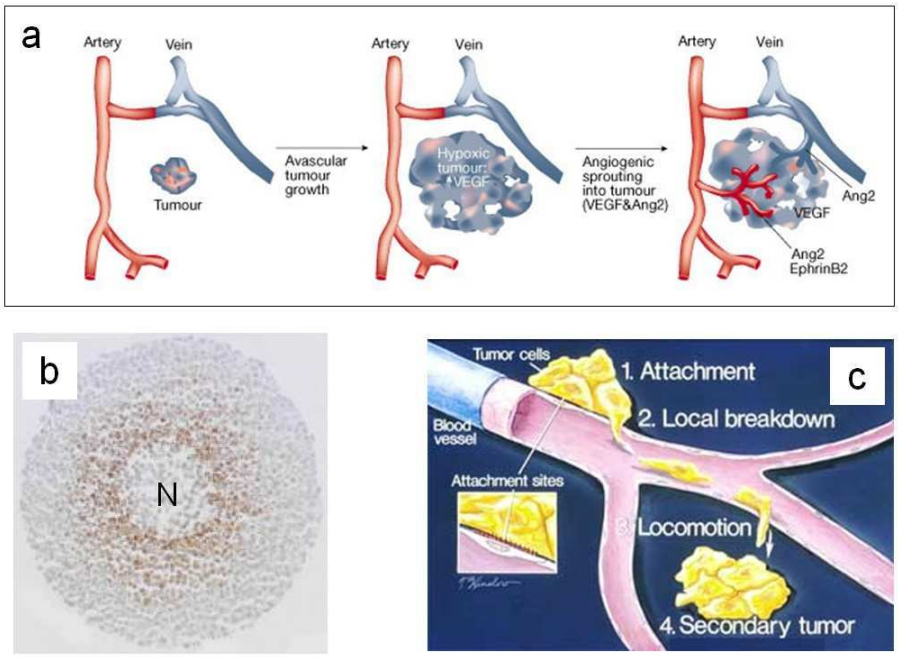

Figure 4.1 – Stages of tumor growth. From the avascular to the vascular stage: angiogenesis (from Yancopoulos *et al*.,2000) (a). Spheroid of 600 μm diameter stained with Pimonidazole to show regions of hypoxia (in brown). Staining starts approximately 150 mm from the surface, and increases in intensity towards the center with a loosely packed necrotic center (from Tupper J *et al.*, 2004) (b). Metastatic stage and formation of secondary tumor (Permalink, 2005)(c).

Over time, these new blood vessels become also a preferential route for the malignant mass to shed into circulation millions of abnormal cells that, transported by the blood flow, would reach distant sites and lead eventually to the develop secondary tumors. This is the *metastatic phase*, typically occurring for a few solid tumors. This briefly describes the multiple phases and stages that characterize the evolution of tumors; representations of these phases are shown in ***Figure 4.1***. In this chapter, the focus will be on tumor initiation, and on a novel continuum model for the evolution of avascular tumors. However angiogenesis is currently studied and its introduction in the model is one of the future objectives.

Most continuum models for avascular tumors describe the malignant mass as a homogeneous, viscous fluid and employ reaction-diffusion-advection equations for predicting the distribution and transport of nutrients and cells (Roose *et al*. 2007). Cell diffusion, convection and chemotactic motion are included, and cell proliferation is governed by mass and momentum balance equations. The first model was by Casciari *et al*. (1992). More advanced models also included intracellular mechanical interactions

(pressure, shear, adhesion) and interaction of cells with the interstitial fluid pervading the extracellular matrix. In these cases, momentum balance equations and constitutive relations are also required for describing the stress-strain response of each individual phase. One of the earlier models (Byrne and Chaplain, 1996) treated the tumor cells as a viscous liquid and introduced, quite artificially, a hydrostatic pressure within the tumor domain representing the IFP. More sophisticated models since treated solid and fluid phases independently. For instance, Roose *et al.* (2003) modelled the tissue matrix as a linear poroelastic solid, whilst the interstitial fluid was prescribed to obey Darcy's law. Cell growth was incorporated in the stress-strain relationship, still imposing small displacements. See also Sarntinoranont *et al*. (2003).

Byrne *et al.* (2003) has proposed a new class of models derived in the multi-phase framework of mixture theory. Mixture theory consists in a macroscopic description (level of observation) of the system where conservation laws are introduced in analogy with the balance laws of single bodies. Additional terms are introduced to account for the interaction among phases. The disadvantage of this approach is that no connection is made with the microscopic reality. Interfacial properties are absent from both conservation laws and constitutive equations - a serious deficiency when applied to porous media (Gray and Miller, 2005). Within this approach the cellular phase (for both tumor and healthy tissues) is modelled as a viscous fluid and the interstitial fluid as inviscid. Although, the mixture theory formalism is potent and flexible, major challenges lie in the treatment of the interfaces arising the different phases. Traditionally, two classes have been proposed: the sharp interface method, considering the interface as a sharp discontinuity; and the diffuse interface method, considering the interface as a diffuse zone. The sharp interface approach – difficult to implement for interfaces separating pure media (interstitial fluid) and mixtures (tumor cells and healthy tissue) – has been followed by Preziosi and Tosin (2009), and Preziosi and Vitale (2011). However, necrotic cells are not distinguished from live tumor cells: tumors are modelled as if necrotic cells are no longer part of the tumor. They are hinted at in the source/sink term but the related balance equations are missing. Their inclusion would require accounting for an additional interface between living and dead cells, which is not sharp in nature. On the other hand, the diffuse interface approach introduces an artificial mixture at the interface, and the challenge here is to derive physically, mathematically, and numerically consistent thermodynamic laws for these interfaces. Wise *et al*. (2008), Cristini *et al*. (2009); Oden *et al.* (2010) and Hawkis Daarud *et al*. (2012) have all followed this approach. However,

they include only one interface, separating the tumor cells from the healthy tissue. Strictly, this is insufficient in the mixture theory formalism where each interface should be accounted for throughout the whole computational domain. The models lack some rigour because the designation of phases as distinct from chemical constituents comprising a phase is unclear. Consequently some of the balance equations contain terms that cannot be justified on a theoretical basis. These simplified approaches lead to fourth-order-in-space parabolic partial differential equations, of Cahn-Hilliard type. This entails some difficulties for three-dimensional solutions with finite element methods because higher order basis functions are needed than in the realm of second order spatial operators (Gomez *et al*. 2008). Further, considering more than two or three phases becomes cumbersome, especially if a solid phase is included.

There is a need for tumor growth models for the dynamics of multiple phases and interfaces in a physically and numerically sound way. Recently the thermodynamically constrained averaging theory (TCAT) framework has been established (Gray and Miller (2005); Gray *et al*. (2012)) for continuum, porous media models that are thermodynamically consistent across scales. Here, the TCAT formalism will be used for predicting the growth of tumors under different physiologically relevant conditions. We show that second-order differential equations can accommodate more phases than most of the existing models. The interface behaviour is modelled through surface tension (Dunlop *et al*. 2011, Ambrosi *et al*. 2012) and adhesion (Baumgartner *et al.*, 2000). More than the 60% of the human body consist of fluids and a lot of biological tissues can be classified (and modeled) as porous media. Many porous media models are formulated at the macroscale, adequate for describing system behaviour while filtering out the high frequency spatial variability. The standard continuum mechanics approach to formulating these models is a direct approach wherein the conservation equations are written at the larger scale and a rational thermodynamic approach is employed to obtain closure relations. Although this approach can be mathematically consistent, the use of rational thermodynamics fails to retain a connection between larger scale variables and their microscale precursors (Maugin 1999, Jou *et al*. 2001). Thus mathematical elegance is achieved typically at the price of inconsistent variable definitions and an inability to relate quantities at one scale to those at another scale. By averaging conservation and thermodynamic equations, TCAT avoids both of these pitfalls and leads to equations that are both thermodynamically and physically consistent.

4.4 THE MULTIPHASE SYSTEM

The proposed computational model comprises the following phases: i) the tumor cells (TC), which partition into living cells (LTC) and necrotic cells (NTC); ii) the healthy cells (HC); iii) the extracellular matrix (ECM); and iv) the interstitial fluid (IF) (see ***Figure 4.2***).

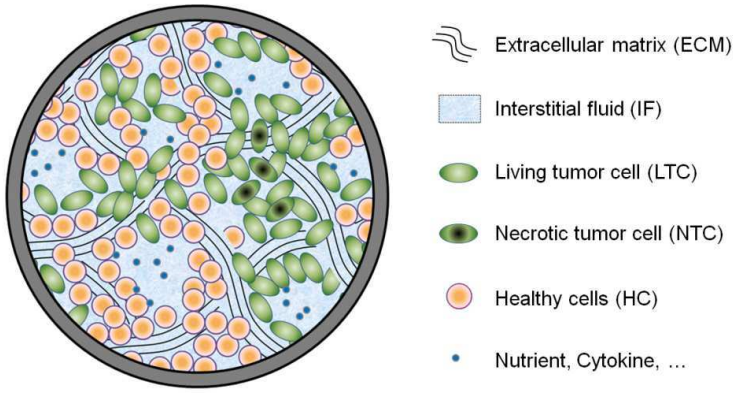

Figure 4.2 - The multiphase system within a representative elementary volume (REV).

The ECM and IF pervade the whole computational domain, whereas the TC and HC are limited only to the subdomains with the tumor mass and the healthy tissue, respectively. The ECM is modelled as a solid, while all other phases are fluids. The tumor cells become necrotic upon exposure to low nutrient concentrations or excessive mechanical pressure. The interstitial fluid, transporting nutrients, is a mixture of water and biomolecules, as nutrients, oxygen and waste products. In the following mass and momentum conservation equations, α denotes an arbitrary phase, *t* the tumor cells (TC), *h* the healthy cells (HC), *s* the extra cellular matrix (ECM), and *l* the interstitial fluid (IF).

4.5 GENERAL GOVERNING EQUATIONS

The governing equations are derived by averaging from the microscale to the macroscale and then using closure techniques to parameterize the resultant equations. These techniques have been employed for transport and for multiphase systems elsewhere (Gray and Miller 2009, Jackson *et al.* 2009) and the procedure is the same for the current system, although the number of phases is different. An important feature of the approach is that the interphase contacts are explicitly accounted for.

The ECM is treated as a porous solid and porosity is denoted by ε, so that the volume fraction occupied by the ECM is $\varepsilon^s = 1 - \varepsilon$. The rest of the volume is occupied by the tumor

cells (ε^t); the healthy cells (ε^h); and the interstitial fluid (ε^l). Indeed, the sum of the volume fractions for all phases has to be unit

$$\varepsilon^s + \varepsilon^h + \varepsilon^t + \varepsilon^l = 1 \tag{4.1}$$

The saturation degree of the phases is: $S^\alpha = \varepsilon^\alpha / \varepsilon$. Indeed, based on the definition of porosity ε and volume fraction ε^α in eqn (4.1) it follows that

$$S^h + S^t + S^l = 1 \tag{4.2}$$

The mass balance equation for an arbitrary phase α based on application of the averaging theorems is written as

$$\frac{\partial\left(\varepsilon^\alpha \rho^\alpha\right)}{\partial t} + \nabla\cdot\left(\varepsilon^\alpha \rho^\alpha \mathbf{v}^{\bar{\alpha}}\right) - \sum_{\kappa\in\Im_{c\alpha}} \overset{\kappa\to\alpha}{M} = 0 \tag{4.3}$$

where ε^α is the volume fraction; ρ^α is the density, $\mathbf{v}^{\bar{\alpha}}$ is the local velocity vector, $\overset{\kappa\to\alpha}{M}$ are the mass exchange terms accounting for transport of mass at the interface between the phases κ and α, and $\sum_{\kappa\in\Im_{c\alpha}}$ is the summation over all the phases exchanging mass at the interfaces with the phase α. However, if the interface is treated as massless, the transfer is to the adjacent phases, designated as κ. An arbitrary species i dispersed within the phase α has to satisfy mass conservation too, and therefore the following equation is derived by averaging

$$\frac{\partial\left(\varepsilon^\alpha \rho^\alpha \omega^{\overline{i\alpha}}\right)}{\partial t} + \nabla\cdot\left(\varepsilon^\alpha \rho^\alpha \omega^{\overline{i\alpha}} \mathbf{v}^{\bar{\alpha}}\right) + \nabla\cdot\left(\varepsilon^\alpha \rho^\alpha \omega^{\overline{i\alpha}} \mathbf{u}^{\overline{\overline{i\alpha}}}\right) - \varepsilon^\alpha r^{i\alpha} + \sum_{\kappa} \overset{i\alpha\to i\kappa}{M} = 0 \tag{4.4}$$

where $\omega^{\overline{i\alpha}}$ identifies the mass fraction of the species i dispersed with the phase α, $\varepsilon^\alpha r^{i\alpha}$ is a reaction term that allows to take into account the reactions between the species i and the other chemical species dispersed in the phase α, and $\mathbf{u}^{\overline{\overline{i\alpha}}}$ is the diffusive velocity of the species i.

In particular, the mass conservation equation of the nutrient species i in the IF (phase l) reads

$$\frac{\partial\left(\varepsilon^{l}\rho^{l}\omega^{\bar{i}\bar{l}}\right)}{\partial t}+\nabla\cdot\left(\varepsilon^{l}\rho^{l}\omega^{\bar{i}\bar{l}}\mathbf{v}^{\bar{l}}\right)+\nabla\cdot\left(\varepsilon^{l}\rho^{l}\omega^{\bar{i}\bar{l}}\mathbf{u}^{\bar{\bar{i}}\bar{\bar{l}}}\right)+\overset{il\to it}{M}=0 \tag{4.5}$$

where it is assumed that no chemical reaction occurs within the phase and that the exchange of mass in the liquid is only with the tumor phase. Summing eqn (4.5) over all species gives

$$\frac{\partial\left(\varepsilon^{l}\rho^{l}\right)}{\partial t}+\nabla\cdot\left(\varepsilon^{l}\rho^{l}\mathbf{v}^{\bar{l}}\right)+\overset{l\to t}{M}=0 \tag{4.6}$$

where

$$\overset{l\to t}{M}=\sum_{i\in l}\overset{il\to it}{M} \tag{4.7}$$

Note that the mass exchange from the liquid to the tumor is actually to the living cell (LTC) portion of the tumor phase. The necrotic portion of the tumor is inert and does not exchange any nutrient with the IF. Also there is no need to make a distinction between the solvent part of the liquid phase and any of the dissolved species. All species are in the liquid phase. However, due to the relatively low concentrations of chemicals, the solvent phase is the dominant species and hence the global physical properties of the IF, such as density, intrinsic permeability and dynamic viscosity are essentially those of the solvent.

The tumor phase *t* comprises a necrotic portion with mass fraction $\omega^{N\bar{t}}$ and a growing phase with living cells whose mass fraction is $1-\omega^{N\bar{t}}$. Thus the conservation equation for each fraction would be similar to eqn (4.5). Assuming that there is no diffusion of either necrotic or living cells, and that there is no exchange of the necrotic cells with other phases the mass conservation equation for the necrotic portion reads as

$$\frac{\partial\left(\varepsilon^{t}\rho^{t}\omega^{N\bar{t}}\right)}{\partial t}+\nabla\cdot\left(\varepsilon^{t}\rho^{t}\omega^{N\bar{t}}\mathbf{v}^{\bar{t}}\right)-\varepsilon^{t}r^{Nt}=0 \tag{4.8}$$

where $\varepsilon^{t}r^{Nt}$ is the rate of death of tumor cells, or in other words the rate of generation of necrotic cells. Differently than a mass exchange term between phases ($\overset{l\to t}{M}$ in eqn (4.6) for instance), the reaction term $\varepsilon^{t}r^{Nt}$ is an intra-phase exchange term. The mass balance equation for the living tumor cells is given as

$$\frac{\partial\left[\varepsilon^t\rho^t\left(1-\omega^{N\bar{t}}\right)\right]}{\partial t}+\nabla\cdot\left[\varepsilon^t\rho^t\left(1-\omega^{N\bar{t}}\right)\mathbf{v}^{\bar{t}}\right]+\varepsilon^t r^{Nt}-\overset{l\to t}{M}=0 \tag{4.9}$$

where $\overset{l\to t}{M}$ includes the exchange of nutrients and solvent from the IF to the tumor. Summation of these two equations yields an overall mass conservation equation for the tumor phase as

$$\frac{\partial\left(\varepsilon^t\rho^t\right)}{\partial t}+\nabla\cdot\left(\varepsilon^t\rho^t\mathbf{v}^{\bar{t}}\right)-\overset{l\to t}{M}=0 \tag{4.10}$$

We can expand eqn (4.8) by use of the product rule and substitute in eqn (4.10) to obtain an alternative form of the necrotic species equation as

$$\varepsilon^t\rho^t\frac{\partial\omega^{N\bar{t}}}{\partial t}+\varepsilon^t\rho^t\mathbf{v}^{\bar{t}}\cdot\nabla\omega^{N\bar{t}}+\omega^{N\bar{t}}\overset{l\to t}{M}-\varepsilon^t r^{Nt}=0 \tag{4.11}$$

For the ECM and HC, the mass conservation equation becomes respectively

$$\frac{\partial\left(\varepsilon^s\rho^s\right)}{\partial t}+\nabla\cdot\left(\varepsilon^s\rho^s\mathbf{v}^{\bar{s}}\right)=0 \tag{4.12}$$

$$\frac{\partial\left(\varepsilon^h\rho^h\right)}{\partial t}+\nabla\cdot\left(\varepsilon^h\rho^h\mathbf{v}^{\bar{h}}\right)=0 \tag{4.13}$$

For the ECM and the HC phases no mass exchange is expected with any other phase

The momentum equation for the arbitrary phase α, including multiple species i, is

$$\begin{aligned}&\frac{\partial\left(\varepsilon^\alpha\rho^\alpha\mathbf{v}^{\bar{\alpha}}\right)}{\partial t}+\nabla\cdot\left(\varepsilon^\alpha\rho^\alpha\mathbf{v}^{\bar{\alpha}}\mathbf{v}^{\bar{\alpha}}\right)-\nabla\cdot\left(\varepsilon^\alpha\bar{\bar{\mathbf{t}}}^{\bar{\alpha}}\right)+\\&-\varepsilon^\alpha\rho^\alpha\mathbf{g}^{\bar{\alpha}}-\sum_{\kappa\in\Im_{c\alpha}}\left(\sum_{i\in\Im_s}\overset{i\kappa\to i\alpha}{M_v}\mathbf{v}^{\bar{\alpha}}+\overset{\kappa\to\alpha}{\mathbf{T}}\right)=0\end{aligned} \tag{4.14}$$

where $\mathbf{g}^{\bar{\alpha}}$ is the body force, $\overset{i\kappa\to i\alpha}{M_v}\mathbf{v}^{\bar{\alpha}}$ represents the momentum exchange from the κ to the α phase due to mass exchange of species i, $\bar{\bar{\mathbf{t}}}^{\bar{\alpha}}$ is the stress tensor and $\overset{\kappa\to\alpha}{\mathbf{T}}$ is the interaction force between phase α and the adjacent interfaces. When the interface properties are negligible, this last term is simply the force interaction between adjacent phases. Given the characteristic times scales (hours and days) of the problem and the

small difference in density between cells and aqueous solutions, inertial forces as well as the force due to mass exchange are neglected, thus the momentum equation simplifies to

$$-\nabla\cdot\left(\varepsilon^{\alpha}\bar{\bar{\mathbf{t}}}^{\alpha}\right)-\varepsilon^{\alpha}\rho^{\alpha}\bar{\mathbf{g}}^{\alpha}-\sum_{\kappa\in\Im_{c\alpha}}\overset{\kappa\to\alpha}{\mathbf{T}}=0 \tag{4.15}$$

From TCAT, see ***Appendix A***, it can be shown that the stress tensor for a fluid phase is of the form $\bar{\bar{\mathbf{t}}}^{\alpha}=-p^{\alpha}\mathbf{1}$, with p^{α} being the averaged fluid pressure and **1** the unit tensor, and that the momentum balance equation can be simplified to

$$\varepsilon^{\alpha}\nabla p^{\alpha}+\mathbf{R}^{\alpha}\cdot(\bar{\mathbf{v}}^{\alpha}-\bar{\mathbf{v}}^{s})=0 \tag{4.16}$$

where $\mathbf{R}^{\alpha}$ is the resistance tensor.

4.6 CONSTITUTIVE EQUATIONS

No special assumption has been made yet for the constitutive behaviour of the different phases, except for the fluid phases described by eqn (4.16). In this paragraph, constitutive relations are explicitly presented for describing i) the tumor cell growth and ii) the tumor cell death, as a function of the nutrients' mass fraction and local mechanical stresses, for eqn (4.6) and eqn (4.8), respectively; iii) the rate of nutrient consumption from the IF, in particular, to the living tumor cells, for eqn (4.5); iv) the diffusion of nutrients within the porous ECM, for eqn (4.5); v) the interaction force among the phases, for eqn (4.15); vi) the mechanical behaviour of the ECM; and vii) the differential pressure between the fluid phases.

The formulation presented in the above paragraph can be further simplified by assuming that the densities of the phases are constant and equal

$$\rho^{s}=\rho^{h}=\rho^{t}=\rho^{l}=\rho=const \tag{4.17}$$

4.6.1 Tumor cell growth.

This is regulated by a variety of nutrient species and intracellular signalling. However, without losing generality, in the present model one single nutrient is considered: oxygen. The case of multiple species can be easily obtained as a straightforward extension of the current formulation. Tumor cell growth is related to the exchange of nutrients between the IF and the living portion of the tumor. Therefore the mass exchange term in eqn (4.6)

represents tumor growth and, similarly to a part of the relevant equation in Preziosi and Vitale (2011), takes the form

$$\underset{growth}{\overset{l\to t}{M}} = \sum_{i\in l} \overset{il\to it}{M} = \left[\gamma^{t}_{growth} \left\langle \frac{\omega^{\overline{nl}} - \omega^{\overline{nl}}_{crit}}{\omega^{\overline{nl}}_{env} - \omega^{\overline{nl}}_{crit}} \right\rangle_{+} H\left(p^{t}_{crit} - p^{t} \right) \right] (1-\omega^{N\bar{t}}) \varepsilon S^{t} \qquad (4.18)$$

where the coefficient γ^{t}_{growth} accounts for the nutrient uptake and the consumption of water needed for cell growth from the IF; $\omega^{\overline{nl}}$ is the local mass fraction of the nutrient, a fundamental variable in the problem; $\omega^{\overline{nl}}_{crit}$ is a constant critical value below which cell growth is inhibited; and the constant $\omega^{\overline{nl}}_{env}$ is the environmental mass fraction of the nutrient. Also, p^{t} denotes the tumor cell pressure and its critical value p^{t}_{crit} above which growth is inhibited. The Macaulay brackets $\langle\ \rangle_{+}$ indicate the positive value of its argument. Note that, since the local nutrient mass fraction $\omega^{\overline{nl}}$ within the tumor domain can be equal or smaller than $\omega^{\overline{nl}}_{env}$, it derives that the non-negative part of the argument of the Macaulay brackets varies between 1 ($\omega^{\overline{nl}} = \omega^{\overline{nl}}_{env}$) and 0 ($\omega^{\overline{nl}} < \omega^{\overline{nl}}_{crit}$). Consequently the growth rate for the viable tumor cells could at most be equal to γ^{t}_{growth}. Also in eqn (4.18), H is the Heaviside function which is zero for $p^{t} > p^{t}_{crit}$ and is unity for $p^{t} < p^{t}_{crit}$. Note that $\omega^{N\bar{t}} = \dfrac{\varepsilon^{N\bar{t}} \rho^{N\bar{t}}}{\varepsilon^{t} \rho^{t}}$ is the mass fraction of tumor cells that are necrotic and hence $(1-\omega^{N\bar{t}})\varepsilon S^{t}$ is the volume fraction of viable tumor cells.

4.6.2 Tumor cell death.

The rate of tumor cell death in eqn (4.8) can be described by the relation

$$\varepsilon^{t} r^{N^{t}} = \left[-\gamma^{t}_{necrosis} \left\langle \frac{\omega^{\overline{nl}} - \omega^{\overline{nl}}_{crit}}{\omega^{\overline{nl}}_{env} - \omega^{\overline{nl}}_{crit}} \right\rangle_{-} + \delta^{t}_{a} H(p^{t} - p^{t}_{necr}) \right] (1-\omega^{N\bar{t}}) \varepsilon S^{t} \qquad (4.19)$$

where $\gamma^{t}_{necrosis}$ is the rate of cell death. All the other terms are similar to those presented in eqn (4.18). However, the negative part of the argument of the Macaulay brackets $\langle\ \rangle_{-}$ is considered. Also, p^{t}_{necr} is the pressure above which the tumor stress has effect on the cell death rate, and δ_a is the additional necrosis induced by a pressure excess. Note that

the mathematical form of eqn (4.19) is very similar to eqn (4.18) in that cell death is assumed to be solely regulated by insufficient concentration of nutrients (oxygen) and excessive mechanical pressure. No drugs or other pro-apoptotic molecules are used in the present model, but eqn (4.19) can be readily modified to include also this contribution. Mathematically, a therapeutic agent or drug would be treated just as a 'nutrient'. Effects of cells membrane rupture and consequent transfer of liquid from the tumor cell phase to the interstitial fluid has been not yet included in the model. These aspects will certainly be included in future extensions of the current computational model. This will be also connected with the release of chemo-attractants and subsequent infiltration of macrophages. As such, these aspects can influence the local interstitial fluid pressure.

4.6.3 The rate of nutrient consumption.

As tumor grows, nutrients are taken up from the IF so that the sink term in eqn (4.5) takes the following form

$$\overset{nl\to t}{M} = \overset{nl\to nt}{M} = \left[\gamma_{growth}^{\bar{nl}} \left\langle \frac{\omega^{\bar{nl}} - \omega_{crit}^{\bar{nl}}}{\omega_{env}^{\bar{nl}} - \omega_{crit}^{\bar{nl}}} \right\rangle_{+} H\left(p_{crit}^{t} - p^{t} \right) + \gamma_{0}^{\bar{nl}} \sin\left(\frac{\pi}{2} \frac{\omega^{\bar{nl}}}{\omega_{env}^{\bar{nl}}} \right) \right] (1 - \omega^{N\bar{t}}) \varepsilon S^{t} \quad (4.20)$$

Nutrient consumption from IF is due to two contribution namely i) the growth of the tumor cells, as given by the first term within the square brackets in eqn (4.20); ii) the normal metabolism of the healthy cells, as presented in the second term. Indeed, $\gamma_{growth}^{\bar{nl}}$ is related to the tumor growth, as discussed above; whereas the coefficient $\gamma_{0}^{\bar{nl}}$ relates to the normal cell metabolism. Being the nutrient mass fraction $\omega^{\bar{nl}}$ in the tumor extra-cellular spaces always equal to or smaller than $\omega_{env}^{\bar{nl}}$, the argument of the sine function varies between $\pi/2$ and 0. The part of consumption of oxygen related to the cells metabolism depends on the oxygen availability and becomes zero when the mass fraction of oxygen is zero; this allows having always positive values of the local mass fraction of oxygen since negative values have not physical meaning.

4.6.4 The diffusion of nutrients through the ECM.

To approximate the diffusive flux in eqn (4.5), Fick's law is used ($\rho^{l}\omega^{\bar{nl}}\mathbf{u}^{\bar{\bar{il}}} = -D^{\bar{nl}}\rho^{l}\nabla\omega^{\bar{nl}}$). The effective diffusion coefficient of nutrients in the extracellular spaces is given as

$$D_{eff}^{\overline{nl}} = D_0^{\overline{nl}} \left(\varepsilon S^l \right)^{\delta} \tag{4.21}$$

where $D_0^{\overline{nl}}$ is the diffusion coefficient in the unbound interstitial fluid and δ is a constant coefficient greater than one which takes into account the tortuosity of the porous network. Actually the effective diffusion coefficient of oxygen has not a linear dependence on the volume fraction of the IF, because it depends on the connectivity grade of the extra cellular spaces. δ is a parameter that has to be calibrated experimentally.

4.6.5 The interaction force among the phases.

$\mathbf{R}^{\alpha}$ of eqn (4.16) is the resistance tensor that accounts for the frictional interactions between phases. For example, porous medium flow of a single fluid encounters resistance to flow due to interaction of the fluid with the solid. If one has to model the flow at the microscale, a viscous stress tensor within the fluid phase would be employed. At the macroscale, the effects of the viscous interaction are accounted for as being related to the difference in velocities of the phases. The coefficient of proportionality is the resistance tensor. In multiphase flow, resistance tensors must be developed that account for the velocity differences between each pair of phases. Eqn (4.14) contains the interaction vector $\overset{\kappa\to\alpha}{\mathbf{T}}$ that arises between each pair of phases. In the full implementation of the TCAT analysis, the simplest result is that this vector is proportional to the velocity difference between the two indicated phases with the resistance tensor being the coefficient of proportionality. In the present version of the model, the interaction force $\overset{s\to\alpha}{\mathbf{T}}$ between the fluid phase α and the solid phase s (the ECM) is explicitly taken into account while the macroscopic effect of the interaction forces between the fluid phases $\overset{l\to t}{\mathbf{T}}$, $\overset{l\to h}{\mathbf{T}}$ and $\overset{t\to h}{\mathbf{T}}$ is taken care of through the relative permeability $k_{rel}^{\alpha s}$. The form of $\left(\mathbf{R}^{\alpha}\right)^{-1}$ is here assumed following the modelling of multiphase flow in porous media (Lewis and Schrefler, 1998), that is to say

$$\left(\mathbf{R}^{\alpha}\right)^{-1} = \frac{k_{rel}^{\alpha s}\mathbf{k}^{\alpha s}}{\mu^{\alpha}\left(\varepsilon^{\alpha}\right)^2} \qquad (\alpha = h,t,l) \tag{4.22}$$

where $\mathbf{k}^{\alpha s}$ and μ^{α} are the intrinsic permeability tensor and the dynamic viscosity, respectively. Since there is no information available about this relative permeability

which is a nonlinear function of the saturation and varies between 0 and 1, the following form is assumed

$$k_{rel}^{\alpha} = \left(S^{\alpha}\right)^2 \qquad (\alpha = h,t,l) \tag{4.23}$$

Eqn (4.23) respects the constraint $\sum_{\alpha=h,t,l} k_{rel}^{\alpha} < 1$ and gives realistic results in agreement with the classical models present in the literature on porous media mechanics (Brooks and Corey (1964), Corey *et al*. (1956), Van Genuchten.(1980)). A more accurate determination of $k_{rel}^{\alpha s}$ should derive from specific experiments or by the application of Lattice-Boltzmann modelling or analysis of micro-models. By introducing (22) in (16), the relative velocity of the phase α is derived as

$$\mathbf{v}^{\bar{\alpha}} - \mathbf{v}^{\bar{s}} = -\frac{k_{rel}^{\alpha s}\mathbf{k}^{\alpha s}}{\mu^{\alpha}\varepsilon^{\alpha}}\nabla p^{\alpha} \qquad (\alpha = h,t,l) \tag{4.24}$$

The intrinsic permeability tensor $\mathbf{k}^{ls}$ of the interstitial fluid phase is constant and isotropic.

Experimental evidence confirms that cells would stay in contact with the ECM if the mechanical pressure gradients exerted over the cell phase are smaller than a critical value (Baumgartner *et al.* 2000). For this reason, for the healthy and tumor cells the intrinsic permeability tensors (i.e. $\mathbf{k}^{hs}$ and $\mathbf{k}^{ts}$) are isotropic but not constant, and are computed using the following equation

$$\mathbf{k}^{\alpha s} = \max\left(\bar{\mathbf{k}}^{\alpha s}\left\langle 1 - \frac{a_{\alpha}}{\left|\nabla p^{\alpha}\right|}\right\rangle_{+},\ \frac{\bar{\mathbf{k}}^{\alpha s}}{100}\right) \qquad (\alpha = h,t) \tag{4.25}$$

This represents in mathematical terms the fact that if cells adhere firmly to the ECM, the phase permeability within the ECM is reduced. The minimum value of the permeability (set equal to $\bar{\mathbf{k}}^{\alpha s}/100$) eliminates the indeterminacy in the case $\left|\nabla p^{\alpha}\right| < a_{\alpha}$, contained in the approach of Preziosi and Tosin (2009). This is an analogue in fluid dynamics to the stick-slip behaviour in contact mechanics (Zavarise et al, 1992).

4.6.6 The mechanical behaviour of the ECM.

The closure relation for the stress tensor acting on the ECM (sole solid phase) is

$$\mathbf{t}^{\bar{s}}_{eff} = \mathbf{t}^{\bar{s}}_{tot} + \bar{\alpha} p^s \mathbf{1} \tag{4.26}$$

with $\mathbf{t}^{\bar{s}}_{eff}$ the effective stress tensor in the sense of porous media mechanics and the solid pressure p^s given as (Gray and Schrefler, 2007)

$$p^s = \chi^h p^h + \chi^t p^t + \chi^l p^l \tag{4.27}$$

where χ^α is the solid surface fraction in contact with the respective fluid phase, known as the Bishop parameter. This parameter is a function of the degree of saturation and is taken here equal to this last one (i.e. $\chi^\alpha = S^\alpha$). The Biot coefficient $\bar{\alpha}$ is equal to 1 because of the incompressibility of the ECM. Indeed, this does not mean that the ECM cannot deform. The constitutive behaviour of the solid phase is that of an elasto-visco-plastic solid in large deformation regime. (Zienkiewicz and Taylor, 2000).

4.6.7 The differential pressure between the three fluid phases.

The differential pressure between the fluid phases is a different concept from the interaction forces dealt with in section 3.2.5. In brief, the interaction forces are in play when there is flow. The different velocities of the different phases set up resistance forces between the phases. These are the interaction forces discussed above. Differential pressure, on the other hand, can exist even at equilibrium. It is not related to flow processes but is a statement that the pressures in adjacent phases can be different. In multiple fluid flow in porous media, this difference in pressures can be attributed to the curvature of the interface between fluid phases and to the surface tension. In the tumor system, the interfaces between phases are also capable of sustaining a jump in pressure between phases. In fact cells have surface tension which influences their growth and adhesion behaviour (Dunlop *et al*. 2011, Bidan *et al.* 2012, Ambrosi *et al*. 2012). At the microscale, the pressure difference between the cell phases and the fluid phases is equal to the interfacial tension, σ_c, multiplied by the interfacial curvature. After transformation to the macroscale, a macroscale measure is needed as a surrogate for the interfacial curvature. In porous media analyses, a surrogate for the pressure difference between fluid phases is proposed heuristically as a function of the fluid saturations (e.g., Brooks and Corey 1966, van Genuchten 1990). The cell pressure becomes very large when the available pore space is occupied by the cells, i.e. when S^l tends to zero. This behaviour is depicted in ***Figure 4.3***. The following equation is proposed as a model for the pressure

difference between the interstitial fluid phase pressure p^l and those of the cell phases p^t and p^h

$$\Delta p = p^t - p^l = p^h - p^l = \sigma_c \tan\left[\frac{\pi}{2}\left(S^t + S^h\right)^b\right] \tag{4.28}$$

where σ_c and b are constants. The use of eqn (4.28) to account at the macroscale for the curvature of the interface between the phases is an approximation that assumes the distribution of the cells within the pore space does not impact the pressure difference between the phases. This expression can be refined subsequently in light of experimental analysis.

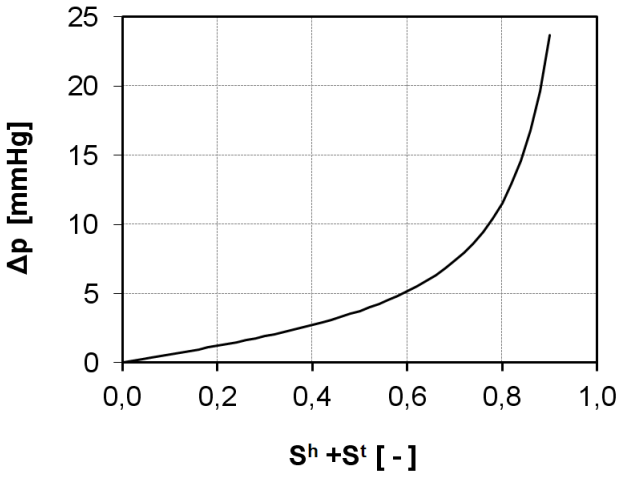

Figure 4.3 - Pressure difference - saturation relationship.

4.7 FINAL SYSTEM OF EQUATIONS

The primary variables of the model are: the tumor saturation $-S^t$, the healthy cell saturation $-S^h$, the IF pressure $-p^l$, and the nutrient mass fraction $-\omega^{\overline{nl}}$, together with the displacement of the solid phase (ECM) $\mathbf{u}^s$. The time derivative of the latter is the ECM velocity $\mathbf{v}^s$. After substituting for the explicit form of the constitutive equations, the final form of the governing equations is obtained. The mass balance equations of the ECM, TC, HC and IF are, respectively:

$$\frac{\partial\left(1-\varepsilon\right)}{\partial t} + \nabla\cdot\left[\left(1-\varepsilon\right)\frac{\partial \mathbf{u}^s}{\partial t}\right] = 0 \tag{4.29}$$

$$\frac{\partial\left(\varepsilon S^t\right)}{\partial t} + \nabla\cdot\left(\varepsilon S^t \frac{\partial \mathbf{u}^s}{\partial t}\right) - \nabla\cdot\left(\frac{k_{rel}^t \mathbf{k}^{ts}}{\mu^t}\nabla p^t\right) = \frac{1}{\rho}\overset{l\to t}{M}_{growth} \tag{4.30}$$

$$\frac{\partial\left(\varepsilon S^{h}\right)}{\partial t}+\nabla\cdot\left(\varepsilon S^{h}\frac{\partial\mathbf{u}^{s}}{\partial t}\right)-\nabla\cdot\left(\frac{k_{rel}^{h}\mathbf{k}^{hs}}{\mu^{h}}\nabla p^{h}\right)=0 \tag{4.31}$$

$$\frac{\partial\left(\varepsilon S^{l}\right)}{\partial t}+\nabla\cdot\left(\varepsilon S^{l}\frac{\partial\mathbf{u}^{s}}{\partial t}\right)-\nabla\cdot\left(\frac{k_{rel}^{l}\mathbf{k}^{ls}}{\mu^{l}}\nabla p^{l}\right)=-\frac{1}{\rho}\overset{l\to t}{M}_{growth} \tag{4.32}$$

Summing eqs (4.30-32), using the constraint equations on porosity and saturation, gives

$$\nabla\cdot\left(\frac{\partial\mathbf{u}^{s}}{\partial t}\right)-\nabla\cdot\left(\frac{k_{rel}^{t}\bar{\mathbf{k}}^{ts}}{\mu^{t}}\nabla p^{t}\right)-\nabla\cdot\left(\frac{k_{rel}^{h}\mathbf{k}^{hs}}{\mu^{h}}\nabla p^{h}\right)-\nabla\cdot\left(\frac{k_{rel}^{l}\mathbf{k}^{ls}}{\mu^{l}}\nabla p^{l}\right)=0 \tag{4.33}$$

The mass fraction of the necrotic cells is obtained from eqn (4.11) as

$$\frac{\partial\omega^{N\bar{t}}}{\partial t}=\frac{1}{\varepsilon S^{t}\rho}\left[\varepsilon^{t}r^{Nt}-\left(\omega^{N\bar{t}}\overset{l\to t}{M}_{growth}\right)-\left(\varepsilon S^{t}\rho\mathbf{v}^{\bar{t}}\right)\cdot\nabla\omega^{N\bar{t}}\right] \tag{4.34}$$

The mass balance equation of the nutrient, using the Fick' Law to approximate the diffusive velocity ($\rho^{l}\omega^{\bar{n}\bar{l}}\mathbf{u}^{\bar{\bar{i}}\bar{l}}=-D^{\bar{n}\bar{l}}\rho^{l}\nabla\omega^{\bar{n}\bar{l}}$) and assuming eqn (4.17) is:

$$\frac{\partial\left(\varepsilon S^{l}\omega^{\bar{n}\bar{l}}\right)}{\partial t}+\nabla\cdot\left(\varepsilon S^{l}\omega^{\bar{i}\bar{l}}\mathbf{v}^{\bar{i}}\right)-\nabla\cdot\left(\varepsilon S^{l}D_{eff}^{\bar{n}\bar{l}}\nabla\omega^{\bar{n}\bar{l}}\right)=-\frac{\overset{nl\to t}{M}}{\rho} \tag{4.35}$$

Expanding eqn (4.35) by use of the product rule and substituting eqn (4.6) gives an alternative form of the advection-diffusion equation of the nutrient species:

$$\varepsilon S^{l}\frac{\partial\omega^{\bar{n}\bar{l}}}{\partial t}-\nabla\cdot\left(\varepsilon S^{l}D_{eff}^{\bar{n}\bar{l}}\nabla\omega^{\bar{n}\bar{l}}\right)=\frac{1}{\rho}\left(\omega^{\bar{n}\bar{l}}\overset{l\to t}{M}-\overset{nl\to t}{M}\right)-\varepsilon S^{l}\mathbf{v}^{\bar{l}}\cdot\nabla\omega^{\bar{n}\bar{l}} \tag{4.36}$$

The linear momentum balance of the solid phase in a rate form (Schrefler, 2002) is

$$\nabla\cdot\left(\frac{\partial\bar{\bar{\mathbf{t}}}_{eff}^{s}}{\partial t}-\frac{\partial p^{s}}{\partial t}\mathbf{1}\right)=0 \tag{4.37}$$

where the interaction between the solid and fluids, inclusive of the cell populations, has been accounted for through the effective stress principle, i.e., eqs (4.26-27).

Finally for the solid phase the constitutive relationship between the effective stresses $\bar{\bar{\mathbf{t}}}_{eff}^{s}$ and the elastic strains $\mathbf{e}_{el}^{s}$, which is the difference between total strains $\mathbf{e}^{s}$ and visco-plastic strains $\mathbf{e}_{vp}^{s}$, reads as

$$\frac{\partial \bar{\bar{\mathbf{t}}}^{s}_{eff}}{\partial t} = \mathbf{D}_s \frac{\partial \mathbf{e}^{s}_{el}}{\partial t} = \mathbf{D}_s \left(\frac{\partial \mathbf{e}^{s}}{\partial t} - \frac{\partial \mathbf{e}^{s}_{vp}}{\partial t} \right) \tag{4.38}$$

where $\mathbf{D}_s$ is the tangent matrix containing the mechanical properties of the solid skeleton. The elasto-visco-plastic behavior of tumor is currently under investigation; an more exhaustive description of the mechanical model will be presented in the future being the enhancement of the mechanical part of the model is a short time objective of the research.

4.8 SPATIO-TEMPORAL DISCRETIZATION AND COMPUTATIONAL PROCEDURE

The weak form of equations (4.30), (4.31), (4.33), (4.36) and (4.37) is obtained by means of the standard Galerkin procedure and is then discretized in space by means of the finite element method (Lewis and Schrefler, 1998). Integration in the time domain is carried out with the generalized mid-point rule where an implicit procedure is used. Within each time step the equations are linearized by means of the Newton-Raphson method. For the FE discretization the primary variables are expressed in terms of their nodal values as

$$\begin{aligned} &\omega^{\overline{nl}}(t) \cong \mathbf{N}_n \bar{\boldsymbol{\omega}}^{\overline{nl}}(t) \qquad S^{t}(t) \cong \mathbf{N}_t \bar{\mathbf{S}}^{t}(t) \qquad S^{h}(t) \cong \mathbf{N}_h \bar{\mathbf{S}}^{h}(t) \\ &p^{l}(t) \cong \mathbf{N}_l \bar{\mathbf{p}}^{l}(t) \qquad \mathbf{u}^{s}(t) \cong \mathbf{N}_u \bar{\mathbf{u}}^{s}(t) \end{aligned} \tag{4.39}$$

where $\bar{\boldsymbol{\omega}}_i^{\overline{nl}}(t)$, $\bar{\mathbf{S}}_i^{t}(t)$, $\bar{\mathbf{S}}_i^{h}(t)$, $\bar{\mathbf{p}}_i^{l}(t)$, $\bar{\mathbf{u}}_i^{s}(t)$ are vectors of nodal values of the primary variables at time instant *t*, and $\mathbf{N}_n$, $\mathbf{N}_t$, $\mathbf{N}_h$, $\mathbf{N}_l$, and $\mathbf{N}_u$ are vectors of shape functions related to these variables.

For the solution of the resulting governing equations, a staggered scheme is adopted with iterations within each time step to preserve the coupled nature of the system. The convergence properties of such staggered schemes have been investigated by Turska *et al.*, (1994). In particular, for the iteration convergence within each time step a lower limit of $\Delta t/h^2$ has to be observed. Such a limit has also been found by Murthy *et al.*, (1989) for Poisson equations and by Rank *et al.* (1983) invoking the discrete maximum principle. The existence of this limit means that we cannot diminish at will the time step below a certain threshold without also decreasing the element size.

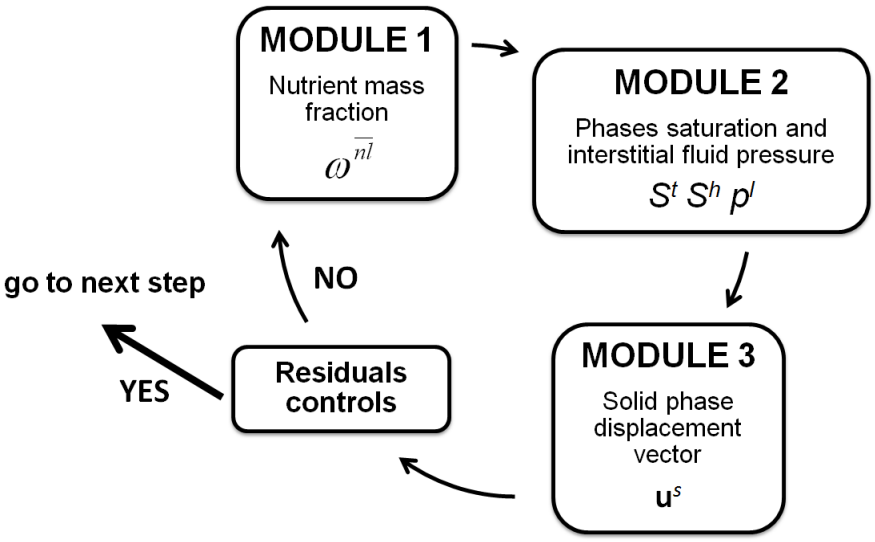

Figure 4.4 – Computational procedure implemented in Cast3M.

Three computational units are used in the staggered scheme: the first is for the nutrient mass fraction, the second to compute S^t, S^h, and p^l, and the third is used to obtain the displacement vector $\mathbf{u}^s$. Within each coupling iteration, eqn (4.36) is solved for the mass fraction of the nutrient $\omega^{\overline{nl}}$. Then the group of eqs (4.30, 4.31, 4.33) is solved in a fully coupled way for S^t, S^h, p^l. In this second computational unit, at each iteration i the approximate solution S_i^t, S_i^h, p_i^l is used to update the mass fraction of the necrotic tumor cells $\omega_i^{N\bar{t}}$, eqn (4.34), the mass exchange term, eqn (4.18), and the reaction term, eqn (4.19). Once convergence is achieved for the second computational unit, the pressure in the cells phases (given by eqn (4.28)) is used to compute the solid pressure, eqn (4.27). The solid pressure is needed to solve the momentum balance equation (eqn (4.37)). Once convergence is achieved within a time step the procedure can march forward. The computational procedure is represented in ***Figure 4.4***.

Taking into account the chosen staggered scheme, the final system of equations can be expressed in a matrix form as follows, where some of the coupling terms have been placed in the source terms and are updated at each iteration to preserve the coupled nature of the problem.

$$\mathbf{C}_{ij}(\mathbf{x})\frac{\partial \mathbf{x}}{\partial t}+\mathbf{K}_{ij}(\mathbf{x})\mathbf{x}=\mathbf{f}_i(\mathbf{x}) \tag{4.40}$$

With

$$\mathbf{C}_{ij} = \begin{pmatrix} \mathbf{C}_{nn} & 0 & 0 & 0 & 0 \\ 0 & \mathbf{C}_{tt} & \mathbf{C}_{th} & \mathbf{C}_{tl} & 0 \\ 0 & \mathbf{C}_{ht} & \mathbf{C}_{hh} & \mathbf{C}_{tl} & 0 \\ 0 & \mathbf{C}_{lt} & \mathbf{C}_{lh} & \mathbf{C}_{ll} & 0 \\ 0 & 0 & 0 & 0 & \mathbf{C}_{uu} \end{pmatrix}$$

$$\mathbf{K}_{ij} = \begin{pmatrix} \mathbf{K}_{nn} & 0 & 0 & 0 & 0 \\ 0 & \mathbf{K}_{tt} & \mathbf{K}_{th} & \mathbf{K}_{tl} & 0 \\ 0 & \mathbf{K}_{ht} & \mathbf{K}_{hh} & \mathbf{K}_{hl} & 0 \\ 0 & \mathbf{K}_{lt} & \mathbf{K}_{lh} & \mathbf{K}_{ll} & 0 \\ 0 & 0 & 0 & 0 & 0 \end{pmatrix}, \qquad \mathbf{f}_i = \begin{pmatrix} \mathbf{f}_n \\ \mathbf{f}_t \\ \mathbf{f}_h \\ \mathbf{f}_l \\ \mathbf{f}_u \end{pmatrix} \tag{4.41}$$

where $\mathbf{x}^{\mathrm{T}} = \left\{ \overline{\boldsymbol{\omega}}^{\overline{nl}}, \overline{\mathbf{S}}^{t}, \overline{\mathbf{S}}^{h}, \overline{\mathbf{p}}^{l}, \overline{\mathbf{u}}^{\mathrm{s}} \right\}$. The non linear coefficient matrices $\mathbf{C}_{ij}(\mathbf{x})$, $\mathbf{K}_{ij}(\mathbf{x})$ and $\mathbf{f}_i(\mathbf{x})$ are given in the ***Appendix D***.

The modular computational structure allows to take into account more than one chemical species, simply adding a computational unit (equivalent to the first one used for the nutrient) for each of the additional chemical species considered.

The procedure has been implemented in the code CAST3M (*http://www-cast3m.cea.fr*) of the French Atomic Energy Commission taking advantage of previous work done on modelling concrete at early age (Gawin *et al*., 2006). There is a striking analogy between the two physical problems (concrete hydration and tumor growth) as far as the balance equations are concerned. In both we have one solid phase and immiscible fluid phases together with reactions and mass exchanges.

4.9 THREE APPLICATIONS OF BIOLOGICAL INTEREST

The computational framework above has been applied to solve three cases of practical interest: i) growth of a multicellular tumor spheroid (MTS) *in vitro*; ii) growth of a multicellular tumor spheroid (MTS) *in vivo*; and iii) growth of a tumor along micro-vessels (tumor cord model). For all cases, the growth of the tumor mass, including the necrotic mass and living tumor cells; and the consumption of nutrient (oxygen) are analyzed over time. A direct comparison with experimental data is presented for case i). The extracellular matrix (ECM) is assumed rigid for all three cases. This assumption will be relaxed in future studies. Results are presented in terms of volume fractions, ε^t, ε^h and ε^l, pressures, p^c and p^l, and mass fraction of oxygen $\omega^{\overline{nl}}$.

4.9.1 Growth of a multicellular tumor spheroid (MTS) in vitro

MTS can be efficiently used to study the *in vitro* growth of tumors in the avascular stage. The tumor size can be easily measured experimentally using microscopy techniques and can be predicted quite accurately by analytical and computational methods. Here, the time evolution of a MTS is considered, assuming that the cellular mass is floating in a quiescent, cell culture medium. The geometry and boundary conditions of the problem are described in ***Figure 4.5***. Modeled as a half sphere imposing cylindrical symmetry the MTS comprises three phases: i) the living and necrotic tumor cells (LTC and NTC); ii) the extracellular matrix (ECM); and iii) the interstitial fluid (IF). At time t = 0 h, these phases coexist in the red area shown in ***Figure 4.5***, having a radius of 50 μm. Within this region, the initial volume fraction of the tumor cells (TC) is set to 0.01; whereas the volume fraction of the ECM is set to 0.05 throughout the computational domain. Note that, assuming a characteristic cell diameter of *10* μm, the initial number of tumor cells in the red area would be ~ 10.

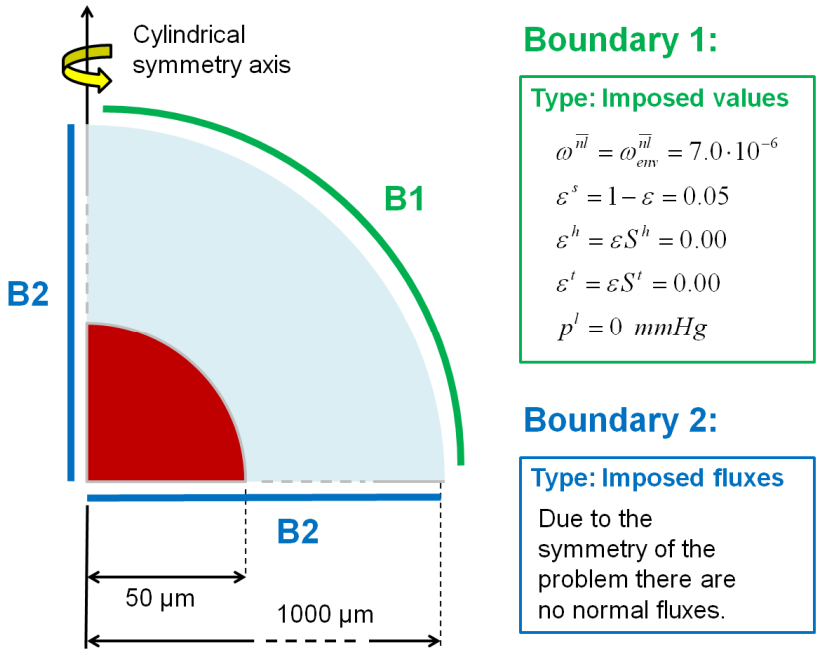

Figure 4.5 - Geometry and boundary conditions for an MTS (red) in a medium (not to scale).

Table 4.1 - Initial conditions for an MTS in a medium.

	ε^s	ε^t	ε^h	p^l	$\omega^{\overline{nl}}$
Red zone	0.05	0.01	0.00	0.00	$7 \cdot 10^{-6}$
Blu zone	0.05	0.00	0.00	0.00	$7 \cdot 10^{-6}$

Table 4.2 - Input parameters used to simulate the first case

Parameter	Symbol	Value	Unit
Density of the phases	ρ	1000	kg/m^3
Diffusion coefficient of oxygen in the interstitial fluid	$D_0^{\bar{nl}}$	$3.2\cdot10^{-9}$	m^2/sec
Coefficient δ (eqn (4.21))	δ	2.00	—
Intrinsic permeability for interstitial fluid phase	k^{ls}	$1.8\cdot10^{-15}$	m^2
Intrinsic permeability for tumor cell phase	k^{ts}	$5\cdot10^{-20}$	m^2
Adhesion of tumor cells (to ECM)	a_t	$1\cdot10^{6}$	N/m^3
Growth coefficient of tumor cells (eqn (14.8))	γ^t_{growth}	0.016	—
Critical mass fraction of oxygen (eqs (4.18,4.20))	$\omega^{\bar{nl}}_{crit}$	$3\cdot10^{-6}$	—
Critical pressure for cell growth (eqs (4.18,4.20))	p^t_{crit}	1330	Pa
Necrosis coefficient (eqn (4.19))	$\gamma^t_{necrosis}$	0.016	—
Cells pressure above which necrosis occurs (eqn (4.19))	p^t_{necr}	930	Pa
Pressure dependent additional necrosis (eqn (4.19))	δ^t_a	$5\cdot10^{-4}$	—
Consumption coeff. related to growth in eqn (4.20)	$\gamma^{\bar{nl}}_{growth}$	$4\cdot10^{-4}$	—
Consumption coeff. related to metabolism in eqn (4.20)	$\gamma^{\bar{nl}}_0$	$6\cdot10^{-4}$	—
Coefficient σ_c in eqn (4.28)	σ_c	532	Pa
Coefficient b in eqn (4.28)	b	1	—

The blue shell in ***Figure 4.5*** - the cell culture medium surrounding the MTS - is the rest of the computational domain up to 1,000 μm. These initial conditions are summarized in ***Table 4.1***. At the outer boundary (B1), the primary variables S^t, $\omega^{\bar{nl}}$ and p^l are fixed with time (Dirichlet boundary conditions). At the symmetry boundaries B2, zero flux (Neumann boundary conditions) is imposed for all the phases. The atmospheric pressure is taken as the reference pressure. In this example, oxygen is the sole nutrient species, and its mass fraction is fixed to be $\omega^{\bar{nl}}_{env} = 7\cdot10^{-6}$ at B1 and throughout the computational domain at t = 0 h. The non-apoptotic cell death rate is calculated by eqn (4.19), where the critical value of the oxygen mass fraction is given by $\omega^{\bar{nl}}_{crit} = 3\cdot10^{-6}$, and the cell pressure above which the cell death rate increases is $p^t_{necr} = 930$ Pa. The necrotic regions are those where the mass fraction of necrotic cells $\omega^{N\bar{t}} = \dfrac{\varepsilon^{N\bar{t}}\rho^{N\bar{t}}}{\varepsilon^t\rho^t}$ exceeds 0.5**.** All other governing parameters are listed in ***Table 4.2***.

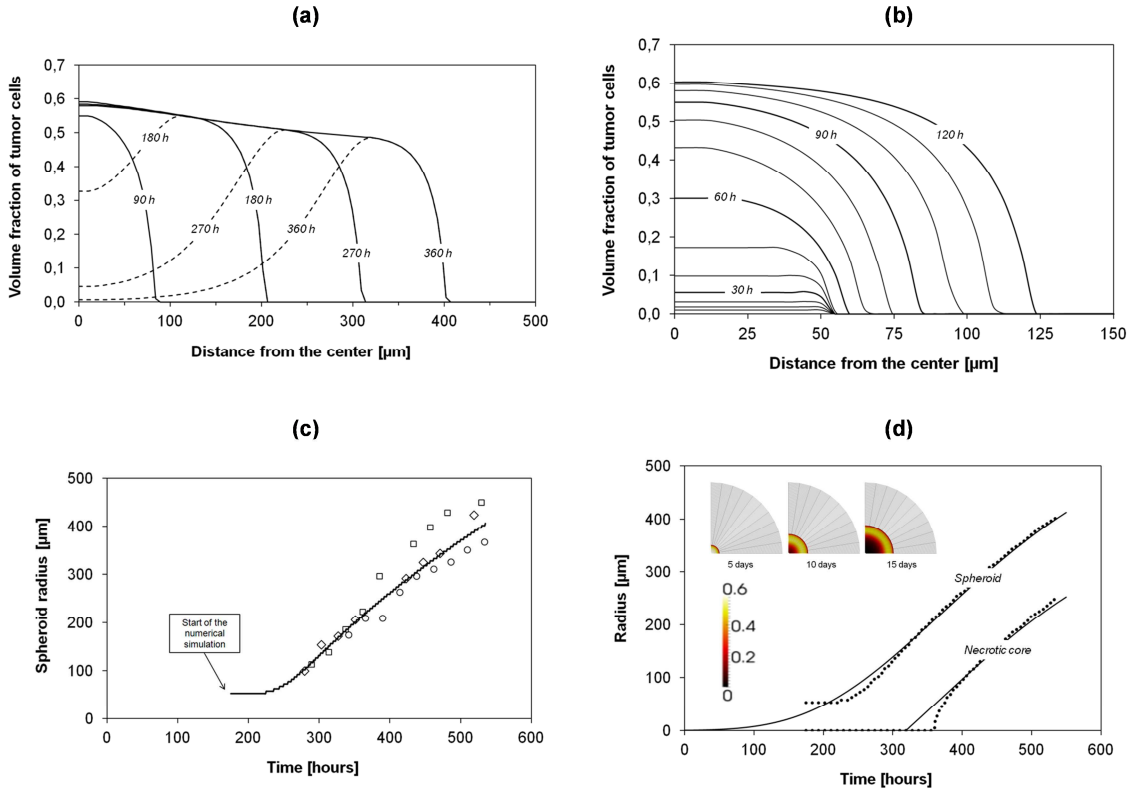

Figure 4.6 - (a) Volume fraction of the tumor cells (total and living) during 360h. (b) Volume fraction of the tumor cells phase over 120h; lines drawn at every 10h of simulations. (c) Numerical results compared with different in vitro experiments. The symbols are data obtained in the following in vitro cultures: squares = FSA cells (methylcholantrene-transformed mouse fibroblasts, Yuhas *et al.*, 1977); diamonds = MCF7 cells (human breast carcinoma, Chignola *et al.*, 1995); circles = 9L cells (rat glioblastoma, Chignola *et al.*, 2000). (d) Numerical results (points) for spheroid and necrotic core radii, and their interpolations (solid lines).

The volume fractions of the tumor cells ε^t (TC – solid line) and of the living tumor cells (LTC – dashed line) with time is presented in ***Figure 4.6.a***. The radius for which the volume fraction ε^t is zero gives the actual radius r^{sph} of the MTS. With time, the TC front moves outward and r^{sph} grows. The difference between the solid and dashed lines (TC – LTC) identifies the volume fraction of the necrotic tumor cells. The LTC lines present a peak that moves outward with time, implying a continuous growth of the necrotic area within the MTS. ***Figure 4.6.a*** clearly shows that r^{sph} grows from 50 μm (t = 0h) to ~ 400 μm at 360h. The early evolution of the tumor mass is shown with more details in ***Figure 4.6.b***. Starting from a 50 μm radius with $S^t = 0.01$, the tumor does not grow significantly in size within the first 50h. The tumor cells are rapidly dividing, increasing the volume fraction but not the size of the tumor mass. Thence, the tumor enlarges with a monotonic growth of r^{sph}. The tumor radius ($r^{sph}(t)$) is presented in ***Figure 4.6.c*** (solid line) along with experimental data (open symbols).

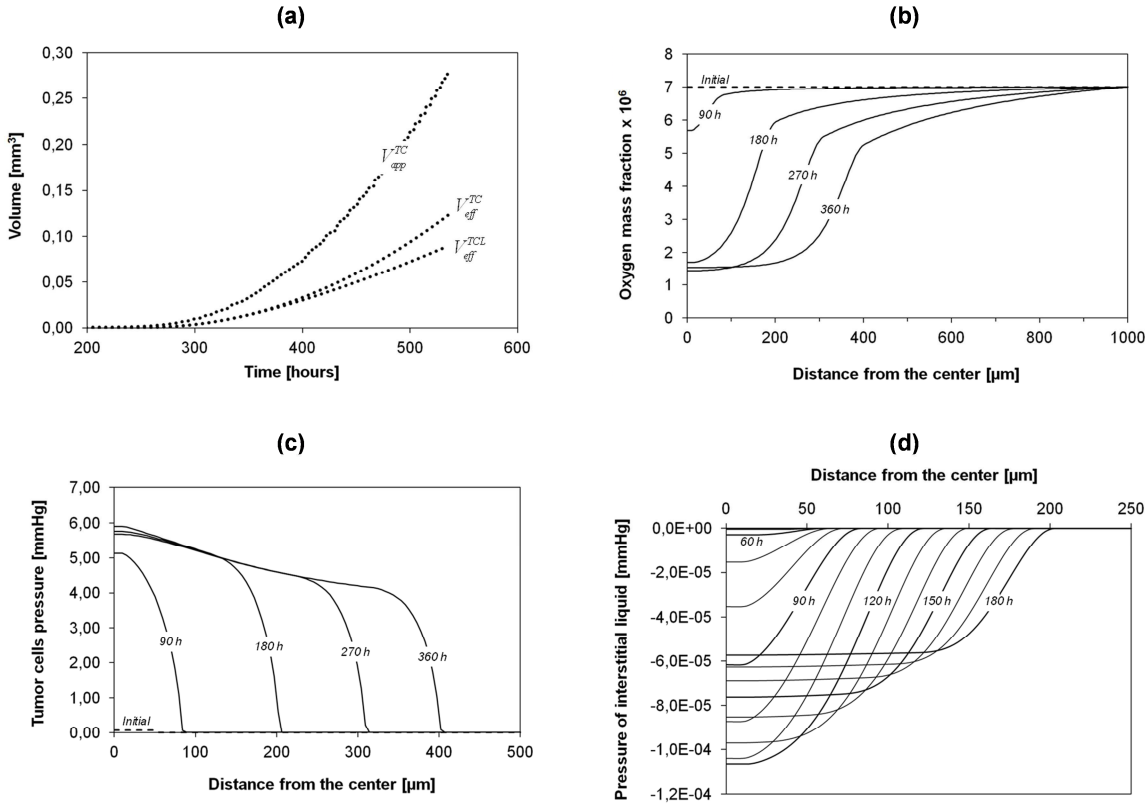

Figure 4.7 - (a) Apparent volume of the tumor spheroid, effective volume of the tumor cells, and the effective volume of the living tumor cells, over time. (b) Mass fraction of oxygen over 360h. (c) Pressure in the tumor cells phase over 360h. (d) Numerical prediction of the interstitial fluid pressure over 180h; Lines drawn at every 10h of simulations.

Notably, our prediction agrees well with three different MTS datasets (Yuhas *et al*. 1977; Chignola *et al*. 1995; Chignola *et al*. 2000). The growth rate of tumor is lower for the first 80h. The numerical results are interpolated in ***Figure 4.6.d*** using the Gompertzian growth function

$$r_{(t)}^{sph} = r_{\infty} \exp(-a \exp(-\beta t)) \tag{4.42}$$

where r_{∞} = 600 μm is the tumor radius r^{sph} at sufficiently large times (nominally t → ∞), a and β are two constants derived from numerical data (a = 7.5 and β = 0.00545 h^{-1}). The time t in eqn (4.42) is measured in hours. For the necrotic core, a similar functional relationship is here proposed as

$$r_{(t)}^{nc} = \left\langle r_{\infty} \exp(-a \exp(-\beta t)) - \delta_{living} \right\rangle_{+} \tag{4.43}$$

where δ_{living} is a constant, penalty term related to the thickness of the outer shell comprising mostly viable cells (LTC) which are still well nourished and oxygenated. The

shell thickness depends on the cell line and nutrients availability (Mueller-Klieser *et al.*, 1986), but it is well accepted that at distances larger than 100 – 200 μm, nutrient diffusion is impaired. From our simulation, the shell thickness is 150 μm. ***Figure 4.6.d*** also shows the necrotic core and the viable shell at three different times: necrotic cells are in the darker zone.

Note that the measured (apparent) volume V_{app}^{TC} of the MTS could be very different from the effective volume V_{eff}^{TC}. ***Figure 4.7.a*** shows these along with the effective volume of the living tumor cells V_{eff}^{TCL}; these are defined as

$$V_{app}^{TC} = \int_{\Omega} H\left(\varepsilon^t - \varepsilon_0^t\right) d\Omega \qquad V_{eff}^{TC} = \int_{\Omega} \varepsilon^t d\Omega \qquad V_{eff}^{LTC} = \int_{\Omega} \left(1 - \omega^{\bar{N}t}\right) \varepsilon^t d\Omega \quad (4.44)$$

where $\varepsilon_0^t = 0.01$, H is the Heaviside function which is zero for $\varepsilon^t \leq \varepsilon_0^t$ and unity for $\varepsilon^t > \varepsilon_0^t$, and Ω is the computational domain. The apparent volume contains also the IF while the effective volume comprises tumor cells alone. ***Figure 4.7.a*** shows that for small times, V_{eff}^{TC} and V_{eff}^{LTC} are equal as necrosis is initially negligible.

The evolution of the oxygen mass fraction, the sole nutrient species considered here for cell proliferation and metabolism, is shown in ***Figure 4.7.b***. As the spheroid increases in size, gradients of oxygen concentration develop from the periphery, where the oxygen mass fraction is fixed to $\omega_{env}^{\bar{n}l} = 7 \cdot 10^{-6}$, to the center of the spheroid. Once the nutrient concentration in the center goes below an imposed critical value ($\omega_{crit}^{\bar{n}l} = 3 \cdot 10^{-6}$), cell necrosis commences. Note that at the boundary between the tumor and the surrounding cell culture medium, a significant change in the gradient of the mass fraction of oxygen is observed as a kink in the curves (see ***Figure 4.7.b***) - due to the lower effective diffusivity in the tumor. After a certain time, in the necrotic core the mass fraction of oxygen reaches a minimum value of about 1.5×10^{-6}, lower than the threshold critical value ($\omega_{crit}^{\bar{n}l} = 3 \cdot 10^{-6}$). The oxygen concentration continues to fall below the threshold value until all cells are dead since in the necrotic region (here defined as the region where at least 50% of the cells are dead) the still living cells consume oxygen and slowly die. From ***Figure 4.7.b*** the necrotic core could be also identified as the portion of the MTS

with a relatively homogeneous mass fraction of oxygen. The reasons: i) necrotic cells do not consume oxygen, hence no nutrient gradient in the core; ii) the local consumption of oxygen (regulated by eqn (4.20)) decreases substantially and tends to zero with the reduction of the oxygen availability.

The pressure of the tumor cells within the computational domain (computed using eqn (4.28)) is plotted in ***Figure 4.7.c***. The maximum pressure of about 6.0 mmHg (~ 800 Pa) in the core of the MTS is lower than the critical pressure for cell death ($p^t_{necr} = 930$ Pa). Thus oxygen deficiency is the sole cause of cell necrosis in the current example. Note that for relatively low saturations, the relationship between pressure and volume fraction is almost linear (see ***Figure 4.3***). Hence, the trends shown in the ***Figures 4.6.a*** and ***Figure 4.7.c*** are similar. However with increasing saturation level of the tumor cells, the relationship with the pressure becomes nonlinear and so the peak pressure in ***Figure 4.7.c*** is more pronounced than the peak volume fraction ε^t ($\varepsilon^t = S^t/\varepsilon$) in ***Figure 4.6.a***. The interstitial fluid pressure (p^l) is plotted in ***Figure 4.7.d***. Within the first 50h, the tumor cells grow locally, whilst the overall external radius of the tumor mass stays constant at its original value (50 μm). As the IF is consumed by the tumor cells, and the assumption (4.17) allows satisfying the volume balance locally the IF pressure gradient remains unaltered. ***Figure 4.7.d*** shows that until 50h the IF pressure gradient is zero so that no additional interstitial fluid from the environment is needed (oxygen moves only by diffusion). After 50h, the spheroid increases its radius; hence with tumor growth the interstitial fluid must flow inward, per constraint eqn (4.2). Therefore the IF pressure in the MTS core decreases. The intrinsic permeability of the interstitial fluid phase is relatively high compared to that of the tumor cells phase (see ***Table 4.2***). For this reason, the variations in pressure (***Figure 4.7.d*****)** are minimal but significant to explain that IF flows into the viable tumor shell during growth. Indeed, the interstitial fluid pressure computed is slightly lower than in the surrounding tissue. This has to be ascribed to the lack of vasculature networks and lymphatic systems in the current model. The high interstitial fluid pressure measured in tumors is mostly associated to the higher permeability of the fenestrated tumor endothelium and lack, or reduction, in lymphatic flow. Therefore the plasma permeating the tumor from the vascular compartment cannot be drained out efficiently through the dysfunctional lymphatic systems leading the progressive liquid accumulation in the extracellular space and consequent pressure built up (Jain and Stylianopoulos, 2010). All this will be included in future extensions of the

model incorporating also the vascular compartment and the lymphatic system. It should also be noted that, in the present computational model, the IFP depends among others strongly on the pressure difference-saturation relationship of *sub-paragraph 4.6.7* and possibly also on the deformation of the ECM. This aspect is currently under investigation.

4.9.2 Multicellular tumor spheroid (MTS) in vivo

In this second example, the tumor is growing within the healthy tissue, which substitutes the cell culture medium in the previous case. Therefore, the initial configuration of the system comprises four phases: i) the living and necrotic tumor cells (LTC and NTC); ii) the host cells of the healthy tissue surrounding the tumor mass (HC); iii) the extracellular matrix (ECM); and iv) the interstitial fluid (IF). The ECM and IF are distributed throughout the computational domain. The growing MTS pushes on the healthy cells as its radius increases.

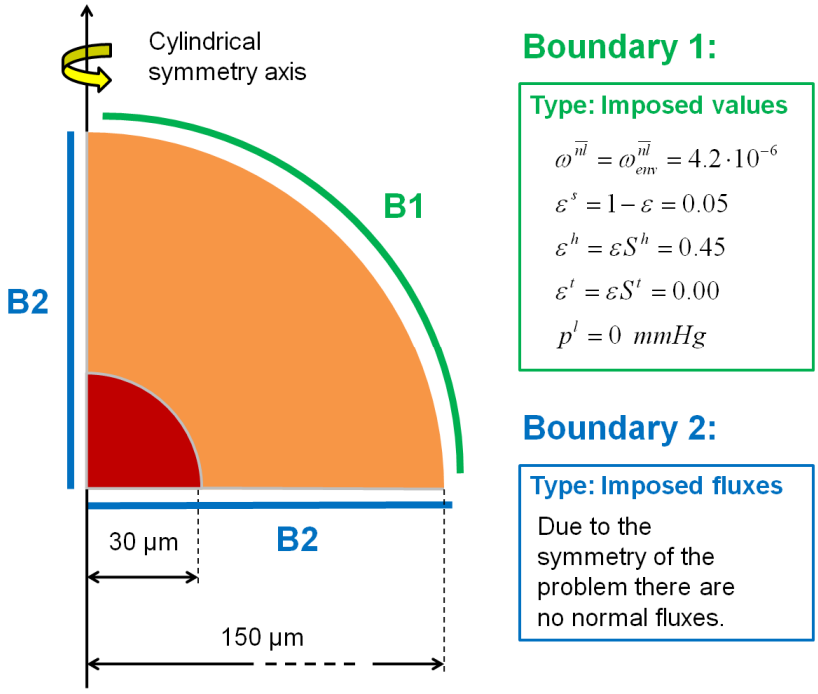

Figure 4.8 - Geometry and boundary conditions for a MTS growing within a healthy tissue. (not to scale)

Table 4.3 - Initial conditions for a MTS growing within a healthy tissue.

	ε^s	ε^t	ε^h	p^l	$\omega^{\overline{nl}}$
Red zone	0.05	0.45	0.00	0.00	$4.2 \cdot 10^{-6}$
Blu zone	0.05	0.00	0.45	0.00	$4.2 \cdot 10^{-6}$

Table 4.4 - Additional input parameters for the second case.

Parameter	Symbol	Value	Unit
Intrinsic permeability for host cell phase	k^{hs}	$5 \cdot 10^{-20}$	m^2
Adhesion of host cells[a] (to ECM)	a_h	$1 \cdot 10^6$ / $1.5 \cdot 10^6$	N/m^3
Growth coefficient of tumor cells (eqn (4.18))	γ^t_{growth}	0.0096	—
Necrosis coefficient (eqn (4.19))	$\gamma^t_{necrosis}$	0.0096	—
Consumption coeff. related to growth in eqn (4.20)	$\gamma^{\overline{nl}}_{growth}$	$2.4 \cdot 10^{-4}$	—

[a] In the second case the effect of cells adhesion is analyzed; then more than one value is used

Also, it is anticipated that the diffusion of nutrients towards the tumor mass would be reduced by the presence of the healthy tissue. As the tumor, the thin healthy tissue corona is assumed here to be not vascularised. The geometry and boundary conditions of the problem are described in ***Figure 4.8***. The MTS is modelled considering a half sphere and imposing cylindrical symmetry. The red region contain the tumor cells (TC) with an initial radius of 30 μm (t = 0 h) and an initial volume fraction set to 0.45. The orange region is the healthy tissue extending till the outer boundary B1 of the computational domain of 150 μm. The volume fraction of the host cells in the healthy zone is initially homogeneous and set to 0.45 (t = 0 h). At B1, the primary variables S^t, S^h, $\omega^{\overline{nl}}$ and p^l are prescribed and constant (Dirichlet boundary condition). At the boundaries B2, zero flux (Neumann boundary condition) is imposed for all phases and nutrients due to the radial symmetry. The atmospheric pressure is the reference pressure. As in the previous example, oxygen is the sole nutrient and its mass fraction is fixed at $\omega^{\overline{nl}}_{env} = 4.2 \cdot 10^{-6}$ on B1 and throughout the computational domain at t = 0h. The chosen mass fraction of oxygen corresponds to the average of the dissolved oxygen in the plasma of a healthy individual. Although in this case the vasculature is not explicitly considered, the radius of the computational domain (here 150 μm) can be taken as an indicator of the vascularisation grade of the host tissue: higher radii correspond to smaller vascularisation and vice versa. Due to the lower reference environmental mass fraction of oxygen $\omega^{\overline{nl}}_{env}$, the parameters γ^t_{growth} and $\gamma^t_{necrosis}$, that govern growth and necrosis respectively, and one coefficient of the oxygen sink term function ($\gamma^{\overline{nl}}_{growth}$, see eqn 4.20) are different from the first example (see ***Table 4.4***). The initial conditions are listed in ***Table 4.3*** while the parameters of the healthy phase are given in ***Table 4.4***. All the other parameters are the same as in ***Table 4.2***.

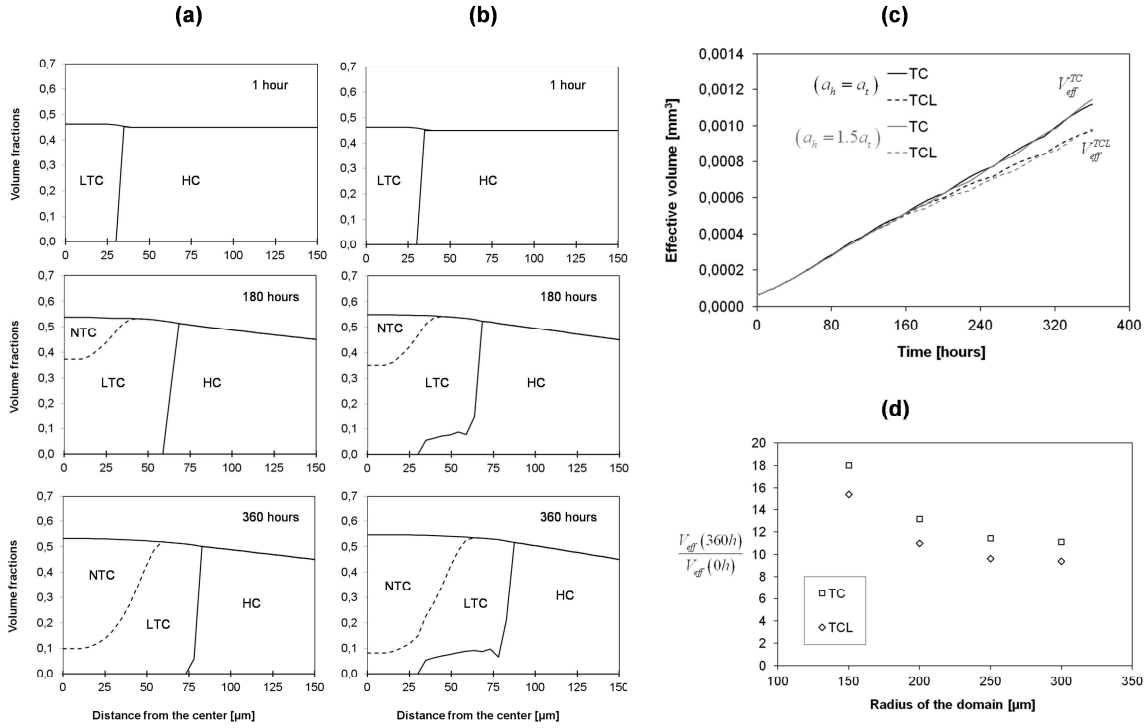

Figure 4.9 - (a,b)Numerical prediction of the volume fractions of the living tumor cells (LTC), the necrotic tumor cells (NTC) and the host cells (HC), at different times (from up to down: 1h, 180h, and 360h). The left column (a) is for $a_h = a_t$, while the right column (b) is for $a_h = 1.5 \cdot a_t$. (c) Evolution of the effective volume of the tumor cells, and the effective volume of the living tumor cells. The black lines refer to the case ($a_h = a_t$), while the grey lines refer to the case ($a_h = 1.5a_t$). (d) Scaled effective volume of tumor (normalized by initial value) after 360 hours for different radii of the computational domain.

The adhesions of the cells to the ECM (a_t and a_h) has a more significant effect than in the first case, since there were no healthy cells surrounding the tumor mass. This example shows clearly that the relative cell adhesion plays a major role in affecting the overall tumor growth. The panels in ***Figure 4.9a*** and ***Figure 4.9.b*** show the variation of the tumor cell volume fractions over time for two different adhesion conditions, namely $a_h = a_t$ (left column, ***Figure 4.9.a***) and $a_h = 1.5\ a_t$ (right column, ***Figure 4.9.b***). The times for the 3 panels are 1h, 180h and 360h. As for the first example, the variation of the volume fraction for the tumor cells (TC) is presented as a solid line, the living portion of the tumor cells (LTC) by a dashed line; the difference between the two gives the fraction of necrotic cells (NTC). As expected, the overall tumor mass expands with time and a necrotic area appears in the core. Interestingly, the panels reveal a significant difference in the evolution of the volume fractions depending on the adhesion conditions. When $a_h = a_t$ (***Figure 4.9.a***), the growing tumor mass displaces completely the healthy cells;

whereas for $a_h > a_t$ (***Figure 4.9.b***), the tumor spheroid during its growth pushes on the healthy cells and partially invades their domain. Interestingly, tumor invasion of the surrounding healthy tissue is controlled by the relative adhesion properties of the cell populations. Diffuse interface models and fourth order differential equations as used by Hawkins-Daarud *et al*. (2012) are not needed to capture the invasive behaviour.

Surprisingly, cell adhesion does not affect the overall volume size as clearly seen in ***Figure 4.9.c*** where the effective volumes of the tumor and the living tumor cells are plotted for the two adhesive conditions defined above. On the other hand, by comparing ***Figure 4.9.c*** and ***Figure 4.7.a,*** the growth patterns of an MTS in a medium and an MTS in tissue appear quite dissimilar. This is mostly due to the presence of the adhesive host cells phase that contrasts the tumor growth and reduces the nutrient supply. In addition to the difference in growth pattern, a one to two orders of magnitude difference in effective tumor volume can also be observed. Hence the experimental results obtained *in vitro* are not indicative of the *in vivo* cases since the growth environments are very different.

The radius of the computational domain can be taken as an indicator of the vascularisation grade of the host tissue, because at the boundary B1 the mass fraction is fixed to be $\bar{\omega}^{nl}_{env} = 4.2 \cdot 10^{-6}$ (mass fraction of dissolved oxygen in the plasma of a healthy individual). We have solved the case with $a_h = 1.5a_t$ for r_{ext}= 200 μm, r_{ext} = 250 μm and r_{ext} = 300 μm, (values of the initial thickness of host cells respectively of 170 μm, 220 μm and 270 μm) to evaluate the influence of the vascularisation grade on the growth of tumor. The ratio between the effective tumor volume at 360h and at t = 0h has been plotted in ***Figure 4.9.d*** for the different considered spherical domains: after 360 hours the volume of the tumor is 18 times the initial volume for r_{ext}= 150 μm, and 13 times the initial volume for r_{ext}= 200 μm, hence if we increase r_{ext} the growth rate decreases.

4.9.3 Tumor growth along microvessels (tumor cord model).

In this last case, tumor cells grow in proximity of two otherwise healthy blood vessels that are the only source of oxygen. The presence of capillary vessels has an important impact on the tumor development and on its spatial configuration (Astanin and Preziosi (2009)); this is confirmed in our application case where the progressive migration of tumor cells among adjacent vessels is also shown.

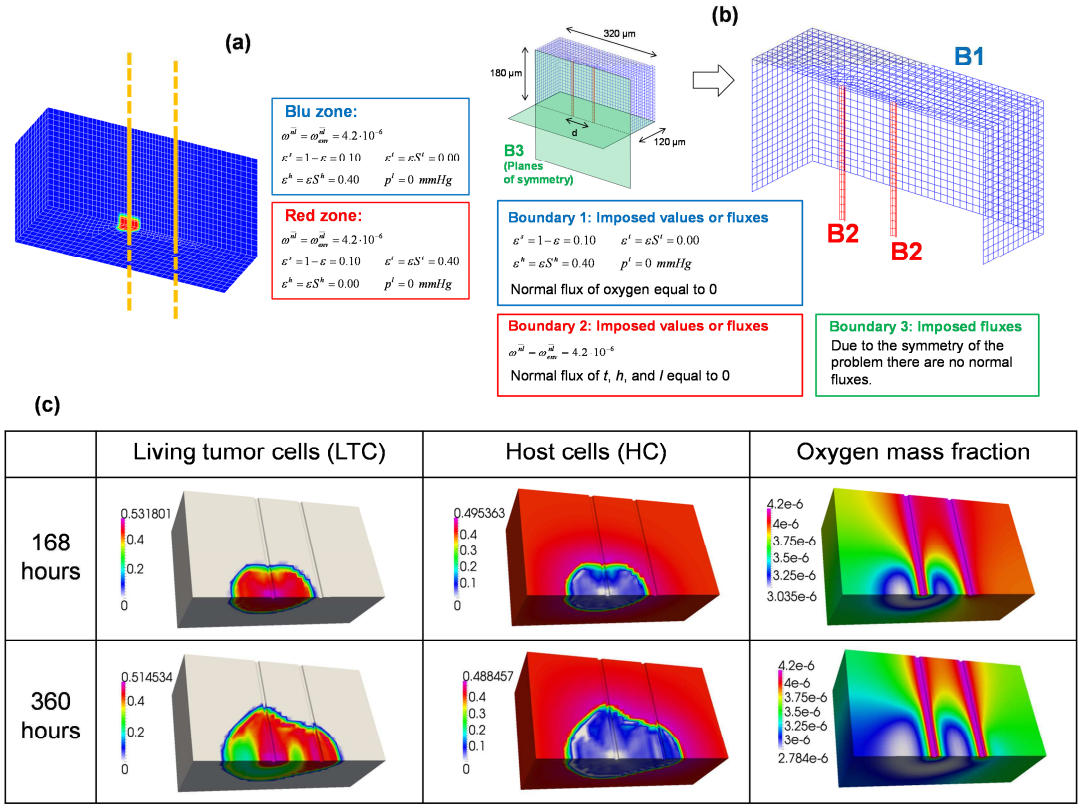

Figure 4.10 - Initial conditions of the third case. Yellow shows the axes of the two capillary vessels. (b) Geometry and boundary conditions. (c) Volume fractions of the living tumor cells (first column) of the healthy cells (second column) and mass fraction of oxygen (third column) for the case S1.

The system comprises four phases: i) the living and necrotic tumor cells (TLC and NTC); ii) the healthy tissue surrounding the tumor mass; iii) the extracellular matrix (ECM); and iv) the interstitial fluid (IF). The ECM and IF are distributed throughout the computational domain. The geometry and the boundary conditions of the problem are described in ***Figure 4.10.b***. We consider two straight blood vessels of 8 μm diameter. The tumor cells are initially located around one vessel only (see ***Figure 4.10.a***). Two different separation distances between the vessels are considered: in the first simulation (S1) the distance is 80 μm; in the second (S2) the distance is 100 μm. Note that in these cases, a full three dimensional (3D) computational solution is required. The geometry has two planes of symmetry (i.e. the median horizontal plane and that passing through the two vessels, ***Figure 4.10.b***); hence only a quarter of the complete geometry is discretized. The FE mesh here is more complex than that of the previous cases. The parameters used are those of the second case, as treated in the paragraph 4.2, with the exception of the volume fraction of the ECM, here set to 0.1.

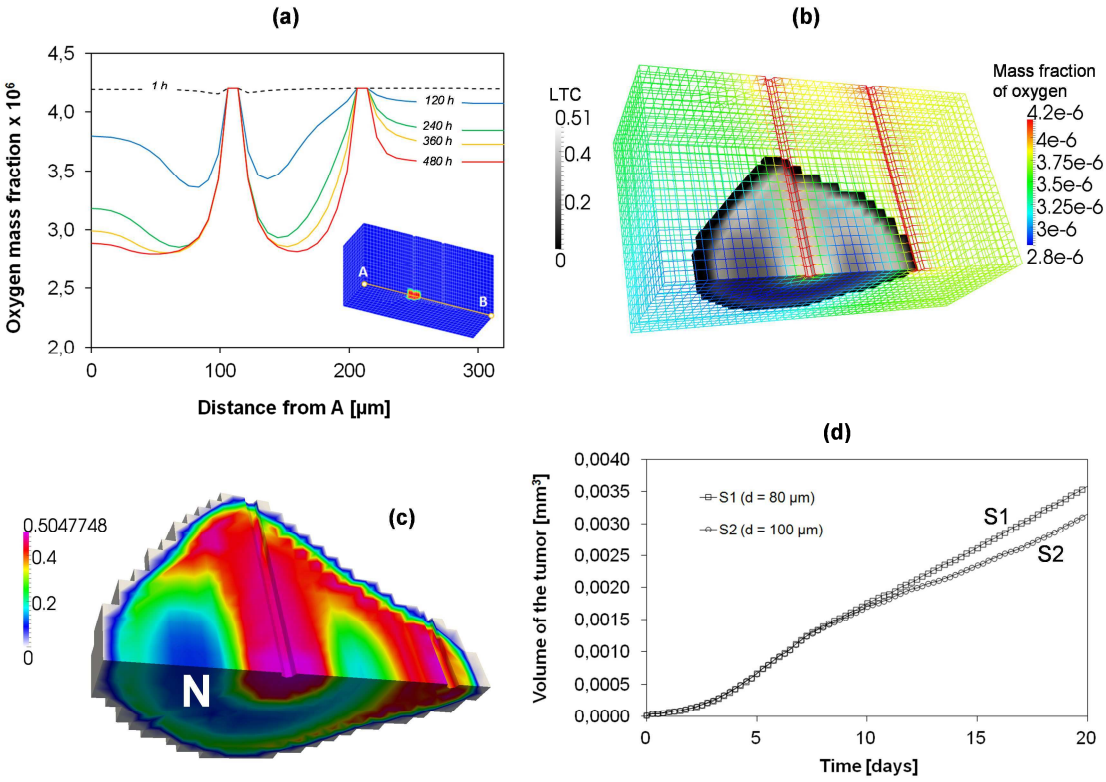

Figure 4.11 - (a) Mass fraction of oxygen along the line joining points A and B for S2. (b) Volume fractions of the LTC and oxygen mass fraction for S2 at 15 days. (c) Volume fractions of the LTC for S2 at 20 days. "N" indicates the necrotic areas. (d) Volume of the tissue invaded by the tumor.

The mass fraction of the oxygen, ($\omega_{env}^{\overline{nl}} = 4.2 \cdot 10^{-6}$) is imposed as a boundary condition on the cylindrical surface of the two blood vessels. At the remaining bounding surfaces the flux of oxygen is zero. The fluxes of all the phases (*l*, *h*, *t*) are zero at the two symmetry planes and at the cylindrical surface of the two capillary vessels. For the remaining boundary the imposed conditions are shown in ***Figure 4.10.b***. The initial conditions are summarized in ***Figure 4.10.a***.

The volume fractions at 7 and 15 days of the healthy cell phase HC, and of the living tumor cells phase TCL are shown in ***Figure 4.10.c*** for case S1. The healthy cells are almost completely replaced by the tumor cells and after 15 days necrosis occurs in parts of the tumor which are more distant from the left blood vessel. ***Figure 4.10.c*** shows also the oxygen mass fraction at 7 days and 15 days for the same simulation. The strong decrease in the oxygen mass fraction, caused by the presence of the tumor, can be readily observed by comparing the areas populated by the abnormal and healthy cells.

In the second numerical simulation (S2), the distance between the two vessels is higher than in case S1. The progressive expansion of the tumor mass from the left to the right vessel is therefore less. The results for the oxygen mass fraction are qualitatively similar to that of S1. ***Figure 4.11.a*** shows the mass fraction of oxygen along a line passing through the two vessels, at different days. The effects of consumption of oxygen coming from the vessels are evident. Oxygen is here replenished only through the two blood vessels (two peaks). ***Figure 4.11.b*** shows the tumor and the local mass fraction of oxygen (in the computational grid) at 15 days; clearly the higher values of the oxygen mass fraction are close to the two capillary vessels ($\bar{\omega}^{nl}_{vessel} = 4.2 \cdot 10^{-6}$). In S2, the tumor has not yet completely reached the right vessel after 15 days. In ***Figure 4.11c***, the volume of the tumor after 20 days is represented for S2, and the necrotic area is clearly visible (only the finite elements in which the volume fraction of the tumor phase is higher than 0.01 are shown). In ***Figure 4.11.d***, the time evolution of the tumor volume is plotted for the two cases, S1 and S2. The plotted volume is that of the finite elements with a volume fraction of the tumor cells higher than 0.01. Note that initially there is no difference between the two cases because the growth is mainly influenced by the left vessel. After 10 days, the growth rate increases for the S1 case due to the additional nutrient supply coming from the right vessel.

4.10 CONCLUSIONS AND PERSPECTIVES

A tumor growth model has been developed based on multiphase porous media mechanics. The governing differential equations have been derived by means of the Thermodynamically Constrained Averaging Theory. These are mass balance equations for the different phases with the appropriate linear momentum balance equations. The equations have been discretized by means of the finite element method and a staggered procedure has been adopted for their solution. The lower limit of the ratio between time step size and square of the element size, necessary for a proper numerical behaviour of staggered schemes and Poisson type equations, has been determined by means of numerical tests.

The computational framework has been applied to three examples of practical interest, namely a multicellular tumor spheroid (MTS) immersed in a cell culture medium; a tumor spheroid surrounded by healthy tissue; and a tumor cord. Multiple phases have been

considered in the model including i) the living and necrotic tumor cells (LTC and NTC); ii) the extracellular matrix (ECM); iii) the interstitial fluid (IF) and iv) the healthy cells (HC). For all cases, growth of the tumor mass, including the necrotic and living tumor cells areas; and the consumption of nutrient (oxygen) are analyzed over time within the whole computational domain.

For an MTS suspended in its culture medium, a direct comparison with three different experimental cases in the literature is presented. The agreement between the computational prediction of the tumor radius and the experimentally measured values is good. Also, the tumor growth follows the well know Gompertzian growth pattern demonstrating again the accuracy of the computational model. Interestingly, the early development of the malignant mass is characterized by a rapid division of the tumor cells accompanied by an equally rapid increase in tumor cell volume saturation, whilst the overall tumor size stays almost constant. This was observed up to 50-60h from the beginning. This early phase is then followed by fast exponential growth (Gompertzian growth pattern). The model allows the volume of each individual phase to be calculated at each time.

In the second example, the MTS is surrounded by a healthy tissue. The coexistence of two different cell populations (healthy and tumor) allows quantification of their relative adhesion to the ECM on tumor growth. In this respect two different conditions are analyzed showing that when the healthy cells adhere less to the ECM, the tumor advancing front displaces uniformly the healthy tissue; in the opposite case the tumor cells infiltrate the healthy tissue at discrete points. Interestingly, this result has been achieved without involving diffuse interface models and fourth order differential equations. The presence of the healthy tissue leads to an overall reduction in tumor growth mostly due to the lower nutrient transport and geometrical confinement.

In the third example, the of tumor cells along microvessels is predicted in a fully 3D geometry, with a clear delineation of necrotic and living tumor regions. The progressive migration of tumor cells among adjacent vessels in search of additional sources of nutrients and oxygen is revealed. Also shown is that a larger distance between adjacent vessels needs longer time tumor to grow, also demonstrating our model’s capability to account for the vasculature.

The numerical accuracy and physical soundness of the computational model will increase the level of complexity that we can address in tumor biophysics - such as the contribution of the ECM stiffness, relative cell adhesion and IF pressure on the infiltration and development of malignant masses. Also, modelling the transport of therapeutic agents, in the form of individual drug molecules as well as nanoparticle, and angiogenic vascular growth will be introduced in future extensions. A direct comparison of the predicted tumor behaviour with experimental data derived from patients using clinically relevant imaging modalities should provide a validation of the presented approach. The modular structure of the framework allows straightforward inclusion of additional phases and nutrient types.

Faced with a continuously aging world population and the surge in cancer incidence, the approach presented here should engender novel therapeutic strategies and treatment optimization for improving the prognosis, outcome of intervention and quality of life.

REFERENCES OF CHAPTER 4

Ambrosi D, Preziosi L, Vitale G 2012 The interplay between stress and growth in solid tumors *Mech. Res. Comm.* **42** 87-91.

Anderson A R 2005 A hybrid mathematical model of solid tumour invasion: the importance of cell adhesion *Math Med. Biol.* **22** 163-186.

Astanin S, Preziosi L 2009 Mathematical modelling of the Warburg effect in tumour cords *J. Theor. Biol.* **258**(4) 578-590.

Baumgartner W, Hinterdorfer P, Ness W, Raab A, Vestweber D, Schindler H and Drenckhahn D 2000 Cadherin interaction probed by atomic force microscopy *Proc. Nat. Acad. Sc.* (*USA*) **97** 4005–4010.

Bearer E L, Lowengrub J S, Frieboes H B, Chuang Y L, Jin F, Wise S M, Ferrari M, Agus D B and Cristini V 2009 Multiparameter computational modeling of tumor invasion *Cancer Res.* **69** 4493-4501.

Bidan C M, Kommareddy K P, Rumpler M, Kollmannsberger P, Bréchet Y J M, Fratzl P and Dunlop J W C 2012 How linear tension converts to curvature: geometric control of bone tissue growth, *PLoS ONE* 7,5, e36336.

Brooks R H and Corey A T 1964 Hydraulic properties of porous media *Hydrol. Pap. 3 (Colorado State University, Fort Collins).*

Brooks R H and Corey A T 1966 Properties of porous media affecting fluid flow *J. Irrig. Drain. Div. Am. Soc. Civ. Eng.* **92** (IR2) 61-88.

Byrne H M and Chaplain M A J 1996 Modelling the role of cell-cell adhesion in the growth and development of carcinomas *Math. Comput. Modelling* **24** 1-17.

Byrne H M, King J R and McElwain D L S 2003 A two-phase model of solid tumor growth *Appl. Math. Lett.* **16** 567-573.

Casciari J J, Sotirchos S V and Sutherland R M 1992 Mathematical modelling of and growth micrtoenvironment in EMT6/Ro multicellular tumor spheroids *Cell Proliferation* **25** 1-22.

Casey A E 1934 The experimental alteration of malignancy with an homologous mammalian tumor material-i. *Am. J. Cancer*, 21, 760-775.

Chaplain M A 2000 Mathematical modelling of angiogenesis *J. Neurooncol.* **50** 37-51.

Chignola R, Foroni R, Franceschi A, Pasti M, Candiani C, Anselmi C, Fracasso G, Tridente G and Colombatti M 1995 Heterogeneous response of individual multicellular tumour spheroids to immunotoxins and ricin toxin *Br J Cancer* **72** 607-14.

Chignola R, Schenetti A, Andrighetto G, Chiesa E, Foroni R, Sartoris S, Tridente G and Liberati D 2000 Forecasting the growth of multicell tumour spheroids: implications for the dynamic growth of solid tumours *Cell Prolif.* **33** 219-29.

Corey A T, Rathjens C H, Henderson J H and Wyllie M R J 1956 Three-phase relative permeability *Trans. AIME* **207** 349–351.

Cristini V, Li X, Lowengrub J S and Wise S M 2009 Nonlinear simulation of solid tumor growth using a mixture model: invasion and branching *J. Math. Biol.* **58** 723-763.

Deisboeck T S, Wang Z, Macklin P and Cristini V 2011 Multiscale cancer modelling *Annu. Rev. Biomed. Eng.* **13** 127-155.

Dunlop J W, Gamsjäger E, Bidan C, Kommareddy K P, Kollmansberger P, Rumpler M, Fischer F D and Fratzl P 2011 The modeling of tissue growth in confined geometries, effect of surface tension *Proc. CMM-2011 (Warsaw) Computer Methods in Mechanics.*

Folkman J 1971 Tumor angiogenesis: Therapeutic implications *N. Engl. J. Med.* **285** 1182-1186

Folkman J 2001a Angiogenesis *Harrison's Textbook of Internal Medicine 15th edition* Braunwald E, Fauci A S, Kasper D L, Hauser S L, Longo D L and Jameson J L eds. *(New York: McGraw-Hill)* 517–530.

Folkman J 2001b Angiogenesis-dependent diseases *Semin. Oncol.* **6** 536–542.

Gawin D, Pesavento F and Schrefler B A 2006 Hygro-thermo-chemo-mechanical modelling of concrete at early ages and beyond. Part I: Hydration and hygro-thermal phenomena *Int. J. Num. Meth. Engng* **67** 299-331.

Gomez H, Calo V M, Bazilevs Y and Hughes T R J 2008 Isogeometric analysis of the Cahn-Hilliard phase field model *Comput. Methods Appl. Mech. Engrg.* **197** 4333-4352.

Gray W G, Leijnse A, Kolar R L and Blain C A 1993 *Mathematical Tools for Changing Spatial Scales in the Analysis of Physical Systems*, CRC Press, 232 pp.

Gray W G and Miller C T 2005 Thermodynamically constrained averaging theory approach for

modeling flow and transport phenomena in porous medium systems: 1. Motivation and overview *Advances in Water Resources* **28** 161–180.

Gray W G and Miller C T 2009 Thermodynamically constrained averaging theory approach for modeling flow and transport phenomena in porous medium systems: 5. Single-fluid-phase transport *Advances in Water Resources* **32** 681–711.

Gray W G, Miller C T and Schrefler B A 2012 Averaging theory for description of environmental problems: What have we learned *Advances in Water Resources* (in press)

Gray W G and Schrefler B A 2007 Analysis of the solid stress tensor in multiphase porous media *IJ Num. Anal. Meth. Geomechanics* **31** 541-581.

Hawkins-Daarud A, van der Zee K G and Oden J T 2012 Numerical simulation of a thermodynamically consistent four-species tumor growth model *Int. J. Numer. Meth. Biomed. Engng.* **28** 3-24.

Jackson AS, Miller CT and Gray WG 2009 Thermodynamically constrained averaging theory approach for modelling flow and transport phenomena in porous medium systems: 6. Two-fluid-phase flow *Advances in Water Resources* **32** 779-795.

Jain R K and Stylianopoulos T 2010 Delivering nanomedicine to solid tumors *Nat Rev Clin Oncol.* **7**(11) 653-64.

Jain R K 1999 Transport of molecules, particles, and cells in solid tumors *Annu Rev Biomed Eng.* **1** 241-63.

Jongschaap R J J and Öttinger H C 2001 Equilibrium thermodynamics-Callen's postulational approach *J. Non-Newtonian Fluid Mech*. **96** 5–17.

Jou D, Casas-Vazquez J and Lebon G 2001 *Extended Irreversible Thermodynamics*, Springer-Verlag, Berlin.

Lowengrub J S, Frieboes H B, Jin F, Chuang Y-L, Li X, Macklin P, Wise S M and Cristini V 2010 Nonlinear modeling of cancer: bridging the gap between cells and tumors *Nonlinearity* ***23***(1) doi:10.1088/0951-7715/23/1/R01.

Lewis R W and Schrefler B A (1998) The Finite Element Method in the Static and Dynamic Deformation and Consolidation of Porous Media, Wiley, Chichester.

Lyden D, Hattori K, Dias S, Costa C, Blaike P, Butros L, Chadburn A, Heissig B, Marks W, Witte L *et al.* 2001 Impaired recruitment of bone-marrow-derived endothelial and hematopoietic precursor cells blocks tumor angiogenesis and growth *Nat. Med.* **7** 1194–1201.

Maugin G A 1999 *The Thermomechanics of Nonlinear Irreversible Behaviors: An Introduction*, World Scientific Press, Singapore.

Mueller-Klieser W, Freyer J P and Sutherland R M 1986 Influence of glucose and oxygen supply conditions on the oxygenation of multicellular spheroids *Br J Cancer* **53** 345-53.

Murthy V, Valliappan S and Khalili-Naghadeh N 1989 Time step constraints in finite element analysis of the Poisson type equation *Computers and Structures* **31** 269-273.

Oden J T, Hawkins A and Prudhomme S 2010 General diffusive-interface theories and an approach to predictive tumor growth modeling *Math. Models and Methods in Applied Sciences* **20** 477-517.

Perfahl H, Byrne H M, Chen T, Estrella V, Alarcòn T, Lapin A, Gatenby R A, Gillies R J, Lloyd M C, Maini P K, Reuss M and Owen M R (2011) Multiscale modelling of vascular tumor growth in 3D: the roles of domain size and boundary conditions *PLoS ONE,* April 2011, Vol. 6, Issue 4, e14790.

Permalink D 2005 Cancers Use "Cellular Bookmarks" *Cancer News Blog Archives* (from Medicineworld.Org).

Preziosi L and Tosin A 2009 Multiphase modelling of tumour growth and extracellular matrix interaction: Mathematical tools and applications *J. Math. Biol.* **58**(4-5) 625-656.

Preziosi L and Vitale G 2011 Mechanical aspects of tumour growth: Multiphase modelling, adhesion, and evolving natural configurations, in M. Ben Amar, A. Goriely, M. M. Müller, L. F. Cugliandolo, Eds., *New Trends in the Physics and Mechanics of Biological Systems*, p. 177-228, Lecture Notes of the Les Houches Summer School, vol. 92, Oxford University Press.

Preziosi L and Vitale G 2011 A multiphase model of tumour and tissue growth including cell adhesion and plastic re-organisation *Math. Models and Methods in Applied Sciences* **21**(9) 1901-1932.

Rank E, Katz C and Werner H 1983 On the importance of the discrete maximum principle in transient analysis using finite element methods *Int. J. Num. Meth. Engng.* **19** 1771-1782.

Roose T, Netti P A, Munn L L, Bucher Y and Jain R K 2003 Solid stress generated by spheroid growth estimated using a linear poroelasticity model *Microvascular Res.* **66** 204-212.

Roose T, Chapman S J and Maini P K 2007 Mathematical Models of Avascular Tumor Growth, SIAM REVIEW **49**(2) 179-208.

Sarntinoranont M, Rooney F and Ferrari M 2003 Interstitial stress and fluid pressure within a growing tumor *Ann Biomed Eng. 2003 Mar* **31**(3) 327-335.

Schrefler B A 2002 Mechanics and thermodynamics of saturated-unsaturated porous materials and quantitative solutions. *Applied Mechanics Reviews* (ASME) **55**(4) 351–388.

Taubes G 2012 Unraveling the obesity-cancer connection *Science* **335** 28-32.

Turska E, Wisniewski K and Schrefler B A 1994 Error propagation of staggered solution procedures for transient problems *Computer Methods in Appl. Mech. and Engng.* **144** 177-188.

Tupper J, Greco O, Tozer G M and Dachs G U 2004 Analysis of the horseradish peroxidase/indole-3-acetic acid combination in a three-dimensional tumor model *Cancer Gene Ther.* **11**(7) 508-513.

van Genuchten M T 1980 A closed-form equation for predicting the hydraulic conductivity of unsaturated soils *Soil. Sci. Soc. Am. J.* **44** 892–898.

van Genuchten M T, Rolston D E and German P F (Eds.) 1990 Transport of water and solutes in macropores, Geoderma, **46**(1-3) 1-297.

Walenta S, Doetsch J, Mueller-Klieser W and Kunz-Schughart L A 2000 Metabolic imaging in multicellular spheroids of oncogene-transfected fibroblasts *J HistochemCytochem* **48** 509-22.

Wise S M, Lowengrub J S, Frieboes H B and Cristini V 2008, Three-dimensional multispecies nonlinear tumor growth—I Model and numerical method *J. Theor. Biol.* **253** 524-543.

Yancopoulos G D, Davis S, Gale N W, Rudge J S, Wiegand S J and Holash J 2000 Vascular-specific growth factors and blood vessel formation *Nature* **407**(6801) 242-248.

Yuhas J M, Li A P, Martinez A O and Ladman A J 1977 A simplified method for production and growth of multicellular tumor spheroids *Cancer Res* **37** 3639-43.

Zavarise G, Wrigger P and Schrefler B A 1995 On augmented Lagrangian algorithms for thermomechanical contact problems with friction, *Int. J. Num. Meth. Eng*., 38, 2929-2949.

Zienkiewicz O C and Taylor R L 2000 *The Finite Element Method*, Vol. 2 Solid Mechanics,Butterworth Heinemann, Oxford.

APPENDICES

A. LINEAR MOMENTUM BALANCE EQUATION FOR A FLUID PHASE

The general conservation of momentum eqs (1.15 and 4.14) will be denoted for the fluid phase using the letter *f* as a qualifier.

$$\begin{aligned}&\frac{\partial\left(\varepsilon^f\rho^f\mathbf{v}^{\bar{f}}\right)}{\partial t}+\nabla\cdot\left(\varepsilon^f\rho^f\mathbf{v}^{\bar{f}}\mathbf{v}^{\bar{f}}\right)-\nabla\cdot\left(\varepsilon^f\mathbf{t}^{\bar{\bar{f}}}\right)+\\&-\varepsilon^f\rho^f\mathbf{g}^{\bar{f}}-\sum_{\kappa\in\Im_{cf}}\left(\sum_{i\in\Im_s}\overset{i\kappa\to if}{M_v}\mathbf{v}^{\bar{f}}+\overset{\kappa\to f}{\mathbf{T}}\right)=0\end{aligned}\tag{A.1}$$

where $\mathbf{g}^{\bar{f}}$ is the body force, $\overset{i\kappa\to if}{M_v}\mathbf{v}^{\bar{f}}$ represents the momentum exchange from the κ to the f phase due to mass exchange of species *i*, $\overset{\kappa\to f}{\mathbf{T}}$ is the interaction force between phase *f* and the adjacent interfaces, and $\mathbf{t}^{\bar{\bar{f}}}$ is the stress tensor. If the inertial terms are considered to be negligible, as is the case for slow flow in a porous medium, the first two terms in eqn (A.1) can be neglected. Additionally, the momentum exchange due to mass transfer, $\overset{i\kappa\to if}{M_v}\mathbf{v}^{\bar{f}}$ may also be considered small since this term is of the same order of magnitude as the inertial terms. Thus the momentum equation simplifies to

$$-\nabla\cdot\left(\varepsilon^f\mathbf{t}^{\bar{\bar{f}}}\right)-\varepsilon^f\rho^f\mathbf{g}^{\bar{f}}-\sum_{\kappa\in\Im_{cf}}\overset{\kappa\to f}{\mathbf{T}}=0\tag{A.2}$$

The TCAT method of closure involves arranging terms in the entropy inequality into force-flux pairs. At equilibrium each member of the force-flux pair will be zero. This equilibrium constraint guides closure of the conservation system for near equilibrium situations. In the case here where the flows are slow, the near-equilibrium state assumption is appropriate. Based on the TCAT procedure, the elements of the entropy inequality relating to flow velocity that arise in the entropy inequality are

$$\begin{aligned}&-\frac{1}{\theta^{\bar{\bar{f}}}}\left[\varepsilon^f\rho^f\mathbf{g}^{\bar{f}}+\varepsilon^f\rho^f\nabla\left(\zeta^{\bar{f}}+\psi^{\bar{f}}\right)-\nabla\left(\varepsilon^f p^f\right)+\sum_{\kappa\in\Im_{cf}}\overset{\kappa\to f}{\mathbf{T}}\right]\cdot\left(\mathbf{v}^{\bar{f}}-\mathbf{v}^{\bar{s}}\right)\\&+\frac{\varepsilon^f}{\theta^{\bar{\bar{f}}}}\left(\mathbf{t}^{\bar{\bar{f}}}+p^f\mathbf{1}\right):\mathbf{d}^{\bar{\bar{f}}}\geq 0\end{aligned}\tag{A.3}$$

In this equation, $\overline{\overline{\theta}}^{f}$ is the macroscale temperature of the *f* phase, $\overline{\psi}^{f}$ is the gravitational potential, $\overline{\varsigma}^{f}$ is the chemical potential, p^f is the fluid pressure, $\overline{\mathbf{v}}^{s}$ is the velocity of the solid phase and $\overline{\overline{\mathbf{d}}}^{f}$ the rate of strain tensor of the phase *f* ($\overline{\overline{\mathbf{d}}}^{f} = \frac{1}{2}\left[\nabla\overline{\mathbf{v}}^{f} + \left(\nabla\overline{\mathbf{v}}^{f}\right)^{T}\right]$). All of these quantities are macroscale averages.

Consider the variability in volume fraction of the *f* phase to be small. For this situation, $\nabla\overline{\psi}^{f} + \mathbf{g} = 0$. Additionally, consider an isothermal case such that the Gibbs-Duhem equation provides $\rho^f\nabla\overline{\varsigma}^{f} - \nabla p^f = 0$. Application of these two conditions to eqn (A.3) reduces it to

$$\frac{\varepsilon^f}{\overline{\overline{\theta}}^{f}}\left(\overline{\overline{\mathbf{t}}}^{f} + p^f\mathbf{1}\right):\overline{\overline{\mathbf{d}}}^{f} - \frac{1}{\overline{\overline{\theta}}^{f}}\left[-p^f\nabla\varepsilon^f + \sum_{\kappa\in\Im_{cf}}\overset{\kappa\to f}{\mathbf{T}}\right]\cdot\left(\overline{\mathbf{v}}^{f} - \overline{\mathbf{v}}^{s}\right) \geq 0 \qquad \text{(A.4)}$$

This equation contains two independent force-flux products. The stipulation that both elements of each product pair must be zero at equilibrium and the requirement that the grouping of terms must be non-negative suggests the linear relations

$$\sum_{\kappa\in\Im_{cf}}\overset{\kappa\to f}{\mathbf{T}} - p^f\nabla\varepsilon^f = -\mathbf{R}^f\cdot\left(\overline{\mathbf{v}}^{f} - \overline{\mathbf{v}}^{s}\right) \qquad \text{(A.5)}$$

and

$$\overline{\overline{\mathbf{t}}}^{f} + p^f\mathbf{1} = \mathbf{A}^f:\overline{\overline{\mathbf{d}}}^{f} \qquad \text{(A.6)}$$

In the first relation, $\mathbf{R}^f$ is a symmetric, positive, semi-definite tensor accounting for the resistance to flow. In the second relation, $\mathbf{A}^f$ is fourth order tensor that accounts for the dependence of the stress tensor on the rate of strain. At the macroscale for slow flow, this tensor is taken to be zero such that

$$\overline{\overline{\mathbf{t}}}^{f} = -p^f\mathbf{1} \qquad \text{(A.7)}$$

is the resulting form of the stress tensor. We note that this does not imply that the fluid is inviscid. The effects of viscosity are accounted for at the macroscale by the momentum exchange term $\overset{\kappa\to f}{\mathbf{T}}$. Substitution of the closure relations eqns (A.5) and (A.7) into Eqn (A.2) provides the momentum equation in the form

$$\varepsilon^f \nabla p^f - \varepsilon^f \rho^f \mathbf{g}^{\bar{f}} + \mathbf{R}^f \cdot \left(\mathbf{v}^{\bar{f}} - \mathbf{v}^{\bar{s}} \right) = 0 \tag{A.8}$$

Typically this relation is expressed as

$$-\mathbf{K}^f \cdot \left(\nabla p^f - \rho^f \mathbf{g}^{\bar{f}} \right) = \varepsilon^f \left(\mathbf{v}^{\bar{f}} - \mathbf{v}^{\bar{s}} \right) \tag{A.9}$$

where $\mathbf{K}^f = \left(\varepsilon^f \right)^2 \left(\mathbf{R}^f \right)^{-1}$ is called the hydraulic conductivity.

The hydraulic conductivity depends on the properties of both the flowing fluid and the solid porous material. For an isotropic medium, $\mathbf{K}^f = K^f \mathbf{1}$. The morphology and topology of the solid media are important in determining the hydraulic conductivity of the cellular solid phases. The conductivity is influenced by the cell size distribution, shape of the cells, tortuosity of passages, specific surface area, and porosity (the sum of the fluid volume fractions). It also depends on the density and viscosity of the fluid. Neglecting gravity in eqn (A.8) yields eqn (4.16).

B. TIME DISCRETIZATION OF CREEP, SHRINKAGE AND THERMAL STRAINS

The creep rheological model has been described in ***Chapter 1*** and consists of a Kelvin-Voigt chain and two dashpots combined in serial way, ***Figure 1.6***.

The creep strain is updated as follows:

$$\mathbf{e}_{cr}^{n+1} = \mathbf{e}_{cr}^{n} + \Delta\mathbf{e}_{cr1}^{n+1} + \Delta\mathbf{e}_{cr2}^{n+1} + \Delta\mathbf{e}_{cr3}^{n+1} \tag{B.1}$$

For the ***creep cell 1*** combining the eqs (1.68 - 1.72), we obtain a non-linear second-order differential equation (eqn (B.2)) that is here discretized in time.

$$\frac{\dot{\bar{t}}}{\bar{k}_{bc1}} = \tau_{bc1} \ddot{e}_{bc1} + \left(\tau_{bc1} \frac{\dot{\bar{k}}_{bc1}}{\bar{k}_{bc1}} + 1 \right) \dot{e}_{bc1} \tag{B.2}$$

The stiffness of the spring k_{bc1} depends on the hydration degree (see eqn 1.71). Assuming $\bar{k}_{bc1} = k_{bc1}^{n+0.5} \cong k_{bc1}\left(\frac{\Gamma^{n+1} + \Gamma^n}{2} \right)$ and $\dot{\bar{k}}_{bc1} \cong \frac{1}{\Delta t}\left(k_{bc1}^{n+1} - k_{bc1}^{n} \right)$ constant during the time step, and introducing $\omega = \tau_{bc1} \frac{\dot{\bar{k}}_{bc1}}{\bar{k}_{bc1}} + 1$, (B.2) can be discretized in time as follows:

$$\frac{\tilde{t}^{n+1}-\tilde{t}^{n}}{\Delta t}\frac{1}{\bar{k}_{bc1}}=\tau_{bc1}\frac{\dot{e}_{bc1}^{n+1}-\dot{e}_{bc1}^{n}}{\Delta t}+\omega\frac{\dot{e}_{bc1}^{n+1}+\dot{e}_{bc1}^{n}}{2} \tag{B.3}$$

Some operations give:

$$\tilde{t}^{n+1}-\tilde{t}^{n}=\dot{e}_{bc1}^{n+1}\left(\bar{k}_{bc1}\tau_{bc1}+\frac{\bar{k}_{bc1}\omega}{2}\Delta t\right)-\dot{e}_{bc1}^{n}\left(\bar{k}_{bc1}\tau_{bc1}-\frac{\bar{k}_{bc1}\omega}{2}\Delta t\right) \tag{B.4}$$

Adding and removing $\dot{e}_{bc1}^{n}\left(\bar{k}_{bc1}\tau_{bc1}+\frac{\bar{k}_{bc1}\omega}{2}\Delta t\right)$ gives:

$$\tilde{t}^{n+1}-\tilde{t}^{n}=\left(\dot{e}_{bc1}^{n+1}+\dot{e}_{bc1}^{n}\right)\left(\bar{k}_{bc1}\tau_{bc1}+\frac{\bar{k}_{bc1}\omega}{2}\Delta t\right)-2\dot{e}_{bc1}^{n}\bar{k}_{bc1}\tau_{bc1} \tag{B.5}$$

Hence $\Delta\mathbf{e}_{cr1}^{n+1}$ can be estimated as:

$$\Delta e_{cr1}^{n+1}\cong\frac{\left(\dot{e}_{bc1}^{n+1}+\dot{e}_{bc1}^{n}\right)}{2}\Delta t=\frac{\tilde{t}^{n+1}-\tilde{t}^{n}}{\frac{2\bar{k}_{bc1}\tau_{bc1}}{\Delta t}+\bar{k}_{bc1}\omega}+\frac{\tau_{bc1}}{\frac{\tau_{bc1}}{\Delta t}+\frac{\omega}{2}}\dot{e}_{bc1}^{n} \tag{B.6}$$

Extending to the 3D case, the creep strain of the first cell can be expressed as:

$$\Delta\mathbf{e}_{cr1}^{n+1}=\mathbf{e}_{cr1}^{n+1}-\mathbf{e}_{cr1}^{n}=\mathbf{A}_{cr1}+\mathbf{B}_{cr1}\tilde{\mathbf{t}}^{n}+\mathbf{C}_{cr1}\tilde{\mathbf{t}}^{n+1} \tag{B.7}$$

The vector $\mathbf{A}_{cr1}$ reads:

$$\mathbf{A}_{cr1}=\frac{\tau_{bc1}}{\frac{\tau_{bc1}}{\Delta t}+\frac{\omega}{2}}\dot{\mathbf{e}}_{cr1}^{n} \tag{B.8}$$

where the creep rate $\dot{\mathbf{e}}_{cr}^{n}$ is updated at the end of each time step ($\dot{\mathbf{e}}_{cr1}^{n}=2\frac{\Delta\mathbf{e}_{cr1}^{n}}{\Delta t}-\dot{\mathbf{e}}_{cr1}^{n-1}$). The two matrices $\mathbf{B}_{cr1}$ and $\mathbf{C}_{cr1}$ read:

$$\mathbf{B}_{cr1}=\frac{-1}{\frac{2\bar{k}_{bc1}\tau_{bc1}}{\Delta t}+\bar{k}_{bc1}\omega}\mathbf{P}\qquad\qquad\mathbf{C}_{cr1}=-\mathbf{B}_{cr1} \tag{B.9}$$

in which the matrix **P** by means of a creep Poisson ratio (taken equal to the elastic one) is:

$$\mathbf{P}=\begin{pmatrix} 1 & -\nu & -\nu & 0 & 0 & 0 \\ -\nu & 1 & -\nu & 0 & 0 & 0 \\ -\nu & -\nu & 1 & 0 & 0 & 0 \\ 0 & 0 & 0 & 2(1+\nu) & 0 & 0 \\ 0 & 0 & 0 & 0 & 2(1+\nu) & 0 \\ 0 & 0 & 0 & 0 & 0 & 2(1+\nu) \end{pmatrix} \tag{B.10}$$

For the ***creep cells 2*** and ***3*** the strain increments are:

$$\Delta\mathbf{e}_{cr2}^{n+1}=\mathbf{e}_{cr2}^{n+1}-\mathbf{e}_{cr2}^{n}=\frac{1}{2\eta_{bc2}}\mathbf{P}\left(\tilde{\mathbf{t}}^{n}+\tilde{\mathbf{t}}^{n+1}\right) \tag{B.11}$$

$$\Delta\mathbf{e}_{cr3}^{n+1}=\mathbf{e}_{cr3}^{n+1}-\mathbf{e}_{cr3}^{n}=\frac{1}{2\eta_{dc3}}\mathbf{P}\left(\tilde{\mathbf{t}}^{n}+\tilde{\mathbf{t}}^{n+1}\right)=\frac{\delta_{dc}\left|\mathbf{q}_{\mathrm{w}}\right|}{2}\mathbf{P}\left(\tilde{\mathbf{t}}^{n}+\tilde{\mathbf{t}}^{n+1}\right) \tag{B.12}$$

The thermal strain and the instantaneous part of the shrinkage strain are computed as follows:

$$\left(\Delta\dot{\mathbf{e}}_{th}\right)^{n+1}=\alpha_{T}\left(T^{n+1}-T^{n}\right)\mathbf{1} \tag{B.13}$$

$$\left(\Delta\dot{\mathbf{e}}_{sh}^{inst}\right)^{n+1}=-\frac{\mathbf{1}}{3K^{T}_{\left(\Gamma^{n+0.5}\right)}}\left[\left(\overline{\alpha}_{(\Gamma)}p^{s}\right)^{n+1}-\left(\overline{\alpha}_{(\Gamma)}p^{s}\right)^{n}\right] \tag{B.14}$$

the viscous part of the shrinkage strain $\left(\Delta\dot{\boldsymbol{\varepsilon}}_{sh}^{visc}\right)^{n+1}$ is computed using the creep rheological model in which the stresses are now the solid pressures $\left(\overline{\alpha}_{(\Gamma)}\mathbf{1}p^{s}\right)^{n+1}$ and $\left(\overline{\alpha}_{(\Gamma)}\mathbf{1}p^{s}\right)^{n}$ using the previous described approach (eqs (B.1 - B.12)).

C. COEFFICIENTS OF THE MATRICES APPEARING IN EQUATION (1.98)

The coefficients which are not reported are equal to zero.

$$\mathbf{C}_{gg}=\int_{\Omega}\mathbf{N}_{\mathrm{p}}^{T}\left[\varepsilon\left(1-S^{l}\right)\frac{M_{A}}{RT}\mathbf{N}_{\mathrm{p}}\right]d\Omega \tag{C.1}$$

$$\mathbf{C}_{gc}=\int_{\Omega}\mathbf{N}_{\mathrm{p}}^{T}\left[-\rho^{gA}\varepsilon\frac{\partial S^{l}}{\partial p^{c}}\mathbf{N}_{\mathrm{p}}-\varepsilon\left(1-S^{l}\right)\frac{M_{A}}{RT}\frac{\partial p^{gW}}{\partial p^{c}}\mathbf{N}_{\mathrm{p}}\right]d\Omega \tag{C.2}$$

$$\mathbf{C}_{gt}=\int_{\Omega}\mathbf{N}_{\mathrm{p}}^{T}\left\{\varepsilon\left(1-S^{l}\right)\left[-\frac{M_{A}}{RT}\left(\frac{\partial p^{gW}}{\partial T}-\frac{p^{gW}}{T}\right)-\frac{M_{A}}{RT^{2}}p^{g}\right]\mathbf{N}_{t}\right\}d\Omega \tag{C.3}$$

$$\mathbf{C}_{cc} = \int_{\Omega} \mathbf{N}_{\mathrm{p}}^{T} \left[\varepsilon \left(\rho^{l} - \rho^{gW} \right) \frac{\partial S^{l}}{\partial p^{c}} \mathbf{N}_{\mathrm{p}} + \varepsilon \left(1 - S^{l} \right) \frac{M_{W}}{RT} \frac{\partial p^{gW}}{\partial p^{c}} \mathbf{N}_{\mathrm{p}} \right] d\Omega \tag{C.4}$$

$$\mathbf{C}_{ct} = \int_{\Omega} \mathbf{N}_{\mathrm{p}}^{T} \left[\varepsilon \left(1 - S^{l} \right) \frac{M_{W}}{RT} \left(\frac{\partial p^{gW}}{\partial T} - \frac{p^{gW}}{T} \right) \mathbf{N}_{t} \right] d\Omega \tag{C.5}$$

$$\mathbf{C}_{tc} = \int_{\Omega} \mathbf{N}_{t}^{T} \left(-H_{vap} \rho^{l} \varepsilon \frac{\partial S^{l}}{\partial p^{c}} \mathbf{N}_{\mathrm{p}} \right) d\Omega \tag{C.6}$$

$$\mathbf{C}_{tt} = \int_{\Omega} \mathbf{N}_{t}^{T} \left[\left(\rho C_{p} \right)_{\mathrm{eff}} \mathbf{N}_{t} \right] d\Omega \tag{C.7}$$

$$\left(\mathbf{C}_{uu} \right)_{ij} = -\int_{\Omega} \mathbf{B}^{\mathrm{T}} \mathbf{D}_{\mathrm{s}} \mathbf{B} d\Omega \tag{C.8}$$

$$\begin{aligned} \mathbf{K}_{gg} = & \int_{\Omega} \left(\nabla \mathbf{N}_{\mathrm{p}} \right)^{\mathrm{T}} \left(\rho^{gA} \frac{k_{rel}^{g} \mathbf{k}}{\mu^{g}} \nabla \mathbf{N}_{\mathrm{p}} \right) d\Omega + \\ & + \int_{\Omega} \left(\nabla \mathbf{N}_{\mathrm{p}} \right)^{\mathrm{T}} \left(\rho^{g} \frac{M_{A} M_{W}}{M_{g}^{2}} D^{\overline{Wg}} \frac{p^{gW}}{\left(p^{g} \right)^{2}} \nabla \mathbf{N}_{\mathrm{p}} \right) d\Omega \end{aligned} \tag{C.9}$$

$$\mathbf{K}_{gc} = \int_{\Omega} \left(\nabla \mathbf{N}_{\mathrm{p}} \right)^{\mathrm{T}} \left(-\rho^{g} \frac{M_{A} M_{W}}{M_{g}^{2}} D^{\overline{Wg}} \frac{1}{p^{g}} \frac{\partial p^{gW}}{\partial p^{c}} \nabla \mathbf{N}_{\mathrm{p}} \right) d\Omega \tag{C.10}$$

$$\mathbf{K}_{gt} = \int_{\Omega} \left(\nabla \mathbf{N}_{\mathrm{p}} \right)^{\mathrm{T}} \left(-\rho^{g} \frac{M_{A} M_{W}}{M_{g}^{2}} D^{\overline{Wg}} \frac{1}{p^{g}} \frac{\partial p^{gW}}{\partial T} \nabla \mathbf{N}_{\mathrm{p}} \right) d\Omega + \tag{C.11}$$

$$\begin{aligned} \mathbf{K}_{cg} = & \int_{\Omega} \left(\nabla \mathbf{N}_{\mathrm{p}} \right)^{\mathrm{T}} \left(-\rho^{g} \frac{M_{A} M_{W}}{M_{g}^{2}} D^{\overline{Wg}} \frac{p^{gW}}{\left(p^{g} \right)^{2}} \nabla \mathbf{N}_{\mathrm{p}} \right) d\Omega + \\ & + \int_{\Omega} \left(\nabla \mathbf{N}_{\mathrm{p}} \right)^{\mathrm{T}} \left(\rho^{gW} \frac{k_{rel}^{g} \mathbf{k}}{\mu^{g}} \nabla \mathbf{N}_{\mathrm{p}} + \rho^{l} \frac{k_{rel}^{l} \mathbf{k}}{\mu^{l}} \nabla \mathbf{N}_{\mathrm{p}} \right) d\Omega + \end{aligned} \tag{C.12}$$

$$\begin{aligned} \mathbf{K}_{cc} = & \int_{\Omega} \left(\nabla \mathbf{N}_{\mathrm{p}} \right)^{\mathrm{T}} \left(\rho^{g} \frac{M_{A} M_{W}}{M_{g}^{2}} D^{\overline{Wg}} \frac{1}{p^{g}} \frac{\partial p^{gW}}{\partial p^{c}} \nabla \mathbf{N}_{\mathrm{p}} \right) d\Omega + \\ & + \int_{\Omega} \left(\nabla \mathbf{N}_{\mathrm{p}} \right)^{\mathrm{T}} \left(-\rho^{l} \frac{k_{rel}^{l} \mathbf{k}}{\mu^{l}} \nabla \mathbf{N}_{\mathrm{p}} \right) d\Omega \end{aligned} \tag{C.13}$$

$$\mathbf{K}_{ct} = \int_{\Omega} \left(\nabla \mathbf{N}_{\mathrm{p}} \right)^{\mathrm{T}} \left(\rho^{g} \frac{M_{A} M_{W}}{M_{g}^{2}} D^{\overline{Wg}} \frac{1}{p^{g}} \frac{\partial p^{gW}}{\partial T} \nabla \mathbf{N}_{t} \right) d\Omega + \tag{C.14}$$

$$\mathbf{K}_{tg} = \int_{\Omega} \left(\nabla \mathbf{N}_{t} \right)^{\mathrm{T}} \left(-H_{vap} \rho^{l} \frac{k_{rel}^{l} \mathbf{k}}{\mu^{l}} \nabla \mathbf{N}_{\mathrm{p}} \right) d\Omega \tag{C.15}$$

$$\mathbf{K}_{tc} = \int_{\Omega} \left(\nabla \mathbf{N}_t\right)^{\mathrm{T}} \left(H_{vap} \rho^l \frac{k_{rel}^l \mathbf{k}}{\mu^l} \nabla \mathbf{N}_{\mathrm{p}} \right) d\Omega \tag{C.16}$$

$$\mathbf{K}_{tt} = \int_{\Omega} \left(\nabla \mathbf{N}_t\right)^{\mathrm{T}} \left(\boldsymbol{\lambda}_{\mathrm{eff}} \nabla \mathbf{N}_t\right) d\Omega \tag{C.17}$$

$$\mathbf{f}_g = \int_{\Omega} \mathbf{N}_{\mathrm{p}}^T \left(\rho^{gA} \varepsilon \frac{\partial S^l}{\partial \Gamma} - \rho^{gA} \left(1 - S^l\right) \frac{\partial \varepsilon}{\partial \Gamma} \right) \frac{\partial \Gamma}{\partial t} d\Omega \tag{C.18}$$

$$\mathbf{f}_c = -\int_{\Omega} \mathbf{N}_{\mathrm{p}}^T \left[\left(\rho^l S^l + \rho^{gW} S^g \right) \frac{\partial \varepsilon}{\partial \Gamma} + \varepsilon \left(\rho^l - \rho^{gW} \right) \frac{\partial S^l}{\partial \Gamma} + 0.228 c \xi_{\infty} \right] \frac{\partial \Gamma}{\partial t} d\Omega \tag{C.19}$$

$$\begin{aligned} \mathbf{f}_t = & \int_{\Omega} \mathbf{N}_t^T L_{hydr} \frac{\mathrm{d}\Gamma}{\mathrm{d}t} d\Omega \\ & + \int_{\Omega} \mathbf{N}_t^T H_{vap} \left(0.228 c \xi_{\infty} + \rho^l \varepsilon \frac{\partial S^l}{\partial \Gamma} + \rho^l S^l \frac{\partial \varepsilon}{\partial \Gamma} \right) \frac{\partial \Gamma}{\partial t} d\Omega \\ & - \int_{\Omega} \mathbf{N}_t^T \left\{ \nabla H_{vap} \cdot \left[\rho^l \frac{k_{rel}^l \mathbf{k}}{\mu^l} \nabla \left(p^g - p^c \right) \right] \right\} d\Omega \end{aligned} \tag{C.20}$$

$$\mathbf{f}_u = \int_{\Omega} \mathbf{B}^T \left(\mathbf{D}_s \frac{\partial \mathbf{e}_{th}}{\partial t} \right) d\Omega + \int_{\Omega} \mathbf{B}^T \left(\mathbf{D}_s \frac{\partial \mathbf{e}_{sh}}{\partial t} \right) d\Omega + \int_{\Omega} \mathbf{B}^T \left(\mathbf{D}_s \frac{\partial \mathbf{e}_{cr}}{\partial t} \right) d\Omega \tag{C.21}$$

D. COEFFICIENTS OF THE MATRICES APPEARING IN EQUATION (4.41)

In the following equations K^s is the Bulk modulus of the solid skeleton and $\frac{\partial \mathbf{e}_{sw}^s}{\partial t} = \frac{\mathbf{1}}{3K^s} \frac{\partial p^s}{\partial t}$ is the swelling strain rate depending on the solid pressure (eqn (4.27)).

$$\mathbf{C}_{nn} = \int_{\Omega} \mathbf{N}_n^T \left(\varepsilon S^l \mathbf{N}_n \right) d\Omega \tag{D.1}$$

$$\mathbf{C}_{tt} = \int_{\Omega} \mathbf{N}_t^T \left[\varepsilon \mathbf{N}_t + \frac{S^t}{K^s} \left(S^t \frac{\partial p^t}{\partial S^t} + S^h \frac{\partial p^h}{\partial S^t} + p^t - p^l \right) \mathbf{N}_t \right] d\Omega \tag{D.2}$$

$$\mathbf{C}_{th} = \int_{\Omega} \mathbf{N}_t^T \left[\frac{S^t}{K^s} \left(S^t \frac{\partial p^t}{\partial S^h} + S^h \frac{\partial p^h}{\partial S^h} + p^h - p^l \right) \mathbf{N}_h \right] d\Omega \tag{D.3}$$

$$\mathbf{C}_{tl} = \int_{\Omega} \mathbf{N}_t^T \left[\frac{S^t}{K^s} \left(S^t \frac{\partial p^t}{\partial p^l} + S^h \frac{\partial p^h}{\partial p^l} + S^l \right) \mathbf{N}_l \right] d\Omega \tag{D.4}$$

$$\mathbf{C}_{ht} = \int_{\Omega} \mathbf{N}_h^T \left[\frac{S^h}{K^s} \left(S^t \frac{\partial p^t}{\partial S^t} + S^h \frac{\partial p^h}{\partial S^t} + p^t - p^l \right) \mathbf{N}_t \right] d\Omega \tag{D.5}$$

$$\mathbf{C}_{hh} = \int_{\Omega} \mathbf{N}_h^T \left[\varepsilon \mathbf{N}_h + \frac{S^h}{K^s} \left(S^t \frac{\partial p^t}{\partial S^h} + S^h \frac{\partial p^h}{\partial S^h} + p^h - p^l \right) \mathbf{N}_h \right] d\Omega \tag{D.6}$$

$$\mathbf{C}_{hl} = \int_{\Omega} \mathbf{N}_h^T \left[\frac{S^h}{K^s} \left(S^t \frac{\partial p^t}{\partial p^l} + S^h \frac{\partial p^h}{\partial p^l} + S^l \right) \mathbf{N}_l \right] d\Omega \tag{D.7}$$

$$\mathbf{C}_{lt} = \int_{\Omega} \mathbf{N}_l^T \left[\frac{1}{K^s} \left(S^t \frac{\partial p^t}{\partial S^t} + S^h \frac{\partial p^h}{\partial S^t} + p^t - p^l \right) \mathbf{N}_t \right] d\Omega \tag{D.8}$$

$$\mathbf{C}_{lh} = \int_{\Omega} \mathbf{N}_l^T \left[\frac{1}{K^s} \left(S^t \frac{\partial p^t}{\partial S^h} + S^h \frac{\partial p^h}{\partial S^h} + p^h - p^l \right) \mathbf{N}_h \right] d\Omega \tag{D.9}$$

$$\mathbf{C}_{ll} = \int_{\Omega} \mathbf{N}_l^T \left[\frac{1}{K^s} \left(S^t \frac{\partial p^t}{\partial p^l} + S^h \frac{\partial p^h}{\partial p^l} + S^l \right) \mathbf{N}_l \right] d\Omega \tag{D.10}$$

$$\left(\mathbf{C}_{uu} \right)_{ij} = -\int_{\Omega} \mathbf{B}^{\mathrm{T}} \mathbf{D}_s \mathbf{B} d\Omega \tag{D.11}$$

$$\mathbf{K}_{nn} = \int_{\Omega} \left(\nabla \mathbf{N}_n \right)^{\mathrm{T}} \left(\varepsilon S^l D_{eff}^{\overline{nl}} \nabla \mathbf{N}_n \right) d\Omega \tag{D.12}$$

$$\mathbf{K}_{tt} = \int_{\Omega} \left(\nabla \mathbf{N}_t \right)^{\mathrm{T}} \left(\frac{k_{rel}^t \mathbf{k}^{ts}}{\mu^t} \frac{\partial p^t}{\partial S^t} \nabla \mathbf{N}_t \right) d\Omega \tag{D.13}$$

$$\mathbf{K}_{th} = \int_{\Omega} \left(\nabla \mathbf{N}_t \right)^{\mathrm{T}} \left(\frac{k_{rel}^t \mathbf{k}^{ts}}{\mu^t} \frac{\partial p^t}{\partial S^h} \nabla \mathbf{N}_h \right) d\Omega \tag{D.14}$$

$$\mathbf{K}_{tl} = \int_{\Omega} \left(\nabla \mathbf{N}_t \right)^{\mathrm{T}} \left(\frac{k_{rel}^t \mathbf{k}^{ts}}{\mu^t} \frac{\partial p^t}{\partial p^l} \nabla \mathbf{N}_l \right) d\Omega \tag{D.15}$$

$$\mathbf{K}_{ht} = \int_{\Omega} \left(\nabla \mathbf{N}_h \right)^{\mathrm{T}} \left(\frac{k_{rel}^h \mathbf{k}^{hs}}{\mu^h} \frac{\partial p^h}{\partial S^t} \nabla \mathbf{N}_t \right) d\Omega \tag{D.16}$$

$$\mathbf{K}_{hh} = \int_{\Omega} \left(\nabla \mathbf{N}_h \right)^{\mathrm{T}} \left(\frac{k_{rel}^h \mathbf{k}^{hs}}{\mu^h} \frac{\partial p^h}{\partial S^h} \nabla \mathbf{N}_h \right) d\Omega \tag{D.17}$$

$$\mathbf{K}_{hl} = \int_{\Omega} \left(\nabla \mathbf{N}_h \right)^{\mathrm{T}} \left(\frac{k_{rel}^h \mathbf{k}^{hs}}{\mu^h} \frac{\partial p^h}{\partial p^l} \nabla \mathbf{N}_l \right) d\Omega \tag{D.18}$$

$$\mathbf{K}_{lt} = \int_{\Omega} \left(\nabla \mathbf{N}_l \right)^{\mathrm{T}} \left(\frac{k_{rel}^t \mathbf{k}^{ts}}{\mu^t} \frac{\partial p^t}{\partial S^t} \nabla \mathbf{N}_t + \frac{k_{rel}^h \mathbf{k}^{hs}}{\mu^h} \frac{\partial p^h}{\partial S^t} \nabla \mathbf{N}_t \right) d\Omega \tag{D.19}$$

$$\mathbf{K}_{lh} = \int_{\Omega} \left(\nabla \mathbf{N}_l \right)^{\mathrm{T}} \left(\frac{k_{rel}^t \mathbf{k}^{ts}}{\mu^t} \frac{\partial p^t}{\partial S^h} \nabla \mathbf{N}_h + \frac{k_{rel}^h \mathbf{k}^{hs}}{\mu^h} \frac{\partial p^h}{\partial S^h} \nabla \mathbf{N}_h \right) d\Omega \tag{D.20}$$

$$\mathbf{K}_{ll} = \int_{\Omega} \left(\nabla \mathbf{N}_l \right)^{\mathrm{T}} \left(\frac{k_{rel}^t \mathbf{k}^{ts}}{\mu^t} \frac{\partial p^t}{\partial p^l} \nabla \mathbf{N}_l + \frac{k_{rel}^h \mathbf{k}^{hs}}{\mu^h} \frac{\partial p^h}{\partial p^l} \nabla \mathbf{N}_l + \frac{k_{rel}^l \mathbf{k}^{ls}}{\mu^l} \nabla \mathbf{N}_l \right) d\Omega \tag{D.21}$$

$$\mathbf{f}_n = \int_\Omega \mathbf{N}_n^T \left(\frac{1}{\rho} \left(\bar{\omega}^{nl} \overset{l\to t}{M} - \overset{nl\to t}{M} \right) - \varepsilon S^l \bar{\mathbf{v}}^l \cdot \nabla \bar{\omega}^{nl} \right) d\Omega \tag{D.22}$$

$$\mathbf{f}_t = \int_\Omega \mathbf{N}_t^T \left[\frac{1}{\rho} \overset{l\to t}{\underset{growth}{M}} - S^t \operatorname{tr}\left(\frac{\partial \mathbf{e}^s}{\partial t} - \frac{\partial \mathbf{e}_{sw}^s}{\partial t} \right) - \nabla\left(S^t\right) \cdot \left(\varepsilon \frac{\partial \mathbf{u}^s}{\partial t} \right) \right] d\Omega \tag{D.23}$$

$$\mathbf{f}_h = \int_\Omega \mathbf{N}_h^T \left[-S^h \operatorname{tr}\left(\frac{\partial \mathbf{e}^s}{\partial t} - \frac{\partial \mathbf{e}_{sw}^s}{\partial t} \right) - \nabla\left(S^h\right) \cdot \left(\varepsilon \frac{\partial \mathbf{u}^s}{\partial t} \right) \right] d\Omega \tag{D.24}$$

$$\mathbf{f}_l = \int_\Omega \mathbf{N}_l^T \left[-\operatorname{tr}\left(\frac{\partial \mathbf{e}^s}{\partial t} - \frac{\partial \mathbf{e}_{sw}^s}{\partial t} \right) \right] d\Omega \tag{D.25}$$

$$\mathbf{f}_u = \int_\Omega \mathbf{B}^T \left(\mathbf{D}_s \frac{\partial \mathbf{e}_{vp}^s}{\partial t} \right) d\Omega + \int_\Omega \mathbf{B}^T \left(\mathbf{D}_s \frac{\partial \mathbf{e}_{sw}^s}{\partial t} \right) d\Omega \tag{D.26}$$